

ALMA MATER STUDIORUM – UNIVERSITÀ DI BOLOGNA

DOTTORATO DI RICERCA IN BIOINGEGNERIA

Ciclo XXVII

Settore concorsuale di afferenza: 09/G2

Settore scientifico disciplinare: ING-INF/06

**Computational Modelling
of Cardiac Electrophysiology:
from Cell to Bedside**

Presentata da

Elisa Passini

Coordinatore Dottorato:

Prof. Elisa Magosso

Supervisore:

Stefano Severi, PhD

Revisori:

Prof. Mauro Ursino

Prof. Ronald Wilders

Prof. Esther Pueyo

Esame Finale Anno 2015

ALMA MATER STUDIORUM – UNIVERSITÀ DI BOLOGNA

DOTTORATO DI RICERCA IN BIOINGEGNERIA

Ciclo XXVII

Settore concorsuale di afferenza: 09/G2

Settore scientifico disciplinare: ING-INF/06

**Computational Modelling
of Cardiac Electrophysiology:
from Cell to Bedside**

Presented by

Elisa Passini

PhD Coordinator:

Prof. Elisa Magosso

Supervisor:

Stefano Severi, PhD

Reviewers:

Prof. Mauro Ursino

Prof. Ronald Wilders

Prof. Esther Pueyo

Final Exam Year 2015

To my Super Supervisor

***“It is a truth universally acknowledged,
that a single cell in possession of a good membrane,
must be in want of a model...”***

Adapted from *Pride & Prejudice*,
by Jane Austen

TABLE OF CONTENTS

TABLE OF CONTENTS	9
SUMMARY	13
SOMMARIO	19
INTRODUCTION	21
CHAPTER 1	
Basic Concepts of the Electrical Activity of the Heart and its Mathematical Modelling	23
THE CARDIAC ELECTRICAL ACTIVITY	25
MODELLING THE CARDIAC ELECTRICAL ACTIVITY.....	31
CHAPTER 2	
Human Ventricular Action Potential Models: a Literature Review	35
MODELS ON THE MARKET	37
MODELS COMPARISON.....	40
<i>References</i>	47
SECTION I	
Extracellular Calcium and Action Potential Duration: the Fine Balance between L-Type Calcium Current Inactivation Mechanisms	51

CHAPTER 3**A Novel Markov Model of L-Type Calcium Current to Explore Inactivation Mechanisms..... 53**

Abstract..... 55

INTRODUCTION 55

METHODS 58

RESULTS 61

DISCUSSION AND CONCLUSIONS 67

CHAPTER 4**Extracellular Electrolyte Changes During Head-Down Bed-Rest: Effects on Action Potential Duration..... 69**

Abstract..... 71

INTRODUCTION 71

METHODS 72

RESULTS 75

DISCUSSION AND CONCLUSIONS 80

References 83**SECTION II****Haemodialysis Therapy Impact on Cardiac****Electrophysiology 87****CHAPTER 5****Human Atrial Cell Models to Analyse Haemodialysis-related Effects on Cardiac Electrophysiology: Work in Progress..... 89**

Abstract..... 91

INTRODUCTION 91

CARDIAC CELL MODELLING AND HAEMODIALYSIS 93

ATRIAL CELL MODELLING: MATERIALS AND METHODS 94

ATRIAL CELL MODELLING: EFFECTS OF HD-RELATED CHANGES 101

DISCUSSION AND CONCLUSIONS	114
CHAPTER 6	
Recurrent Intradialytic Paroxysmal Atrial Fibrillation: Hypotheses on Onset Mechanisms Based on Clinical Data and Computational Analysis.....	119
Abstract.....	121
INTRODUCTION.....	121
CASE REPORT	122
COMPUTATIONAL ANALYSIS.....	125
INSIGHTS INTO THE MECHANISMS OF INTRADIALYTIC ATRIAL FIBRILLATION	128
DISCUSSION AND CONCLUSIONS	134
References	137
SECTION III	
Computational Modelling of Human Hypertrophic Cardiomyopathy	149
CHAPTER 7	
Pro-Arrhythmic Mechanisms and Potential Therapeutic Targets in Human Hypertrophic Cardiomyopathy.....	151
Abstract.....	153
INTRODUCTION.....	154
METHODS	158
RESULTS	166
CONCLUSIONS.....	195
References	197
GENERAL CONCLUSIONS	199
APPENDIX A.....	207

APPENDIX B.....	223
LIST OF PUBLICATIONS.....	245
RINGRAZIAMENTI.....	247
ACKNOWLEDGEMENTS.....	249

SUMMARY

Introduction

Heart diseases are the leading cause of death worldwide, both for men and women. However, the ionic mechanisms underlying many cardiac arrhythmias and genetic disorders are not completely understood, thus leading to a limited efficacy of the current available therapies and leaving many open questions for cardiac electrophysiologists.

On the other hand, experimental data availability is still a great issue in this field: most of the experiments are performed *in vitro* and/or using animal models (e.g. rabbit, dog and mouse), even when the final aim is to better understand the electrical behaviour of *in vivo* human heart either in physiological or pathological conditions.

Computational modelling constitutes a primary tool in cardiac electrophysiology: *in silico* simulations, based on the available experimental data, may help to understand the electrical properties of the heart and the ionic mechanisms underlying a specific phenomenon. Once validated, mathematical models can be used for making predictions and testing hypotheses, thus suggesting potential therapeutic targets.

Aims

This PhD thesis aims to apply computational cardiac modelling of human single cell action potential (AP) to three clinical scenarios, in order to gain new insights into the ionic mechanisms involved in the electrophysiological changes observed *in vitro* and/or *in vivo*:

- The first context is blood electrolyte variations, which may occur in patients due to different pathologies and/or therapies. In particular, we focused on extracellular Ca^{2+} and its effect on the AP duration (APD).

- The second context is haemodialysis (HD) therapy: in addition to blood electrolyte variations, patients undergo a lot of other different changes during HD, e.g. heart rate, cell volume, pH, and sympatho-vagal balance.
- The third context is human hypertrophic cardiomyopathy (HCM), a genetic disorder characterised by an increased arrhythmic risk, and still lacking a specific pharmacological treatment.

The general aim of this PhD thesis can therefore be referred to as “From Cell to Bedside”, meaning to correlate single cell electrophysiology with some specific clinical patient phenotypes, by using *in silico* techniques to highlight the mechanisms more likely contributing to them at the ionic level.

Methods

Many computational AP models published in literature, both atrial and ventricular, have been considered during this thesis. These models have been modified when needed, to improve their suitability to specific conditions, not originally taken into account during their development/validation. In particular, a new hybrid ventricular model has been developed, by using an existing one as basis and changing part of its original formulation.

All models provide a full description of the ionic currents and intracellular dynamics underlying the cardiac cell AP, represented by means of ordinary differential equations solved by using a variable order solver, based on numerical differentiation formulas. The models have been implemented mostly in Matlab (Mathworks Inc.) and CHASTE (Cancer, Heart and Soft Tissue Environment, University of Oxford), an open-source software specifically developed for cardiac modelling and based on C⁺⁺.

In addition to the traditional single cell modelling techniques, the population of models (POMs) approach has been considered in the last Section of the thesis: instead of a single AP model, representative of the average cell behaviour, simulations have been run on thousands of models at the same time, hence representing the effect of biological variability.

Results Outline

Here below is a summary of the main results for the three different conditions investigated in this PhD thesis, each one illustrated in a different Section:

- In **Section I** the effects of extracellular Ca^{2+} ($[\text{Ca}^{2+}]_o$) changes on the human ventricular AP have been investigated: an increase of $[\text{Ca}^{2+}]_o$ shortens AP and a decrease of $[\text{Ca}^{2+}]_o$ lengthens it. Both AP duration (APD) increase and decrease are associated with a higher arrhythmic risk; therefore this dependence has to be considered in all the situations in which $[\text{Ca}^{2+}]_o$ variations may occur. However, most of the AP models currently available in literature do not reproduce properly the effect of $[\text{Ca}^{2+}]_o$ changes on AP.
- ✓ In **Chapter 3** a new Markov model for the L-type Ca^{2+} current has been proposed and integrated into the O'Hara-Rudy human ventricular AP: this hybrid model well simulates the inverse APD- $[\text{Ca}^{2+}]_o$ dependence, not reproduced by the original one. Its development has been driven by the hypothesis that Ca^{2+} -dependent inactivation is usually underestimated in AP models: our simulations confirmed the crucial role of this mechanism in determining the APD- $[\text{Ca}^{2+}]_o$ relationship. Therefore, the hybrid model can be applied to clinical conditions in which blood electrolyte concentrations change overtime, to evaluate the corresponding changes at the AP level and potential pro-arrhythmic effects.
- ✓ In **Chapter 4**, the hybrid model described in Chapter 3 has been used to investigate the impact of blood electrolyte changes measured during bed-rest. Bed-rest is a ground-based experiment used to simulate on Earth the effect of microgravity on the human body, thus assessing the possibly increased arrhythmic risk for astronauts during space flights. Simulation results in single cells and 1D cable were compared with ECG data analysis, providing evidence of a biphasic trend in repolarisation: RT intervals decrease during bed-rest and increase afterwards. The electrolyte concentrations have been used as model inputs to simulate volunteer conditions before, during, and after bed-rest. Simulated AP and pseudo-ECG were both in agreement with the recorded ECG, suggesting that electrolyte variations occurring during bed-rest may be responsible for the repolarisation changes, and thus correlating the

electrophysiological phenotype with the modification at the cellular level. This project has been done in collaboration with Prof. Enrico G Caiani (Department of Electronics, Information and Bioengineering, Politecnico di Milano, Italy) and the experimental data have been acquired by the European Space Agency (ESA).

- **Section II** investigates the impact of haemodialysis (HD) therapy on the electrical activity of the heart, focusing on the electrolyte variations occurring during a regular HD session and evaluating the corresponding changes at cellular level. Here, human atrial AP models have been considered, since atrial fibrillation (AF) incidence is high in end-stage renal disease (ESRD) patients.
- ✓ **Chapter 5** presents a benchmarking of all the atrial AP models currently available in literature, with respect to their suitability to the HD context. All models have been tested for variations in cell volume, extracellular electrolyte (K^+ , Ca^{2+} and Na^+) and acetylcholine concentration, computing a set of AP and Ca^{2+} -transient biomarkers to compare simulation results with the expected behaviour, based on literature review. Some models proved to be more appropriate than others for single aspects, but all of them showed some drawbacks. Suggestions have been given for the potential development of a new atrial model, expected to reproduce properly all the HD-induced effects on human atrial AP.
- ✓ **Chapter 6** illustrates the case study of an ESRD patient showing recurring paroxysmal AF during HD therapy. Experimental data, i.e. blood electrolyte concentrations and heart rate, have been used to reproduce *in silico* the patient pre-HD and pre-AF conditions at cellular level, using a modified version of the Courtemanche atrial AP model, described in Chapter 5. By integrating simulation results and clinical observations, we formulated a new hypothesis about the mechanisms involved in AF onset during HD: AF episodes are induced by the presence of a trigger (ectopic beats) that acts upon an acute substrate induced by intra-dialytic electrolyte variations, especially K^+ (increased AP depolarization time and shortened refractory period), on the background of autonomic nervous system changes. This project has been

done in collaborations with Simonetta Genovesi, MD and Antonio Vincenti, MD (Department of Health Sciences, University of Milano Bicocca, Italy).

- ✓ In **Section III (Chapter 7)** the population of models (POMs) approach has been used to study the electrical remodelling occurring in human hypertrophic cardiomyopathy (HCM), in order to identify possible therapeutic targets for this disease. The POMs approach accounts for inter- and intra- subjects variability, which indeed seems to play an important role in HCM and which cannot be taken into account when considering a single AP model, representative of the average cellular behaviour.
- ✓ As first, a control (CTRL) population of models has been built to reproduce an experimental dataset of AP and Ca^{2+} transient (CaT) biomarkers, acquired on human single cells from non-failing non-hypertrophic controls.
- ✓ Then, a HCM population has been developed by applying to the CTRL population the electrophysiological changes measured in diseased cells, together with a few novel hypotheses based on literature review. The simulated HCM biomarkers resulted to be in agreement with the experimental ones, and the contribution of each single electrophysiological change to the global HCM phenotype has been evaluated.
- ✓ The occurrence of repolarisation abnormalities, e.g. early after-depolarisations (EADs) and repolarisation failure (RF), has been investigated in the HCM population and the ionic mechanisms more likely to be responsible for them have been identified.
- ✓ Since specific compounds are already available, the Late Na^+ current (I_{NaL}) and the $\text{Na}^+/\text{Ca}^{2+}$ exchanger (I_{NCX}) have been considered as potential therapeutic targets. Both I_{NaL} and I_{NCX} selective blocks showed an anti-arrhythmic effect, partially reversing the HCM phenotype and suppressing repolarisation abnormalities. The combination of both proved to be even more effective, suggesting the simultaneous block of I_{NaL} and I_{NCX} as a successful anti-arrhythmic therapy in human HCM.

- ✓ This project has been done as a visiting student in the Department of Computer Science, University of Oxford (UK), under the supervision of Prof. Blanca Rodriguez, Alfonso Bueno-Orovio, PhD and Ana Mincholé, PhD, and in collaboration with Raffaele Coppini, MD and Elisabetta Cerbai, MD (NeuroFarBa Department, University of Florence, Italy).

To summarize, the results presented in this thesis have improved the understanding of the ionic mechanisms underlying electrophysiological properties related to arrhythmic risk in specific clinical contexts, thus confirming computational modelling as a valuable tool in cardiac electrophysiology, especially when fully integrated with experimental data.

SOMMARIO

Le malattie cardiache e cardiovascolari sono ad oggi la causa principale di morte nel mondo. Tuttavia, i meccanismi ionici responsabili di aritmie o di altre malattie cardiache non sono ancora del tutto conosciuti: questo spesso porta a una minore o mancata efficacia delle terapie attualmente disponibili, e lascia numerose domande aperte per gli elettrofisiologi. Inoltre, la difficoltà di acquisizione dei dati sperimentali rimane ancora uno dei problemi più grandi in questo campo. Infatti la maggior parte dei dati vengono raccolti *in vitro* e/o utilizzando modelli animali come coniglio, ratto o cane, sebbene l'obiettivo ultimo sia quello di una più completa comprensione del comportamento elettrico del cuore *in vivo* e nell'uomo, in condizioni sia fisiologiche sia patologiche.

In questo contesto, la modellistica computazionale costituisce uno strumento indispensabile: infatti, le simulazioni *in silico* permettono di superare, almeno in parte, i limiti sperimentali, e di investigare i meccanismi ionici alla base di specifici fenomeni a diversi livelli (singola cellula, tessuto, intero cuore). Una volta validati sui dati sperimentali, i modelli matematici possono essere dunque utilizzati per fare predizioni, testare ipotesi e valutare l'efficacia di eventuali interventi farmacologici.

Lo scopo di questa tesi di dottorato è stato quello di applicare tecniche di modellistica matematica a problemi di elettrofisiologia cardiaca, in particolare utilizzando modelli di potenziale d'azione (PA) umano in tre diversi contesti:

- Variazioni del livello di elettroliti (Na^+ , K^+ e Ca^{2+}) nel sangue, che possono verificarsi nei pazienti a causa di diverse patologie e/o terapie, con possibili conseguenze pro-aritmiche. Sono state considerate in particolare variazioni di Ca^{2+} e il loro effetto sulla durata del PA ventricolare, aspetto solitamente trascurato nei modelli a oggi disponibili. È stato sviluppato un nuovo modello di PA, integrando una nuova formulazione per la corrente di Ca^{2+} in un modello già esistente: il modello ibrido così ottenuto costituisce uno strumento importante per esplorare i contesti clinici in cui le variazioni elettrolitiche possono verificarsi. Come esempio applicativo, sono stati analizzati dati sperimentali

raccolti dall'Agencia Spaziale Europea (ESA) per valutare l'eventuale rischio aritmico per gli astronauti durante i voli nello spazio. Questo studio è stato svolto in collaborazione con il Prof. Enrico Caiani (Dipartimento di Elettronica, Informazione e Bioingegneria, Politecnico di Milano, Italia).

- Variazioni elettrofisiologiche che avvengono durante la terapia dialitica. In questo contesto non si modificano soltanto le concentrazioni elettrolitiche ma anche la frequenza cardiaca, il volume cellulare e l'attività simpato-vagale. Dal momento che la fibrillazione atriale (FA) ha un'incidenza elevata nei pazienti in dialisi, sono stati considerati modelli di PA atriale, confrontando le loro caratteristiche e la loro applicabilità in questo contesto. Come esempio, è stato analizzato il caso di una paziente che presentava FA parossistica in ogni seduta dialitica. Questo studio è stato svolto in collaborazione con la Dott.ssa Simonetta Genovesi e il Dott. Antonio Vincenti, (Dipartimento di Scienze della Salute, Università degli Studi di Milano-Bicocca, Italia).
- Cardiomiopatia ipertrofica (HCM), una malattia genetica caratterizzata da un alto rischio aritmico e causa principale di morte cardiaca improvvisa nei giovani adulti (<35 anni). Per tener conto della variabilità biologica, che sembra avere un ruolo determinante in questa patologia, soprattutto nella risposta individuale a un possibile trattamento farmacologico, è stato utilizzato un nuovo approccio computazionale: le popolazioni di modelli. Questo studio è stato svolto durante un periodo di ricerca all'estero presso il Dipartimento di Computer Science dell'Università di Oxford, sotto la supervisione della Prof. Blanca Rodriguez, il Dott. Alfonso Bueno-Orovio, e la Dott.ssa Ana Mincholé.

Il filo conduttore di questa tesi può quindi essere riassunto dall'espressione "Dalla Cellula al Paziente". Non a caso, in tutti gli scenari analizzati, lo scopo principale è stato quello di correlare i cambiamenti elettrofisiologici a livello cellulare con il fenotipo osservato a livello macroscopico nel paziente, per identificare i meccanismi ionici che vi contribuiscono e suggerire di conseguenza possibili approcci farmacologici. I risultati ottenuti hanno confermato l'importanza dei modelli matematici come supporto all'elettrofisiologia cardiaca, specialmente quando l'approccio *in silico* viene utilizzato in sinergia con quello *in vitro*.

INTRODUCTION

CHAPTER 1

Basic Concepts of the Electrical Activity of the Heart and its Mathematical Modelling

THE CARDIAC ELECTRICAL ACTIVITY

The heart is situated slightly to the left of the middle of the thorax, underneath the sternum, between the lungs. It is supported inside a structure known as the pericardial sac, a double membrane structure containing a serous fluid to reduce friction during heart contractions.

There are four major chambers in the heart: the larger, lower, thicker walled chambers are the ventricles, while the smaller, upper, thinner chambers are the atria. The bottom of the ventricles is called the apex and their top part is known as the base. Both the atria and the ventricles are separated into independent left and right halves by the septal wall. The function of the right atrium is to collect deoxygenated blood from the body. After contraction of the atria, this blood is passed to the right ventricle and pumped into the lungs (pulmonary circulation) to produce the gas exchange between carbon dioxide and oxygen. The re-oxygenated blood from the lungs is then collected in the left atrium, from where it moves to the left ventricle which pumps it out to the body. Since the right ventricle only pumps blood through the pulmonary circulation system of the lungs, whilst the left ventricle pumps blood to the rest of the body, the left ventricle is considerably thicker than the right.

Mechanical contraction of the heart is caused by the electrical activation of myocardial cells. The electrical activation sequence (Figure 1.1, left side) of the human heart starts at the sinoatrial node, located in the right atrium at the superior vena cava. This node consists of specialized muscle cells which are self-excitatory, pacemaker cells, able to generate an electrical impulse at a rate of about 70 per minute. From the sinoatrial node, the wave of electrical activation propagates throughout the atria, but cannot propagate directly across the annulus of separation between the atria and the ventricles. The atrioventricular node, located at the boundary between the atria and ventricles, is the only conducting path from the atria to the ventricles in a normal heart. Conduction velocity through the atrioventricular node is considerably delayed in order to supply enough time to the atria to fill the ventricles with blood before the beginning of their contraction. Propagation then proceeds through a specialized conduction system, called the bundle of His. After a short distance, it separates into two bundle branches propagating along each side of

the septum, constituting the left and right bundle branches. Both branches then continue to subdivide into a complex network of fibres called the Purkinje fibre network, which spreads across the endocardial surface and into the sub-endocardial region of both ventricles. The fast conduction through the bundle branches and Purkinje fibres causes the entire endocardium to be excited almost simultaneously, although apical regions contract first and the basal regions are usually the latest to be excited.

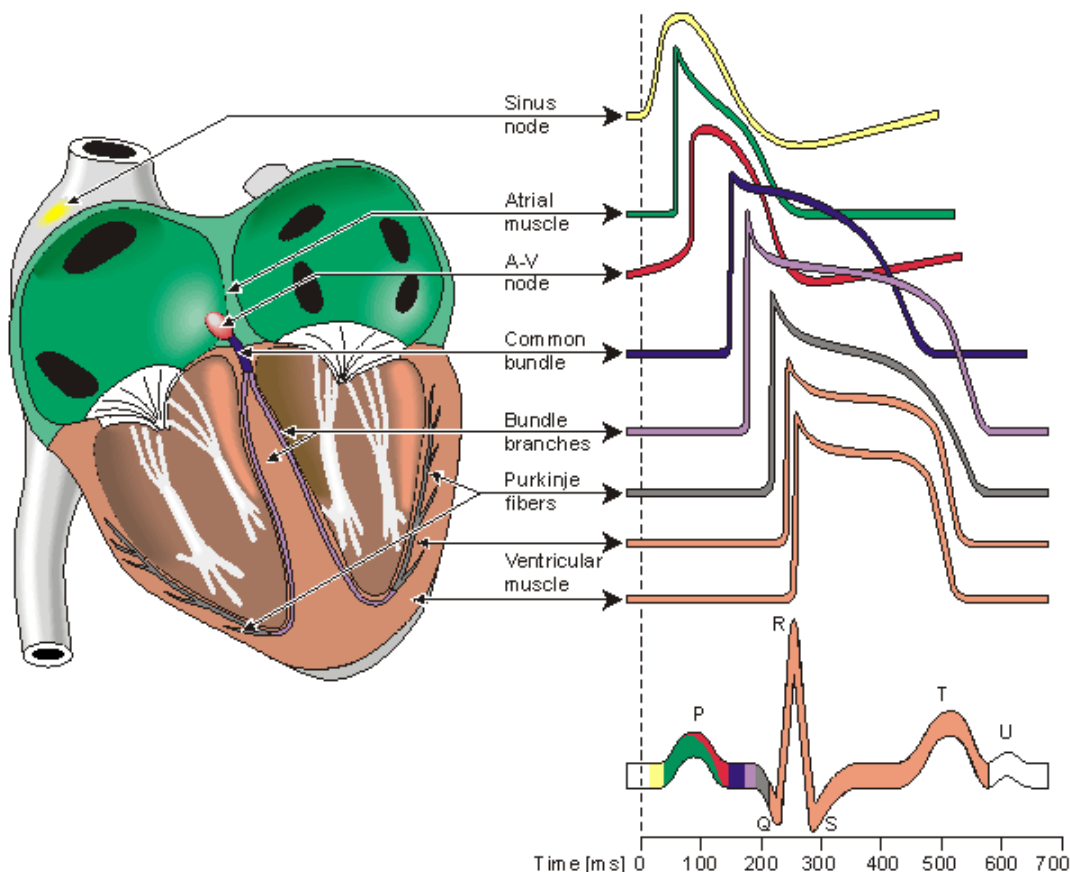


Figure 1.1: *Electrophysiology of the heart. The different action potentials for each of the specialized cells found in the heart, and their contribution to the total electrocardiogram waveform are shown (modified from [1]).*

Cardiac Action Potential and ECG

Cardiac muscle cells or myocytes are approximately flattened tubes, about 80-100 μm long in human ventricular tissue, with elliptic cross sections with a major axis of 10-20 μm . They are arranged in discrete layers of fibres called sheets, roughly parallel to the heart surfaces (epicardium and endocardium), with the fibre axis continuously rotating counter clockwise from epicardium to endocardium in a range of 100° - 120° as viewed from the top of epicardium. Each cardiac muscle cell

is bounded by a thin (5-7 nm) phospholipid membrane or sarcolemma. This membrane encapsulates a small volume that is known as the intracellular space, whereas the extracellular or interstitial space is therefore defined as the space that lies outside the sarcolemma. The membrane is heterogeneous, with numerous large, complex proteins embedded within it, combined to form small pores in the cell membrane. Under most circumstances these pores are selectively permeable, allowing the pass of only specific ions through the membrane and only under certain conditions, reason why they are commonly called ion channels.

The main ions that are of interest in cardiac electrophysiology are Na^+ , K^+ , Ca^{2+} and Cl^- . At resting, the intracellular and extracellular concentrations of each ion are substantially different. In principle, this difference on concentrations would produce a chemical force that would make ions to flow down their concentration gradient to create a uniform distribution at both sides of the membrane. Nevertheless, different ionic concentrations also imply a net electrical charge difference between both sides of the membrane, what causes the establishment of an electrical gradient that acts to oppose the chemical gradient, thus allowing intra- and extracellular concentrations to be different. Consequently, at rest the cell membrane maintains a net membrane potential, which for cardiac muscle cells generally is between -90 and -80 mV, and the cell membrane is said to be in a polarized state.

However, under electrical excitation of the cell this electrochemical equilibrium is broken: this allows ions to flow through those ion channels to which they are permeable, if opened. Any positive increase of the transmembrane potential towards zero is therefore known as depolarization, while the term repolarization refers to the returning of the cell to its negative resting state.

Small perturbations in the potential difference across the cell membrane produce only a passive, linear response of the cardiac cell, followed by the returning of the transmembrane potential towards its resting state. On the contrary, when a sufficiently large stimulus is applied (i.e. able to rise the transmembrane potential above the threshold potential), an active, non-linear response, known as the action potential (AP) will be elicited.

Depending on the region of the heart, the cardiac AP may have different shapes and properties (Figure 1.1, right side): all these differences, together with the

particular activation sequence described above, are responsible for the macroscopical electrical activity of the heart, as measured in the electrocardiogram (ECG). In a conventional 12 lead ECG, ten electrodes are placed on the patient's limbs and on the surface of the chest. The overall magnitude of the heart's electrical potential is then measured from twelve different angles and recorded over a period of time. In this way, the overall magnitude and direction of the heart's electrical depolarization is captured at each moment throughout the cardiac cycle. The graph of voltage versus time produced by this non-invasive medical procedure, and referred to as ECG, is characterised mainly by 3 waves: a P wave (atrial depolarization), a QRS complex (ventricular depolarization) and a T wave (ventricular repolarization).

Despite these differences in shape and properties, the cardiac AP it is mainly characterised by 5 different phases, related to the opening/closing of the different ion channels (mainly Na^+ , Ca^{2+} and K^+), as shown in Figure 1.2:

- **Phase 0** (upstroke) when the threshold is reached, there is a rapid influx of Na^+ through the Na^+ channels, creating the fast Na^+ current (I_{Na}) who rise the membrane potential up to positive values.
- **Phase 1**: the Na^+ channels close, while K^+ channels open. Throughout the whole action potential duration there are different K^+ currents that tend to bring the transmembrane potential back to its resting value. In this phase, the main contribution is the one of the transient outward K^+ current, which causes a small deflection in the membrane voltage, called “notch”.
- **Phase 2**: the outward K^+ currents are counteracted by the opening of Ca^{2+} channels, responsible for the “plateau phase”, in which the membrane potential decreases very slightly. The duration of this phase may vary from one cell to the other, e.g. it is very short in atrial cells and longer in ventricular ones.
- **Phase 3**: when the Ca^{2+} channels close, the “rapid” and “slow” delayed rectifier K^+ currents (I_{Kr} and I_{Ks} respectively) play the major role, bringing the transmembrane potential back to its resting value.
- **Phase 4**: the cell is in its resting state; the resting membrane potential is depending mostly on the inward rectifying K^+ current (I_{K1}).

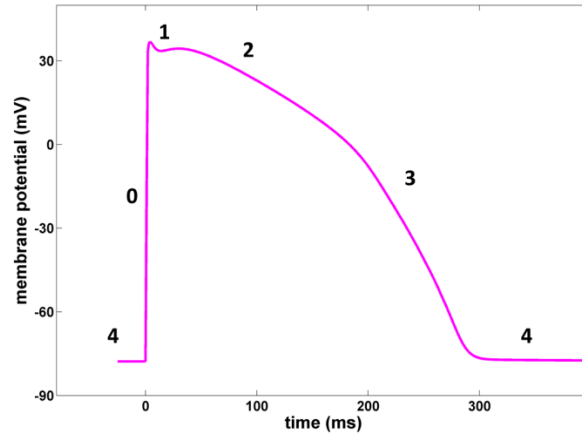


Figure 1.2: Representative action potential trace of a human ventricular endocardial cell.

Different cell types may have different ionic currents and formulations, causing the differences in shapes, e.g. ventricular vs atrial cells. An example is given in Figure 1.3, by comparing atrial and ventricular cells.

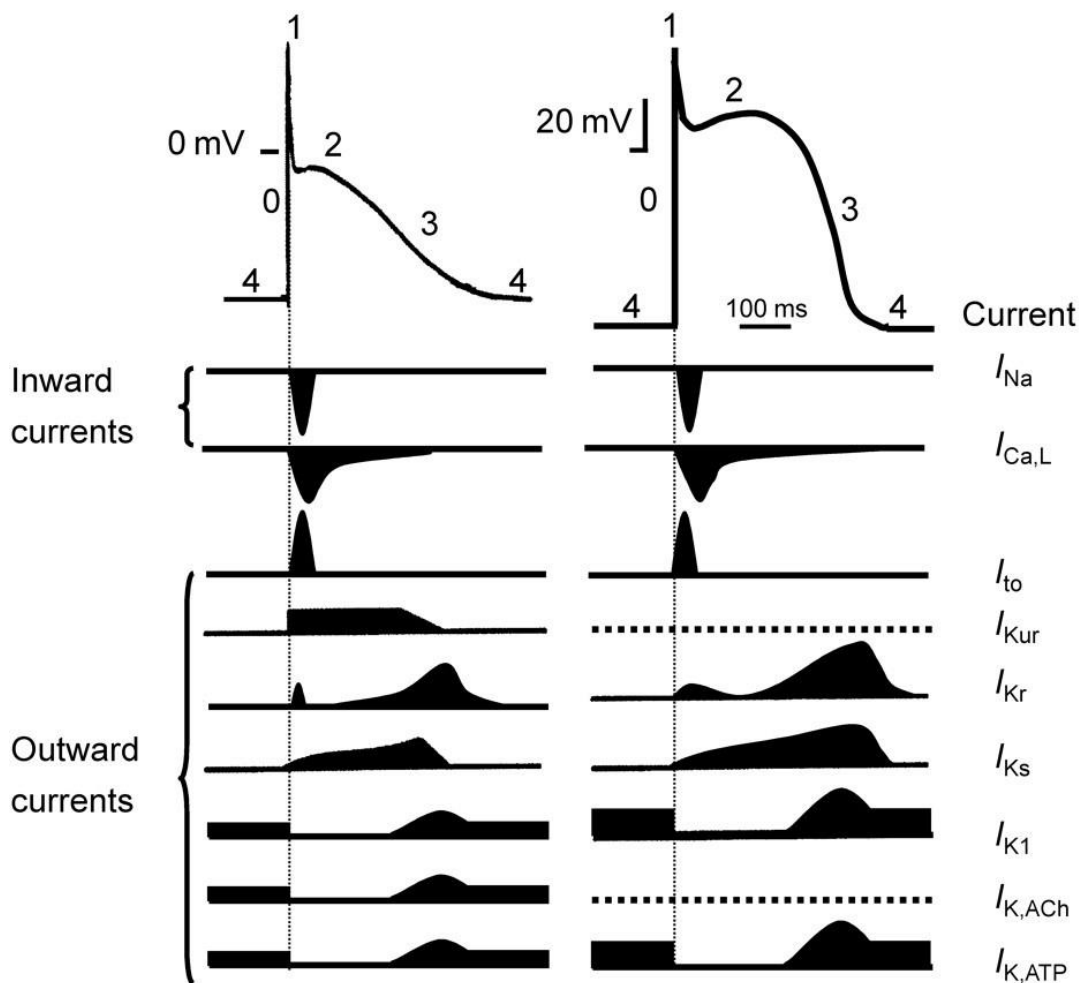


Figure 1.3: Main differences between atrial (left) and ventricular (right) action potentials, with the underlying ionic currents (modified from [2]).

Arrhythmias and pro-arrhythmic mechanisms

Sudden Cardiac Death (SCD) is a sudden, unexpected loss of heart function: the heart stops beating and blood stops flowing to the brain and other vital organs, causing death if not treated within minutes. Most SCD are caused by abnormal heart rhythms, called arrhythmias, in which heart beat is too fast, too slow or irregular: they are due to problems with the electrical conduction of the heart.

There are different types of arrhythmias: extra beats, either atrial or ventricular, supraventricular tachycardia, which include atrial flutter and atrial fibrillation, ventricular arrhythmias, i.e. ventricular tachycardia or fibrillation, and brady-arrhythmias. Most arrhythmias can be effectively treated, by medications or medical procedures, such as a pacemaker and surgery.

There are many pro-arrhythmic mechanisms which make the heart more vulnerable to arrhythmias. As an example, in Figure 1.4 and Figure 1.5 APD alternans and after-depolarisations (early, EADs and delayed DADs) are shown.



Figure 1.4: Cardiac action potential traces showing APD alternans, i.e. a beat to beat variability in the AP duration (modified from [3]).

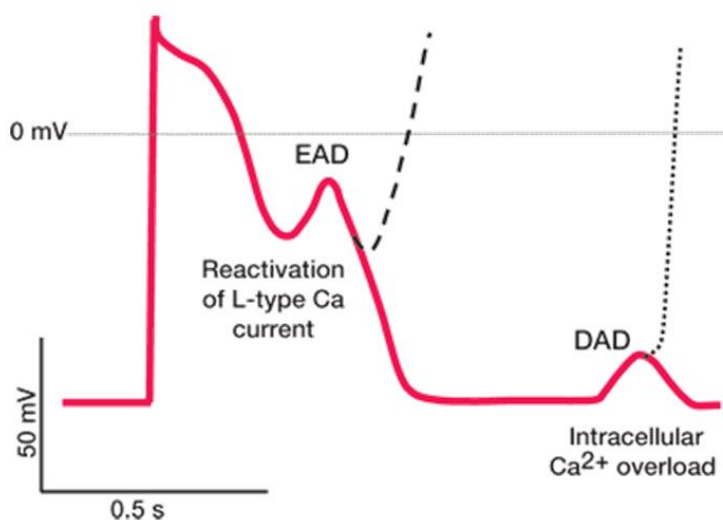


Figure 1.5: Cardiac AP illustrating EAD and DAD mechanisms (modified from [4]).

MODELLING THE CARDIAC ELECTRICAL ACTIVITY

Equivalent Electric Circuit of the Membrane

The action potential (AP) represents a transient change of the transmembrane voltage of the cell, and it is the result of all the ionic currents (mostly Na^+ , K^+ and Ca^{2+}) flowing across the membrane. Considering the equivalent electric circuit, the membrane itself can be represented by a dielectric, with a capacitance of about $1\mu\text{F}/\text{cm}^2$, and each ionic current can be represented by a resistor (Figure 1.6).

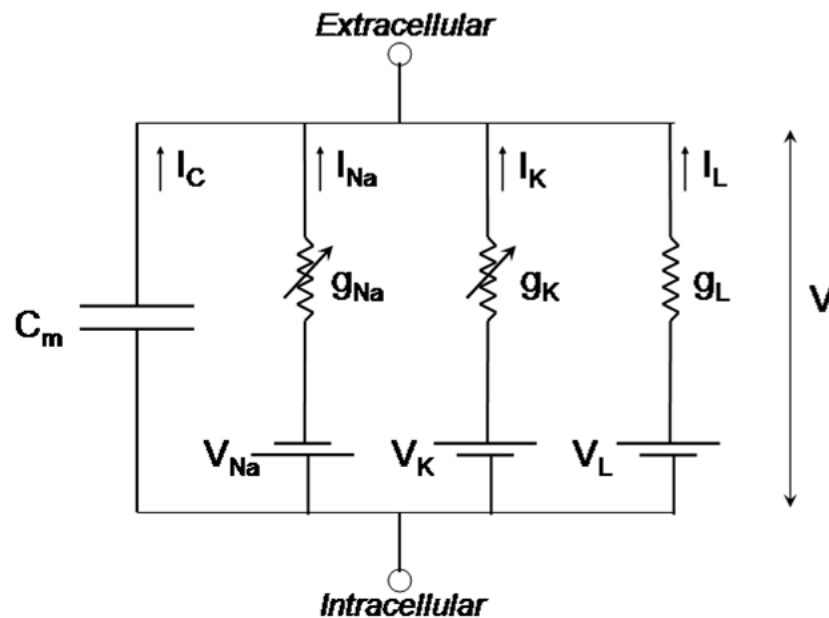


Figure 1.6: *Equivalent electric circuit of cell membrane.*

The action potential of a single cell can be then reconstructed by solving the following differential equation, where V_m represents the transmembrane voltage, C_m the capacitance of the cell and I_{tot} the total current flowing, consisting of the sum of all the different ionic currents (I_{ion}) and the stimulus current (I_{stim}), required from the cell to reach the voltage threshold, thus developing a full action potential.

$$I_{tot} = I_{ion} + I_{stim} = C_m \cdot \frac{dV_m}{dt}$$

The Hodgkin and Huxley formalism

The first AP mathematical model was developed by Alan Lloyd Hodgkin and Andrew Huxley, in 1952 [5], to explain the ionic mechanisms underlying the initiation and propagation of neural APs in the squid giant axon. In 1963, they received the Nobel Prize in Physiology or Medicine.

The Hodgkin-Huxley model was developed by performing a series of voltage clamp experiments on giant squid axons, i.e. holding the membrane to a constant voltage value, and measuring the corresponding current flow.

They identified three different contributions to the total current:

- Na^+ current
- K^+ current
- Leakage current (carried by unspecified ions)

The leakage current was formulated simply as a maximal conductance times the corresponding driving force, while Na^+ and K^+ current formulations included also a voltage-dependent gating mechanism, regulating the channel opening/closing.

$$I_{Na} = g_{Na} \cdot m^3 \cdot h \cdot (V_m - V_{Na})$$

$$I_K = g_K \cdot n^4 \cdot (V_m - V_K)$$

$$I_L = g_L \cdot (V_m - V_L)$$

Here, $g_{Na} = 120$, $g_K = 36$ and $g_L = 0.3$ (mS/cm^2) are the maximal conductances associated with the Na^+ , K^+ and leakage currents, respectively. $E_{Na} = 115$, $E_K = -12$ and $E_L = 10.613$ (mV) are the reversal potentials of each ion, according to the Nernst equation and relative to the resting membrane potential. Gating variables m , h and n are voltage dependent and their values (always between 0 and 1) describe the probability for the channel to be in an open state. When their value is 0 the gate is completely close and no current will flow, whereas when the value is 1 the gate is completely open. The leakage current does not have any gating mechanisms, the K^+ current has only a gating variable, while the Na^+ current has two of them: therefore,

the state of the Na^+ gate relies on the product of both gating variable, and only when they are both equal to 1 the gate is completely open.

Each gating variable is described by a differential equation:

$$\frac{dn}{dt} = \alpha_n \cdot (1 - n) - \beta_n \cdot n$$

Here, α_n and β_n are known as rates and are usually voltage-dependent. Figure 1.7 shows the action potential generated by the Hodgkin-Huxley model, again relative to the resting membrane potential, and the three gating variable traces over time.

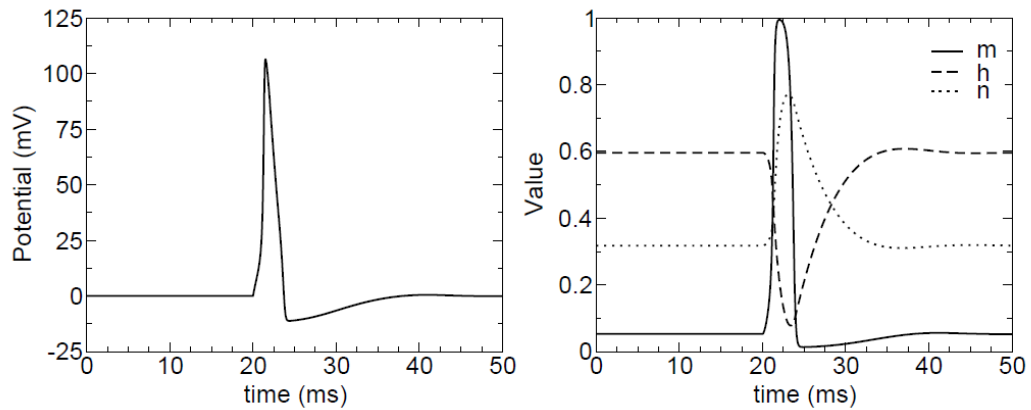


Figure 1.7: Transmembrane potential generated by the Hodgkin and Huxley model (left panel) and the corresponding gating variables over time (right panel).

From Hodgkin-Huxley to Cardiac Models

Starting from Hodgkin and Huxley, AP mathematical models have gained a relevant role in the investigation of cellular electrophysiology. Their possible application to the heart has been soon realized and right from the beginning, cardiac cell modelling allowed to gain insights by predicting phenomena which have been later confirmed experimentally.

The earliest example consists in the pioneering work by Noble, who modified the Hodgkin-Huxley model to simulate Purkinje fibres in mammals, identifying the energy-saving properties of the inward rectifier potassium current [6].

Due to the limited availability of human cardiomyocytes for experimental research, most electrophysiological models had been formulated for animals (mouse, guinea pig, rabbit, dog, etc.). However, animal and human cardiomyocytes

differ in major aspects, such as action potential shape and duration, range of normal heart rates, action potential restitution and relative importance of ionic currents in the action potential generation. As all these factors may influence the mechanism of arrhythmias initiation and dynamics, simulation results obtained with animal models may prove inadequate to represent phenomena observed in human.

In recent years, more and more data on human ionic currents have been gathered from human cardiomyocytes. In addition, by cloning techniques voltage-clamp measurements of human ion channels have been acquired in heterologous cells. As a consequence, new several models have been developed to describe the origins of the human cardiac action potential, an important step towards a wider application in clinical practice.

In 2012, two comprehensive reviews of human atrial models have been published, [7, 8], comparing the different structure and ionic current formulations, and discussing the differences in AP and Ca^{2+} transient biomarkers.

As for ventricular cells, there is not any comprehensive review which includes the most recently published AP models. Therefore, in the next chapter we present a literature review of the current state of the art in human ventricular AP models.

CHAPTER 2

Human Ventricular Action Potential Models: a Literature Review

MODELS ON THE MARKET

Human ventricular cells modelling has begun in 1998 with a study by Priebe and Beuckelmann [9] (PB98), aimed at understanding the effects of electrophysiological alterations in heart failure. They used the Luo–Rudy model of guinea pig ventricular myocytes [10] as basis, parameterized anew with available human data, measured in normal and diseased myocytes.

The PB98 model has been the only one available until 2004, when two further models of human ventricular cells were introduced by Iyer et al. [11] (IW04) and Ten Tusscher et al. [12] (TP04). Both these models provide a more detailed description of ionic currents and fluxes, which reflects new insights in channel function understanding as well as the availability of new measurements from human cells and channels. The IW04 model describes the electrophysiology of sub-epicardial cells (Epi), applying Markovian models for most channels: however, this choice lead to a significant increase in complexity and hence computational time required for simulation. In contrast, the TP04 model uses the common Hodgkin-Huxley formulation for all currents, and in addition to Epi also considers sub-endocardial (Endo) and Midwall (M) cells. A comprehensive comparison of PB98, TP04 and IW04 models, including ion currents, action potential morphology and duration, rate adaptation and other properties, has been performed by Ten Tusscher et al. [13]. A revisited version of TP04 has been published by the same group in 2006 [14] (TP06), including more details on intracellular Ca^{2+} -handling and cell compartmentalisation.

Two years later, Bueno-Orovio et al. [15] performed a new comparison of these models, proposing at the same time a minimal ventricular human model, specifically designed to reproduce tissue-level characteristics. An additional comparison of the IW04 and TP04 models as been performed by Niederer et al. [16], highlighting their significant differences in terms of voltage, ionic currents and concentrations during an action potential, although both models aim to represent the same physiological system. These differences can be partially explained by the different experimental data which have been used to characterise them.

More recently (2010), a model of human ventricular AP has been proposed by Grandi et al. [17] (GB10), using the rabbit model proposed by Shannon et al. [18] as basis, and including new formulations of ionic current densities and kinetics, according to novel human experimental data. With respect to the TP06 model, the GB10 shows a better steady-state AP response to frequency changes and to potassium current blockades. However, the GB10 model does not properly reproduce S_1S_2 restitution properties nor APD rate adaptation dynamics, as reported by Carro et al. [19]. Those drawbacks probably have been acquired from the rabbit model used as basis, since S_1S_2 restitution and APD rate adaptation are notably different in rabbit with respect to human. Indeed, in a recent review the GB10 model has been even referred to as a rearrangement of a rabbit model rather than a real new human model [20]. In 2011, Carro et al. [19] developed a refinement of the GB10 model (CP11), to rectify these drawbacks. In particular, they reformulated the L-type calcium current dynamics, in order to accurately reproduce S_1S_2 restitution and APD rate adaptation.

The most recent model of human ventricular cell has been proposed by O'Hara et al. [21] (OR11) in 2011. This model was developed and validated by using an extensive dataset, including many previously unpublished experimental data, from more than 100 undiseased human hearts. Due to the extensive validation on these new data, the authors claimed to have substantially increased human specific model accuracy: in fact, the model was shown to reproduce several physiological behaviours and drug blocks. Moreover, the effects of Ca^{2+} /Calmodulin-dependent protein kinase II (CaMKII) were incorporated as well.

In Table 2.1 the published models of human ventricular electrophysiology available in literature are listed, together with a non-exhaustive reference to their extensions and/or refinements. Indeed, cardiac computational modelling has reached the stage in which many of the more recent works are focused on 'fixing' problems in previous models, as soon as new and better data become available and modellers discover possible applications for which the published models are not well-suited [20]. We chose to neglect minimal/reduced models, in which a single mathematical process represents multiple channel properties, since they have been developed mainly for multicellular simulations, while in this thesis we are mostly using single cells.

Table 2.1: Computational models of human ventricular cell electrophysiology.

Model	Model extensions	Cell types	Citations Scopus 2014	Comments	Ref #
Priebe & Beuckelmann (PB98) 1998		n.s.	244	First human model, but largely based on animal data. Formulations for normal and failing hearts.	[9]
	Seemann et al. 2003	Endo, M, Epi	19	Focus on regional heterogeneity	[22]
Iyer et al. (IW04) 2004		Epi	130	Joint first human models prevalently based on human data.	[11]
Ten Tusscher et al. (TP04) 2004		Endo, M, Epi	477		[12]
	Ten Tusscher et al. (TP06) 2006	Endo, M, Epi	217	More detail on intracellular calcium handling	[14]
	Fink et al. 2008	Epi	40	From TP06, new formulations for IK1 and HERG,	[23]
	Grandi et al. 2009	Endo, M, Epi	17	From TNNP04, new ICaL formulation to reproduce APD shortening with increased [Ca] _o	[24]
Grandi et al. (GB10) 2010		Endo, Epi	90	From Shannon <i>et al.</i> 2004.	[17]
	Carro et al. 2011	Endo, Epi	11	From Grandi <i>et al.</i> 2010 to study arrhythmias	[19]
O'Hara et al. (OR11) 2011		Endo, M, Epi	96	Substantially increased human-specific model accuracy from human data	[21]

Upon consideration of all these models, a legitimate question could be: “Why so many different models of the same human ventricular cell? Which one is the best?”.

Unfortunately, the answer is not a simple one. In fact, each model has to be evaluated in its specific context, i.e. the experimental data which have been considered for its parameters identification and validation. Therefore, all the listed models (even the oldest ones) may have their advantages as well as their limitations, depending on the applications taken into account; i.e. a particular model may reproduce correctly the effects of a specific currents blockade, but it may be unsuitable for rate dependence analysis.

As an example, it is worth noting that the model with more citations in literature (based on Scopus Data, updated 31/12/2014) is TT04: in fact, even if quite old, this model is still widely used, especially for multidimensional simulations, because it is relatively good in variety of context and computationally much more efficient than its updated version (TT06) or the most recent models, as OR11 or GB10, which includes a very detailed description of intracellular processes and compartments.

MODELS COMPARISON

Among all the models included in Table 2.1, we chose to compare the 6 ones which have been more widely used: PB98, IW04, TT04, TT06, GB10 and OR11.

Action Potential Properties

All the considered models have been implemented in Matlab (Mathworks, Inc) and paced at 1 Hz until steady state (500 s), i.e. intracellular concentrations (Na^+ , Ca^{2+} and K^+) stable over time. The current stimulus has been set to 2 ms of duration, with amplitude equal to twice the AP threshold for each model. Since PB89 and IW04 don't reproduce different cell types, and their AP shape is similar to epicardial cells, we considered Epi cells only for all the models.

Simulated AP traces are shown in Figure 2.1 **Errore. L'origine riferimento non è stata trovata.** Each model has been represented using a different colour, but all the other model traces are shown in grey, to facilitate comparison. The high variability of AP shapes and duration among the models is mostly dependent on the different data used to construct them. In fact, after fitting the model parameters on

voltage-clamp data, current conductances are often “manually” adjusted to fit the AP data available.

For each model a set of AP biomarkers has been evaluated: the results are compared in Table 2.2 together with the time required for the simulations.

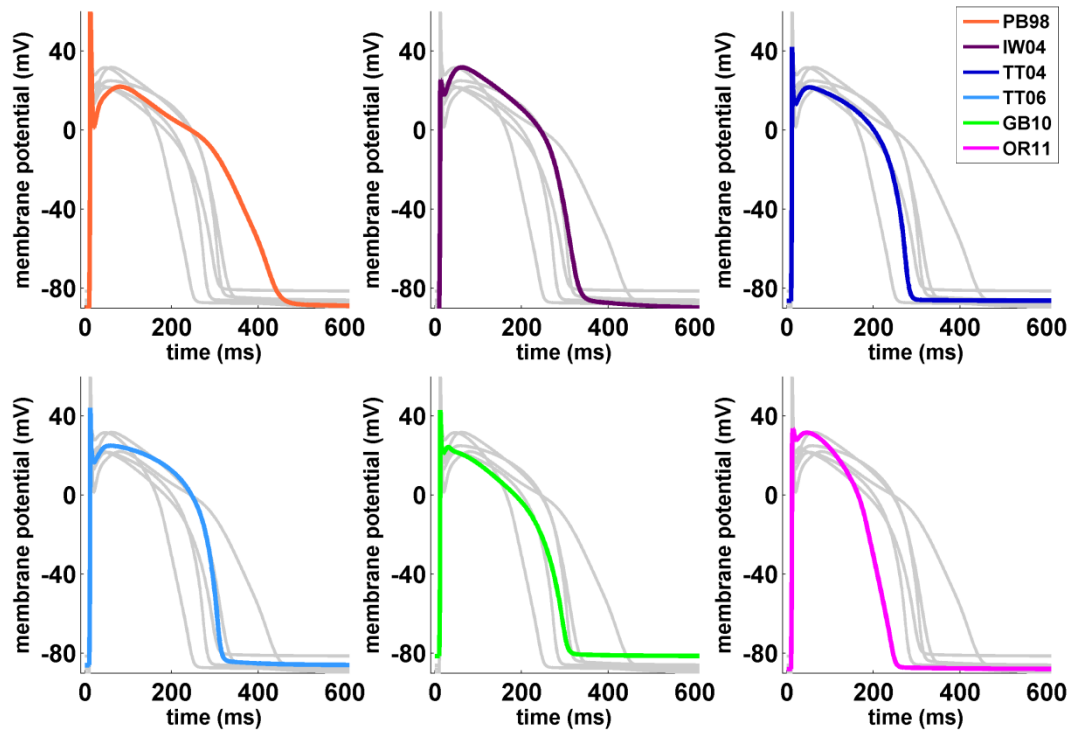


Figure 2.1: Simulated AP traces for the six considered models.

Table 2.2: AP biomarkers comparison for the six considered models

		PB98	IW04	TP04	TP06	GB10	OR11
RMP	(mV)	-89.8	-90.7	-86.3	-86.0	-81.4	-87.9
AP peak	(mV)	61.0	31.7	42.1	44.1	42.6	33.6
dV/dt_{MAX}	(V/s)	422	210	355	365	384	205
APD₅₀	(ms)	298	278	232	268	232	184
APD₉₀	(ms)	418	319	266	299	287	229
nODEs	-	22	67	17	19	39	55
t_{SIM}	(n.u.)	1.18	4.36	1.00	1.04	1.83	2.42

RMP: resting membrane potential; **AP peak**: max AP voltage; **dV/dt_{MAX}**: max upstroke velocity; **APD₅₀** and **APD₉₀**: AP duration, computed at 50% and 90% of repolarization; **nODEs**: number of ordinary differential equations in the model; **t_{SIM}**: time required to compute 500 s, normalised according to the fastest model.

As expected, the computational time is highly dependent on the number of differential equations: it is therefore very easy to understand why TT04 is still one of the most used human ventricular AP model, even if not very recent. At the same time, it is obvious how the large number of Markovian current models in IW04 affect its computational performances.

Intracellular Compartments

Intracellular compartments and Ca^{2+} release from the sarcoplasmic reticulum (SR) were first introduced in cardiac models by DiFrancesco and Noble [25]: indeed, their Purkinje cell model described intracellular Ca^{2+} dynamics in details, by including separate pools for cytosolic, non-junctional SR (NSR) and junctional SR (JSR) Ca^{2+} concentrations. Later on, it has been acknowledged that both the cellular and sub-cellular structure considerably shape the temporal evolution of Ca^{2+} concentration profiles.

However, model design in terms cellular compartmentalisation may be very different from one model to the other. Within human ventricular models, structure ranges from the simplest approach, as in TP04 (cytosol and SR only), to the most complex models with many different sub-compartments (cytosol, junctional space, sub-sarcolemma, NSR and JSR). In addition, most of the models also include different Ca^{2+} buffers for each compartment, especially the most recent ones, i.e. GB10 and OR11.

Table 2.3 shows the main structural properties of the considered human ventricular models, e.g. the number and size of intracellular compartments and the corresponding Ca^{2+} buffers.

The main challenge of the compartmental approach is the lack of corresponding distinct anatomical structures inside the cell. Thus, there is not a straightforward way of choosing the appropriate compartmentalization. This also explains the great variability among the different models.

Table 2.3: Main properties of the considered human ventricular AP models.

		PB98	IW04	TP04	TP06	GB10	OR11	
Cell Volumes (pL)	CYTO		25.85	25.84	16.40	21.45	25.85	
	SL					0.66		
	JS			0.0012		0.0547	0.0178	0.7603
	SR	NSR	2.10	2.10	1.09	1.09	1.16	2.10
		JSR	0.18	0.16				0.18
	TOT		28.13	28.10	17.50	17.55	23.29	28.89
Calcium Buffers (mM)	CYTO	CMDN	0.05	0.05	0.15	0.20	0.02	0.05
		TRPN low	0.07	0.07			0.07	
		TRPN high		0.14			0.14	
	JS	BSR	-	-	0.40	0.40	0.02	0.05
		BSL low	-	-			0.13	1.12
		BSL high					0.05	
	SR	CSQN	10	15	10	10	2.6	10

The six compartments refer to: bulk myoplasm (cytosol, **CYTO**); network SR (**NSR**); junctional SR (**JSR**); junctional space (**JS**); sub-sarcolemmal space (**SSL**). The Ca^{2+} buffers are: Calmodulin (**CMDN**), Troponin (**TRPN**), Calsequestrin (**CSQN**), SR Ca^{2+} buffers (**BSR**); junctional and sarcolemmal Ca^{2+} buffers (**BSL**).

Extracellular and Intracellular Concentrations

Extracellular ionic concentrations are quite similar in all the considered models, since they are the ones used for experimental recordings in single cells, often done in standard conditions. As for intracellular ionic concentrations, the differences between models are higher, especially when considering Ca^{2+} concentrations in the different compartments. A summary of the extra- and intra- cellular concentrations for every model is shown in Table 2.4: . Extracellular concentrations are constant in the models, while for intracellular concentrations the reported values are the diastolic ones, after pacing the models for 500 s at 1 Hz.

It is worth noticing that the GB10 model is the only one including Cl^- concentrations, together with the Ca^{2+} activated Cl^- current and a background Cl^- current. We ran a few simulations blocking this current, and actually its effect on the AP is quite negligible, at least in physiological conditions. In addition, in GB10 both intracellular K^+ and Cl^- are clamped to constant values.

Table 2.4: Extracellular and intracellular ionic concentrations for the considered models.

		PB98	IW04	TP04	TP06	GB10	OR11
Extracellular Concentrations	$[\text{Na}^+]_o$ (mM)	138	138	140	140	140	140
	$[\text{K}^+]_o$ (mM)	4.0	4.0	5.4	5.4	5.4	5.4
	$[\text{Ca}^{2+}]_o$ (mM)	2.0	2.0	2.0	2.0	1.8	1.8
	$[\text{Cl}^-]_o$ (mM)	-	-	-	-	150	-
Intracellular Concentrations	$[\text{Na}^+]_i$ (mM)	10.6	9.8	11.6	10.4	8.4	7
	$[\text{K}^+]_i$ (mM)	140	125	140	140	120*	144
	$[\text{Ca}^{2+}]_i$ (nM)	200	86	200	130	87	85
	$[\text{Ca}^{2+}]_{SL}$ (nM)					100	
	$[\text{Ca}^{2+}]_{JS}$ (nM)		140		360	200	85
	$[\text{Ca}^{2+}]_{SR}$ (mM)	2.5	0.3	0.2	3.7	0.6	1.6
	$[\text{Cl}^-]_i$ (mM)	-	-	-	-	15*	-

$[Y]_o$: extracellular concentration for Y; $[Y]_i$: intracellular concentration for Y; SL: sarcolemmal space; JS: junctional space; SR: sarcoplasmic reticulum.

* in GB10, $[\text{K}^+]_i$ and $[\text{Cl}^-]_i$ are clamped to constant values.

Membrane Ionic Currents and Ca^{2+} subsystem

The main ionic currents are present in all the considered models: I_{Na} , I_{CaL} , I_{to} , I_{K1} , I_{Kr} , I_{Ks} , Na^+/K^+ pump (I_{NaK}) and $\text{Na}^+/\text{Ca}^{2+}$ exchanger (I_{NCX}). However, there are a few differences in the small currents (e.g. background ones), and in Ca^{2+} related channels/pumps distribution. To avoid unnecessary complexity, we will focus on the differences between the three most recent models: TP06, GB10 and OR11.

A summary of ionic currents distribution is shown in Table 2.5, together with the corresponding intracellular compartments in which they are distributed. As for ionic fluxes, the two connected compartments for each of them are shown.

Table 2.5: Ionic currents and fluxes with the corresponding intracellular compartments for the six considered human ventricular AP models.

		PB90	IW04	TT04	TT06	GB10	OR11
Na⁺ currents	I_{Na}	CYTO	CYTO	CYTO	CYTO	11% JS 89% SL	CYTO
	I_{NaL}	-	-	-	-	-	CYTO
	I_{CaNa}	-	-	-	-	90% JS 10% SL	JS
	I_{NaB}	CYTO	CYTO	CYTO	CYTO	11% JS 89% SL	CYTO
Ca²⁺ currents	I_{CaL}	CYTO	CYTO	CYTO	JS	90% JS 10% SL	JS
	I_{CaB}	CYTO	CYTO	CYTO	CYTO	11% JS 89% SL	CYTO
K⁺ currents	I_{to}	CYTO	CYTO	CYTO	CYTO	CYTO	CYTO
	I_{K1}	CYTO	CYTO	CYTO	CYTO	CYTO	CYTO
	I_{Kr}	CYTO	CYTO	CYTO	CYTO	CYTO	CYTO
	I_{Ks}	CYTO	CYTO	CYTO	CYTO	CYTO	CYTO
	I_{CaK}	-	CYTO	-	-	90% JS 10% SL	JS
	I_{Kp}	-	-	CYTO	CYTO	11% JS 89% SL	CYTO
Cl⁻ currents	I_{ClB}	-	-	-	-	CYTO	-
	I_{ClCa}	-	-	-	-	11% JS 89% SL	-
Pumps and Exchangers	I_{NaK}	CYTO	CYTO	CYTO	CYTO	11% JS 89% SL	CYTO
	I_{NCX}	CYTO	CYTO	CYTO	CYTO	11% JS 89% SL	20% JS 89% CYTO
	I_{pCa}	-	CYTO	CYTO	CYTO	11% JS 89% SL	CYTO
SR Fluxes	J_{rel}	JSR <-> CYTO	JSR <-> JS	SR -> CYTO	SR <-> JS	JSR <-> JS	JSR -> JS
	J_{leak}	NSR -> CYTO	-	SR <-> CYTO	SR <-> CYTO	JSR <-> JS	NSR -> CYTO
	J_{up}	CYTO -> NSR	CYTO <-> NSR	CYTO -> SR	CYTO -> SR	CYTO <-> SR	CYTO -> NSR
	J_{tr}	NSR <-> JSR	NSR <-> JSR	-	-	-	NSR <-> JSR
Intracellular Fluxes	J_{diffCa}	-	CYTO <-> JS	-	CYTO <-> JS	CYTO/SL SL/JS	CYTO <-> JS
	J_{diffNa}	-	-	-	-	CYTO/SL SL/JS	CYTO <-> JS
	J_{diffK}	-	-	-	-	-	CYTO <-> JS

As an example, in TP06 and OR11, all the I_{CaL} actually flows into the JS. Even if it is well known that most of the L-type Ca channels are located in the junctional portion of the membrane, this seems to be a rather extreme choice. More realistically in GB10, based on rat data [26], 90% of the channels are located in the JS membrane and the remaining 10% in the cytoplasm.

Another difference is in the I_{NCX} distribution. It is still not completely clear if Na^+/Ca^{2+} exchanger proteins are located preferentially in T-tubules [27] or have a

more uniform distribution in the ventricular sarcolemma [28]. In GB10 the I_{NCX} channels are distributed evenly throughout the cell membrane (89% in the SL, 11% in the JS), while in OR11 the fraction located in the JS is slightly higher (20%). O'Hara et al. indicated this choice as necessary in order to correctly reproduce the rate dependence of intracellular Ca^{2+} peak [21]. It is worth noticing that all the ionic currents were considered uniformly distributed throughout the cell membrane in the GB10 model (89% in the SL, 11% in the JS), as suggested e.g. for I_{NaK} in mammalian cardiomyocytes [29]. On the contrary, they were considered absent from JS membrane in TP06 and OR11.

A visual comparison of TT06, GB10 and OR11, showing all the ionic currents, fluxes and compartments for this three models, is given in Figure 2.2.

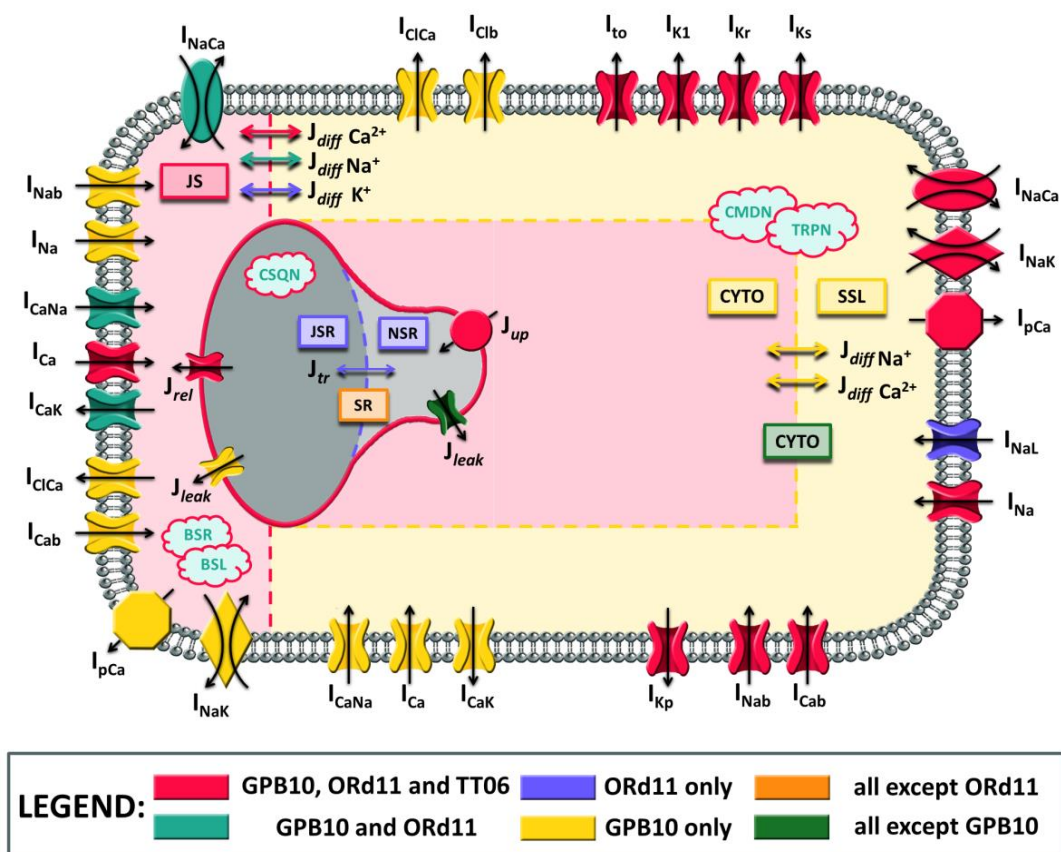


Figure 2.2: Visual comparison of the three most recent human ventricular model properties, in particular showing the distribution of each ionic current on the cell, and the ions diffusion (credit: Caterina Passini).

It is worth noticing that, after this literature review has been completed (2013), a new mathematical model have been published for human ventricular cells by Asakura-Noma [30], as well as a new paper comparing the behaviour of some of the human ventricular models considered here in tissue, by Elshrif and Cherry [31].

References

- [1] J. Malmivuo and R. Plonsey, *Bioelectromagnetism: Principles and Applications of Bioelectric and Biomagnetic Fields*. 1995.
- [2] U. Ravens and E. Cerbai, “Role of potassium currents in cardiac arrhythmias” *Europace*, vol. 10, no. 10, pp. 1133–7, Oct. 2008.
- [3] Z. Qu, Y. Xie, A. Garfinkel, and J. N. Weiss, “T-wave alternans and arrhythmogenesis in cardiac diseases” *Front Physiol*, vol. 1, p. 154, Jan. 2010.
- [4] Longo, Fauci, Kasper, Hauser, Jameson, and LoScalzo, *Harrison’s Principles of Internal Medicine*, 18th ed. 2012.
- [5] A. L. Hodgkin and A. F. Huxley, “A quantitative description of membrane current and its application to conduction and excitation in nerve” *J Physiol*, vol. 117, no. 4, pp. 500–44, Aug. 1952.
- [6] D. Noble, “A modification of the Hodgkin--Huxley equations applicable to Purkinje fibre action and pace-maker potentials” *J Physiol*, vol. 160, pp. 317–52, Feb. 1962.
- [7] M. Wilhelms, H. Hettmann, M. M. Maleckar, J. T. Koivumäki, O. Dössel, and G. Seemann, “Benchmarking electrophysiological models of human atrial myocytes” *Front Physiol*, vol. 3, p. 487, Jan. 2012.
- [8] O. Dössel, M. W. Krueger, F. M. Weber, M. Wilhelms, and G. Seemann, “Computational modeling of the human atrial anatomy and electrophysiology” *Med Biol Eng Comput*, vol. 50, no. 8, pp. 773–99, Aug. 2012.
- [9] L. Priebe and D. J. Beuckelmann, “Simulation study of cellular electric properties in heart failure” *Circ Res*, vol. 82, no. 11, pp. 1206–23, Jun. 1998.
- [10] C. H. Luo and Y. Rudy, “A dynamic model of the cardiac ventricular action potential. I. Simulations of ionic currents and concentration changes” *Circ Res*, vol. 74, no. 6, pp. 1071–96, Jun. 1994.
- [11] V. Iyer, R. Mazhari, and R. L. Winslow, “A computational model of the human left-ventricular epicardial myocyte” *Biophys J*, vol. 87, no. 3, pp. 1507–25, Sep. 2004.
- [12] K. H. W. J. ten Tusscher, D. Noble, P. J. Noble, and A. V Panfilov, “A model for human ventricular tissue” *Am J Physiol Heart Circ Physiol*, vol. 286, no. 4, pp. H1573–89, Apr. 2004.
- [13] K. H. W. J. Ten Tusscher, O. Bernus, R. Hren, and A. V Panfilov, “Comparison of electrophysiological models for human ventricular cells and tissues” *Prog Biophys Mol Biol*, vol. 90, no. 1–3, pp. 326–45, 2006.
- [14] K. H. W. J. ten Tusscher and a V Panfilov, “Alternans and spiral breakup in a human ventricular tissue model” *Am J Physiol Heart Circ Physiol*, vol. 291, no. 3, pp. H1088–100, Sep. 2006.
- [15] A. Bueno-Orovio, E. M. Cherry, and F. H. Fenton, “Minimal model for human ventricular action potentials in tissue” *J Theor Biol*, vol. 253, no. 3, pp. 544–60, Aug. 2008.

- [16] S. a Niederer, M. Fink, D. Noble, and N. P. Smith, “A meta-analysis of cardiac electrophysiology computational models” *Exp Physiol*, vol. 94, no. 5, pp. 486–95, May 2009.
- [17] E. Grandi, F. S. Pasqualini, and D. M. Bers, “A novel computational model of the human ventricular action potential and Ca transient” *J Mol Cell Cardiol*, vol. 48, no. 1, pp. 112–21, Jan. 2010.
- [18] T. R. Shannon, F. Wang, J. Puglisi, C. Weber, and D. M. Bers, “A mathematical treatment of integrated Ca dynamics within the ventricular myocyte” *Biophys J*, vol. 87, no. 5, pp. 3351–71, Nov. 2004.
- [19] J. Carro, J. F. Rodríguez, P. Laguna, and E. Pueyo, “A human ventricular cell model for investigation of cardiac arrhythmias under hyperkalaemic conditions” *Philos Trans A Math Phys Eng Sci*, vol. 369, no. 1954, pp. 4205–32, Nov. 2011.
- [20] D. Noble, A. Garny, and P. J. Noble, “How the Hodgkin-Huxley equations inspired the Cardiac Physiome Project,” *J Physiol*, vol. 590, no. Pt 11, pp. 2613–2628, 2012.
- [21] T. O’Hara, L. Virág, A. Varró, and Y. Rudy, “Simulation of the undiseased human cardiac ventricular action potential: model formulation and experimental validation” *PLoS Comput Biol*, vol. 7, no. 5, p. e1002061, May 2011.
- [22] G. Seemann, F. B. Sachse, D. L. Weiss, and O. Dössel, “Quantitative reconstruction of cardiac electromechanics in human myocardium: regional heterogeneity” *J Cardiovasc Electrophysiol*, vol. 14, no. 10 Suppl, pp. S219–28, Oct. 2003.
- [23] M. Fink, D. Noble, L. Virag, A. Varro, and W. R. Giles, “Contributions of HERG K⁺ current to repolarization of the human ventricular action potential” *Prog Biophys Mol Biol*, vol. 96, no. 1–3, pp. 357–76, Jan. 2008.
- [24] E. Grandi, F. S. Pasqualini, C. Pes, C. Corsi, A. Zaza, and S. Severi, “Theoretical investigation of action potential duration dependence on extracellular Ca²⁺ in human cardiomyocytes” *J Mol Cell Cardiol*, vol. 46, no. 3, pp. 332–42, Mar. 2009.
- [25] D. DiFrancesco and D. Noble, “A model of cardiac electrical activity incorporating ionic pumps and concentration changes” *Philos Trans R Soc Lond B Biol Sci*, vol. 307, no. 1133, pp. 353–98, Jan. 1985.
- [26] D. R. Scriven, P. Dan, and E. D. Moore, “Distribution of proteins implicated in excitation-contraction coupling in rat ventricular myocytes” *Biophys J*, vol. 79, no. 5, pp. 2682–91, Nov. 2000.
- [27] J. S. Frank, G. Mottino, D. Reid, R. S. Molday, and K. D. Philipson, “Distribution of the Na⁽⁺⁾-Ca²⁺ exchange protein in mammalian cardiac myocytes: an immunofluorescence and immunocolloidal gold-labeling study” *J Cell Biol*, vol. 117, no. 2, pp. 337–45, Apr. 1992.
- [28] W. J. Lederer, S. He, S. Luo, W. duBell, P. Kofuji, R. Kieval, C. F. Neubauer, A. Ruknudin, H. Cheng, M. B. Cannell, T. B. Rogers, and D. H. Schulze, “The molecular biology of the Na⁽⁺⁾-Ca²⁺ exchanger and its functional roles in heart, smooth muscle cells, neurons, glia, lymphocytes, and nonexcitable cells” *Ann N Y Acad Sci*, vol. 779, pp. 7–17, Apr. 1996.
- [29] A. A. McDonough, Y. Zhang, V. Shin, and J. S. Frank, “Subcellular distribution of sodium pump isoform subunits in mammalian cardiac myocytes” *Am J Physiol*, vol. 270, no. 4 Pt 1, pp. C1221–7, Apr. 1996.

- [30] K. Asakura, C. Y. Cha, H. Yamaoka, Y. Horikawa, H. Memida, T. Powell, A. Amano, and A. Noma, “EAD and DAD mechanisms analyzed by developing a new human ventricular cell model” *Prog Biophys Mol Biol*, vol. 116, no. 1, pp. 11–24, Sep. 2014.
- [31] M. M. Elshrif and E. M. Cherry, “A quantitative comparison of the behavior of human ventricular cardiac electrophysiology models in tissue” *PLoS One*, vol. 9, no. 1, p. e84401, Jan. 2014.

SECTION I

Extracellular Calcium and Action Potential Duration: the Fine Balance between L-Type Calcium Current Inactivation Mechanisms

CHAPTER 3

A Novel Markov Model of L-Type Calcium Current to Explore Inactivation Mechanisms

The content of this chapter has been published in:

Passini E, Severi S.

Extracellular Calcium and L-Type Calcium Current Inactivation Mechanisms: a Computational Study.

Computing in Cardiology, Vol. 40, 2013

Passini E, Severi S.

Computational Analysis of Extracellular Calcium Effect on Action Potential Duration

Biophysical Journal, Vol. 106, Issue 2, 2014

Computational Modelling of Cardiac Electrophysiology: from Cell to Bedside

Abstract

Extracellular calcium concentration ($[Ca^{2+}]_o$) affects cardiac action potential (AP): their inverse dependence has already been assessed in vivo and in vitro.

Both shortening and prolongation of AP are associated with an increased risk of arrhythmias and $[Ca^{2+}]_o$ variations may occur in many different contexts (e.g. pathological hypo/hyper-calcaemia, haemodialysis therapy, bed-rest experiments).

Computational modeling could provide a useful support to investigate this phenomenon: however, $[Ca^{2+}]_o$ dependence is not reproduced properly by most of the commonly used human AP models

The aim of this study has been to modify one of the most recent human ventricular cell model in order to improve its response to $[Ca^{2+}]_o$ changes.

The original L-Type Ca^{2+} current formulation has been replaced by a new Markov model with 8 states and a cubical structure. The inverse dependence of APD vs $[Ca^{2+}]_o$ has been achieved mainly by strengthening the Ca^{2+} -dependent inactivation mechanism (CDI), with respect to the Voltage-dependent one (VDI), thus confirming that CDI plays an important role in this context.

The modified model has been validated against the same experimental data used for the original one, in order to verify its consistency, and it can then be used to explore “in silico” the effects of electrolyte unbalances on the electrical activity of human cardiomyocytes.

INTRODUCTION

It is well known that extracellular calcium concentration ($[Ca^{2+}]_o$) affects cardiac action potential (AP): in fact, an increase of $[Ca^{2+}]_o$ shortens AP while $[Ca^{2+}]_o$ decrease lengthens it, as observed in different species [1–5], e.g. guinea pig (Figure 3.1, panel A), and human atrial cell [6] (Figure 3.1, panel B). More recently, new experimental data acquired in human ventricular cells confirmed this dependence [7] (Figure 3.1, panel C). Finally, when considering consistency between action potential duration (APD) changes and corrected QT interval (QTc), further confirming data can be found in the literature, e.g. [8] (Figure 3.1, panel D).

Since both APD increase and decrease may lead to arrhythmia onset, $[Ca^{2+}]_o$ dependency of repolarization may have important implications in all clinical contexts where electrolyte changes occur, e.g. haemodialysis therapy (HD), pathological hypo/hypercalcemia, head-down bed-rest experiments, etc.

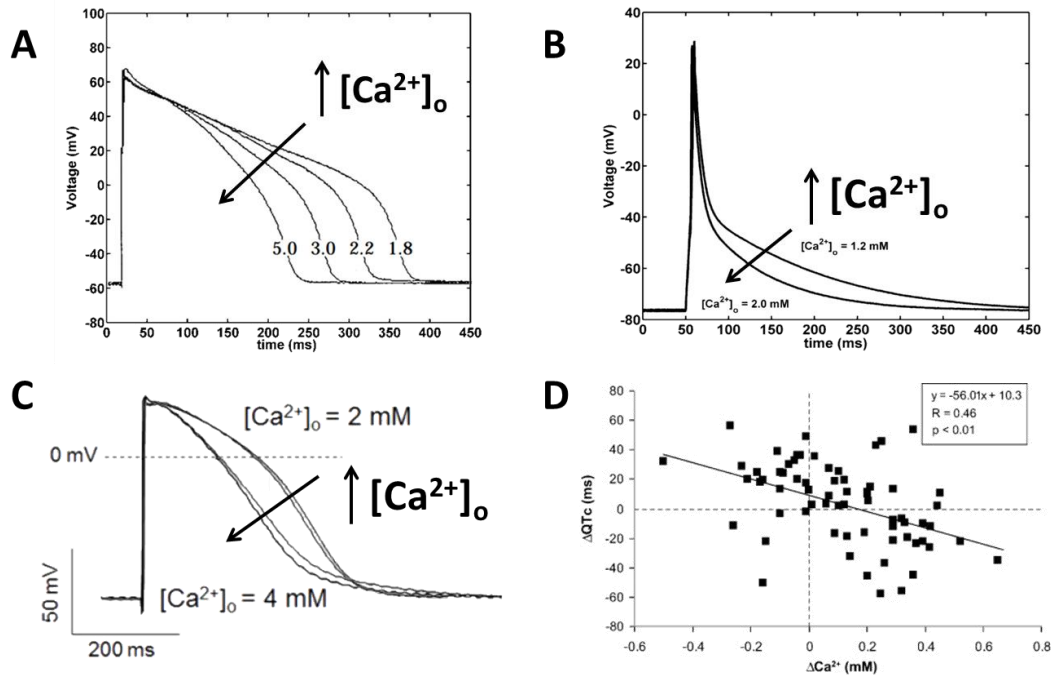


Figure 3.1: Experimental Data from literature showing the inverse dependence of APD vs $[Ca^{2+}]_o$: **A)** guinea pig ventricular cells (modified from [2]); **B)** human atrial cells (modified from [6]); **C)** human atrial cells (modified from [7]); **D)** QTc interval vs $[Ca^{2+}]_o$ variations measured in different patients during Hemodialysis therapy (modified from [8]).

From earlier studies [9], L-type Ca^{2+} current (I_{CaL}) seems the one mostly responsible for the APD- $[Ca^{2+}]_o$ dependence. Two contrasting mechanisms are involved: e.g. when $[Ca^{2+}]_o$ is higher, it increases the I_{CaL} driving force which, by itself, would enhance the current and prolong the APD; on the other hand, a larger I_{CaL} increases its Ca^{2+} -dependent inactivation (CDI) mechanism as well. Since the final outcome is APD shortening, it is apparently CDI which plays the overwhelming role. A summary of these two mechanisms is shown in Figure 3.2.

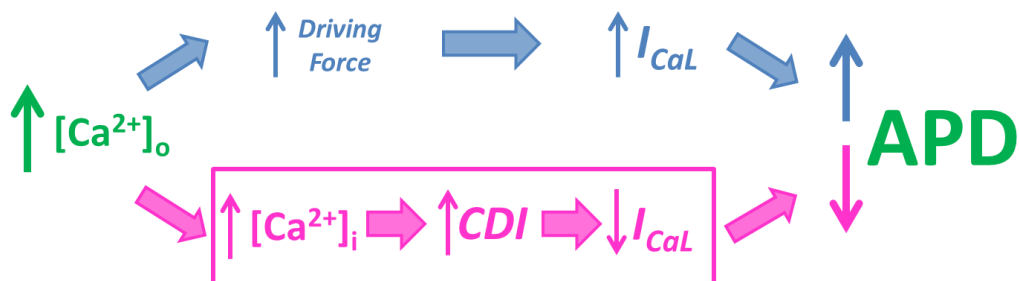


Figure 3.2: Schematic representation of the two mechanisms involved in APD- $[Ca^{2+}]_o$ dependence.

However, many other ionic mechanisms are involved and this is why the APD- $[Ca^{2+}]_o$ dependence is not completely understood. Computational modeling may help to investigate this phenomenon by analysing the single ionic currents involved. However, most of the commonly used human ventricular AP models have been developed considering a single $[Ca^{2+}]_o$ value, and they are not able to reproduce properly the effects of $[Ca^{2+}]_o$ changes: often, their APDs vary in an opposite way, e.g. in the O’Hara-Rudy [10] and in the Grandi-Bers models [11] (Figure 3.3).

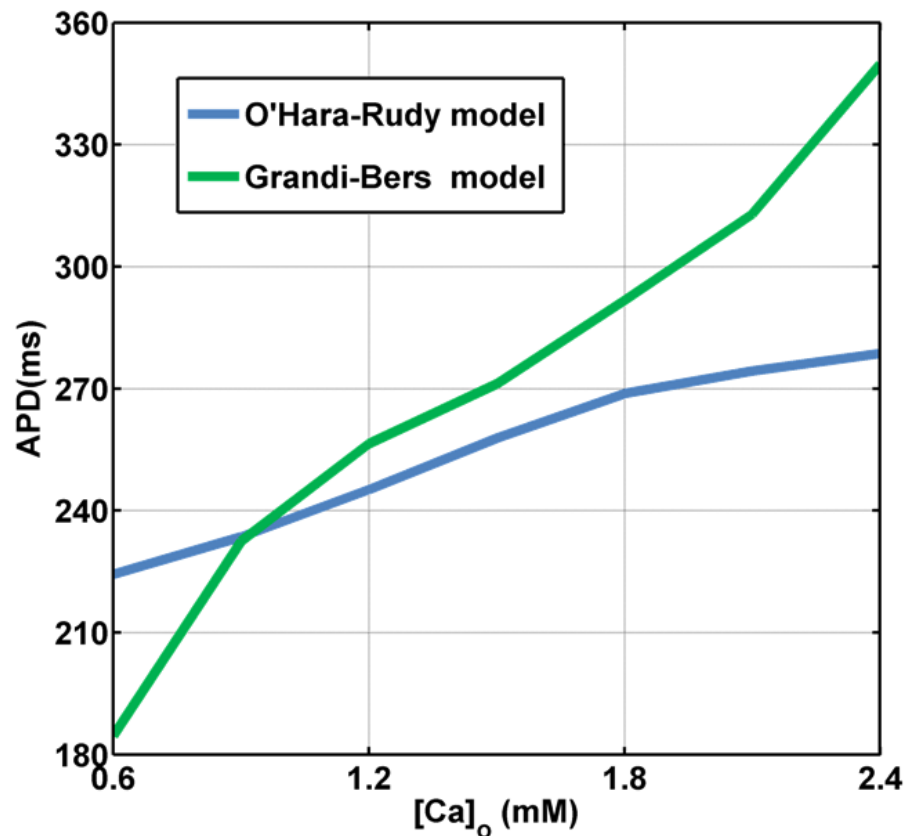


Figure 3.3: APD- $[Ca^{2+}]_o$ dependence in two of the most recent human ventricular AP models: O’Hara-Rudy [10] (blue line) and Grandi-Bers [11] (green line). APD has been computed at 90% of repolarisation, after pacing the models at 1 Hz for 1 s.

The aim of this study has been to modify the most recent human ventricular AP model (O’Hara-Rudy, [10]) in order to improve its APD- $[Ca^{2+}]_o$ dependence without altering model behaviour in control condition, as similarly done for older models in previous works [6, 9].

The proper dependence should be achieved by acting mainly on $ICaL$, for which a new formulation is proposed, strengthening the Ca^{2+} -dependent inactivation (CDI) with respect to the V-dependent one (VDI).

METHODS

The O'Hara-Rudy model of human ventricular myocyte (ORd, [10]) was used as basis. However, the L-Type Ca^{2+} current has been completely revisited: its original Hodgkin-Huxley formulation has been replaced by a new Markov model (Figure 3.4), similar to the one used by Decker-Rudy for canine epicardial cells [12].

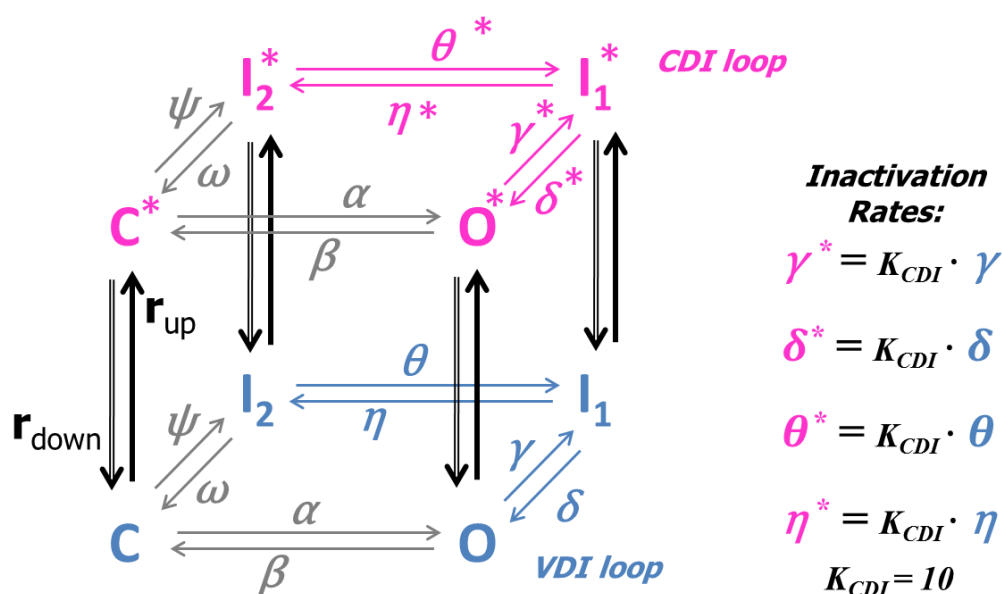


Figure 3.4: Schematic representation of the new Markov model of L-Type Ca^{2+} current: VDI and CDI are represented as two separate loops, interconnected by specific up/down rates

This Markov model consists of two structurally identical loops (Figure 3.5), each including 4 transitions: activation (from C to O), fast inactivation (from O to I_1), slow inactivation (from I_1 to I_2) and recovery (from I_2 to C).

Activation and recovery rates are exactly the same in the two loops; they have been directly derived from the ORd time constant and steady state values of the corresponding gating variables. As for fast and slow inactivation, rates on the CDI loop are 10 times faster than the ones in VDI loop.

All transition rates, even the ones on the CDI loop, are actually V-dependent, according to the hypothesis by Kim et al. [13], where CDI was observed to function simply as a faster VDI, activated by elevated Ca^{2+} .

In fact, in this model CDI and VDI are implemented on two different loops, interconnected by specific up/down rates, modulated by Ca^{2+} concentration, by means of the n gate, used to calculate the r_{up}/r_{down} rates (Figure 3.6).

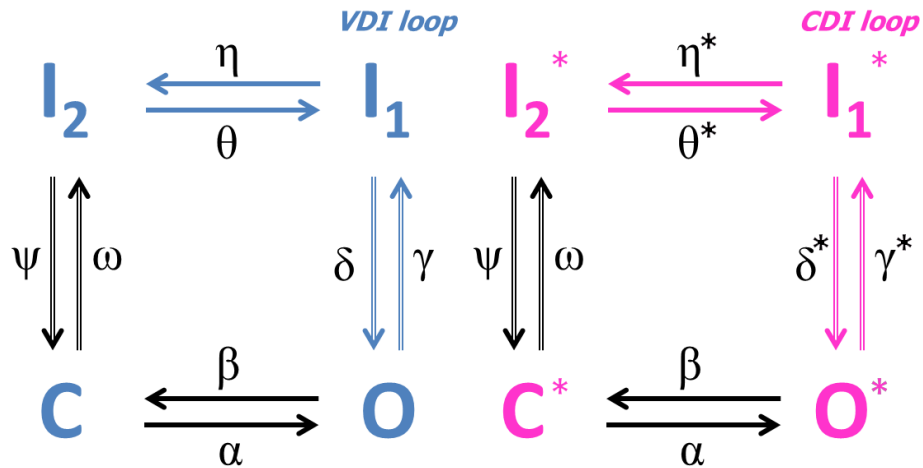


Figure 3.5: VDI (blue) and CDI (pink) loops. Activation and recovery rates (black) are the same in the two loops, while inactivation rates are 10 times faster in the CDI loop.

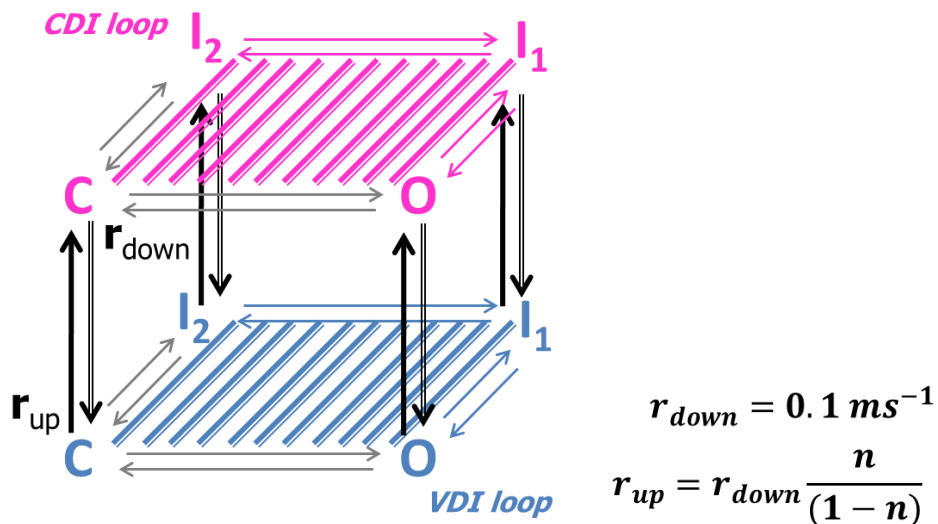


Figure 3.6: VDI (blue) and CDI (pink) loops are interconnected by up/down rates, related to Ca^{2+} concentration by means of the n gate.

In the ORd model, the n gate represents the fraction of channels operating in CDI mode, and it is the only state variable, among the ones involved in I_{CaL} kinetics, which is directly dependent on intracellular Ca^{2+} concentration ($[Ca^{2+}]_i$).

The n formulation is based on the interaction between $[Ca^{2+}]_i$ and Calmodulin (CaM) bound to L-type Ca^{2+} -channels (Figure 3.7): $[Ca^{2+}]_i$ binds to CaM, constitutively attached to the L-Type Ca^{2+} channels (k_1/k_{-1} rates) and when 4 Ca^{2+} ions are bound, the complex may activate CDI (k_2/k_{-2} rates). The original equations for the n gate has been preserved in the modified model, even if kinetic rates have been slightly modified, in order to increase its sensibility to $[Ca^{2+}]_i$ variations.

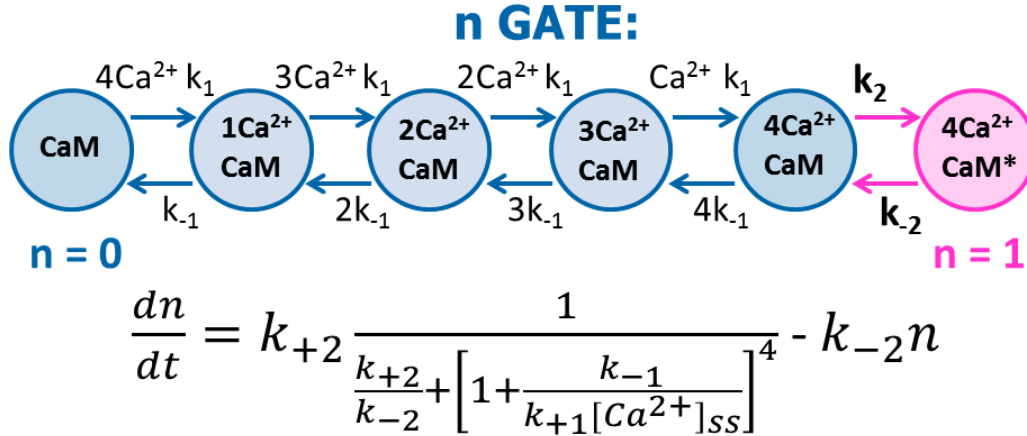


Figure 3.7: Simplified diagram of the n gate (modified from [10]), which depend on Ca^{2+} and it has been used to computer the up/down rates between CDI/VDI loops.

In addition to I_{CaL} formulation, other changes in Ca^{2+} -handling were needed to refine the modified model. These changes mostly addressed Ca^{2+} diffusion, release and uptake from the sarcoplasmic reticulum (SR):

- Since experimental evidence is not clear about Ca^{2+} movement inside the SR [14], Ca^{2+} diffusion inside the SR has been initially speeded up, according to [15]. Afterwards, we decided to simplify model structure, leaving only a single compartment for the SR, instead of the separation between Network SR (NSR) and Junctional SR (JSR);
- 10-fold increase of SERCA pump maximal current;
- 2-fold increase in Ca^{2+} diffusion from sub-sarcolemmal space to cytoplasm;
- 1.2-fold increase of Na^+/Ca^{2+} exchanger maximal current

Model differential equations were implemented in Matlab (Mathworks Inc) and solved with a variable order solver (ode15s), based on numerical differentiation formulas [16]. Simulations were run with the original and modified models at variable $[Ca^{2+}]_o$ in the clinically relevant range 0.6-3 mM. Pacing at 1 Hz was maintained until steady state AP was reached (1000 s) and APD was measured as the interval between AP upstroke and the 90% repolarization level (APD_{90}).

The modified model equations, as implemented in the corresponding Matlab function file, are included in Appendix A.

RESULTS

Model Validation

The modified model has been validated against most of the voltage-clamp and current-clamp experimental data considered in the original ORd model, especially the ones concerning I_{CaL} dynamics. Different voltage-clamp protocols have been reproduced in simulations, and the modified model results were in agreement with both the corresponding experimental data and the original ORd model.

I_{CaL} steady state activation, inactivation and I-V curves have been compared with data from Magyar et al. [17] (Figure 3.8, Figure 3.9 and Figure 3.10 respectively). The I-V curve is slightly different from the experimental data, especially when considering positive voltage, even if it perfectly overlaps the one from the original ORd model. This is related to the activation of the current, which indeed was not modified. Recovery from inactivation has been evaluated using the P_1P_2 protocol, as in Fulop et al. [19] (Figure 3.11).

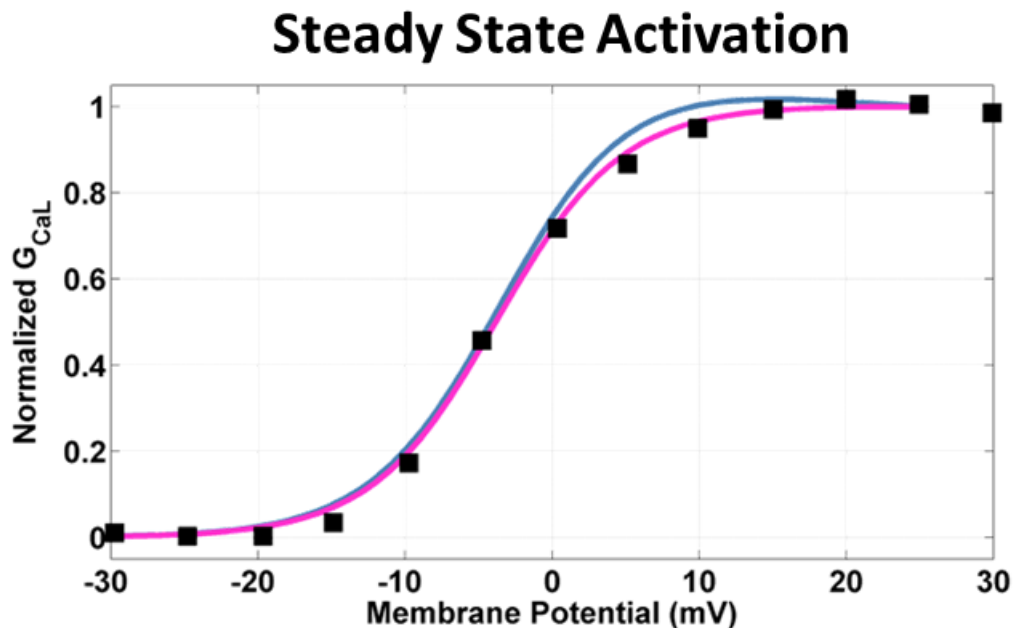


Figure 3.8: Comparison of I_{CaL} steady state activation curves: original ORd model (blue line), modified ORd model (pink line) and experimental data from [18] (black squares).

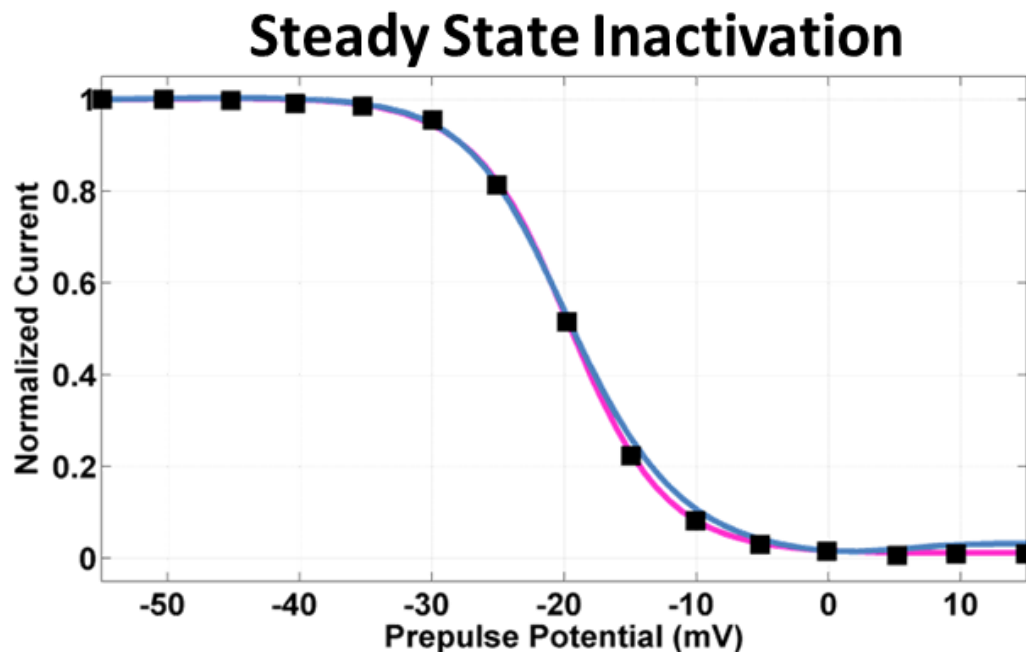


Figure 3.9: Comparison of I_{CaL} steady state inactivation curves: original ORd model (blue line), modified ORd model (pink line) and experimental data from [18] (black squares).

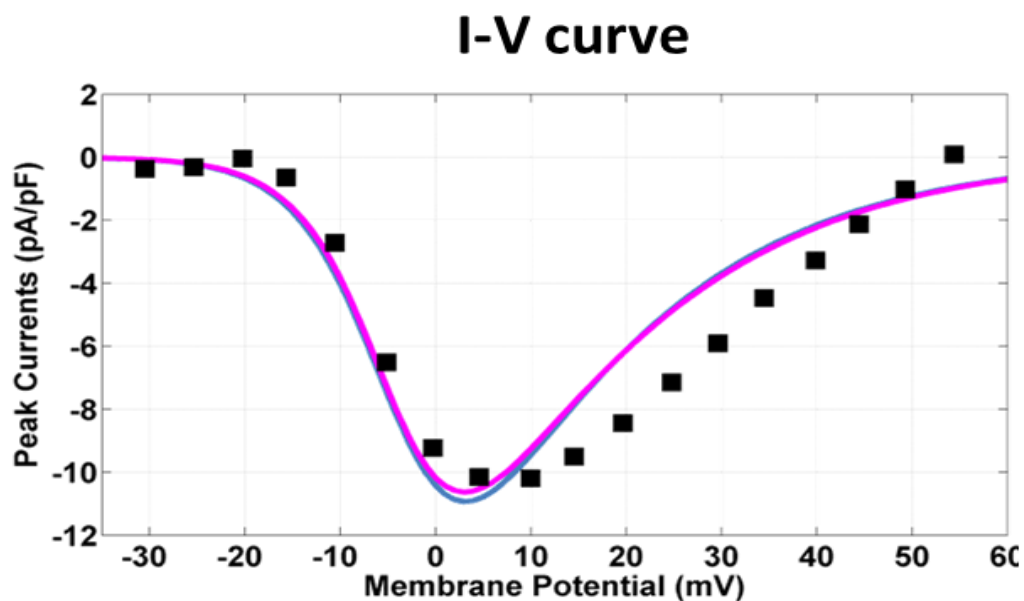


Figure 3.10: Comparison of I_{CaL} I-V curves: original ORd model (blue line), modified ORd model (pink line) and experimental data from [18] (black squares). The original and modified ORd model curves are almost identical, but different from the experimental data, especially for positive potential. This is mostly related to the activation property of the L-type Ca^{2+} current.

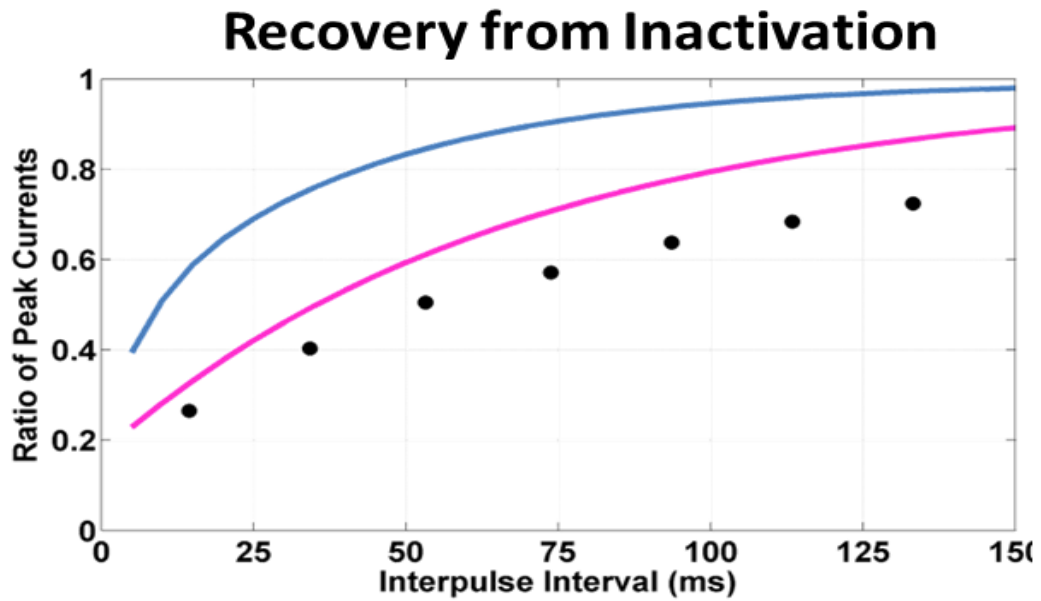


Figure 3.11: Recovery from inactivation, evaluated using the P_1P_2 protocol: original ORd model (blue line), modified ORd model (pink line) and experimental data from [19] (black squares). The modified ORd model actually gets closer to the experimental data than the original one.

Experimental results of CDI blocks are in agreement with the ones reported in the ORd paper [10], measured when considering Ba^{2+} instead of Ca^{2+} current, therefore in absence of CDI: in fact, I_{CaL} inactivation is much slower than in presence of both CDI and VDI. When blocking CDI, the original and modified ORd models show the same qualitative effect (Figure 3.12).

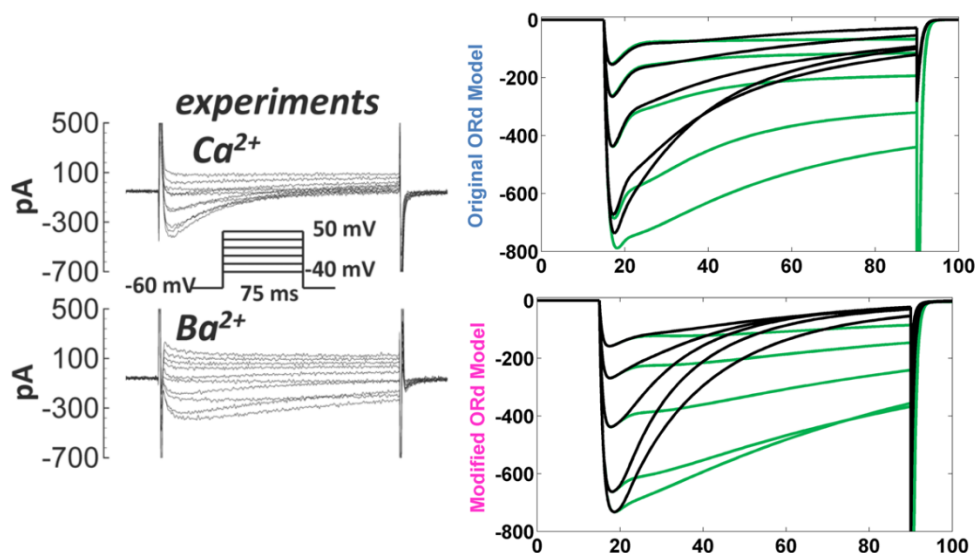


Figure 3.12: A) Experimental recording of Ca^{2+} and Ba^{2+} currents [10]: the latter, in absence of CDI mechanism, shows a much slower inactivation; B) Effects of CDI block on the L-Type Ca^{2+} current for the original and modified ORd models (top and bottom panel, respectively): both models show a slower inactivation, as expected.

Finally, the APD restitution curve, obtained by using a S_1S_2 protocol, is qualitatively reproduced by the modified ORd model. Simulation results are even more close to the experimental data than the ones obtained using the original ORd model (Figure 3.13).

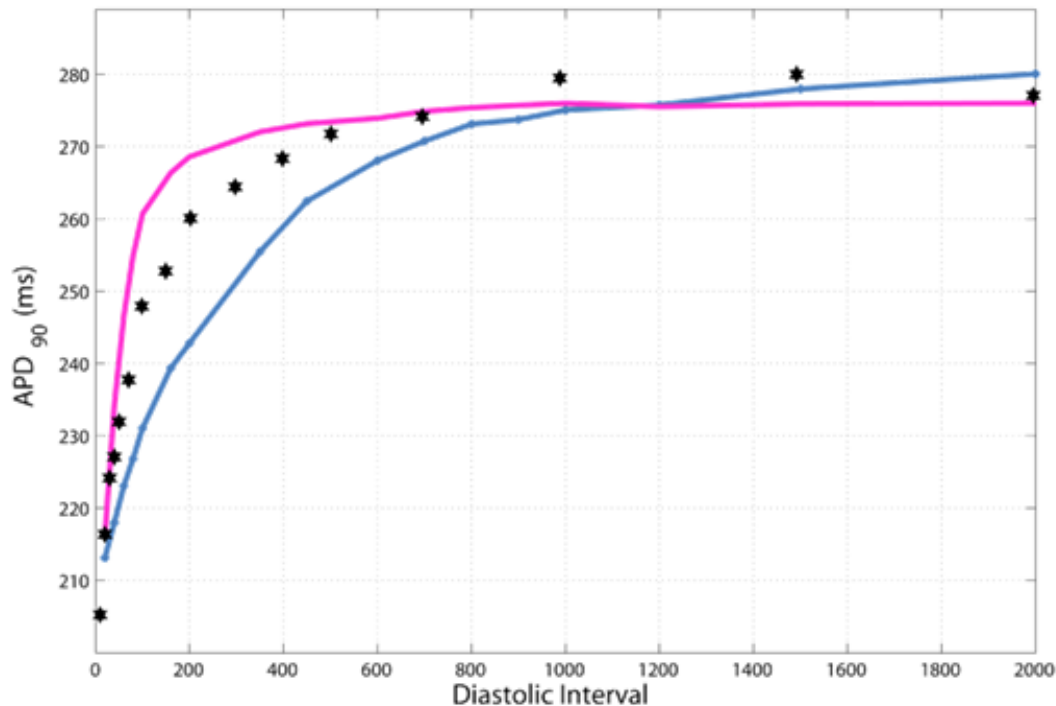


Figure 3.13: Comparison of the S_1S_2 restitution curves: original ORd model (blue line), modified ORd model (pink line) and experimental data from [10] (black squares).

APD- $[Ca^{2+}]_o$ dependence

When $[Ca^{2+}]_o$ was set to the control value (1.8 mM), the modified and the original ORd models provided almost the same simulation results (Figure 3.14, solid lines): ionic currents and AP were very similar in shape and length. In the modified model, I_{CaL} during AP plateau had a lower amplitude, due to the increased CDI.

When $[Ca^{2+}]_o$ variations have been simulated, however, significant differences were found in the two model results, both for AP and I_{CaL} (Figure 3.14, dashed and dotted lines).

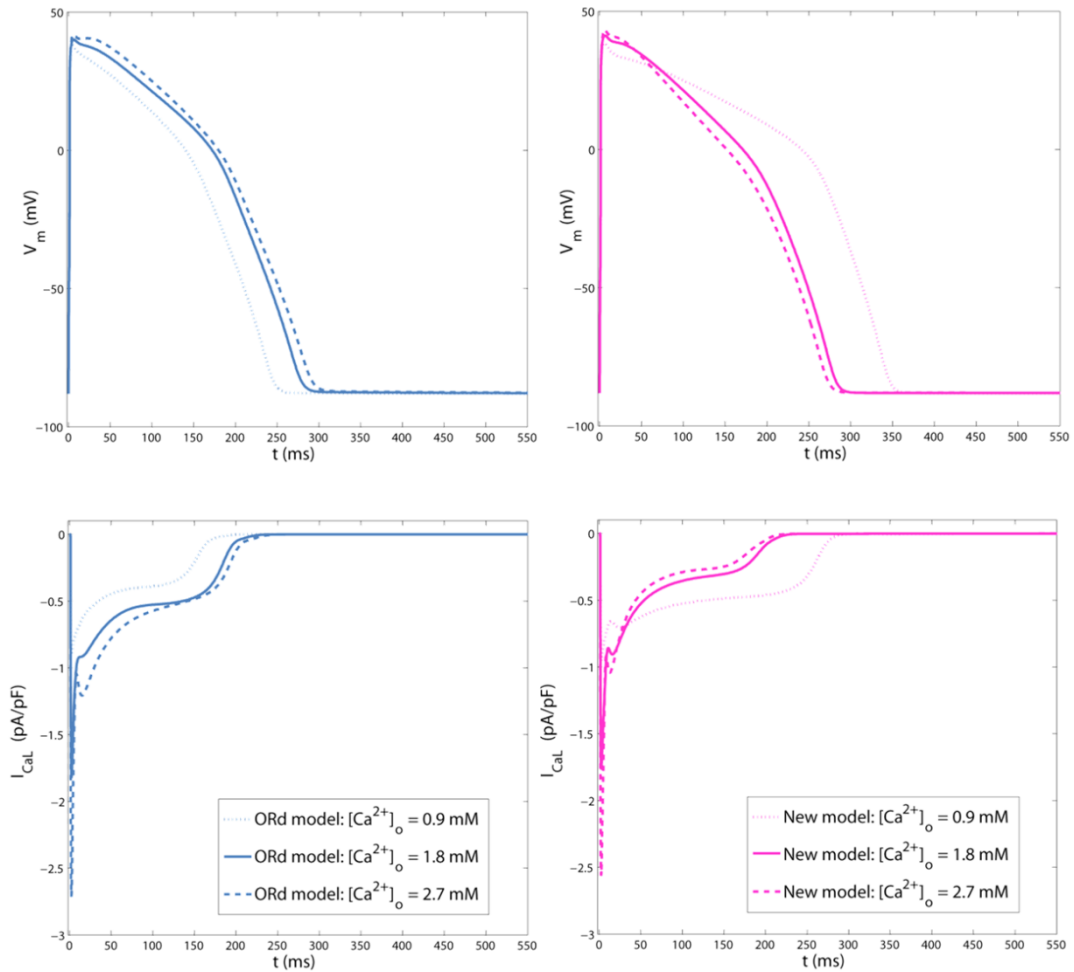


Figure 3.14: Simulation results for the original and modified ORd models, showing APs (top panels) and I_{CaL} (bottom panels) for different $[Ca^{2+}]_o$ concentrations. In control conditions ($[Ca^{2+}]_o = 1.8$ mM) the two model traces are quite similar, but when varying $[Ca^{2+}]_o$ their behave in two opposite ways: the original model APD increases with $[Ca^{2+}]_o$, while the modified model APD decreases.

In the original ORd model, when $[Ca^{2+}]_o$ is set to high values, the increase in driving force causes a larger I_{CaL} , which in turn lengthens AP. In the modified model, instead, the increase in driving force is compensated by a higher CDI, and the corresponding AP is shorter than in control. Only in the modified model the inverse relationship between APD and $[Ca^{2+}]_o$ is reproduced correctly (Figure 3.15).

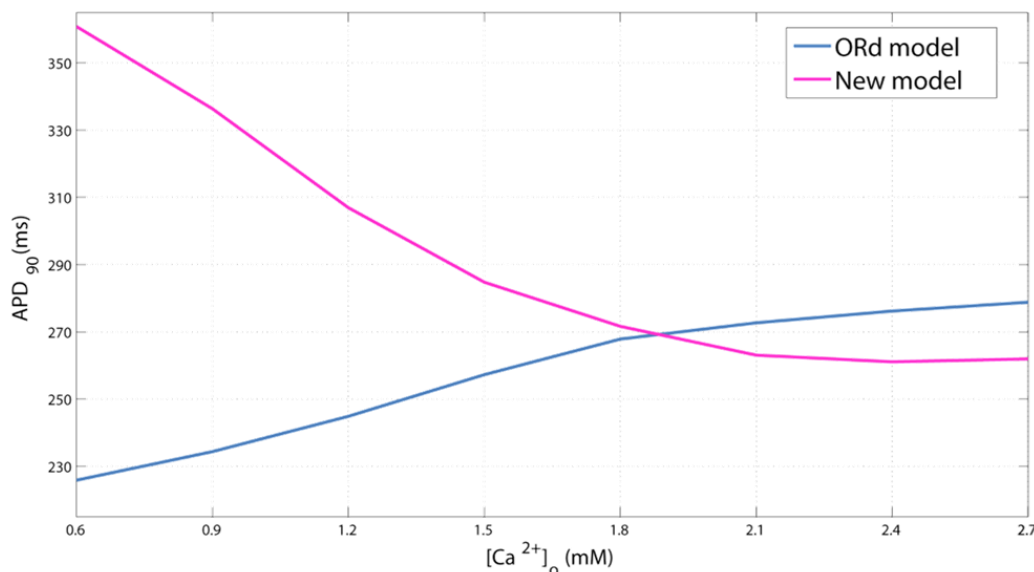


Figure 3.15: The APD- $[Ca^{2+}]_o$ dependence for the original and modified ORd model: only the latter is well reproducing the inverse relationship between APD and $[Ca^{2+}]_o$.

Qualitative comparison with Experimental Data

The modified ORd model can be used in all clinical contexts where electrolyte variations occur, in order to assess a possible increased risk of arrhythmias for patients. A typical case of study is haemodialysis therapy, where patients regularly undergo relevant electrolyte changes (especially Ca^{2+} and K^+) in a few hours.

This kind of analysis had already been performed in a previous study [8], using experimental electrolyte data acquired during hemodialysis sessions as input of another human ventricular AP model [20]. Considering consistency between APD changes and QTc, simulation results had been compared with ECG data. The same comparison has been performed using the modified ORd model presented in this work, and simulation results are shown in Figure 3.16..

Another possible application is head-down bed-rest experiments, used to simulate microgravity effects on the cardiovascular system: during bed-rest blood electrolyte concentrations changes over time, with possible impact on cardiac repolarization [21]. As an example, the next Chapter will present a simulation work done by combining bed-rest data and the modified ORd model described above.

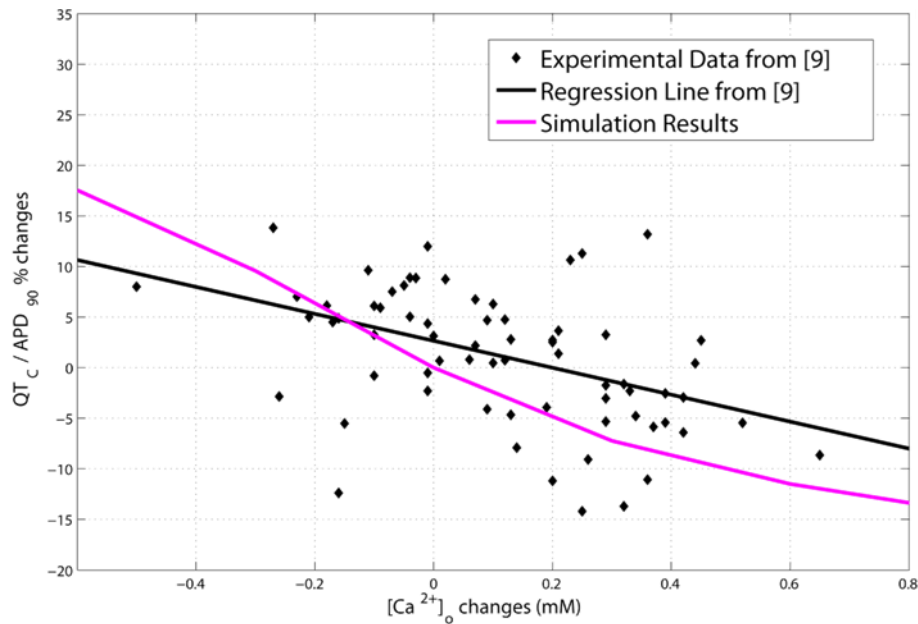


Figure 3.16: Comparison of $[Ca^{2+}]_o$ dependence of measured QTc interval duration and simulated APD (modified ORd model). Scatter plot and regression line show the significant inverse correlation between QTc interval duration and serum $[Ca^{2+}]$ changes measured during haemodialysis sessions (data from [8]). Simulated APD values were normalized to the APD value obtained at the average pre-dialysis Ca^{2+} concentration, i.e. 1.2 mM

DISCUSSION AND CONCLUSIONS

APD dependency on extracellular Ca^{2+} concentration has been analysed in the most recently published human ventricular AP mathematical model [10]. Since this model does not reproduce properly the inverse APD- $[Ca^{2+}]_o$ dependence, observed both in vitro and in vivo [6], some modifications have been implemented, in order to improve its response to $[Ca^{2+}]_o$ changes.

L-type Ca^{2+} current has been replaced by a new Markov model, and CDI mechanisms has been strengthened with respect to VDI. Both inactivation processes have been implemented as voltage-dependent, the former 10 times faster than the latter: therefore, CDI in the modified model works simply as a faster VDI.

The modified model has been validated against the I_{CaL} experimental data used for the original one, in order to verify consistency between the two models in control conditions.

Response to extracellular $[Ca^{2+}]_o$ in the 1-3mM range has been considered, and the modified model succeeded in reproduce the proper variations on APD.

Since the modifications applied to the original ORd model involved mostly I_{CaL} CDI strengthening, it is suggested that this inactivation mechanism may be usually underestimated in computational cardiac models.

The modified model here described may be used to explore a variety of contexts where electrolyte changes occur, e.g. haemodialysis sessions or head-down bed-rest experiments, in order to assess the possible arrhythmic risk for patients.

Limitations and Future Works

The modified ORd model has been validated on most of the experimental protocols shown in the original ORd paper. However, there are many other aspects that should be investigated more in details.

As an example, we considered only the S_1S_2 protocol to assess rate dependence properties in the modified model, while in the original ORd one they consider different simulation protocols, checking also the changes occurring in every single ionic current. In addition, in the original ORd model there is a lot of work showing model results when considering different degrees of I_{Kr} blocks, showing early-after depolarisations (EADs) when blocking 85% of the current.

Therefore, future works will address a further validation of the modified models, to check the consistency in all the aspects considered in the original one.

Finally, the modified model could be used in a population of models study like the one described later on (Chapter 7), as an alternative to the original ORd model. It would be very interesting to see how the changes in Ca^{2+} current and Ca^{2+} -handling may affect the results, especially when considering pro-arrhythmic mechanisms related to Ca^{2+} , such as EADs or DADs.

CHAPTER 4

Extracellular Electrolyte Changes During Head-Down Bed-Rest: Effects on Action Potential Duration

The content of this chapter has been published in:

Passini E, Pellegrini A, Caiani E, Severi S.

**Computational Analysis of Head-Down Bed Rest Effects
on Cardiac Action Potential Duration.**

Computing in Cardiology, Vol. 40, 2013

Computational Modelling of Cardiac Electrophysiology: from Cell to Bedside

Abstract

Several episodes of ventricular arrhythmias have been reported during spaceflights, and cardiovascular deconditioning induced by microgravity exposure has already been assessed.

Strict Head-Down Bed Rest (HDBR) can be used to simulate microgravity effects on the cardiovascular system. Therefore, it represents an invaluable opportunity to study and analyse this phenomenon.

The aim of this work has been to evaluate the possible effect of blood electrolyte changes induced by 21 days of HDBR on the electrical activity of the heart, by using a computational model of human ventricular myocyte.

Simulation results point out a biphasic course of action potential duration, which shortened during HDBR and recovered after the end of it, accordingly with RT interval measurements from ECG data analysis.

INTRODUCTION

It is well known that microgravity affects the cardiovascular system: indeed, there are many effects associated with spaceflights, e.g. reduction in plasma volume, decrease in left ventricular mass and modifications of the autonomic nervous system. Moreover, several episodes of cardiac arrhythmias and conduction disorders have been reported during space missions, such as Gemini and Apollo [22, 23], and aboard space stations [24, 25].

However, the specific causes leading to this suggested increased risk of arrhythmias have not been entirely understood. To further explore this phenomenon, ground-based experiments, such as strict Head Down Bed Rest (HDBR), represent a great opportunity to analyse simulated microgravity effects on cardiovascular system, by monitoring ECG signal and different physiological parameters over time [26]. In this context, computational modeling constitutes a useful tool as well: in fact, changes observed experimentally may be tested in silico in order to evaluate their possible impact on cardiac electrical activity.

The aim of this work has been to verify if the blood electrolyte variations occurring during 21 days of HDBR can be directly linked to the corresponding changes observed in cardiac repolarization phase, by using a computational model of human ventricular action potential (AP) and comparing simulation results with ECG data analysis, PRE, during and POST bed-rest.

METHODS

Bed-Rest Protocol

Experimental data were recorded during a mid-term (21 days) strict -6° Head-Down Bed-Rest (HDBR) campaign held at the German Aerospace Center (DLR, Koln, Germany) by the European Space Agency (ESA) from September 2011 to April 2012.

Ten healthy subjects (aged 23-42 years) were enrolled for this study in a cross-over design, including a control and a countermeasure (CM) group, with a washout period of about 1.5 months between the two HDBR sessions. Subjects in the CM group received a daily supplementation of whey protein (0.6 g/kg body weight) and potassium bicarbonate (KHCO_3 , 90 mmol). In this study, our attention will be focused on the CM group only. Each subject underwent a comprehensive medical examination during the selection process and provided written informed consent to participate in this study, approved by the independent ethics committee Aerktekammer Nordrhein, Duesseldorf, Germany.

The volunteers had to stay in bed with their head down, at 6° below the horizontal, for all the HDBR session (Figure 4.1). They may not stand up, unless a research programme demands it, and must perform all daily activities in bed including eating, showers and sometimes specific exercise. In this way, their bodies start to adapt as if they were in space, where there is no gravity.

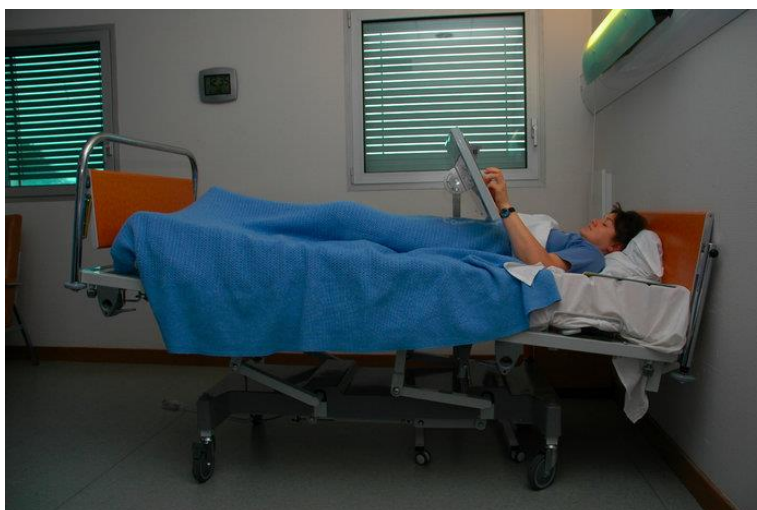


Figure 4.1: During head-down bed-rest studies, volunteers have to stay in bed with their head down, at 6° below the horizontal, for all the experiments session (copyright: ESA)

Experimental Data Acquisition

ECG signals have been acquired using a 24-h high resolution (sampling frequency: 1000 Hz) 12-lead Holter digital recorder (H12+, Mortara Instrument Inc, Milwaukee, WI, USA). Acquisitions were performed 8 days before the beginning of the test (PRE), after 5, 16 and 21 days of Head-Down Tilt (HDT₅, HDT₁₆ and HDT₂₁ respectively) and 4 days after the end (POST).

The RR values classified as “sinusal rhythm” (H-scribe and SuperECG software, Mortara Instrument Inc, Milwaukee, WI, USA) have been considered and the night period only (from 23:00 to 6:30) has been taken into account, in order to avoid possible noise due to subject daily movement.

Selective beat averaging technique [26, 27] was used to obtain averages of P-QRS-T complexes preceded by the same stable heart rate (cycle length from 900 to 1200 ms, 10 ms RR bins). Repolarization phase has been evaluated considering the time distance from the QRS peak and the T-wave end (RT interval).

Blood samples have been collected 7 days before the beginning of the test (PRE), at HDT₁₀ and 5 days after the end (POST). Electrolyte concentrations ([Na⁺], [K⁺], [Cl⁻] and total [Ca²⁺]) were measured, together with many other physiological parameters (e.g. cell volume, glucose, pH, etc.) which will not be considered in this study. Since no direct measurement of ionised Ca²⁺ was available, we chose to estimate it as half of the total Ca²⁺ concentration.

A schedule of the considered HDBR epochs and data acquisitions is reported in Figure 4.2, showing the three different situations: PRE, HDT and POST.

PRE and POST data have been compared to the ones acquired during HDBR test, i.e. HDT₁₆ for ECG and HDT₁₀ for electrolyte concentrations, since measurements have been recorded in different HDT days. Of course, the HDBR effects on HDT₁₆ should be much more pronounced than in HDT₁₀: therefore, simulation results which are based on electrolyte concentrations may show smaller electrophysiological changes, compared to the ones observed in the ECG data.

Finally, experimental results shown in the next section refer to only 8 subjects out of 10, since one participant left during the test and another one had some ECG recording problems.

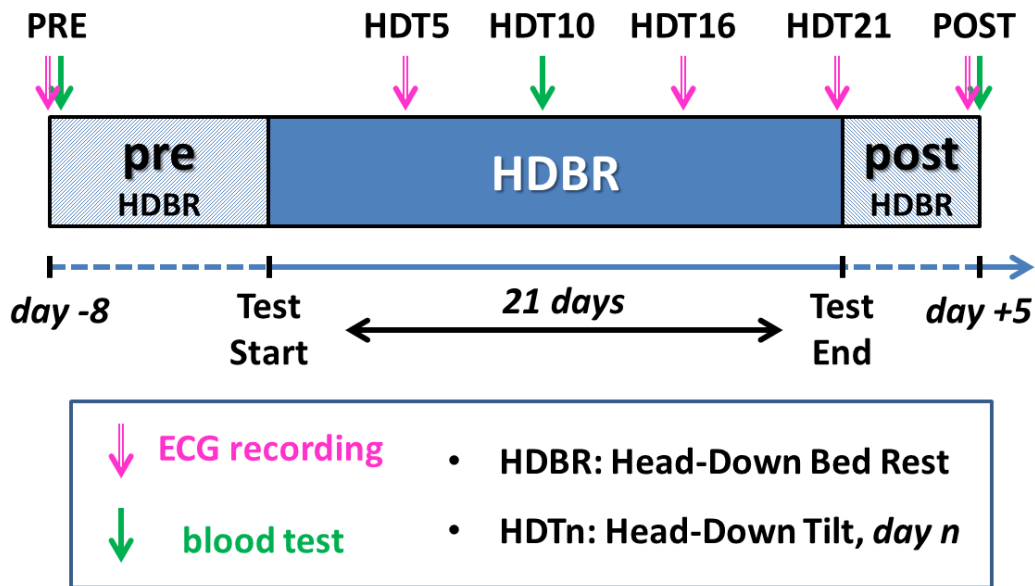


Figure 4.2: Time course diagram of the 21 days Head-Down Bed-Rest (HDBR) campaign considered in this study. The arrows indicate the epochs in which 24-h Holter acquisition and blood analysis have been performed.

Computational Modeling

The most recent human ventricular mathematical model (O’Hara-Rudy, [10]) has been used as basis for simulations. However, the original model is not able to reproduce properly the effects of extracellular Ca^{2+} variations on action potential duration (APD). Therefore, as similarly done in previous works with different models [6, 9], specific modifications were needed in order to reproduce the inverse relationship between extracellular $[\text{Ca}^{2+}]$ and APD. The original L-type Ca^{2+} current formulation has been replaced by a new Markov model and Ca^{2+} -dependent inactivation has been strengthened. Other minor changes were needed to preserve the physiological properties of the whole cell [28]. The modified model has been described in the details in the previous Chapter.

Extracellular electrolyte concentrations were considered in equilibrium with blood and used as model inputs to simulate PRE, HDT₁₀ and POST conditions, as similarly done in a previous work for haemodialysis patients [8].

Single Cell Simulations

Model differential equations were implemented in Matlab (Mathworks Inc.) and solved with a variable order solver (ode15s), based on numerical differentiation formulas [16]. Pacing at 1 Hz was maintained until a steady state AP was reached and APD was measured as the interval between AP upstroke and the 90% repolarization level (APD₉₀).

Multicellular simulations

One dimensional fiber (2 cm length) composed by 100 endo- and 100 epi-cardial cells has been considered. Model equations have been translated into cellML language using COR environment [29] and monodomain equations have been solved with Chaste Software [30, 31], considering an intracellular conductivity of 0.50 mS/cm.

Pseudo-ECG signal has been computed as described by Gima-Rudy [32]; RT interval has been evaluated considering a slope inferior to 1e-4 V/s as T wave end.

RESULTS

Experimental data analysis

ECG analysis provided evidence of a biphasic trend in repolarization: RT interval considerably shortened during bed-rest (HDT₁₆) and then completely recovered at POST, reaching values even higher than in PRE for each considered RR bin, as shown in Figure 4.3.

Since computational simulations have been run considering a cycle length of 1000 ms, we chose to compare simulation results with data from the RR bin between 995 and 1005 ms. Here, the RT interval changes were quite relevant, as shown in Figure 4.4: -19 ms in HDT₁₆vsPRE and -30 ms POSTvsHDT₁₆.

Non parametric Friedman and Wilcoxon tests were applied and significant differences (p<0.001) were found for the three considered groups: PRE, HDT₁₆ and POST.

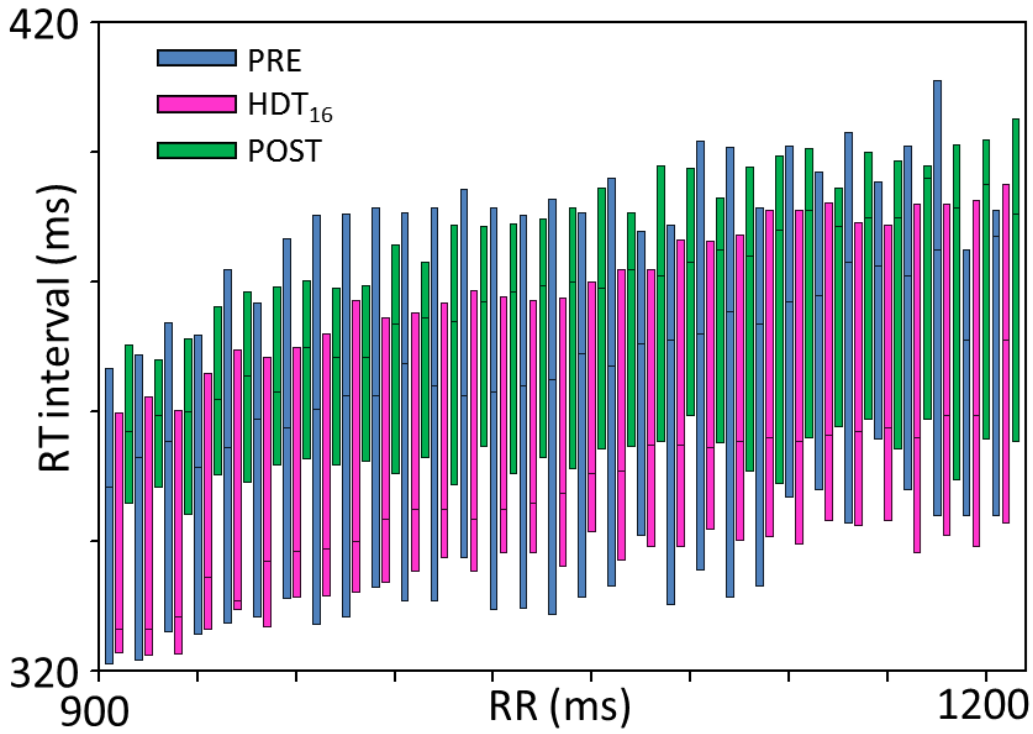


Figure 4.3: Relationship between RR and RT interval. Wisker-plot represents median and 25-75th percentiles for each RR bin in PRE, HDT₁₆ and POST conditions.

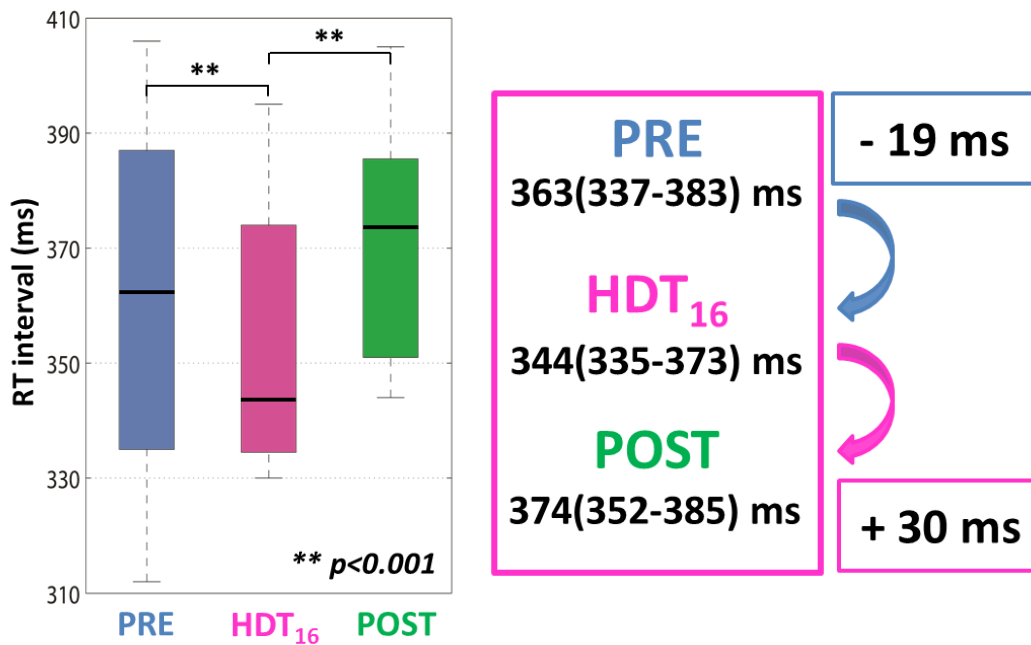


Figure 4.4: RT intervals for RR bin between 995-1005 ms in PRE, HDT₁₆ and POST conditions: the biphasic trend in repolarisation it is quite clear. Data are presented as median(25th-75th).

As for electrolyte concentrations, blood Ca^{2+} concentration showed an opposite trend compared to RT interval: it increased during HDBR and then recovered at POST, as shown in Figure 4.5. Non parametric Wilcoxon test was applied and differences resulted significant in HDT_{10} vs PRE and POST vs HDT_{10} ($p < 0.05$).

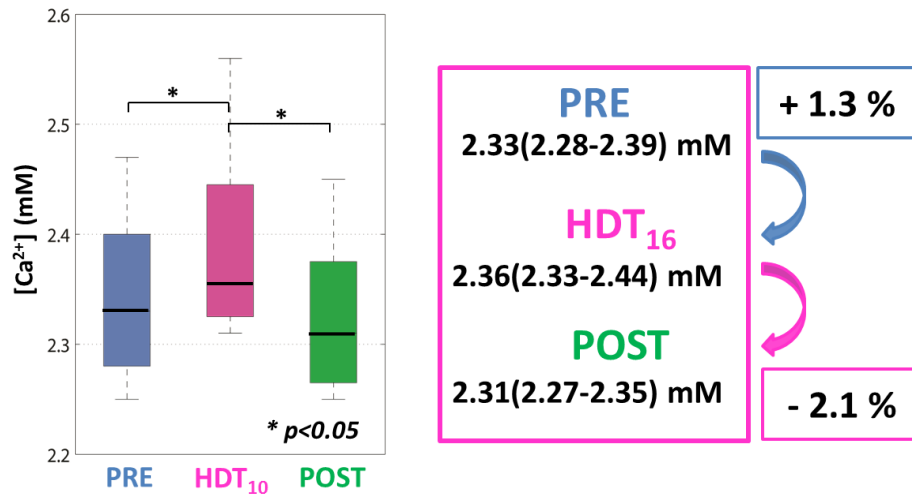


Figure 4.5: Blood Ca^{2+} concentrations in PRE, HDT_{10} and POST conditions: the biphasic trend is opposite to the one found in the RT interval. Data are shown as median(25th-75th).

Relevant differences were found in blood K^+ concentration, even if there was a lot of variability from one subject to the other, and sometime K^+ variations were in an opposite direction. In average, K^+ increased during HDBR and decreased at the end of it, although not completely recovered at POST, as shown in Figure 4.6.

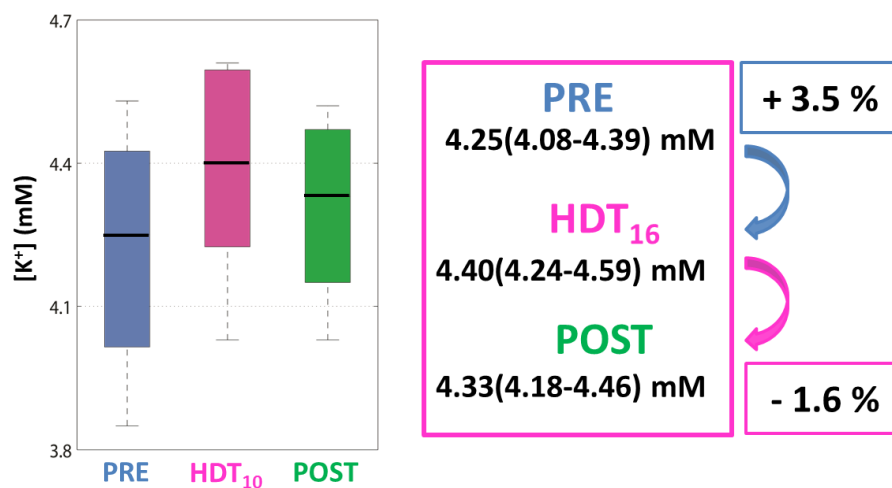


Figure 4.6: Blood Ca^{2+} concentrations in PRE, HDT_{10} and POST conditions: the biphasic trend is opposite to the one found in the RT interval. Data are shown as median(25th-75th).

Changes in $[\text{Na}^+]$ and $[\text{Cl}^-]$ were almost negligible (not shown).

A summary of experimental data results is reported in Table 4.1, considering only the 995-1005 ms bin for the RT interval data.

Table 4.1: Experimental data in PRE, HDT and POST conditions. Since computational simulations have been performed at 1Hz pacing, only the RT interval corresponding to the 905-1005 ms RR bin are shown. Data are presented as Median(25th-75th).

	<i>RT interval (ms)</i>	<i>% changes</i>
PRE	362.5(337.0-382.5)	-
HDT₁₆	343.5(335.3-373.3)	-5.24% vs PRE
POST	373.5(351.5-385.3)	+8.73% vs HDT ₁₆
	<i>total $[\text{Ca}^{2+}]$(mM)</i>	<i>% changes</i>
PRE	2.33(2.28-2.39)	-
HDT₁₀	2.36(2.33-2.44)	+1.29% vs PRE
POST	2.31(2.27-2.35)	-2.12% vs HDT ₁₀
	<i>$[\text{K}^+]$ (mM)</i>	<i>% changes</i>
PRE	4.25(4.08-4.39)	-
HDT₁₀	4.40(4.24-4.59)	+3.53% vs PRE
POST	4.33(4.18-4.46)	-1.59% vs HDT ₁₀

Computational Results

Single cell simulations were run separately for each of the subjects, setting the extracellular electrolyte concentrations equal to the ones measured in PRE, HDT₁₀ and POST conditions.

Consistently with RT interval, APD usually decreased during HDBR and recovered at POST. Indeed, median variations were relatively small (-1.22% HDT₁₀ vs PRE, +0.46% POST vs HDT₁₀), but when considering individual subjects with larger electrolyte variations, there were many subject in which concurrent changes of Ca^{2+} and K^+ produced a greater effect. However, sometimes APD variations were contrasting in different subjects, especially when considering POST vs HDT₁₀. All the APD and electrolyte variations are shown in Table 4.2.

Subject #3 is the one showing the most relevant changes, both in HDT₁₀ vs PRE (APD₉₀ -20 ms) and POST vs HDT₁₀ (APD₉₀ +18 ms). The corresponding AP traces are shown in Figure 4.7.

Table 4.2: Simulation results in terms of APD for each subject during PRE, HDT₁₀ and POST conditions, together with the corresponding electrolyte variations. Notable changes are marked in bold.

Subject	HDT ₁₀ vs PRE			POST vs HDT ₁₀		
	$\Delta [Ca^{2+}]%$	$\Delta [K^+]%$	ΔAPD_{90}	$\Delta [Ca^{2+}]%$	$\Delta [K^+]%$	ΔAPD_{90}
#1	+1.66%	+3.87%	-3.0 ms	-6.94%	+6.70%	+2.0 ms
#2	+0.43%	+2.65%	-3.2 ms	-0.85%	+2.35%	-0.7 ms
#3	+3.64%	+38.44%	-20.0 ms	-4.30%	-15.76%	+18.0 ms
#4	+1.75%	+2.00%	-4.8 ms	-0.43%	-2.84%	+0.8 ms
#5	+2.67%	+3.21%	-5.7 ms	-0.43%	+0.44%	-0.4 ms
#6	-1.26%	+1.77%	-4.1 ms	-4.66%	-12.58%	+10.1 ms
#7	+5.17%	-2.78%	-3.2 ms	-0.82%	+0.48%	-1.5 ms
#8	+2.20%	+2.63%	-2.5 ms	-21.98%	-4.88%	+14.8 ms

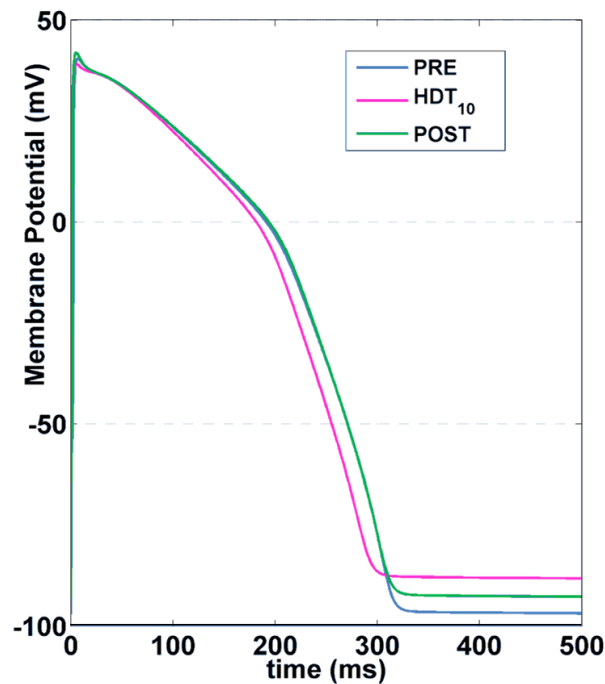


Figure 4.7: Simulated AP traces for subject #3 in PRE, HDT₁₀ and POST conditions.

One dimensional simulations have been performed as first considering median electrolyte variations only. Pseudo-ECG was computed and the simulated RT interval varied in accordance both to single cell APD and measured RT interval (-1.70% HDT₁₀ vs PRE, +0.75% POST vs HDT₁₀).

Pseudo-ECG was simulated also for the single subject presenting the higher APD variations (#3): here the changes of RT interval were significantly larger (-12.45% HDT₁₀ vs PRE, +5.53% POST vs HDT₁₀). His pseudo-ECG traces and T wave in PRE, HDT₁₀ and POST conditions are shown in Figure 4.8.

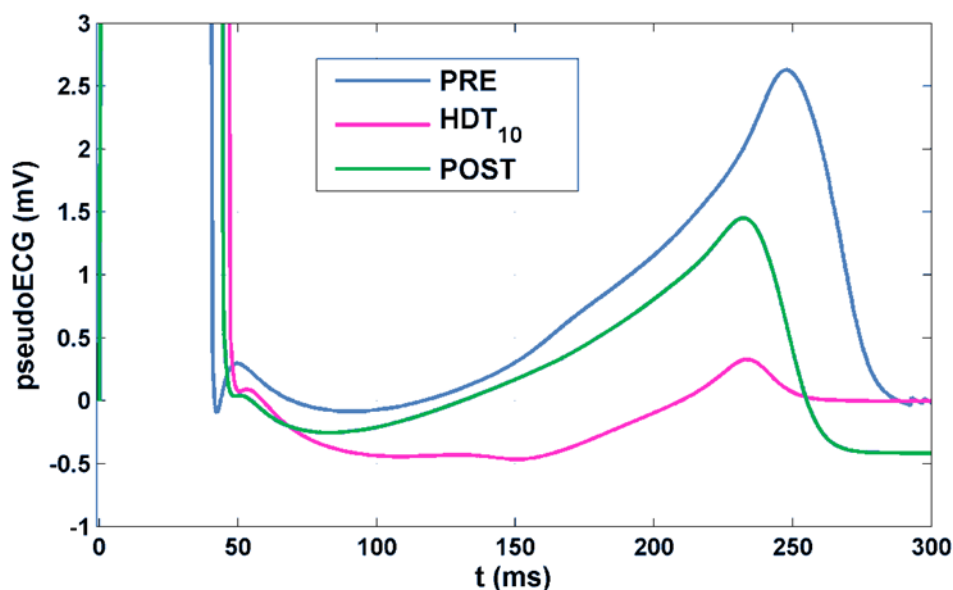


Figure 4.8: Pseudo-ECG for subject #3. Repolarization phase varied considerably in the three different conditions: simulated RT interval highly decreased during HDBR (-36 ms HDT₁₀ vs PRE) and only partially recovered at the end of it (+14 ms POST vs HDT₁₀).

DISCUSSION AND CONCLUSIONS

Experimental data acquired from 8 subjects during 21 days of HDBR have been presented and analysed, in order to assess the effects of simulated microgravity on the cardiovascular system, and possibly clarify the underline mechanisms involved.

ECG recording showed a significant decreased of RT interval during HDBR with respect to PRE and POST conditions. Blood test provided the extent of extracellular electrolytes variations, especially Ca²⁺ and K⁺.

A computational model of human ventricular myocyte has been used to simulate subject conditions PRE, POST and during HDBR, considering the corresponding electrolyte concentrations as inputs. Simulations results showed small but consistent changes in APD and simulated RT interval.

These findings support the hypothesis that electrolyte imbalances occurring during HDBR may be linked to the electrical changes observed experimentally.

However, several additional mechanisms are affected by microgravity. Therefore, for a more comprehensive computational analysis, other factors should be considered in simulations.

Limitations and Future Developments

Simulations have been performed using electrolyte data acquired on HDT₁₀, and compared with ECG analysis from HDT₁₆. 24-h Holter and blood samples collected at the same day could lead to a more precise comparison. Moreover, ionized Ca²⁺ concentration has been estimated as half total Ca²⁺, since no direct measurements were available.

A new mid-term HDBR campaign, involving one control and two CM groups, has been recently completed by ESA. Experimental data, including ionized Ca²⁺ concentration, will be available for further investigations in the near future.

Acknowledgements

We are extremely grateful to all the personnel of ESA and DLR involved in the study for the support to the realization of our experiment, as well as to the experimental subjects for their dedicated collaboration. The research “Evaluation of changes in ventricular repolarization and its relationship with heart rate during bed-rest experiment” has been performed thanks to the contribution of the Italian Space Agency (Contracts no. I/047/10/0 and 2013-033-R.0, recipient Dr. EG Caiani).

References

- [1] B. F. Hoffman and E. E. Suckling, “Effect of Several Cations on Transmembrane Potentials of Cardiac Muscle” *Am J Physiol Hear Circ Physiol*, vol. 186, no. 2, pp. 317–324, Aug. 1956.
- [2] S. Leitch, “Effect of Raised Extracellular Calcium on Characteristics of the Guinea-pig Ventricular Action Potential” *J Mol Cell Cardiol*, vol. 28, no. 3, pp. 541–551, Mar. 1996.
- [3] C.-X. Bai, “Role of Nitric Oxide in Ca²⁺ Sensitivity of the Slowly Activating Delayed Rectifier K⁺ Current in Cardiac Myocytes” *Circ Res*, vol. 96, no. 1, pp. 64–72, Dec. 2004.
- [4] R. S. Kass and R. W. Tsien, “Control of action potential duration by calcium ions in cardiac Purkinje fibers” *J Gen Physiol*, vol. 67, no. 5, pp. 599–617, May 1976.
- [5] J. V. Temte and L. D. Davis, “Effect of Calcium Concentration on the Transmembrane Potentials of Purkinje Fibers” *Circ Res*, vol. 20, no. 1, pp. 32–44, Jan. 1967.
- [6] S. Severi, C. Corsi, and E. Cerbai, “From in vivo plasma composition to in vitro cardiac electrophysiology and in silico virtual heart: the extracellular calcium enigma” *Philos Trans A Math Phys Eng Sci*, vol. 367, no. 1896, pp. 2203–23, Jun. 2009.
- [7] N. Nagy, K. Acsai, A. Kormos, Z. Sebök, A. S. Farkas, N. Jost, P. P. Nánási, J. G. Papp, A. Varró, and A. Tóth, “[Ca²⁺] i-induced augmentation of the inward rectifier potassium current (IK1) in canine and human ventricular myocardium” *Pflugers Arch*, vol. 465, no. 11, pp. 1621–35, Nov. 2013.
- [8] S. Severi, E. Grandi, C. Pes, F. Badiali, F. Grandi, and A. Santoro, “Calcium and potassium changes during haemodialysis alter ventricular repolarization duration: in vivo and in silico analysis” *Nephrol Dial Transplant*, vol. 23, no. 4, pp. 1378–86, Apr. 2008.
- [9] E. Grandi, F. S. Pasqualini, C. Pes, C. Corsi, A. Zaza, and S. Severi, “Theoretical investigation of action potential duration dependence on extracellular Ca²⁺ in human cardiomyocytes” *J Mol Cell Cardiol*, vol. 46, no. 3, pp. 332–42, Mar. 2009.
- [10] T. O’Hara, L. Virág, A. Varró, and Y. Rudy, “Simulation of the undiseased human cardiac ventricular action potential: model formulation and experimental validation.” *PLoS Comput Biol*, vol. 7, no. 5, p. e1002061, May 2011.
- [11] E. Grandi, F. S. Pasqualini, and D. M. Bers, “A novel computational model of the human ventricular action potential and Ca transient.” *J Mol Cell Cardiol*, vol. 48, no. 1, pp. 112–21, Jan. 2010.
- [12] K. F. Decker, J. Heijman, J. R. Silva, T. J. Hund, and Y. Rudy, “Properties and ionic mechanisms of action potential adaptation, restitution, and accommodation in canine epicardium” *Am J Physiol Heart Circ Physiol*, vol. 296, no. 4, pp. H1017–26, Apr. 2009.
- [13] J. Kim, S. Ghosh, D. A. Nunziato, and G. S. Pitt, “Identification of the components controlling inactivation of voltage-gated Ca²⁺ channels” *Neuron*, vol. 41, no. 5, pp. 745–54, Mar. 2004.
- [14] D. M. Bers and T. R. Shannon, “Calcium movements inside the sarcoplasmic reticulum of cardiac myocytes.” *J Mol Cell Cardiol*, vol. 58, pp. 59–66, May 2013.

- [15] E. Picht, A. V Zima, T. R. Shannon, A. M. Duncan, L. A. Blatter, and D. M. Bers, “Dynamic calcium movement inside cardiac sarcoplasmic reticulum during release.” *Circ Res*, vol. 108, no. 7, pp. 847–56, Apr. 2011.
- [16] L. F. Shampine and M. W. Reichelt, “The MATLAB ODE Suite” *SIAM J. Sci Comput*, vol. 18, no. 1, pp. 1–22, Jan. 1997.
- [17] J. Magyar, N. Szentandrassy, T. Bányász, L. Fülöp, A. Varró, and P. P. Nánási, “Effects of thymol on calcium and potassium currents in canine and human ventricular cardiomyocytes” *Br J Pharmacol*, vol. 136, no. 2, pp. 330–8, May 2002.
- [18] J. Magyar, N. Iost, Á. Körtvély, T. Bányász, L. Virág, P. Szigligeti, a. Varró, M. Opincariu, J. Szécsi, J. G. Papp, and P. P. Nánási, “Effects of endothelin-1 on calcium and potassium currents in undiseased human ventricular myocytes” *Pflügers Arch*, vol. 441, no. 1, pp. 144–149, Sep. 2000.
- [19] L. Fülöp, T. Bányász, J. Magyar, N. Szentandrassy, A. Varró, and P. P. Nánási, “Reopening of L-type calcium channels in human ventricular myocytes during applied epicardial action potentials” *Acta Physiol Scand*, vol. 180, no. 1, pp. 39–47, Jan. 2004.
- [20] K. H. W. J. ten Tusscher, D. Noble, P. J. Noble, and A. V Panfilov, “A model for human ventricular tissue” *Am J Physiol Heart Circ Physiol*, vol. 286, no. 4, pp. H1573–89, Apr. 2004.
- [21] E. Passini, A. Pellegrini, E. G. Caiani, and S. Severi, “Computational Analysis of Head-Down Bed Rest Effects on Cardiac Action Potential Duration” *Computing in Cardiology*, vol. 40, 2013.
- [22] J. B. Charles, M. W. Bungo, and W. Fortner, “Cardiopulmonary function” *Sp Physiol Med*, pp. 286–304, 1994.
- [23] L. D. Dietlein, “Summary and conclusions” *Biomed Results APOLLO (NASA SP-368)*, 1975.
- [24] R. F. Smith, K. Stanton, D. Stoop, D. Brown, W. Janusz, and P. King, “Vectorcardiographic Changes during Extended Space Flight (M093). Observations at Rest and during Exercise” *Biomed Results from Skylab NASA SP-377*, 1977.
- [25] J. M. Fritsch-Yelle, U. A. Leuenberger, D. S. D’Aunno, A. C. Rossum, T. E. Brown, M. L. Wood, M. E. Josephson, and A. L. Goldberger, “An episode of ventricular tachycardia during long-duration spaceflight” *Am J Cardiol*, vol. 81, no. 11, pp. 1391–2, Jun. 1998.
- [26] E. G. Caiani, A. Pellegrini, J. Bolea, M. Sotaquira, R. Almeida, and P. Vařda, “Impaired T-wave amplitude adaptation to heart-rate induced by cardiac deconditioning after 5-days of head-down bed-rest” *Acta Astronaut*, vol. 91, no. null, pp. 166–172, Oct. 2013.
- [27] F. Badilini, P. Maison-Blanche, R. Childers, and P. Coumel, “QT interval analysis on ambulatory electrocardiogram recordings: a selective beat averaging approach” *Med Biol Eng Comput*, vol. 37, no. 1, pp. 71–9, Jan. 1999.
- [28] E. Passini and S. Severi, “Extracellular Calcium and L-Type Calcium Current Inactivation Mechanisms: a Computational Study” *Computing in Cardiology*, vol. 40, 2013.
- [29] A. Garny, P. Kohl, and D. Noble, “Cellular Open Resource (COR): A Public CellML Based Environment for Modeling Biological Function” *Int J Bifurc Chaos*, vol. 13, no. 12, pp. 3579–3590, Dec. 2003.

- [30] G. R. Mirams, C. J. Arthurs, M. O. Bernabeu, R. Bordas, J. Cooper, A. Corrias, Y. Davit, S.-J. Dunn, A. G. Fletcher, D. G. Harvey, M. E. Marsh, J. M. Osborne, P. Pathmanathan, J. Pitt-Francis, J. Southern, N. Zemezmi, and D. J. Gavaghan, “Chaste: an open source C++ library for computational physiology and biology” *PLoS Comput Biol*, vol. 9, no. 3, p. e1002970, Jan. 2013.
- [31] J. Pitt-Francis, P. Pathmanathan, M. O. Bernabeu, R. Bordas, J. Cooper, A. G. Fletcher, G. R. Mirams, P. Murray, J. M. Osborne, A. Walter, S. J. Chapman, A. Garny, I. M. M. van Leeuwen, P. K. Maini, B. Rodríguez, S. L. Waters, J. P. Whiteley, H. M. Byrne, and D. J. Gavaghan, “Chaste: A test-driven approach to software development for biological modelling” *Comput Phys Commun*, vol. 180, no. 12, pp. 2452–2471, Dec. 2009.
- [32] K. Gima and Y. Rudy, “Ionic Current Basis of Electrocardiographic Waveforms: A Model Study” *Circ Res*, vol. 90, no. 8, pp. 889–896, Mar. 2002.

SECTION II

Haemodialysis Therapy Impact on Cardiac Electrophysiology

CHAPTER 5

Human Atrial Cell Models to Analyse Haemodialysis-related Effects on Cardiac Electrophysiology: Work in Progress

The content of this chapter has been published in:

Passini E, Genovesi S, Severi S.

Human Atrial Cell Models to Analyse Haemodialysis-related Effects on Cardiac Electrophysiology: Work in Progress.

Computational and Mathematical Methods in Medicine, Vol. 2014, 18 pp

Computational Modelling of Cardiac Electrophysiology: from Cell to Bedside

Abstract

During haemodialysis (HD) sessions, patients undergo significant alterations in the extracellular environment, mostly concerning plasma electrolyte concentrations, pH and volume, together with a modification of sympatho-vagal balance. All these changes may affect cardiac electrophysiology, possibly leading to an increased arrhythmic risk: in particular, intra-dialytic atrial fibrillation incidence is really high.

Computational modelling may help to investigate the impact of HD-related changes on atrial electrophysiology, exploring their effects on the action potential (AP). However, many human atrial AP models are currently available, each one with a peculiar structure and different current formulations. In addition, these models have been developed using the standard electrolyte concentrations used for experiments. Therefore, they may respond in a different way to the same environmental changes.

After an overview of what has been done using the computational approach to investigate the effect of HD therapy on cardiac electrophysiology, the aim of this work has been to review the current state of the art in human atrial AP models, with respect to their suitability in the HD context.

All the published human atrial AP models have been considered (Courtemanche et al. 1998, Nygren et al. 1998, Maleckar et al. 2009, Koivumaki et al. 2011, Grandi et al. 2011, Colman et al. 2013) and tested for extracellular electrolytes and volume changes, as well as different acetylcholine concentrations.

Some models proved to be more appropriate than others when considering a single modification, but finally all of them showed some drawbacks. Therefore, there could be room for a new AP model, hopefully able to physiologically reproduce all the HD-related effects on the human atrial AP.

At the moment, works are still in progress in this specific field.

INTRODUCTION

In the last fifteen years, the increasing interest towards atrial electrophysiology and atrial fibrillation (AF), together with a greater availability of experimental data, led to remarkable developments in human atrial action potential (AP) models [1–6].

As a matter of fact, cardiac computational modelling constitutes an efficient tool to investigate the ionic mechanisms involved at cell level, and has already been used in a variety of clinical contexts, linking patient manifestations to the underlying electrophysiological mechanisms, thus providing useful insights into different atrial pathologies, including AF, especially whenever experimental measurements were lacking or unavailable [6–15].

Haemodialysis (HD) therapy represents a unique model to test *in vivo*, in human, the effects of sudden changes in plasma ionic concentrations and blood volume: in a few hours, patients undergo significant plasma electrolytes variations, together with a significant decrease in extracellular volume. In particular, the HD session causes removal of excess Na^+ and water, the extent of which depends on the inter-dialytic weight gain of the patient. Plasmatic K^+ concentration increases during the inter-dialytic interval, so that during all HD sessions its level must decrease, while Ca^{2+} variations might change depending on the dialysate Ca^{2+} concentration and its relationship with pre-HD plasma Ca^{2+} levels [16, 17].

These processes often lead to an increased arrhythmic risk for the patient, both during HD and in the hours following the therapy. Indeed, the incidence of AF in end-stage renal disease patients is high: reported rates vary between 7% and 27% [18, 19], and HD session may promote AF onset [20, 21].

The aim of this work is as first to briefly review the literature concerning applications of the computational approach to the study of the impact of HD therapy on cardiac electrophysiology. After that, we compared all the currently available human atrial AP models, focusing on their ability to reproduce the electrophysiological changes typically induced by HD sessions, i.e. plasma electrolytes and blood volume variations.

The 6 published human atrial models have been considered: Courtemanche [1], Nygren [2], Maleckar [3], Koivumaki [4], Grandi [5] and Colman [6]. All models have been tested for different concentrations of extracellular electrolytes (Na^+ , Ca^{2+} and K^+) and for cell volume changes. A set of AP and Ca^{2+} -transient (CaT) biomarkers has been considered to compare simulation results, e.g. AP duration (APD), resting membrane potential (RMP), effective refractory period (ERP), CaT duration (CaTD), etc.

In addition, since a modification of the sympatho-vagal balance in favour of vagal activity may occur during HD sessions in patients showing intra-dialytic AF episodes [20], the acetylcholine-activated K^+ current (I_{KACH}) has been added to all models, and the effect of different acetylcholine concentrations has been considered as well.

CARDIAC CELL MODELLING AND HAEMODIALYSIS

Computational models of cardiac AP have already been applied several times to assess the acute effects of HD therapy on cardiomyocyte electrophysiology.

The first attempt in this context was the computational analysis of the heart rate changes during HD [22–24]. Since a reliable model of human sinoatrial node (SAN) AP was lacking (as it is still today), these studies were based on a model of rabbit SAN AP, considering the DiFrancesco-Noble model [25, 26], as modified by Dokos et al. [27]. Simulation results pointed out that changes of blood K^+ , Ca^{2+} and pH produce large heart rate variations, showing how electrolyte and pH changes within physiological range may have a remarkable impact on the pace-making rhythm, independently of the autonomic outflow.

The computational approach has been also used to analyse how Ca^{2+} and K^+ changes during HD can alter ventricular repolarization and therefore AP duration [28]. In this work, a model of human ventricular AP was considered [29] and model predictions on AP prolongation were validated against a wide range of experimental data, i.e. QT interval prolongation recorded during HD sessions. Simulation results pointed out how computational modelling of ventricular AP may be useful to quantitatively predict the complex dependence of AP duration on simultaneous changes in both Ca^{2+} and K^+ . From this study, a model-based clinical indication was inferred: Ca^{2+} content in the dialysis bath should be designed in order to prevent a critical reduction of serum Ca^{2+} , especially in HD sessions with a risk of end-HD hypokalaemia.

The same approach has been applied to atrial electrophysiology: a computational model of human atrial AP has been used to confirm that the intra-dialytic reduction of plasma K^+ level is associated with P-wave prolongation [30]. When comparing the simulated atrial APs at the beginning and at the end of multiple HD sessions, imposing in the model the extracellular electrolyte concentrations and heart rate equal to the experimental values measured *in vivo*, simulation results showed an increase in the time needed to depolarise and a reduction of the effective refractory period (ERP), both occurring during HD. These two phenomena, in presence of a trigger, i.e. repeated premature atrial impulses, frequently induced by a HD session,

might form the electrical substrate for intra-dialytic AF episodes onset. Consistent results were also obtained when performing the same analysis in a multi-scale model of the human atrium and considering a simulated ECG [31].

More recently, we applied computational modelling of atrial cellular electrophysiology to the individual case of a patient in which HD regularly induced paroxysmal AF [20]. Simulation results provided evidence of a slower depolarization and a shortened refractory period in pre-AF vs pre-HD conditions, and these effects were enhanced when adding acetylcholine effect in simulation. Starting from these findings, the possible mechanisms leading to intra-dialytic AF onset were reviewed and re-interpreted, as described in the next chapter. Notably, in a subsequent study, Buiten et al. [21], using the implantable cardioverter defibrillator remote monitoring function, showed that HD is a trigger for AF episodes. In particular, they showed that a lower concentration of K^+ in the dialysis bath is associated with a higher probability of AF episodes, as predicted by our model-based simulation results.

It is worth noting that in all these studies, model inputs were set using experimentally measured quantities, i.e. plasma electrolyte concentrations and heart rate. However, the actual *in vivo* extracellular fluid is the interstitial fluid, rather than the blood. Therefore, it could be questioned whether the plasma electrolyte concentrations are a reliable estimate of the interstitial ones, even if this is usually accepted. Indeed, the distribution of free ions between vascular and interstitial compartments has been reported to agree with Donnan theory, which predicts a theoretical ratio between interstitial and plasma concentrations very close to 1 [32].

ATRIAL CELL MODELLING: MATERIALS AND METHODS

Computational Models of Human Atrial AP

Starting from the first two human atrial cell models (Courtemanche [1]; Nygren [2]), both published in 1998, four more have been released in the last few years (Maleckar, 2009 [3]; Koivumaki, 2011 [4]; Grandi, 2011 [5]; Colman 2013 [6]). Hereafter, the six models will be referred to using the initial letter of the first and

last authors (i.e. **CN**, **NG**, **MT**, **KT**, **GB** and **CZ** respectively). All models consist of a set of ordinary differential equations, each one representing a specific dynamic process occurring in the cell, and the number of equations is related to their complexity: the first models are very simple compared to the most recent ones, where a more detailed description of Ca^{2+} handling and cell compartments is included (see Table . 1). Moreover, the different parameters and ionic current formulations lead to distinct AP morphologies and properties, e.g. AP duration (APD), CaT duration (CaTD), etc.

Since 1998 several papers comparing atrial model performances have been published, mainly concerning CN and NG models, which for many years have been the only ones available [33–39]. The two most recent reviews [38, 39] compared all models except CZ, considering simulations from single cell to whole heart and including both physiological and pathological conditions, thus assessing the current state of the art in atrial computational modelling. Therefore, the comparison of the peculiar properties of these atrial models exceeds the purpose of this work, which rather aims to investigate the acute effects of HD therapy on atrial electrophysiology.

The CN and NG models are almost based on the same human atrial data, and they share most of the transmembrane ionic current formulations: however, CN is developed from the guinea pig ventricular model by Luo and Rudy [40], while NG is developed from the atrial rabbit model by Lindblad et al. [41]. The main differences between the two models are related to Ca^{2+} -handling and the CaT is much shorter and with a larger amplitude in NG. As a result, their AP shapes are quite different: a spike-and-dome AP for CN, and a more triangular one for NG (see Figure 5.1, pink and blue traces).

The MT and KT models are subsequent extensions of NG: the main changes for MT are new formulations for the transient outward (I_{to}) and ultra-rapid delayed rectifier (I_{Kur}) currents, while the KT gives a much more detailed description of Ca^{2+} -handling, especially concerning Ca^{2+} release. The sarcoplasmic reticulum (SR) is divided into 4 different compartments, including also a spatial dimension: as a result, the CaT is slower compared to the previous model ones, but its duration is increased (see Figure 5.2, purple trace). The GB model has been developed from the ventricular model published by the same group [42]: most of the ionic current

formulations have been preserved and adapted to experimental data acquired in human atrial isolated cardiomyocyte. The AP is quite triangular shaped (see Figure 5.1, green line), and the Ca^{2+} handling is mostly derived from the rabbit ventricular model by Shannon et al. [43], again adapted to human atrial data. It is worth noting that in this model the intracellular K^+ concentration is kept constant.

The CZ model is the most recent one: it is based on CN, from which he inherited all the ionic current formulations, except for I_{to} and I_{Kur} , which come from MT. Furthermore, the Ca^{2+} handling has been modified using a structure for the SR similar to the one used in KT, together with the corresponding formulation for Ca^{2+} release and pumps. Conductances have been slightly tuned, to preserve consistency with the original CN model.

In addition to the models listed above, a different version of the CN model has been considered (from now on referred to as **CN***), slightly modified in order to improve its long term stability [44, 45]. This **CN*** model has been recently used to investigate the specific case study of a HD patient which presented recurrent intra-dialytic AF mentioned above, and described in details in the next chapter [20].

Moreover, the KT model has been recently modified by the same authors, improving model prediction in chronic AF [14]. The changes involved mostly L-type Ca^{2+} current (I_{CaL}) formulation and this new version of the model (from now on referred to as **KT***) has been considered as well.

Finally, since this study is mainly focused on extracellular electrolyte changes, the known dependence on extracellular K^+ for both the inward and delayed rectifier K^+ currents has been added to the atrial models, when not already included [46–49].

Hereafter, each model will be identified by a specific colour (CN/CN*, pink; NG, blue; MT, cyan; KT/KT*, purple; GB, green; CZ, red) and simulation results for CN and KT will be shown only when a different behaviour with respect to their updated versions (CN* and KT*) is found.

Simulated APs and CaTs for all the considered models are shown in Figure 5.1 and Figure 5.2 respectively, to allow a quick visual comparison of their main properties.

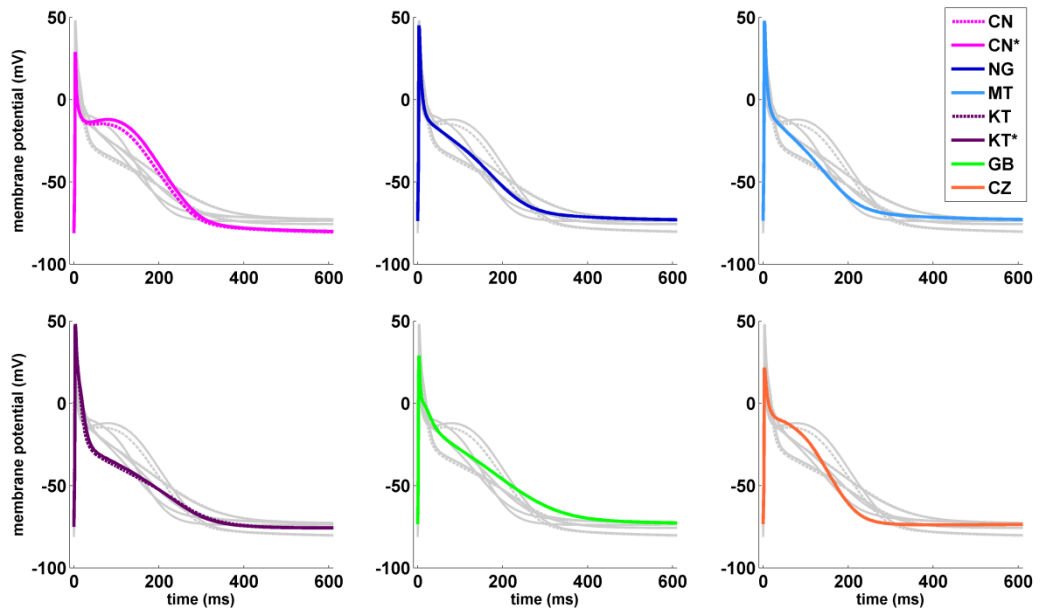


Figure 5.1: Simulated AP traces for all the considered atrial models: each panel shows a specific model AP with its reference colour; all the other model traces have been added in grey, to facilitate the comparison.

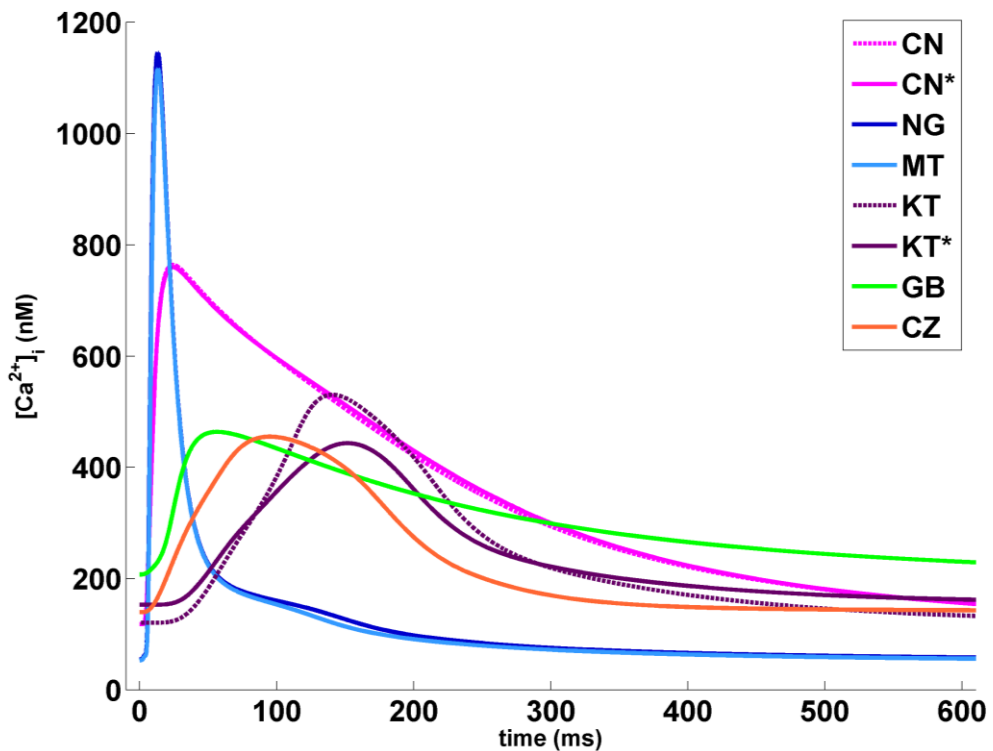


Figure 5.2: CaT traces for all the considered atrial models: the notable differences in timing and amplitude are related to the corresponding different formulations of Ca^{2+} release from the SR.

AP and CaT shapes are very different in each model. As far as the CaTs are concerned, experimental values of diastolic intracellular Ca^{2+} concentration reported in literature span from 120 to 230 nM [50–52]: CN, KT, GB and CZ have values in this range, whereas NG and MT compute lower diastolic concentrations. Measured CaT amplitudes range from 265 to 345 nM [50, 51] and this is best reproduced by CZ and KT. GB produces a slightly smaller CaT while CN, NG and MT show much higher amplitudes. In addition, the CaT has been reported to decay with a time constant of about 200 ms or even slower [51, 53]: such a slow decay is well reproduced by GB and CN only, while in all the other models is much faster.

Model differential equations have been implemented in Matlab (Mathworks Inc.) and a variable order solver has been used to solve them (ode 15s [54]). Pacing was simulated by a current pulse train (pulses of 3 ms, 1 Hz), maintained for 150 s, in order to allow all the models to reach a proper steady state, i.e. intracellular concentrations (Na^+ , Ca^{2+} and K^+) stable over time.

Stimulus current (I_{stim}) amplitude was set to twice the AP threshold for all models, as previously done in [106] (see Table 5.1). When using this stimulus, however, the GB model produces an AP quite different from the one published in the original GB paper: indeed, some of the biomarkers e.g. AP amplitude and upstroke velocity, are highly stimulus-dependent in this model. Therefore, all simulations with the GB model have been done using the stimulus amplitude needed to preserve the original AP characteristics, which is about 6 times the AP threshold and more close as current density to the ones used for the other models.

A summary of all the considered atrial models is shown in Table 5.1, together with some of their main structural properties, i.e. membrane capacitance, intracellular volumes and compartmentalisation, amplitude used for the current stimulus, the number of state variables (each one represented by an ordinary differential equation) and the corresponding publication.

Table 5.1: List of the human atrial AP models considered in this study and some of their properties:

	CN/CN*	NG	MT	KT/KT*	GB	CZ	
Cm (pF)	100	50	50	50	110	100	
Cell Volumes (pL)	<i>CYTO</i>		5.88	5.88	8.10	21.45	13.67
	<i>SSL</i>	13.67	0.12	0.12	-	0.66	-
	<i>JS</i>		-	-	0.05	0.02	0.10
	<i>SR</i>	1.21	0.44	0.44	0.18	1.16	0.27
	<i>whole cell</i>	20.10	49.42	49.42	13.90	33.01	20.10
I_{stim} (pA/pF)	15.0	19.6	19.2	18.8	19.5	12.0	
# ODEs	21	29	30	43	62	39	
Ref	[1]	[2]	[3]	[4, 14]	[5]	[6]	
Year	1998	1998	2008	2011	2011	2013	

Cm, membrane capacitance; *CYTO*, cytosol; *SSL*, sub-sarcolemmal space; *JS*, junctional space; *SR*, sarcoplasmic reticulum; *I_{stim}*, stimulus current amplitude; # *ODEs*, number of differential equations in the model; *Ref*, reference paper; *Year*, year in which the model was first published.

Simulation of the HD-induced effects

In order to investigate the reliability of each atrial model in reproducing the effects of extracellular electrolyte changes possibly occurring during a regular HD session, we performed a sensitivity analysis by varying the extracellular concentrations ($[Na^+]_o$, $[Ca^{2+}]_o$ and $[K^+]_o$) around the original model values (130-140 mM, 1.8 mM and 5.4 mM, respectively).

The explored ranges have been set according to the measured values reported in literature for HD patients, extending them to include also possible outliers, as described in details in the next Section.

At the beginning of the HD session the patient is overhydrated: for this reason, 2-3 litres (or even more) of water are removed from his blood during the treatment. Such a removal is compensated by water refilling from the interstitial fluid and eventually from the intracellular compartment. How fluid accumulation during the inter-dialytic period and fluid removal during the HD session reflects into variations

of intracellular volumes is actually not known in quantitative terms. Therefore, we investigate the effects of a quite large range ($\pm 20\%$) of volume changes.

Finally, to explore the effect of vagal stimulation, we added the acetylcholine-activated K^+ current (I_{KACH}) to all the models, according to the formulation used in [5], and considering the changes induced by 0-15 nM of acetylcholine (ACh).

AP and CaT Biomarkers

In order to compare simulation results from a qualitative point of view, we computed a set of AP biomarkers, considering in particular the ones already used in previous simulation works either to compare the different atrial AP models [39] or to evaluate the effects induced by electrolyte variations on atrial electrophysiology [30]: action potential duration (APD) was measured as the interval between the AP upstroke and the 90% of repolarization (APD_{90}); resting membrane potential (RMP) was measured at the end of diastole; the AP upstroke duration (AP_{ud}) was defined as the time needed by membrane voltage to reach 0 mV, starting from the beginning of the pacing pulse [20, 30]; AP amplitude (AP_{amp}) was measured as the difference between the AP peak and RMP; maximum upstroke velocity (dV/dt_{MAX}) was computed as the maximum derivative of membrane voltage over time during the AP upstroke; the effective refractory period (ERP) was measured by simulating a S_1 – S_2 protocol: it has been defined as the longest S_1 – S_2 interval which failed to elicit a S_2 AP of amplitude $> 80\%$ of the preceding S_1 AP [55].

A summary of all the considered AP biomarkers is shown in Figure 5.3, considering the CN* model AP trace as an example.

In addition, some Ca^{2+} transient (CaT) biomarkers have been considered as well, i.e. CaT duration (CaTD), measured at 90% of CaT decay ($CaTD_{90}$), the time needed to reach the CaT peak, starting from the beginning of the current stimulus (CaT_{tpp}) and the CaT amplitude (CaT_{amp}). Finally, intracellular concentrations ($[Ca^{2+}]_i$, $[Na^+]_i$ and $[K^+]_i$) have been monitored in all simulations and the corresponding values at the end of diastole have been considered for comparison.

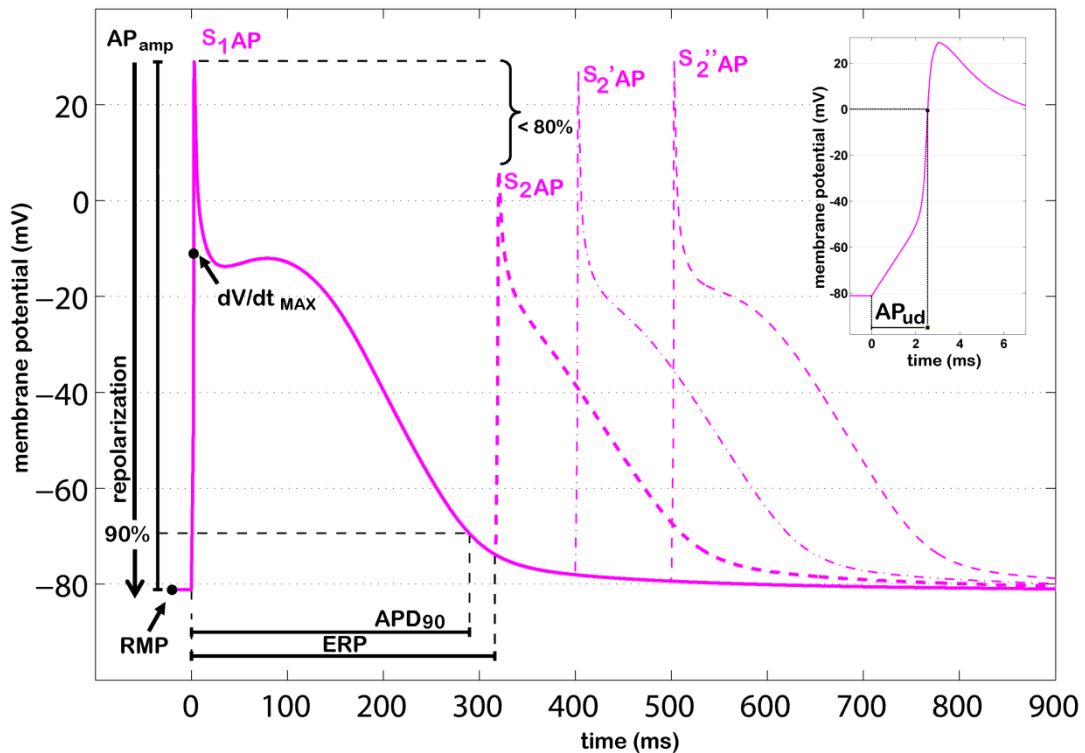


Figure 5.3: AP biomarkers considered to compare simulation results: AP duration at 90% of repolarization (APD_{90}); resting membrane potential (RMP); AP upstroke duration (AP_{ud}); AP amplitude (AP_{amp}); maximum upstroke velocity (dV/dt_{MAX}); effective refractory period (ERP), computed using a S_1 - S_2 protocol and considering the longest S_1 - S_2 interval which failed to elicit a S_2 AP of amplitude $> 80\%$ of the corresponding S_1 AP.

ATRIAL CELL MODELLING: EFFECTS OF HD-RELATED CHANGES

Potassium Variations

In all the considered models the extracellular K^+ concentration ($[K^+]_o$) is set to the standard value used in the perfusion bath during V-clamp experiments, i.e. 5.4 mM. K^+ increases during the inter-dialytic interval and is removed during the HD session: therefore, HD patients often show hyper-kalaemia at the beginning of the therapy and hypo-kalaemia at the end. In order to explore both clinical conditions, we considered the range 3-9 mM. The lower $[K^+]_o$ value (3 mM) has been set considering the experimental post-HD measurements available in literature (e.g. 3.9 ± 0.4 [30], 3.6 ± 0.6 mM [56]). The upper $[K^+]_o$ value (9 mM) is actually a bit high compared to the pre-HD measurements available (e.g. 4.9 ± 0.5 mM in [30], 5.3 ± 0.9

mM in [56]): we extended the range since there are clinical contexts, such as acute ischemia, in which $[K^+]_o$ can locally rise up to 9 mM or more [57].

The main effect of a $[K^+]_o$ decrease should be a hyperpolarization of the cell membrane, due to a different Nernst potential for K^+ ions. In addition, a $[K^+]_o$ decrease leads to a QT interval increase [28], a macroscopic marker of prolonged ventricular APD: therefore, a prolongation of atrial APD is expected as well [58]. On the contrary, ERP should decrease [58, 59], since APD and ERP may be “uncoupled” when varying $[K^+]_o$, as experimentally observed by Downar et al. [60].

Finally, while slowed cardiac tissue conductivity is a well-known effect of severe hyperkalemia, in the range of $[K^+]_o$ concentrations usually measured in HD patients, a positive dependence of conduction velocity on $[K^+]_o$ has been observed: this phenomenon is known as supernormal conduction [61–63]. Consistently, an increase in PwD during hemodialysis, significantly correlated to K^+ decrease, has been reported [30]. In a previous simulation study [30] we have shown how both hypo- and hyper-kalaemia can cause slowed cardiac tissue conductivity: in hypokalaemia, the RMP is significantly lower (hyperpolarized), and therefore the cell needs more time to reach the membrane potential threshold for AP upstroke; in hyper-kalaemia, the RMP is significantly higher (depolarized) and, as a consequence, Na^+ current availability is decreased and the current is much smaller than usual. In single cell simulations, a slow conduction can be associated to a smaller upstroke velocity and to an increase in the time needed for the voltage to rise toward the AP peak: AP_{ud} and dV/dt_{MAX} are then expected to show some kind of U-shape dependence when considering the full $[K^+]_o$ range.

A summary of the AP biomarkers for all the different $[K^+]_o$ is shown in Figure 5.4. When some models fail to repolarise with low $[K^+]_o$, the corresponding biomarkers have not been computed.

The models show quite different trends for some of the biomarkers, especially APD_{90} and ERP (Figure 5.4, panel A and B). In NG, MT and KT^* (Figure 5.4: blue, cyan and purple traces), both the RMP and APD_{90} behave as expected: however, these models fail to repolarise when $[K^+]_o$ is set to low values, exhibiting early after depolarisations (EADs, see e.g. Figure 5.5).

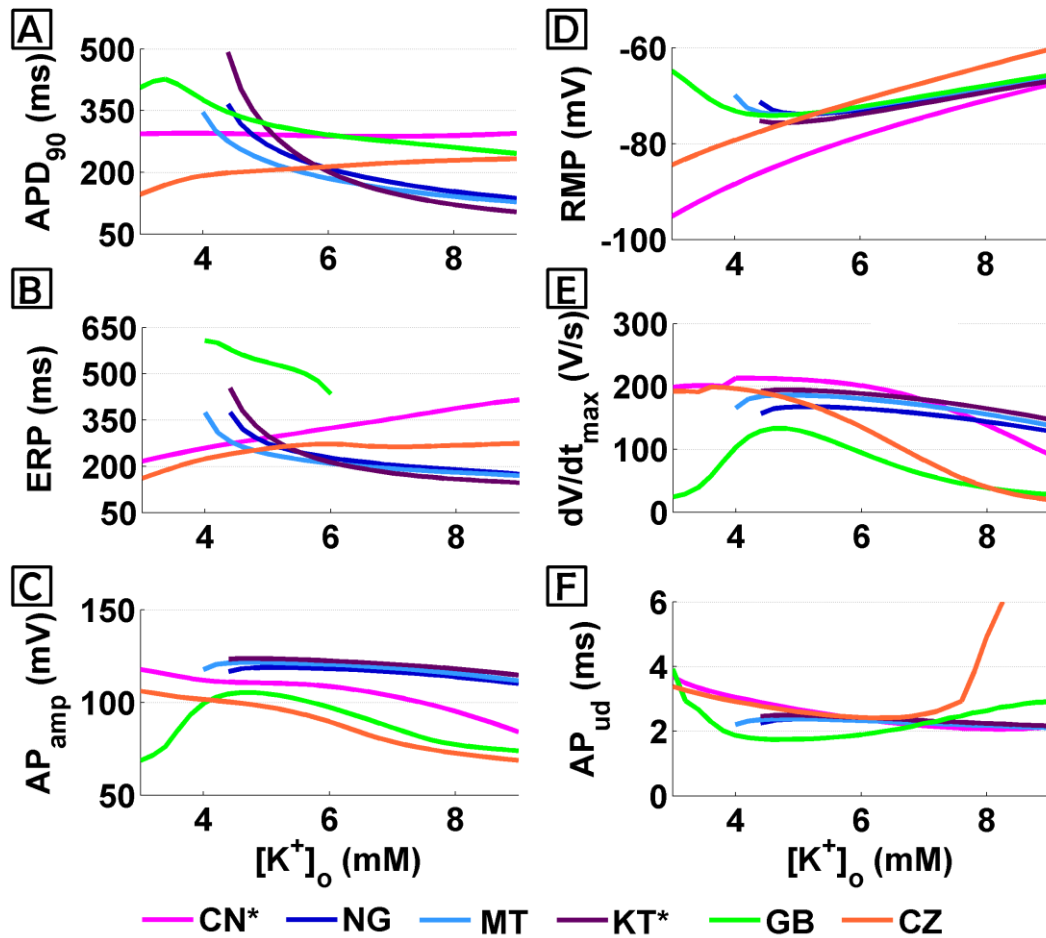


Figure 5.4: AP biomarkers vs $[K^+]_o$ for all the considered models.

Indeed, a decrease in $[K^+]_o$ leads to a reduction in the conductance of the K^+ repolarising currents, i.e. I_{Kr} and I_{K1} , thus prolonging the APD: in these models this effect seems to be over dimensioned, probably due to a low repolarisation reserve, and therefore the membrane potential is not able to go back to its resting value. As an example, in Figure 5.5 are shown the AP traces corresponding to different $[K^+]_o$ levels for the NG model.

This is indeed a great limitation when aiming to apply these models to clinical contexts, since normal plasma K^+ levels are between 3.5 and 5 mM, and especially critical for HD patients because they need to remove the K^+ accumulated during the inter-dialytic period, primarily in the intracellular pool, and therefore they usually end the HD session in hypo-kalaemia.

No significant changes have been observed in these models for dV/dt_{MAX} and AP_{ud} , while the ERP follows the APD_{90} as expected. Finally, the AP_{amp} is inversely related to RMP.

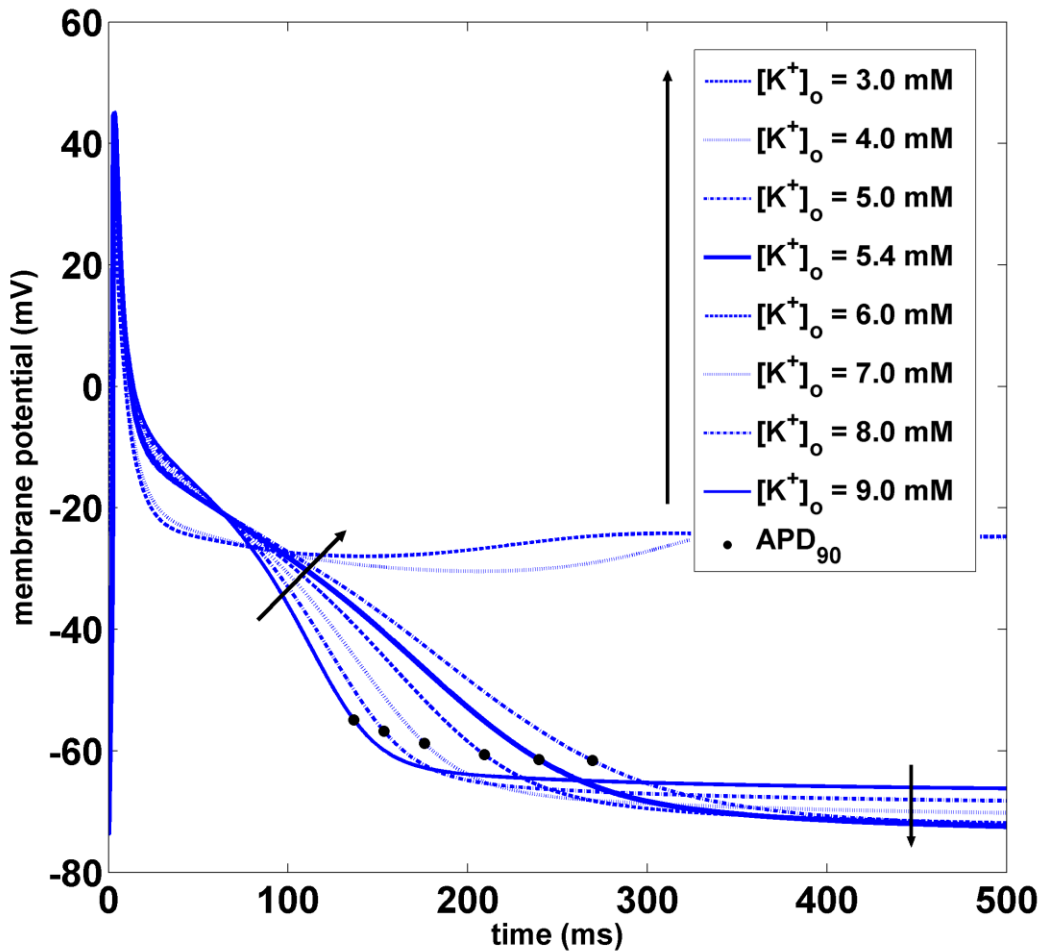


Figure 5.5: AP traces corresponding to different $[K^+]_o$ for the NG model. When decreasing $[K^+]_o$, the RMP becomes lower and the APD_{90} increases, both as expected. However, the model doesn't repolarise for $[K^+]_o$ values lower than 4 mM.

As for the GB model (Figure 5.4: green traces), APD_{90} and RMP are quite similar to NG, MT and KT^* , but their trends change for low $[K^+]_o$: the model repolarises properly for all $[K^+]_o$, but when considering values lower than 4mM the RMP is higher (more depolarised) than expected: therefore, APD_{90} and AP_{amp} are affected accordingly. AP_{ud} and dV/dt_{MAX} show the expected U-shape, related to a reduced conduction for both low and high $[K^+]_o$. As for the ERP, in this model it is always much longer than the corresponding APD_{90} , even if it shows a similar dependence on $[K^+]_o$. In addition, probably due to the high stimulus amplitude needed to stimulate the GB model (as explained in the methods section), the ERP could not be computed for most of the $[K^+]_o$: when considering values below 4 mM or above 6 mM, the S_2 AP peak was never lower than 80% of the corresponding S_1 , no matter how short the diastolic interval considered.

As for the CN* and CZ models (Figure 5.4: pink and red lines), they develop a proper AP for all $[K^+]_o$ and they both show a very strong linear dependence of RMP on $[K^+]_o$: this dependence, by itself, should prolong the APD when decreasing $[K^+]_o$, since the membrane potential needs more time to repolarize and then reaching its resting value.

However, in these models the AP phase 2 shortens as well, so the overall APD_{90} is almost constant, or even decreasing with $[K^+]_o$, in contrast with the expected behaviour; this effect is even more pronounced when considering the ERP. As an example, in Figure 5.6 the AP traces corresponding to different $[K^+]_o$ levels for the CN* model are shown.

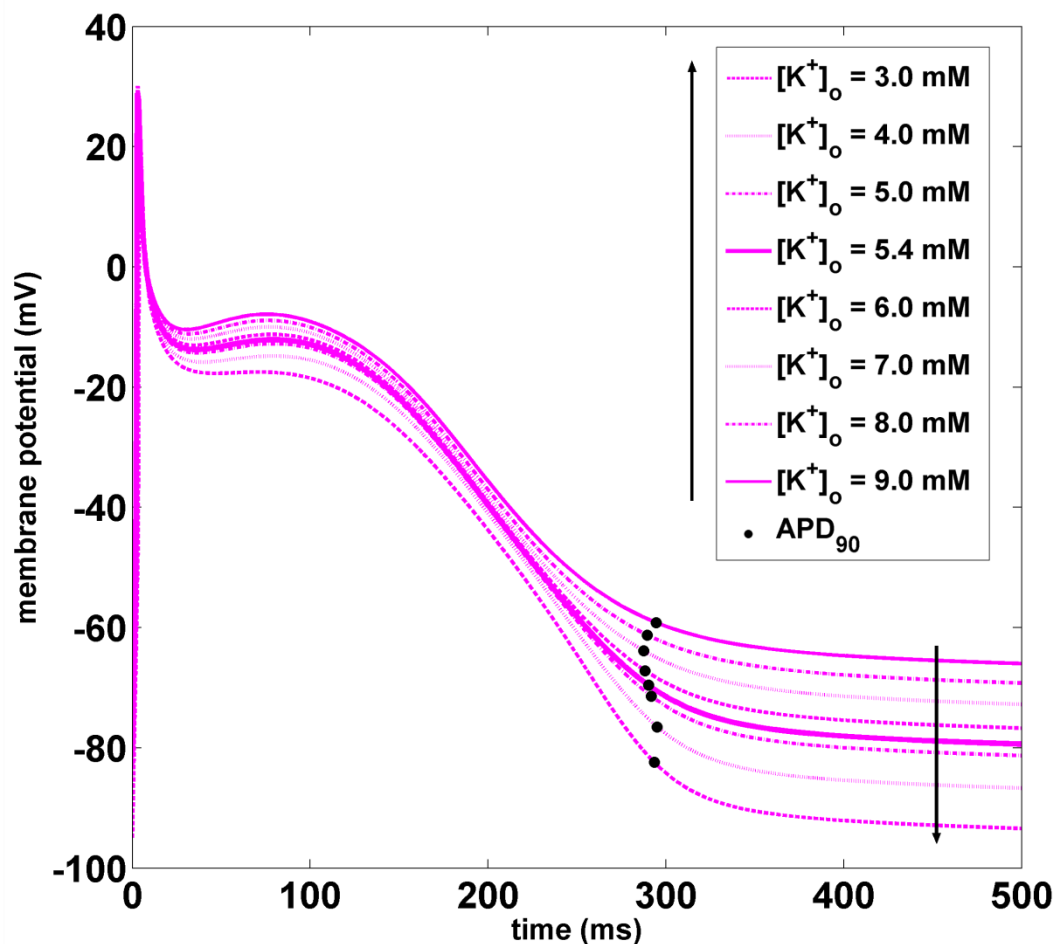


Figure 5.6: AP traces corresponding to different $[K^+]_o$ for the CN model. When decreasing $[K^+]_o$, the RMP becomes lower as expected, but the APD_{90} is almost constant.

In these two models, the AP_{amp} is again inversely related to RMP, and both AP_{ud} and dV/dt_{MAX} suggest a reduced conductivity in the $[K^+]_o$ range boundaries, especially when considering high $[K^+]_o$.

No significant changes were found in CaT biomarkers and intracellular concentrations, in any of the considered models (Figure 5.7).

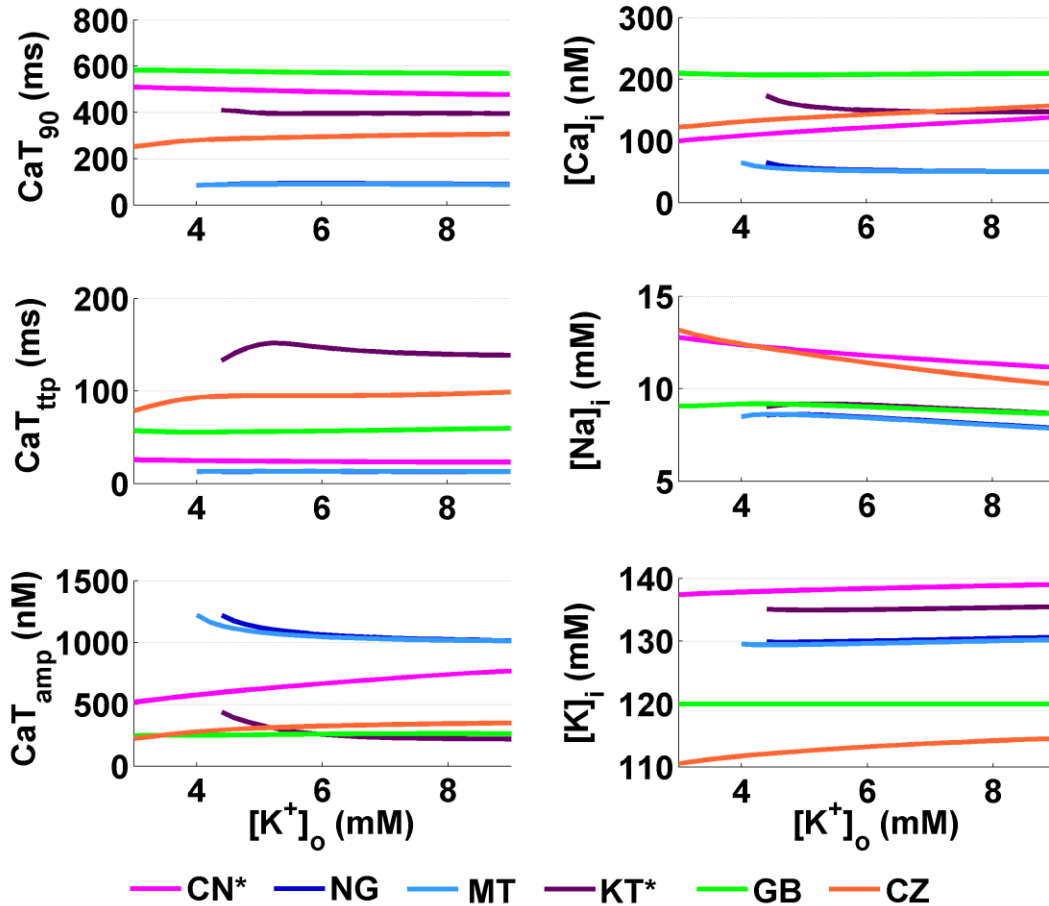


Figure 5.7: CaT biomarkers (left) and diastolic intracellular ionic concentrations (right) vs $[K^+]_o$ for all the considered atrial models.

Calcium Variations

In all the models the extracellular Ca^{2+} concentration ($[Ca^{2+}]_o$) is set to the standard value used in the perfusion bath during V-clamp experiments, i.e. 1.8 mM, which is quite high compared to the normal serum Ca^{2+} measured in vivo (1-1.3 mM), as discussed in detail in [64]. During a regular HD session, depending on the dialysis bath concentration, serum Ca^{2+} can either raise or decrease. Two previous simulation studies explored the effects of $[Ca^{2+}]_o$ on cardiac electrophysiology,

considering the range 1-3 mM [64, 65]. However, serum Ca^{2+} is lower than 1 mM in several patients: reported pre-HD concentrations are e.g. 1.18 ± 0.09 mM in [30] and 1.06 ± 0.16 mM in [28]. Therefore, we decided to extend the explored range to 0.6-3 mM. A summary of the AP biomarkers for the different $[\text{Ca}^{2+}]_o$ is shown in Figure 5.8.

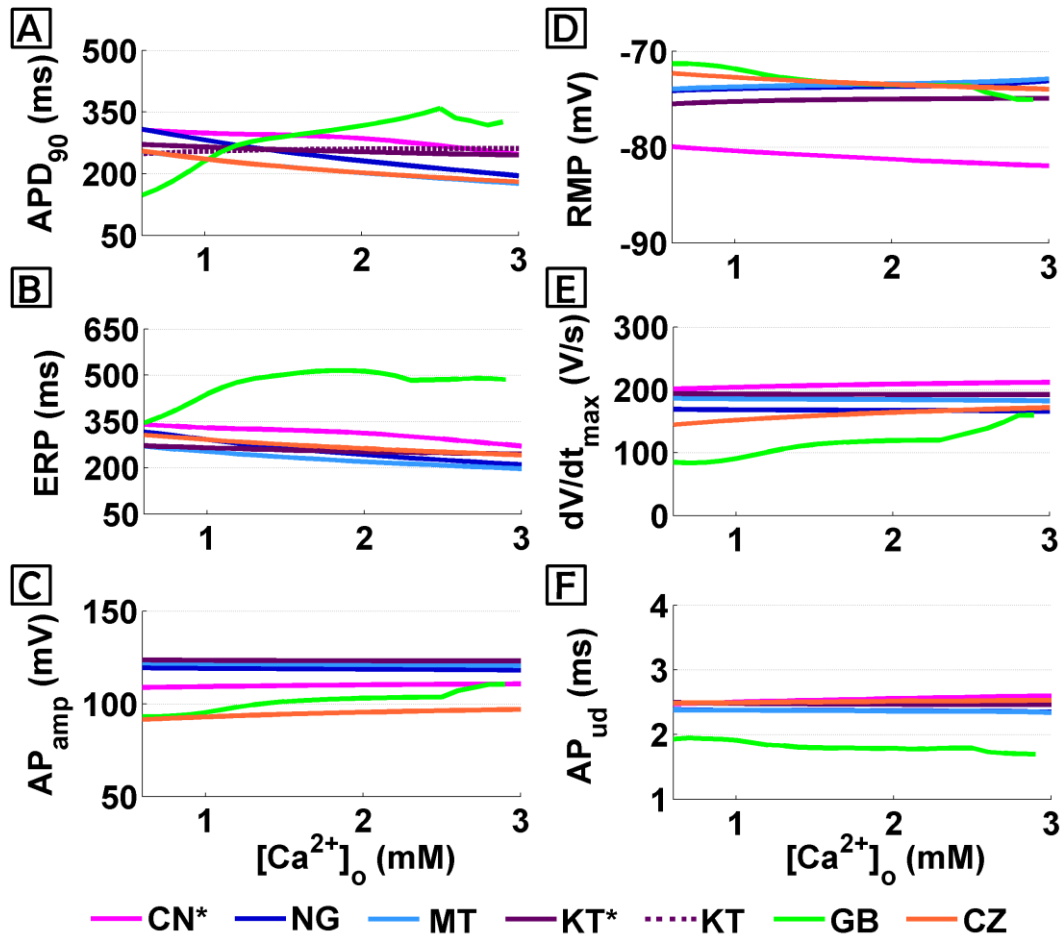


Figure 5.8: AP biomarkers vs $[\text{Ca}^{2+}]_o$ for all the considered models.

The expected effect of $[\text{Ca}^{2+}]_o$ increase is a significant decrease of APD [64, 66]: the increment in driving force enhance the L-type Ca^{2+} current (I_{CaL}) peak, but at the same time the Ca^{2+} -dependent inactivation mechanism is strengthened, thus reducing the overall I_{CaL} and therefore shortening the APD.

Even if the data showing this inverse relationship between APD and $[\text{Ca}^{2+}]_o$ has been recorded in ventricular cells, there are a few recordings confirming that the trend is the same for human atrial cells [64].

Indeed, CN, NG MT, KT* and CZ models are able to reproduce this effect, together with a consistent reduction of ERP (Figure 5.8, panel A and B). Notably, the original KT model shows an opposite trend for both APD_{90} and ERP, fixed in its improved version, where precisely the I_{CaL} formulation was changed. On the contrary, GB proves to be not very stable to $[Ca^{2+}]_o$ variations: APD_{90} and ERP show a biphasic trend, both considerably increasing with $[Ca^{2+}]_o$ from 0.6 to 2.5 mM, and then decreasing until 3 mM, value in which EADs appear (Figure 5.9).

RMP, AP_{amp} and AP_{ud} are almost constant in all models (Figure 5.8, panel C, D and F). As for dV/dt_{MAX} , only GB, CN and CZ show a slight linear dependence with $[Ca^{2+}]_o$ (Figure 5.8, panel E), related to the increase of I_{CaL} peak, which in these models has a greater contribution to the AP phase 0.

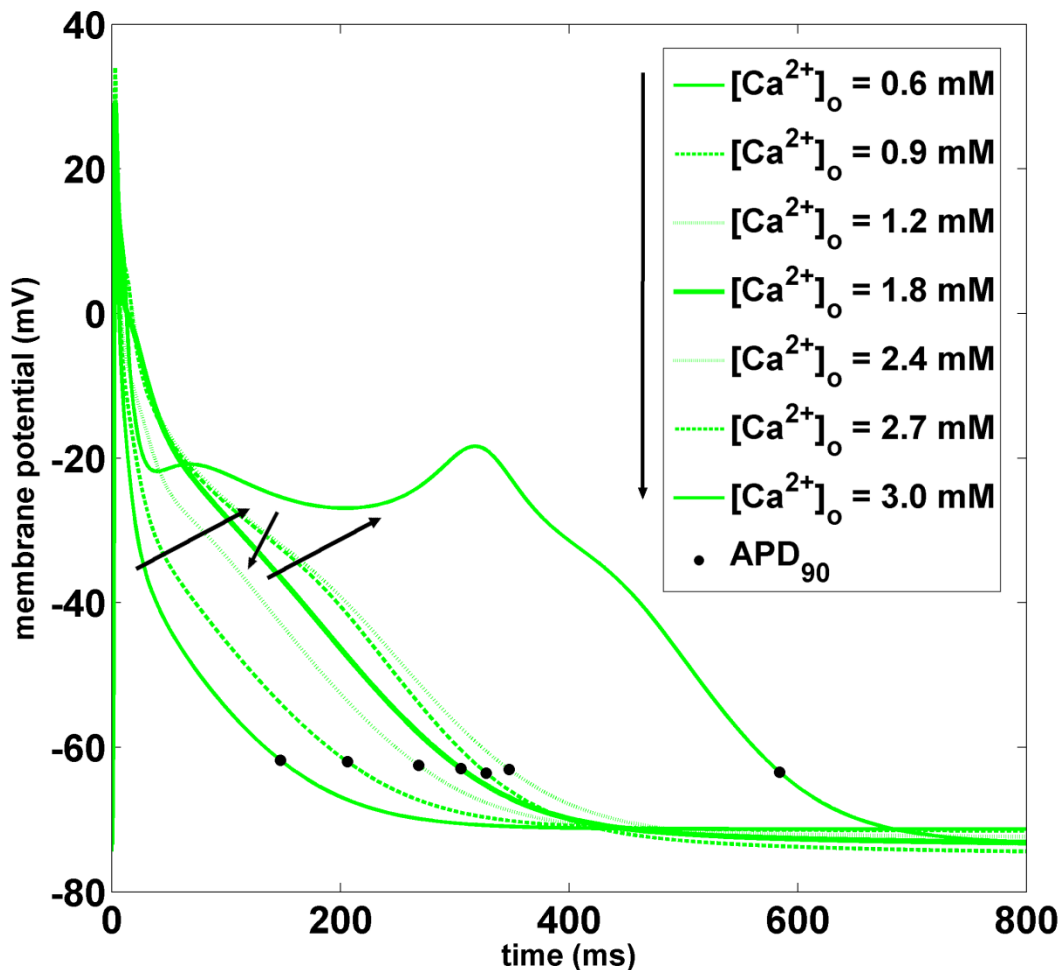


Figure 5.9: AP traces corresponding to different $[Ca^{2+}]_o$ for the GB model. When increasing $[Ca^{2+}]_o$, the APD_{90} first highly increases and then decreases. For $[Ca^{2+}]_o = 3$ mM an EAD appears.

As expected [66], diastolic Ca^{2+} increases with $[\text{Ca}^{2+}]_o$ for all the considered models (Figure 5.10, panel D), whereas a couple of unexpected observations can be made on the CaTs (not shown): CZ seems almost insensitive to $[\text{Ca}^{2+}]_o$ and GB fails to produce a significant CaT for $[\text{Ca}^{2+}]_o$ lower than 1 mM, in which CaT becomes really slow and almost negligible in amplitude.

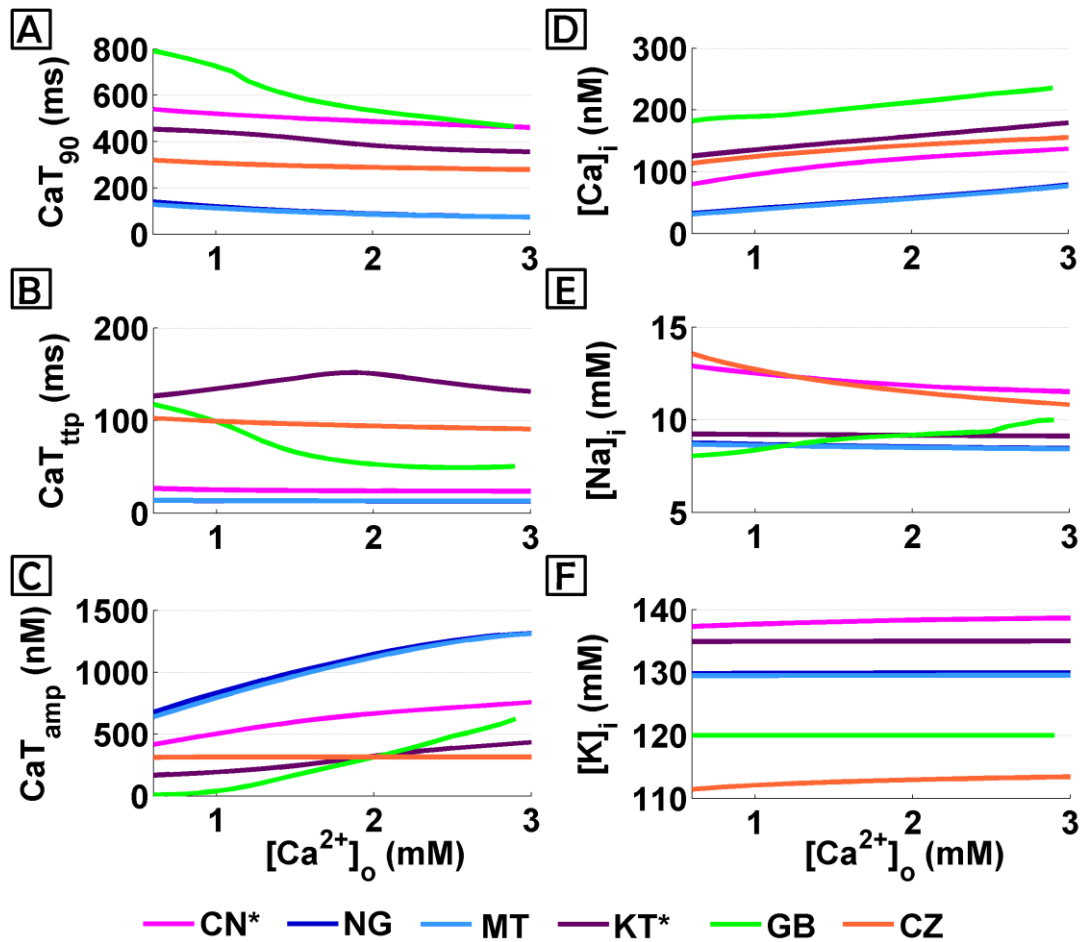


Figure 5.10: CaT biomarkers (left) and diastolic intracellular ionic concentrations (right) vs $[\text{Ca}^{2+}]_o$ for all the considered atrial models.

CaT_{amp} increases with $[\text{Ca}^{2+}]_o$ for all models (Figure 5.10, panel C), in agreement with [66], while CaT timing (CaT_{ttp} e CaT_{90}) is not much affected by $[\text{Ca}^{2+}]_o$ (Figure 5.10, panel A and B), and neither is $[\text{K}^+]_i$ (Figure 5.10, panel F).

On the contrary, $[\text{Na}^+]_i$ is finely tuned by Ca^{2+} : the raise of $[\text{Ca}^{2+}]_o$ increases the outward $\text{Na}^+/\text{Ca}^{2+}$ exchanger current (I_{NCX}), but the corresponding increase of intracellular Ca^{2+} contrasts this effect. At the same time, the Na^+/K^+ pump counteracts $[\text{Na}^+]_i$ variations, in both ways. As a result, $[\text{Na}^+]_i$ concentration is not

much sensitive to $[Ca^{2+}]_o$ in most of the models (Figure 5.10, panel E). However, in CN and CZ, the direct effect of $[Ca^{2+}]_o$ on the I_{NCX} plays the major role and as a consequence the $[Na^+]_i$ decreases slightly. In GB, instead, $[Na^+]_i$ increases, because when $[Ca^{2+}]_o$ increases the inward I_{NCX} is highly strengthened, due to the sub-sarcolemmal space in which $[Ca^{2+}]_i$ locally increases considerably.

Unfortunately, there are no experimental data available in literature on $[Na^+]_i$, I_{NCX} or Na^+/K^+ pump for different $[Ca^{2+}]_o$, either to confirm or deny these findings.

Sodium and Volume Variations

In all the considered models the extracellular Na^+ concentration ($[Na^+]_o$) is set to the standard value used in the perfusion bath during V-clamp experiments, i.e. 130 mM for CN, GB and CZ, 140 mM for NG, MT and KT, in agreement with the normal serum levels of 135-145 mM. Na^+ variation during a regular HD session are usually quite small (e.g. from 139.8 ± 3.4 to 141.6 ± 3.1 in [30], from 129/132 to 133/135 in [20]) and we explored the 120-150 mM range base on the corresponding data available in literature [67, 68].

APD_{90} and ERP slightly increase with $[Na^+]_o$ in all the models except GB, in which they both stay constant (Figure 5.11, panel A and B). RMP and AP_{ud} are almost constant for all the models: the first slightly increases with $[Na^+]_o$ and the other slightly decreases (Figure 5.11, panel D and F). In NG, MT and KT, dV/dt_{MAX} increase with $[Na^+]_o$, together with AP peak and therefore also AP_{amp} (Figure 5.11, panel E and C), while they don't vary in the other models, i.e. CN, CZ and GB.

No significant differences were found in CaT biomarkers nor intracellular concentrations for any of the models, apart from an obvious increase in $[Na^+]_i$ (not shown). Finally, it is worth noting that in CZ and CN, $[Na^+]_i$ regularly shows a stronger sensitivity to changes in extracellular concentrations.

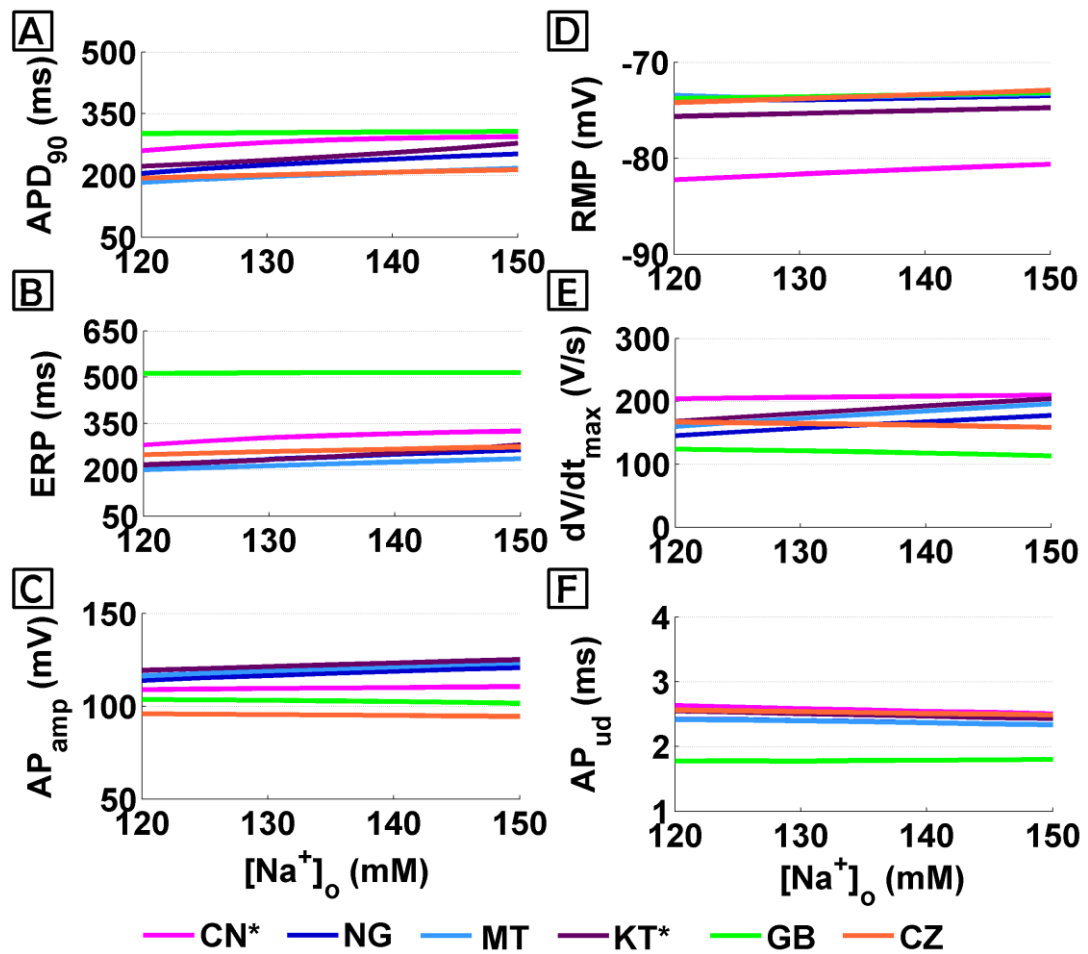


Figure 5.11: AP biomarkers vs $[Na^+]_o$ for all the considered models.

Volume effects have been evaluated by scaling the intracellular volumes of $\pm 20\%$. The corresponding AP biomarkers variations are all negligible (not shown), e.g. KT shows the maximum APD₉₀ change: +22.5 ms on the whole range. The CaTs become slightly slower when the volume increases, but notable changes have been found only in GB: CaTD₉₀ increases of +104 ms on the whole volume range, together with an increase of CaT_{tp} and a reduction of CaT_{amp} (Figure 5.12, panel A, B and C). $[Ca^{2+}]_i$ also increases with volume in GB, while no other significant changes occur in intracellular concentrations (Figure 5.12, panels D, E and F).

Unfortunately there are not experimental data on the effect of changes in $[Na^+]_o$ or volume on cardiac cells to either confirm or deny these findings.

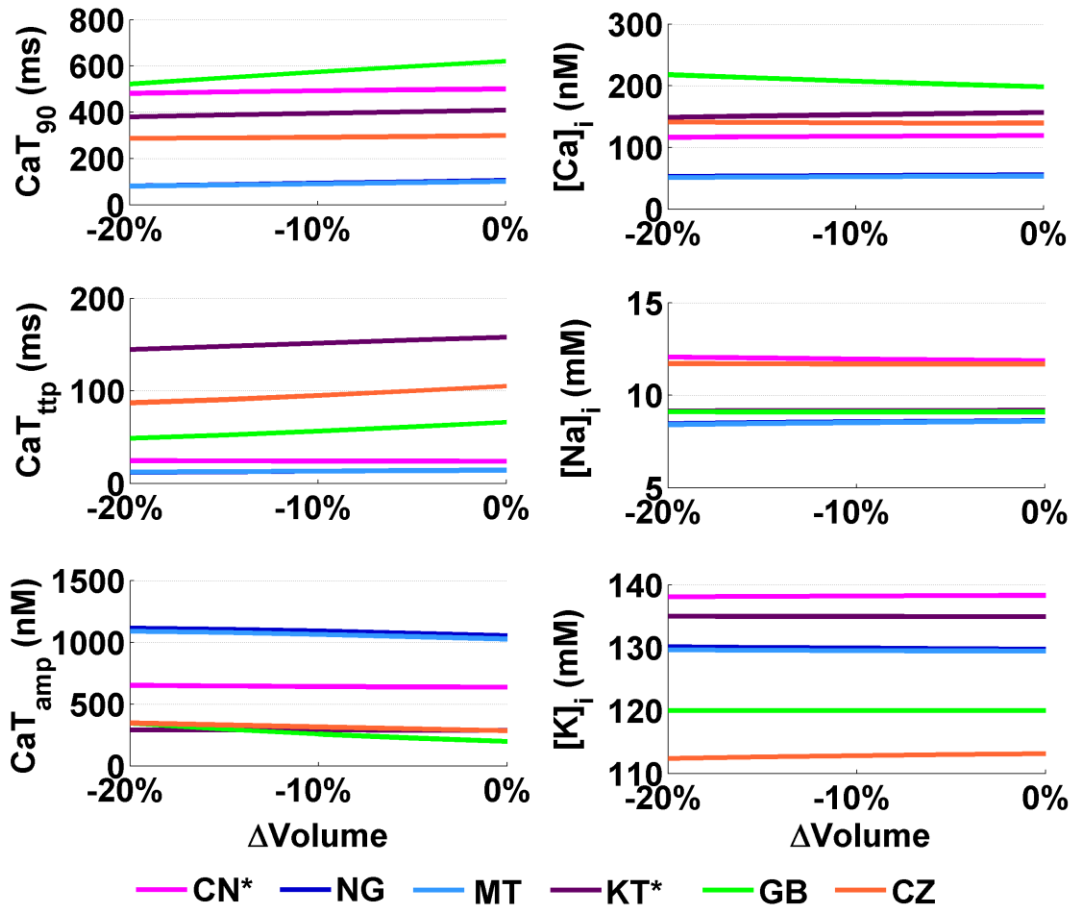


Figure 5.12: *CaT* biomarkers (left) and diastolic intracellular ionic concentrations (right) vs vs volume % changes for all the considered models.

Acetylcholine effects

To analyse the effect of a possible increase in vagal activity, we simulated the effects of acetylcholine in the 0-15 nM range, adding to all models the same I_{KACH} formulation used in [5].

The expected effect of an additional outward K^+ current is a more hyperpolarized RMP, together with a shortening of APD and ERP. This has been confirmed by experimental data [69–71] as well as by previous modelling studies [5, 72, 73].

When considering concentrations higher than 3 nM, all the considered models show a significant decrease of both APD_{90} and ERP (Figure 5.13, panel A and B). In addition, the RMP is indeed hyperpolarised, especially in NG and MT (Figure 5.13, panel D). The AP_{ud} is inversely related to RMP changes (Figure 5.13, panel

F), whereas AP_{amp} and dV/dt_{MAX} keep almost constant (Figure 5.13, panel C and E): therefore, the overall conductivity is slowed down by ACh.

In fact, starting from a more hyperpolarized potential and with no significant changes in dV/dt_{MAX} , the cell needs more time to reach the threshold for I_{Na} activation, to produce the upstroke. On the contrary, in GB both AP_{amp} and dV/dt_{MAX} increase with ACh, mostly due to a larger Na^+ current for lower RMP, thus compensating this effect and limiting the theoretical AP_{ud} increase and the corresponding reduced conductivity.

Negligible effects were found in CaT biomarkers and intracellular concentrations (not shown) when including acetylcholine.

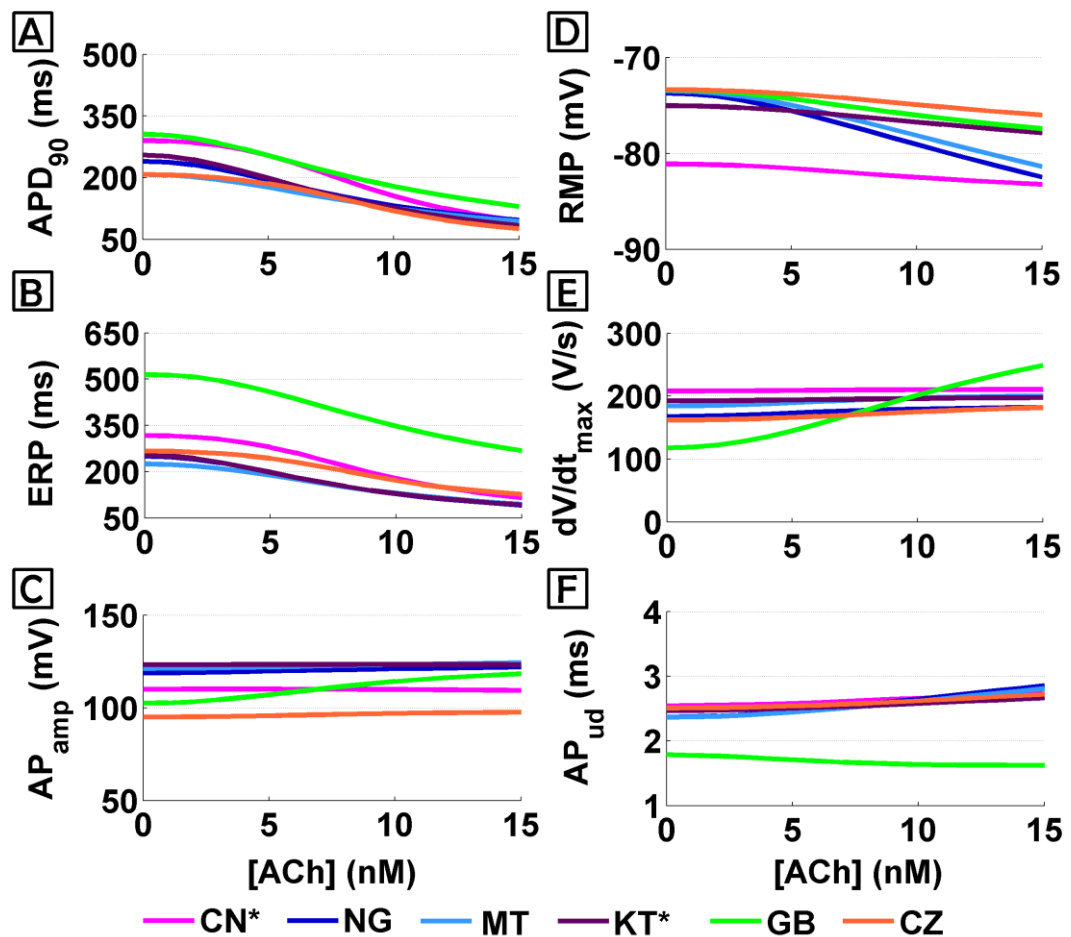


Figure 5.13: AP biomarkers vs ACh concentrations for all the considered models.

DISCUSSION AND CONCLUSIONS

We have briefly pointed out that computational models of cardiac action potential (AP) have been successfully applied to investigate HD-related effects on the electrophysiology of different cardiac tissues (sinoatrial node, ventricle, atrium) often leading to relevant interpretations of macroscopic observations made in clinical ECG and/or useful suggestions about HD treatment personalisation.

However, all these studies have been performed by using cardiac cell models that had been developed on the basis of *in vitro* experimental data, almost always acquired using standard Tyrode's solutions as extracellular fluid. It is obviously correct to simulate the electrical activity of cardiac cells by imposing the same conditions used in experimental protocols as far as the aim is a comparison with *in vitro* experimental data. On the contrary, it can be incorrect to use the same constant concentrations when the ultimate aim of simulations is the analysis of *in vivo*, and therefore dynamical, conditions, such as a HD session. Sometimes, this possible cause of discrepancy has been mitigated by few changes to the original models, e.g. introduction of the effect of extracellular pH on the Na^+/K^+ pump activity in the DiFrancesco-Noble model of SAN cell [22], strengthening of the I_{CaL} Ca^{2+} -dependent inactivation in the Ten Tusscher model of human ventricular A [28].

However, a systematic analysis of the applicability of cardiac cell models to reproduce the specific conditions occurring during HD or, in general, when the extracellular fluid composition changes, is still lacking. In the present paper, we addressed this kind of problem by focusing on human atrial cell models and on the following “cell environment” changes: extracellular electrolyte concentrations (K^+ , Ca^{2+} and Na^+), cell volume and acetylcholine.

We pointed out that several human atrial models are available, with significantly different behaviour upon such environment changes.

Unfortunately, experimental data on human atrial cells induced by extracellular concentrations changes are really rare in literature. This makes a stringent quantitative comparison between simulations and experimental measurements not possible for most of the considered electrophysiological properties.

On the other hand, some qualitative behaviour is expected based on the overall evaluation of: i) knowledge of physiological mechanisms (e.g. the link between membrane resting potential and Nernst K^+ potential); ii) in vitro data measured in different cell types and species (e.g. [50, 64]); iii) in vivo data on macroscopic ECG markers known to be related to atrial cellular electrophysiology (e.g. PWD).

We found a major problem in the NG, MT and KT models: they all fail to repolarize and to produce physiological APs when $[K^+]_o$ is lower than 4 mM. This makes these models not appropriate to simulate the cardiac impact of HD. Indeed, the change in plasma $[K^+]_o$ is one of the more important and quantitatively large effects of HD, since K^+ removal is one of the treatment aims and the end-HD $[K^+]_o$ is almost always much lower than 4 mM [30, 56]. Indeed, even in control condition ($[K^+]_o = 5.4$ mM), the repolarising K^+ currents (especially I_{Kr} and I_{Ks}) of these models are quite tiny when compared to the ones of CN* or CZ, who repolarise properly up to $[K^+]_o = 3$ mM (current peaks are about 10 times smaller). In the NG paper the authors explicitly say that the I_{Kr} conductance has been reduced to fit AP data and that this current has been assigned a very low density [2]. Therefore, an increase of it may improve the performance of these models for low $[K^+]_o$.

The GB model exhibits several shortcomings as well. First of all, although it produces a proper AP at all the tested $[K^+]_o$, it behaves non-physiologically when $[K^+]_o$ is lower than 4 mM: the RMP depolarizes instead of hyperpolarize and, as a consequence, the APD_{90} also goes in the opposite way (shortening) and dV/dt_{MAX} dramatically decreases. Moreover, the excessive sensitivity to the amplitude of the stimulus current makes the computation of the ERP very unstable, leading to too long ERP values or no ERP at all. Since also in GB the repolarising K^+ currents (both I_{Kr} and I_{Ks}) are quite small in amplitude, increasing their magnitude may improve the model stability for low $[K^+]_o$ concentrations. Finally, the GB model responds poorly to $[Ca^{2+}]_o$ changes too: the APD_{90} trend is opposite to what observed in human atrial cells [64], i.e. instead of showing an inverse dependence, it is increasing with $[Ca^{2+}]_o$, even displaying EADs for $[Ca^{2+}]_o$ equal to 3 mM, and the intracellular Ca^{2+} transient is almost non-existent when $[Ca^{2+}]_o$ is lower than 1 mM. Therefore, the GB model turns out to be completely unsuitable to simulate the HD conditions.

As for the wrong dependency of APD on $[Ca^{2+}]_o$ a possible solution should address a modification of the L-type Ca^{2+} current, increasing the Ca^{2+} -dependent inactivation with respect to the Voltage-dependent one, in order to reduce the overall current for higher Ca^{2+} levels, despite the increase in driving force. Indeed, Ca^{2+} -dependent inactivation seems to be underestimated in many AP models [64], and previous modelling works managed to reproduce the inverse APD- $[Ca^{2+}]_o$ just by strengthening this mechanism [65, 74].

The CN* model responds properly to $[K^+]_o$ changes, at least from a qualitative point of view. It also reproduces well the “uncoupling” between APD and ERP variations when $[K^+]_o$ is increased (APD slightly decreases whereas ERP increases): this was experimentally reported by Downar et al. [60] when perfusing cardiac cells with hyperkalaemic ‘ischemic blood’ and interpreted as a secondary effect to changes in resting potential, which is known to affect, in turn, the Na^+ channels. In addition, simulation results for the CN* model predict a decrease in intracellular Na^+ when increasing $[Ca^{2+}]_o$: we are not aware of any available experimental data to confirm/deny this observation, which could have relevant implications.

The CZ model exhibits a good stability, with none repolarization failure nor EADs occurrence. However, it also has a few discrepancies with respect to the expected behaviour: APD decreases with $[K^+]_o$, while the opposite should happen [28] and CaT_{amp} is insensitive to $[Ca^{2+}]_o$ while in all the other models it increases with it, in agreement with experimental data reported in [66].

As for the quantification of cardiac side-effects of HD therapy, overall simulation results confirm that changes in $[K^+]_o$ and $[Ca^{2+}]_o$ are the ones mostly affecting cellular electrophysiology [28, 30], whereas $[Na^+]_o$ and volume seem to have a minor impact.

A qualitative summary of the expected variations in $[K^+]_o$ and $[Ca^{2+}]_o$ during HD and of the corresponding biomarker changes is shown in Table 5.2 and Table 5.3 respectively, comparing experimental/computational data from the literature with the simulations results of this study.

Table 5.2: Qualitative summary of HD-induced $[K^+]_o$ variation on selected AP biomarkers:

	$[K^+]_o$			
	RMP	APD	ERP	AP _{ud}
		↗	↘	↗
		[28, 60]	[59, 60]	[30, 59]
CN	-	+	-	+
NG	-	+	+	-
MT	-	+	+	-
KT*	-	+	+	-
GB	-	+	+	-
CZ	-	-	-	+

Table 5.3: Qualitative summary of HD-induced $[Ca^{2+}]_o$ variation on selected AP biomarkers and intracellular ionic concentrations. Results are shown for a Ca^{2+} increase, but depending on the $[Ca^{2+}]$ concentration in the dialysis bath, a decrease could occur as well, with opposite effects.

	$[Ca^{2+}]_o$				
	APD	ERP	CaT _{amp}	$[Ca^{2+}]_i$	$[Na^+]_i$
	↘	↘	↗	↗	?
	[30, 64–66]		[66]		
CN	-	-	+	+	-
NG	-	-	+	+	=
MT	-	-	+	+	=
KT*	-	-	+	+	=
GB	+	+	+	+	+
CZ	-	-	=	+	-

RMP: resting membrane potential; **APD:** AP duration; **ERP:** effective refractory period; **AP_{ud}:** upstroke delay, inversely correlated with conduction velocity; **CaT_{amp}:** Ca^{2+} -transient amplitude;

black arrows: expected increase/decrease during HD, with the corresponding references,

green/light green: moderate/large biomarker variation in the expected direction;

red/light red: moderate/large biomarker variation in the opposite direction.

Simulation results of acetylcholine effect show a reduction of APD and ERP in all the models, together with a more hyperpolarised RMP, in agreement with experimental data and previous modelling studies [5, 69–73]. In addition, all the models except GB show a reduction in AP_{ud} , suggesting a slower conductivity, also consistent with the increased vulnerability to arrhythmias, such as AF, due to an increased vagal activity [20, 70]. However, there are not experimental evidence to confirm or deny this results, and a more detailed description of autonomic regulation should be considered for future improvements in computational modelling of acetylcholine effects.

Other HD-related effects (e.g. acidosis correction) have not been addressed in our analysis and are left to further investigations.

Finally, it is worth to remember that HD patients are first of all uremic patients: this pathological condition (e.g. “uremic intoxication”) can also affect some aspects of cardiac cellular electrophysiology and should be incorporated into the models. As a relevant example, down-regulation of the Na^+/K^+ pump and high levels of circulating Na^+ pump inhibitor, have been reported in uremic patients compared to individuals with normal renal function, by several investigators [75–80].

In conclusion, computational modelling of human atrial cells constitutes a very useful tool to investigate the electrophysiological changes occurring in patients undergoing HD therapy. Nevertheless, it is always important to select carefully the specific model to use, depending on the particular aspect of interest.

Currently, CN* seems to be the more suitable human atrial model to analyse HD-related effects on atrial electrophysiology, though it is the oldest one and, therefore, it has a less detailed description of several cellular mechanisms: this is why this model has been chosen for the work presented in the next chapter.

Therefore, an additional model could be developed, trying to integrate and reconcile the knowledge of cellular and sub-cellular processes and their reactions to changes in the extracellular environment, taking into account the possible suggestions given above.

In this respect, works are still in progress in this specific field.

CHAPTER 6

Recurrent Intradialytic Paroxysmal Atrial Fibrillation: Hypotheses on Onset Mechanisms Based on Clinical Data and Computational Analysis

The content of this chapter has been published in:

Vincenti A, **Passini E***, Fabbrini P, Luise MC, Severi S, Genovesi G.

Recurrent intradialytic paroxysmal atrial fibrillation: hypotheses on onset mechanisms based on clinical data and computational analysis.

Europace, vol. 16, no. 3, pp. 396–404, Mar. 2014

** Antonio Vincenti and Elisa Passini contributed equally to this work.*

Abstract

Atrial fibrillation (AF) incidence is high in end-stage renal disease (ESRD) patients, and haemodialysis (HD) session may induce paroxysmal AF episodes.

Structural atrium remodelling is common in ESRD patients, moreover, HD session induces rapid plasma electrolytes and blood volume changes, possibly favouring arrhythmia onset. Therefore, HD session represents a unique model to study in vivo the mechanisms potentially inducing paroxysmal AF episodes.

Here, we present the case report of a patient in which HD regularly induced paroxysmal AF. In four consecutive sessions, heart rate variability analysis showed a progressive reduction of low/high frequency ratio before the AF onset, suggesting a relative increase in vagal activity. Moreover, all AF episodes were preceded by a great increase of supraventricular ectopic beats.

We applied computational modelling of cardiac cellular electrophysiology to these clinical findings, using plasma electrolyte concentrations and heart rate to simulate patient conditions at the beginning of HD session (pre-HD) and right before the AF onset (pre-AF), in a human atrial action potential model.

Simulation results provided evidence of a slower depolarization and a shortened refractory period in pre-AF vs. pre-HD, and these effects were enhanced when adding acetylcholine effect.

Paroxysmal AF episodes are induced by the presence of a trigger that acts upon a favourable substrate on the background of autonomic nervous system changes and in the described case report all these three elements were present. Starting from these findings, here we review the possible mechanisms leading to intradialytic AF onset.

INTRODUCTION

The prevalence of atrial fibrillation (AF) in patients with end-stage renal disease (ESRD) undergoing haemodialysis (HD) treatment is high. A recent review by Zimmerman reported a mean prevalence of this type of arrhythmia of 11.6%, even if within a wide range (5.4–27%) [18], presumably due to the different methodologies of the studies taken into consideration. Data from the United States Renal Data System have shown an important increase in AF prevalence (from 3.5% in 1992 to 10.7% in 2006) in HD patients [19]. Many of the risk factors that are associated with AF are the same as those observed in people without ESRD, such as age, the presence of hypertension, heart failure, ischaemic heart disease, and cerebrovascular disease [81]. Moreover, there are some arrhythmic risk factors specific to HD patients, like sudden changes in blood volume and electrolytes plasma level due to the HD session. Like in all other patients the presence of AF is

associated with an increased mortality in patients on HD treatment as well [82]. Episodes of AF induced by HD sessions are phenomena that have not been studied very extensively so far, but are well-known by nephrologists: often they concern episodes of paroxysmal AF which resolve spontaneously. Quite frequently these episodes are interrupted by pharmacological interventions or electrical cardioversion, when they cause any haemodynamic instability that does not allow the completion of the HD session or when it is not possible to keep the patient in the dialysis unit until spontaneous resolution of the episode. On the other hand, many of the asymptomatic episodes are probably not recognized as AF. Starting from the study of a representative case report and its clinical and computational analysis, this review aims to define the mechanisms that may cause episodes of intradialytic AF. In fact, AF episodes triggered by the session in HD patients, offer us a unique occasion to study the characteristics of paroxysmal AF onset: an occasion that cannot easily be found in other patients, whose AF episodes are much less predictable and assessable.

CASE REPORT

Four consecutive HD sessions were analysed in a 73-year-old woman with ESRD, in which HD regularly induced AF episodes that disappeared spontaneously shortly after the end of the HD session. Informed consent was obtained from the patient for the study.

Intradialytic Parameters

In all HD sessions, body weight loss, systolic, and diastolic arterial pressure were monitored hourly. Plasma Na⁺, K⁺, and Ca²⁺ concentrations were measured at the start and at the end of the treatment in Sessions #1 and #2, and hour by hour in Sessions #3 and #4, used for computational analysis.

Electrocardiogram Analysis

A 24 h ECG was recorded from the start of each HD session. All recordings were obtained using a three-channel Holter recorder, (Sorin Group Company). The AF onset time was identified. Arrhythmias were examined during the whole

recording time and expressed as the number of supraventricular ectopic beats (SVEBs), couples, or runs (more than three consecutive ectopic beats). The mean of SVEBs during the 30 min period before AF onset was compared with the mean of all other 30 min periods of registration. A signal-averaged P-wave recording was done before and after an HD session in which AF episodes were not observed. P-wave duration (P_{wd}) was analysed by using a dedicated software derived from the work by Stafford et al. [83] (Sorin Group Company).

Heart Rate Variability

Spectral components of heart rate variability (HRV) were calculated by fast Fourier transform over 256 s (1024 sampling points) epochs. The power spectral components recommended by the Task Force of the European Society of Cardiology and the North American Society of Pacing and Electrophysiology [84] were calculated: (i) very low frequency (VLF) from 0.00 to 0.04 Hz, (ii) low frequency (LF) from 0.04 to 0.15 Hz, (iii) high frequency (HF) from 0.15 to 0.4 Hz. The total spectral power corresponds to the power of the whole spectrum from 0 to 1 Hz. Very low frequency, LF, and HF power components were normalized (normalized units) for total power and the LF/HF ratio was considered.

Statistical Analysis

The differences between the recorded variables during the pre-HD and the pre-AF phases were analysed by using Student's t-test and analysis of variance for repeated measures followed by Fisher's test.

Results

Figure 4.1 shows the Holter ECG recordings during the four studied HD sessions. In all sessions, the arrhythmia developed between the second and the third hour of treatment. The episodes always resolved spontaneously within 2 h from the end of the HD session. The intradialytic plasma electrolyte changes (beginning vs. end HD) were comparable during the studied sessions. In particular, a significant reduction of plasma K⁺ (from 4.5±0.3 to 3.7±0.1 mM, p<0.05) and an increase of plasma Ca²⁺ (from 1.08±0.1 to 1.29±0.1 mM, p<0.01) concentrations were observed.

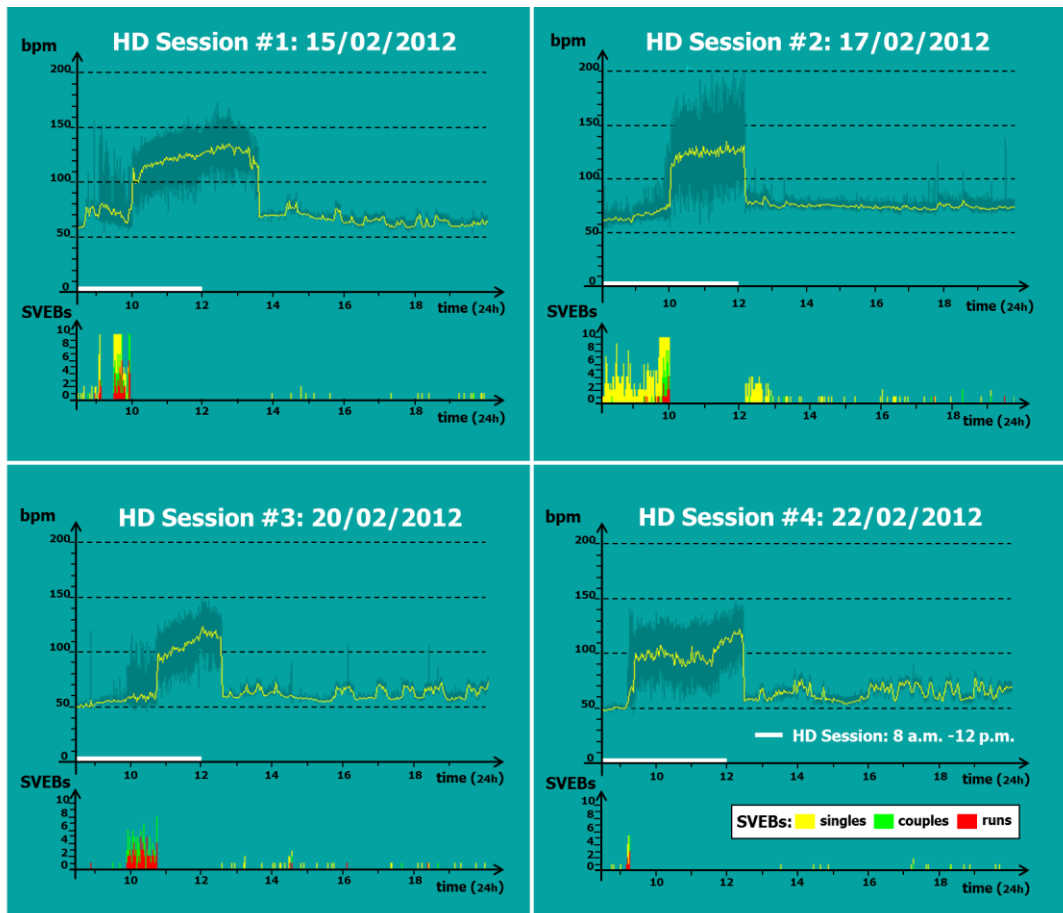


Figure 6.1: ECG Holter recordings during four consecutive HD sessions. Each session started at 8.00 a.m. and ended at 12.00 p.m. (white line): the patient regularly showed paroxysmal AF episodes, triggered during the session and spontaneously terminated at its end. Supraventricular ectopic beats (SVEBs) occurrence is shown in the lower section of each panel: single ectopic beats (yellow), couples (green), and runs (red) significantly increased in the minutes preceding AF onset.

During the HD sessions, the weight loss was 2.58 ± 0.40 kg. Spectral analysis of HRV at 30, 20, and 10 min before the AF onset showed a progressive reduction of LF (from 36.5 ± 14.0 to 26.7 ± 11.2 to 21.3 ± 11.0 nu, $p < 0.01$) with a consequent decrease in the LF/HF ratio (from 0.79 ± 0.5 to 0.51 ± 0.3 to 0.39 ± 0.2 , $p < 0.05$), suggesting a relative increase in vagal compared with sympathetic activity.

All AF episodes were preceded by an increase of supraventricular ectopic beats SVEBs: single (from 4.1 ± 4.8 to $160.5 \pm 97.5/30$ min), couples (from 0.2 ± 0.2 to $46.0 \pm 28.4/30$ min) and runs (from 0.2 ± 0.1 to $43.0 \pm 23.7/30$ min) as compared with the remaining observation period ($p < 0.05$). The duration of the signal-averaged P-wave, recorded in the same patient during a previous HD session in which no AF occurred, increased from 171 ms before the treatment to 185 ms at the end.

COMPUTATIONAL ANALYSIS

Methods

The Courtemanche model [1] of human atrial action potential (AP) provided the basis for simulations. It is not the most recent human atrial model, but it is the one best suited to reproduce the low $[Ca^{2+}]_o$ and $[K^+]_o$ levels occurring during HD [64]. We modified the original model by including the known dependency of I_{K1} and I_{Kr} currents on $[K^+]_o$ [28], and improving its long-term stability [45], as already described in Chapter 5. Moreover, we added the I_{KACh} current, sensible to acetylcholine (ACh) concentration, as recently done by Grandi et al. [5]. These have been the only changes to the Courtemanche formulation. Model differential equations were implemented in Matlab (Mathworks Inc.) and a variable order solver, based on the numerical differentiation formulas, was used to solve them (ode 15s) [54]. Pacing was simulated by a current pulse train (pulses of 3 ms, 1 Hz) with amplitude about twice the AP threshold: the stimulus was maintained for 300 s, to reach steady-state condition, i.e. intracellular concentrations (Na^+ , Ca^{2+} and K^+) stable over time.

We simulated patient's conditions at the beginning of the HD session (pre-HD) and right before the AF onset (pre-AF), by imposing the extracellular electrolyte concentrations and average heart rate, as measured in vivo. Two consecutive HD sessions (#3 and #4) were considered: electrolyte concentrations hour by hour were measured and the value assigned to the pre-AF condition was interpolated in correspondence with AF onset.

Different biomarkers have been considered to quantitatively compare simulation results: action potential duration (APD) was measured as the interval between the AP upstroke and the 90% repolarization level; resting membrane potential was measured at the end of diastole; the AP upstroke duration (AP_{ud}) was quantified as the time needed by membrane voltage to reach 0 mV, starting from the beginning of the pacing pulse [30]; the effective refractory period (ERP) was computed by simulating a S_1 – S_2 protocol, with S_1 and S_2 pulses of equal magnitude delivered at various rates: ERP was then defined as the longest S_1 – S_2 interval which failed to elicit an S_2 AP of amplitude $<80\%$ of the preceding S_1 AP [55].

Results

Representative traces of simulated atrial APs at the beginning of one HD session and right before the AF onset, including also the ACh effect, are shown in Figure 6.2A. For the two considered sessions (#3 and #4), we simulated three different conditions: pre-HD, beginning of the HD session; pre-AF, just before the AF onset; pre-AF+ACh, just before the AF onset, including acetylcholine effect.

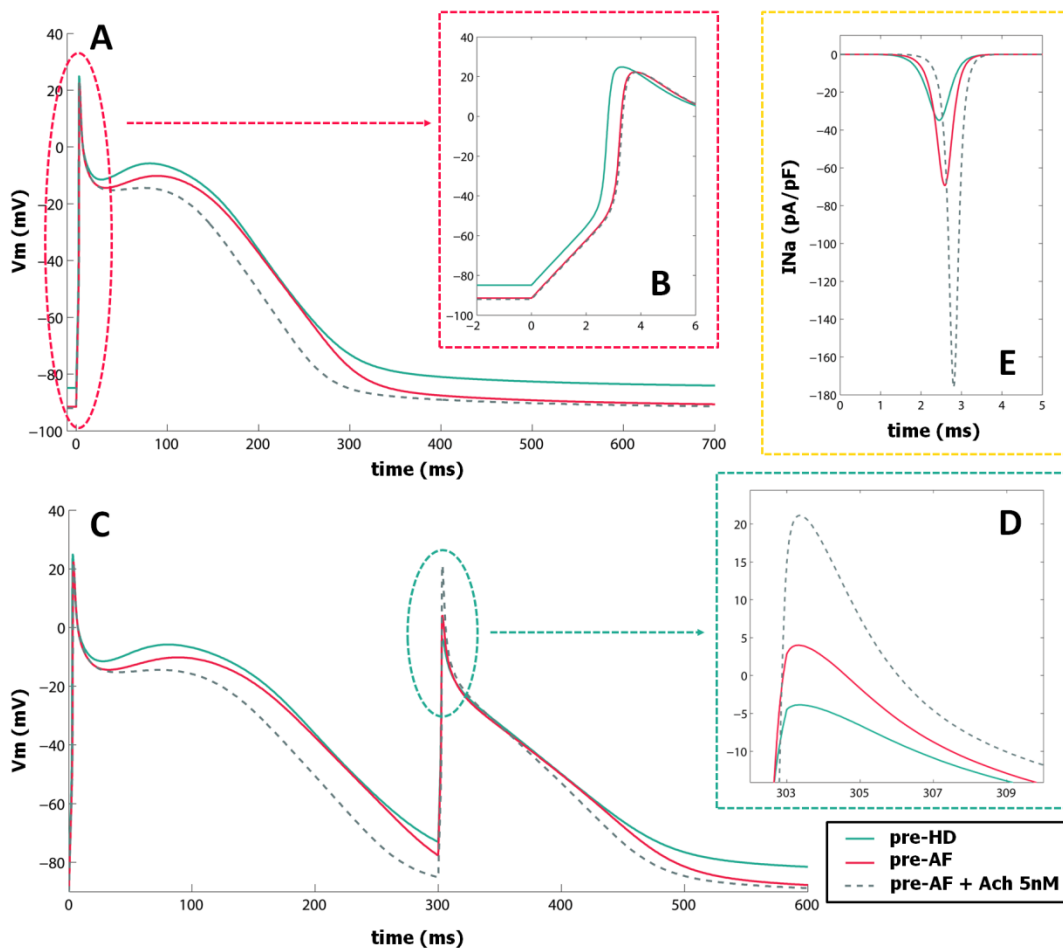


Figure 6.2: Simulated APs for the HD Session #3 (A). The changes in extracellular electrolytes and heart rate leading to AF onset determine a more hyperpolarized resting potential which in turn causes an increase of AP upstroke duration (B). The presence of ACh enhances these effects and also reduces the APD considerably. Atrial myocyte response to S_1 - S_2 protocol, considering a 300 ms S_1 - S_2 interval (C). The peak elicited by S_2 stimulus in pre-HD conditions is remarkably smaller (80%) than the one elicited by S_1 (D). This difference becomes less pronounced when considering pre-AF conditions and more so after adding ACh, suggesting that the ERP decreases accordingly. These differences are mostly due to the greater availability of sodium current at the more negative potential reached in the pre-AF conditions (E).

The corresponding cycle length, extracellular ion concentrations, and ACh concentration (model inputs) have been listed in Table 1, together with all the computed indices already defined in the Methods Section, which have been used to quantitatively estimate the differences between pre-HD and pre-AF conditions (model outputs).

Table 6.1: Case report computational analysis, simulation data and results

	<i>HD Session #3</i>			<i>HD Session #4</i>		
	<i>pre-HD</i>	<i>pre-AF</i>	<i>pre-AF+ACh</i>	<i>pre-HD</i>	<i>pre-AF</i>	<i>pre-AF+ACh</i>
<i>Model inputs</i>						
$[\text{Na}^+]_o$ (mM)	132	135	135	129	133	133
$[\text{K}^+]_o$ (mM)	4.6	3.5	3.5	4.6	3.8	3.8
$[\text{Ca}^{2+}]_o$ (mM)	1.04	1.23	1.23	0.99	1.17	1.17
CL (ms)	1132	1124	1124	1132	1071	1071
ACh (nM)	-	-	5	-	-	5
<i>Model outputs</i>						
APD (ms)	302	306	269	301	304	271
RMP (mV)	-85	-91	-92	-85	-89	-90
AP_{ud} (ms)	3.30	3.80	3.84	3.32	3.64	3.69
ERP (ms)	308	294	254	307	291	261

pre-HD, beginning of the HD session; *pre-AF*, just before the AF onset; *pre-AF+ACh*, just before the AF onset, including acetylcholine effect; **CL**, cycle length (mean value computed on the last 30 sinus beats before the AF onset); **ACh**, simulated acetylcholine concentration; **APD**, action potential duration at 90% of repolarisation; **RMP**, resting membrane potential; **AP_{ud}**, AP upstroke duration; **ERP**, effective refractory period.

K^+ removal during HD induced membrane hyperpolarization, especially in Session #3 where $[\text{K}^+]_o$ reduction was more pronounced. **AP_{ud}** significantly raised (15% and 10%, Sessions #3 and #4, respectively), since more time was needed for the cell to reach the threshold, starting from a hyperpolarized resting condition (Figure 6.2B). Effective refractory period shortening was also significant (-4.55% and -5.21%), while APD kept almost constant; in fact, $[\text{K}]_o$ decrease may have two uncoupled effects on APD and ERP [60].

As an example, in Figure 6.2C, the APs obtained from a S_1 – S_2 interval of 300 ms are shown (Session #3). Since the ERP in pre-HD condition is just above 300 ms, the S_2 stimulus falls within the refractory period and therefore the elicited peak

results considerably smaller (<80%) with respect to the S_1 one. In the pre-AF condition instead, the ERP being shorter, the S_2 peak is higher (Figure 6.2D); this difference is probably due to a greater availability of sodium current at the more negative potential reached in the pre-AF conditions (-69 pA/pF vs. -35 pA/pF, pre-AF vs. pre-HD, Figure 6.2E).

When considering both the pre-AF condition and ACh 5 nM, all the effects described above are enhanced (Table 1, pre-AF+ACh): ERP decreased considerably further (-17.53% and -14.98%, Sessions #3 and #4, pre-AF + ACh with respect to pre-HD). Moreover, a significant reduction of APD occurs (-10.64% and -9.93%).

INSIGHTS INTO THE MECHANISMS OF INTRADIALYTIC ATRIAL FIBRILLATION

Cardiac Morphology in Patients on Haemodialysis Treatment

Patients with ESRD undergoing HD treatment show deteriorated cardiac morphology defined as ‘uraemic cardiomyopathy’, characterized by the presence of fibrosis and changes in the microcirculation [85]. Both studies based on animal models of renal failure and autopsy of uraemic patients have shown the presence of reactive fibrosis (i.e. not due to tissue necrosis), which causes an increase in cardiac mass and a reduction in the volume of the capillary circulation within the myocardium [86]. The process of fibrosis formation develops early at the onset of renal failure [87], is associated with the HD duration, and appears to be independent of the contemporaneous presence of hypertension and/or diabetes mellitus [88].

It has been demonstrated that there are some mediators of cardiac fibrosis that are triggered by uraemia and do not depend on both cardiac pre-load and post-load changes. Among these mediators the ones most extensively studied are oxidative uraemic toxins, parathyroid hormone, hyperphosphataemia, and the renin–angiotensin–aldosterone system. Each of these factors act by means of specific and complex pathways that may be related with one another [89].

Left atrial volume, as measured by echocardiography, has recently emerged as a predictor of death and cardiovascular events in HD patients [90, 91] beyond left

ventricular mass and systolic function. It has also been shown that increased atrial dimensions are associated with increased AF prevalence in ESRD patients [81, 92].

Electrolyte and volume changes during the haemodialysis session

Just before undergoing HD session, patients show extracellular volume expansion, and Na^+ and K^+ overload, associated with metabolic acidosis. Plasmatic Ca^{2+} concentration, however, varies among patients. Haemodialysis treatment achieves a correction of the electrolyte and volume alterations through mechanisms of diffusion and/or convection, which allow the removal of electrolytes and toxins from the blood as well as elimination of liquids.

The main purpose of therapeutic intervention by HD is restoring the right blood volume by elimination of the excess Na^+ and water, that has been accumulated by the patient during the interdialytic interval. The level of ultrafiltration is constantly adjusted to reach the patients' ideal dry weight at the end of the HD session. Plasmatic K^+ concentrations increases during the interdialytic interval, mainly due to ions leakage from the cells as compensatory mechanism for the metabolic acidosis. The nephrologist's clinical concern is to obtain a level of intradialytic K^+ removal sufficient to avoid the development of hyperkalaemia before the next HD session. Patients receive a certain amount of bicarbonates from the dialysis bath, which is useful in the correction of the uraemia-induced metabolic acidosis.

In conclusion, the HD scheme entails a nonphysiological condition due to the intermittent character of the treatment and correction of the uraemia-induced alterations. One single HD session causes removal of excess Na^+ and water, sudden changes in potassium levels (often associated with an increase in calcium levels), and a complete or even excessive correction of the metabolic acidosis [93]. All these processes have important consequences on cardiovascular stability and determine the arrhythmogenic effects of HD sessions.

P-wave and the haemodialysis session

Several investigators have studied the modifications in atrial depolarization during the HD session, examining changes of the P-wave on the surface ECG. The studies present a few methodological differences, as some of them are based on 12-lead ECG registrations and others on high frequency electrocardiography recordings

[signal-averaged ECG (SAECG)] [83, 94]. P-wave duration is considered an expression of intra-atrial conduction velocity and its prolongation (particularly when shown by SAECG) has been associated with a higher incidence of AF, both paroxysmal and persistent, AF episodes after cardiac surgery and acute myocardial infarction, and AF recurrences after electrical cardioversion [95–99].

Other authors focus their attention on P-wave dispersion instead, another ECG parameter considered to be a possible predictor of AF [100]. The results of investigations on Pwd changes HD-related are not univocal. Several studies, performed both with 12-lead ECG [101, 102] and with SAECG [30, 103] show a significant increase in Pwd at the end of the HD session, whereas others describe no Pwd change or even a reduction [104, 105]. Two studies suggest that HD induces an increase in Pwd only during the HD session itself and that P-wave return to basal levels as soon as the patient is disconnected from the dialysis machine [106, 107]. As far as P wave dispersion is concerned, there is general agreement on its increase during the post-HD period, compared with the pre-HD one [101, 102].

There is difference of opinion on the variables that are associated with HD-related Pwd modifications. When looking at the electrolytes, it seems that K^+ is the ion that is most tightly correlated with Pwd and its changes during the HD session. An association between Pwd and plasma K^+ levels at start [106] and end [102] of HD session has been described. Moreover, an inverse correlation between intra-HD plasmatic potassium changes and P-wave modifications was found [30, 103]. Other studies, however, did not find any relationship between levels or changes of K^+ plasma values and Pwd [104, 105, 107]. Any possible associations between P-wave and other haematochemical variables (plasma concentrations of Ca^{2+} , magnesium, phosphate, bicarbonate, and haemoglobin) have been shown by data in literature to be weak or absent.

Several authors have tried to reveal a relationship between the amount of liquids removed during the HD session (i.e. the level of ultrafiltration) and the intradialytic modifications in Pwd. Madias [108, 109] suggests that the phenomenon of intradialytic Pwd prolongation is mediated by the alleviation of the fluid overload. This hypothesis was confirmed both by Ozben and Shimada, who found that the rate of removal of body fluid was an independent predictor of Pwd prolongation during HD [106, 107]. Other authors anyway did not find any significant correlation

between levels of intradialytic ultrafiltration and Pwd changes [30, 105]. A significant correlation has also been shown between left atrial diameter dimension and Pwd [30, 103], indicating an influence of atrial dimensions on the conduction velocity of the electrical stimuli across the cardiac chamber. Finally, a significant prolongation of basal Pwd in HD patients compared with a group of subjects with normal renal function has been reported [103, 104], while pre-HD Pwd was not higher in patients with ESRD compared with the control group in the study performed by Severi et al. [30]. It should be noted, however, that in the latter study the ESRD subjects had been on HD therapy for less than 6 months, whereas in the other studies this period was longer.

As a matter of fact the duration of HD therapy has been associated with an increase in Pwd by several authors [103, 104, 107]. In a prospective study, in which patients were followed from the start of renal replacement therapy, pre-HD Pwd was already significantly increased after 1 year of treatment [110]. These data suggest a role for renal replacement therapy per se in inducing an increase in the intra-atrial conduction velocity in patients with ESRD.

Autonomous nervous system and the haemodialysis session

As discussed before, each HD session causes a reduction in intravascular volume, which may vary depending on the dialysis technique used and the level of ultrafiltration defined, according to patient's needs. As a consequence, the HD session may become a stimulus for the low-pressure baroreceptors, localized in the large veins, in the pulmonary vessels, and in the right atrial and ventricular walls, which could induce an activation of the sympathetic output, resulting in an increased heart rate [111]. While several patients show this kind of response, other patterns of response have been described as well.

The HD session may in fact be associated with phenomena such as hypotension and bradycardia in a considerable proportion of cases [112] and with a reduction of the LF and an increase of the HF component in the spectral analysis of heart rate [113]. A reduction in heart rate has been described even in the absence of intradialytic hypotensive episodes [114–116]. Furthermore, hypotensive-prone patients show a reduction in the LF/HF ratio HD-related, even during the sessions in which their haemodynamic profile is relatively stable [117, 118].

These observations may suggest that, at least in a certain proportion of patients, the HD session is accompanied by a stimulation of the parasympathetic rather than the sympathetic autonomic nervous system or by a displacement of the sympatho-vagal balance in favour of vagal activity. It seems that this was the case in our patient, in whom the LF component of HRV progressively diminished during the phases preceding the arrhythmic episodes, with a consequent reduction in the LF/HF ratio. Even if this concept has been challenged [119, 120], LF/HF ratio is widely accepted as a measure of cardiac sympatho-vagal balance [121, 122]. The HF peak is generally considered to reflect cardiac parasympathetic nerve activity, while the LF should be mostly due to the sympathetic component.

The reasons why vagal stimulation should occur during HD are not clear, but a mechanism such as the activation of a Bezold–Jarisch reflex in response to blood volume reduction could be hypothesized. The Bezold–Jarisch reflex originates in cardiac sensory receptors with non-myelinated vagal afferent pathways, principally located in the left ventricle wall. Stimulation of these inhibitory cardiac receptors increases parasympathetic activity and inhibits sympathetic activity. These effects promote reflex bradycardia, vasodilation, and hypotension and this reflex can arise from the underfilled left ventricle when the intracardiac volume decreases [123].

It has been described how HD has an arrhythmogenic effect. The majority of the studies available in literature deal with the association between HD sessions and ventricular arrhythmias [17, 124–126]. However, there are other works that demonstrate an increase in the frequency of HD-related premature supraventricular beats [17, 125]. In our case report, the number of premature supraventricular impulses increased dramatically during the phases immediately preceding AF onset. It is known that an increase in premature atrial impulses is present before paroxysmal AF episodes, and this increase may have a role in triggering such episodes. The role of the autonomous nervous system and of the vagal stimulation, in particular, in the induction of AF in subjects without ESRD is well known.

The situation observed in our clinical case is probably not infrequent in HD patients: the HD session represents a unique model to test *in vivo*, in human, the acute effects of changes in plasma concentrations, and blood volume. It has been known since a long time that stimulation of the encephalic trunk shortens atrial

refractoriness in a non-homogeneous way and that it causes the appearance of atrial ectopic beats, both isolated and runs, which may easily induce AF onsets [127].

More recently, the existence of an ‘intrinsic’ autonomous nervous system of the heart has been taken into consideration, made up of large vessel receptors and above all of the ganglionated plexi (GP) on the epicardial surface of the atria, near the pulmonary vein ostia [128, 129]. The role of these structures is crucial in the induction of many forms of ‘vagal’ paroxysmal AF and maybe of the forms of AF that are caused by HD as well. Stimulation of the GP, both pharmacologically with mediators such as ACh and electrically, causes the appearance of focal firing from the adjacent pulmonary veins [130–136]. GP stimulation also reduces refractoriness of the atrial cells, thereby rendering AF more easily inducible by premature ectopic beats [137]. The importance of this mechanism, mediated by vagal stimulation of the GP, in causing the onset of AF is confirmed by the fact that transcatheter ablation of the pulmonary veins with electrical isolation turns out to be more effective in suppressing arrhythmias if associated with GP ablation [137, 138].

Administration of drugs that block vagal stimulation has also been shown to suppress firing from the pulmonary veins [139], and to inhibit the appearance of those AFs that are related to stimulation of the ‘intrinsic’ autonomous nervous system [140]. On the contrary, in this type of vagal-mediated AF, traditional class Ic or III antiarrhythmic agents prove to be ineffective. Instead, these molecules have been shown to be effective in preventing the onset of arrhythmia in models of AF induced by repeated atrial stimulations, which allow longer periods of arrhythmia and provoke electrophysiological changes that determine an electrical remodelling of the atrial substrate [141].

In conclusion, there are many similarities between ‘vagal’ paroxysmal AF, very frequently seen in those forms which show no structural heart disease or only ‘minor’ anatomical changes, and the kind of AF provoked by HD sessions; in both cases, the presence of vagal stimulation probably induces a reduction in refractoriness and an increase in SVEBs, which act as triggers in the arrhythmia onset [142]. The phenomenon seems to set in according to a probabilistic mechanism: the more supraventricular premature impulses increase and atrial refractoriness decreases, the higher becomes the chance of triggering an AF episode.

DISCUSSION AND CONCLUSIONS

The onset of paroxysmal AF episodes is induced by the presence of a trigger that acts upon a favourable substrate on the background of autonomic nervous system changes. In the described case report, all these three elements were present (Figure 6.3). In fact, the HD session was associated with (i) an increase in SVEBs right before the AF onset, (ii) an increase in Pwd, indicating a reduction of intra-atrial conduction velocity, (iii) changes in extracellular electrolyte concentrations, i.e. increase of Ca^{2+} and decrease of K^+ , and (iv) a reduction of the LF/HF ratio derived from the spectral analysis of RR variability, suggesting an increase in the vagal component of the autonomic balance.

The human atrial AP model used to simulate patient's conditions showed a slower depolarization phase before the AF onset, suggesting a reduction of intra-atrial conduction velocity, together with a decrease of the ERP. These phenomena were enhanced when adding the activity of KACH-dependent channels to the model.

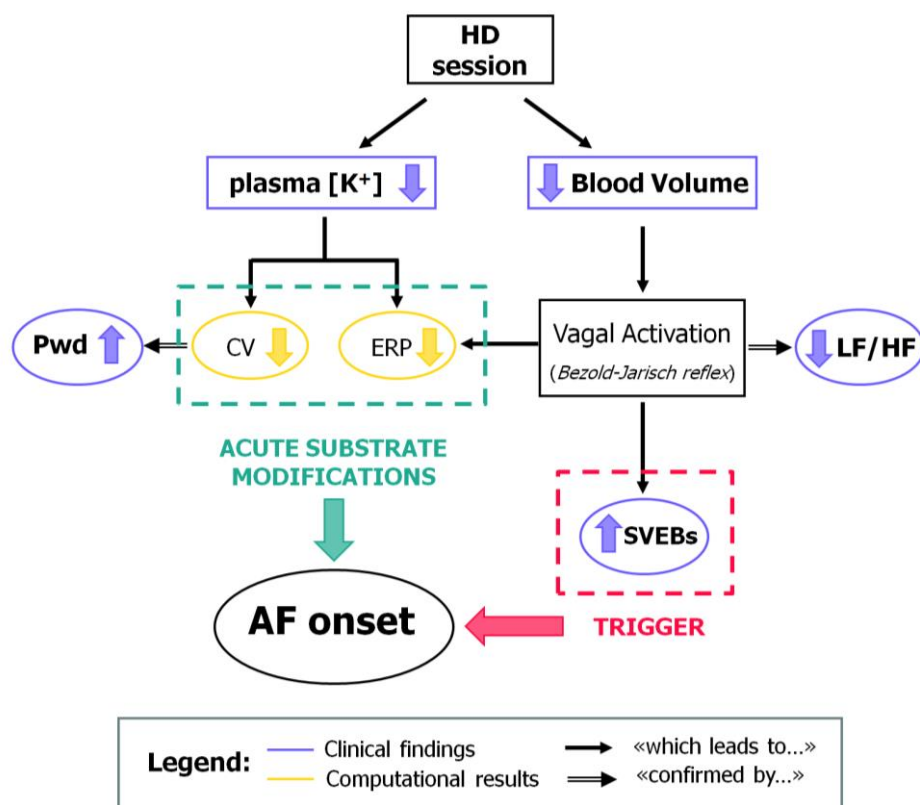


Figure 6.3: Schematic diagram of the mechanisms involved in atrial onset during HD sessions. AF, atrial fibrillation; HD, haemodialysis; CV, conduction velocity; ERP, effective refractory period; Pwd, P-wave duration; SVEBs, supraventricular ectopic beats; LF/HF, low frequency/high frequency ratio.

By considering all the elements described above and relating them to data from the literature, we can hypothesize that intradialytic AF episodes may constitute a kind of ‘in vivo’ model of the vagal-induced paroxysmal forms of AF. As this phenomenon is not seen in all patients during HD, we must conclude that the HD session acts as a triggering factor only in those subjects whose anatomical predisposition and characteristics of sympatho-vagal balance may favour the onset of arrhythmia.

If our hypothesis on the mechanism of arrhythmia triggering is correct, it would be possible that prevalence and incidence of AF in HD patients are higher than described in literature, particularly in asymptomatic patients whose arrhythmic episodes might go unnoticed by the medical staff. It is difficult to find a way to reduce the phenomenon. The demonstration that the slowing down of the intra-atrial conduction velocity induced by HD is inversely proportional to the extent of changes in plasma potassium level [30] would suggest to contain the intradialytic shifts of this ion as much as possible, by changing potassium concentrations in the dialysate and by trying to reduce pre-HD blood potassium level through diet and use of resins. It is even more complicated to find tools to oppose any possible increases in vagal tone related to the HD session. Theoretically, in patients suffering from AF episodes with the characteristics described above, transcatheter electrical isolation of the pulmonary veins could be useful, either with or without ablation of the GP. Anyway, before carrying out such a procedure, which undoubtedly affects the pathophysiological mechanism of these forms of AF, its clinical risks and benefits should be evaluated.

References

- [1] M. Courtemanche, R. J Ramirez, and S. Nattel, “Ionic mechanisms underlying human atrial action potential properties : insights from a mathematical model” *Am J Physiol Heart Circ Physiol*, vol. 275, pp. 1522–1539, 1998.
- [2] A. Nygren, C. Fiset, L. Firek, J W. Clark, D. S. Lindblad, R. B. Clark, and W. R. Giles, “Mathematical model of an adult human atrial cell: the role of K⁺ currents in repolarization” *Circ Res*, vol. 82, no. 1, pp. 63–81, 1998.
- [3] M. M. Maleckar, J L. Greenstein, W. R. Giles, and N. A. Trayanova, “K⁺ current changes account for the rate dependence of the action potential in the human atrial myocyte” *Am J Physiol Heart Circ Physiol*, vol. 297, no. 4, pp. H1398–410, Oct. 2009.
- [4] J T. Koivumäki, T. Korhonen, and P. Tavi, “Impact of sarcoplasmic reticulum calcium release on calcium dynamics and action potential morphology in human atrial myocytes: a computational study” *PLoS Comput Biol*, vol. 7, no. 1, p. e1001067, Jan. 2011.
- [5] E. Grandi, S. V Pandit, N. Voigt, A. J Workman, D. Dobrev, J Jalife, and D. M. Bers, “Human atrial action potential and Ca²⁺ model: sinus rhythm and chronic atrial fibrillation” *Circ Res*, vol. 109, no. 9, pp. 1055–66, Oct. 2011.
- [6] M. A. Colman, O. V Aslanidi, S. Khariche, M. R. Boyett, C. Garratt, J C. Hancox, and H. Zhang, “Pro-arrhythmogenic effects of atrial fibrillation-induced electrical remodelling: insights from the three-dimensional virtual human atria” *J Physiol*, vol. 591, no. Pt 17, pp. 4249–72, Sep. 2013.
- [7] T. Krogh-Madsen, G. W. Abbott, and D. J Christini, “Effects of electrical and structural remodeling on atrial fibrillation maintenance: a simulation study” *PLoS Comput Biol*, vol. 8, no. 2, p. e1002390, Jan. 2012.
- [8] C. Sánchez, A. Corrias, A. Bueno-Orovio, M. Davies, J Swinton, I. Jacobson, P. Laguna, E. Pueyo, and B. Rodríguez, “The Na⁺/K⁺ pump is an important modulator of refractoriness and rotor dynamics in human atrial tissue” *Am J Physiol. Heart Circ Physiol*, vol. 302, no. 5, pp. H1146–59, Mar. 2012.
- [9] Y. Xie, A. Garfinkel, P. Camelliti, P. Kohl, J N. Weiss, and Z. Qu, “Effects of fibroblast-myocyte coupling on cardiac conduction and vulnerability to reentry: A computational study” *Heart Rhythm*, vol. 6, no. 11, pp. 1641–9, Nov. 2009.
- [10] M. Courtemanche, R. J Ramirez, and S. Nattel, “Ionic targets for drug therapy and atrial fibrillation-induced electrical remodeling: insights from a mathematical model” *Cardiovasc Res*, vol. 42, no. 2, pp. 477–89, May 1999.
- [11] H. Zhang, C. J Garratt, J Zhu, and A. V Holden, “Role of up-regulation of IK₁ in action potential shortening associated with atrial fibrillation in humans” *Cardiovasc Res*, vol. 66, no. 3, pp. 493–502, Jun. 2005.
- [12] Y. Gong, F. Xie, K. M. Stein, A. Garfinkel, C. A. Culianu, B. B. Lerman, and D. J Christini, “Mechanism underlying initiation of paroxysmal atrial flutter/atrial fibrillation by ectopic foci: a simulation study” *Circulation*, vol. 115, no. 16, pp. 2094–102, Apr. 2007.
- [13] V. Jacquemet, N. Virag, and L. Kappenberger, “Wavelength and vulnerability to atrial fibrillation: Insights from a computer model of human atria” *Europace*, vol. 7 Suppl 2, pp. 83–92, Sep. 2005.

- [14] J T. Koivumäki, G. Seemann, M. M. Maleckar, and P. Tavi, “In Silico Screening of the Key Cellular Remodeling Targets in Chronic Atrial Fibrillation,” *PLoS Comput Biol*, vol. 10, no. 5, p. e1003620, May 2014.
- [15] E. P. Scholz, P. Carrillo-Bustamante, F. Fischer, M. Wilhelms, E. Zitron, O. Dössel, H. a Katus, and G. Seemann, “Rotor termination is critically dependent on kinetic properties of IKur inhibitors in an in silico model of chronic atrial fibrillation” *PLoS One*, vol. 8, no. 12, p. e83179, Jan. 2013.
- [16] J T. Daugirdas and T. S. Ing, *Handbook of Dialysis*, 2nd Editio. Little, Brown and company. Boston/ New York/ Toronto/ London, 1994.
- [17] S. Genovesi, C. Dossi, M. R. Viganò, E. Galbiati, F. Prolo, A. Stella, and M. Stramba-Badiale, “Electrolyte concentration during haemodialysis and QT interval prolongation in uraemic patients” *Europace*, vol. 10, no. 6, pp. 771–7, Jun. 2008.
- [18] D. Zimmerman, M. M. Sood, C. Rigatto, R. M. Holden, S. Hiremath, and C. M. Clase, “Systematic review and meta-analysis of incidence, prevalence and outcomes of atrial fibrillation in patients on dialysis” *Nephrol Dial Transplant*, vol. 27, no. 10, pp. 3816–22, Oct. 2012.
- [19] W. C. Winkelmayr, A. R. Patrick, J Liu, M. A. Brookhart, and S. Setoguchi, “The increasing prevalence of atrial fibrillation among hemodialysis patients” *J Am Soc Nephrol*, vol. 22, no. 2, pp. 349–57, Feb. 2011.
- [20] A. Vincenti, E. Passini, P. Fabbrini, M. C. Luise, S. Severi, and S. Genovesi, “Recurrent intradialytic paroxysmal atrial fibrillation: hypotheses on onset mechanisms based on clinical data and computational analysis” *Europace*, vol. 16, no. 3, pp. 396–404, Mar. 2014.
- [21] M. S. Buiten, M. K. de Bie, J I. Rotmans, B. A. Gabreëls, W. van Dorp, R. Wolterbeek, S. A. Trines, M. J Schalijs, J W. Jukema, T. J Rabelink, and L. van Erven, “The dialysis procedure as a trigger for atrial fibrillation: new insights in the development of atrial fibrillation in dialysis patients” *Heart*, vol. 100, no. 9, pp. 685–90, May 2014.
- [22] S. Severi and S. Cavalcanti, “Electrolyte and pH dependence of heart rate during hemodialysis: a computer model analysis” *Artif Organs*, vol. 24, no. 4, pp. 245–60, Apr. 2000.
- [23] S. Severi, S. Cavalcanti, E. Mancini, and A. Santoro, “Heart rate response to hemodialysis-induced changes in potassium and calcium levels” *J Nephrol*, vol. 14, no. 6, pp. 488–96, 2001.
- [24] S. Severi, S. Cavalcanti, E. Mancini, and A. Santoro, “Effect of electrolyte and pH changes on the sinus node pacemaking in humans” *J Electrocardiol*, vol. 35, no. 2, pp. 115–24, Apr. 2002.
- [25] D. Noble and S. J Noble, “A model of sino-atrial node electrical activity based on a modification of the DiFrancesco-Noble (1984) equations” *Proc R Soc Lond B Biol Sci*, vol. 222, no. 1228, pp. 295–304, Sep. 1984.
- [26] D. DiFrancesco and D. Noble, “A model of cardiac electrical activity incorporating ionic pumps and concentration changes” *Philos Trans R Soc Lond B Biol Sci*, vol. 307, no. 1133, pp. 353–98, Jan. 1985.
- [27] S. Dokos, B. G. Celler, and N. H. Lovell, “Modification of DiFrancesco-Noble equations to simulate the effects of vagal stimulation on in vivo mammalian sinoatrial node electrical activity” *Ann Biomed Eng*, vol. 21, no. 4, pp. 321–35, 1993.

- [28] S. Severi, E. Grandi, C. Pes, F. Badiali, F. Grandi, and A. Santoro, “Calcium and potassium changes during haemodialysis alter ventricular repolarization duration: in vivo and in silico analysis” *Nephrol Dial Transplant*, vol. 23, no. 4, pp. 1378–86, Apr. 2008.
- [29] K. H. W. J ten Tusscher, D. Noble, P. J Noble, and A. V Panfilov, “A model for human ventricular tissue” *Am J Physiol Heart Circ Physiol*, vol. 286, no. 4, pp. H1573–89, Apr. 2004.
- [30] S. Severi, D. Pogliani, G. Fantini, P. Fabbrini, M. R. Viganò, E. Galbiati, G. Bonforte, A. Vincenti, A. Stella, and S. Genovesi, “Alterations of atrial electrophysiology induced by electrolyte variations: combined computational and P-wave analysis” *Europace*, vol. 12, no. 6, pp. 842–9, Jun. 2010.
- [31] M. W. Krueger, S. Severi, K. Rhode, S. Genovesi, F. M. Weber, A. Vincenti, P. Fabbrini, G. Seemann, R. Razavi, and O. Dössel, “Alterations of atrial electrophysiology related to hemodialysis session: insights from a multiscale computer model” *J Electrocardiol*, vol. 44, no. 2, pp. 176–83, 2011.
- [32] M. Gilányi, C. Ikrényi, J Fekete, K. Ikrényi, and A. G. Kovách, “Ion concentrations in subcutaneous interstitial fluid: measured versus expected values” *Am J Physiol*, vol. 255, no. 3 Pt 2, pp. F513–9, Sep. 1988.
- [33] A. Nygren, L. J Leon, and W. R. Giles, “Simulations of the human atrial action potential,” *Philos Trans R Soc A Math Phys Eng Sci*, vol. 359, no. 1783, pp. 1111–1125, Jun. 2001.
- [34] E. M. Cherry and S. J Evans, “Properties of two human atrial cell models in tissue: restitution, memory, propagation, and reentry” *J Theor Biol*, vol. 254, no. 3, pp. 674–90, Oct. 2008.
- [35] E. M. Cherry, H. M. Hastings, and S. J Evans, “Dynamics of human atrial cell models: restitution, memory, and intracellular calcium dynamics in single cells” *Prog Biophys Mol Biol*, vol. 98, no. 1, pp. 24–37, Sep. 2008.
- [36] K. Tsujimae, S. Murakami, and Y. Kurachi, “In silico study on the effects of IKur block kinetics on prolongation of human action potential after atrial fibrillation-induced electrical remodeling” *Am J Physiol Heart Circ Physiol*, vol. 294, no. 2, pp. H793–800, Feb. 2008.
- [37] D. M. Bers and E. Grandi, “Human atrial fibrillation: insights from computational electrophysiological models” *Trends Cardiovasc Med*, vol. 21, no. 5, pp. 145–50, Jul. 2011.
- [38] O. Dössel, M. W. Krueger, F. M. Weber, M. Wilhelms, and G. Seemann, “Computational modeling of the human atrial anatomy and electrophysiology” *Med Biol Eng Comput*, vol. 50, no. 8, pp. 773–99, Aug. 2012.
- [39] M. Wilhelms, H. Hettmann, M. M. Maleckar, J T. Koivumäki, O. Dössel, and G. Seemann, “Benchmarking electrophysiological models of human atrial myocytes” *Front Physiol*, vol. 3, p. 487, Jan. 2012.
- [40] C. H. Luo and Y. Rudy, “A dynamic model of the cardiac ventricular action potential. I. Simulations of ionic currents and concentration changes” *Circ Res*, vol. 74, no. 6, pp. 1071–96, Jun. 1994.
- [41] D. S. Lindblad, C. R. Murphey, J W. Clark, and W. R. Giles, “A model of the action potential and underlying membrane currents in a rabbit atrial cell” *Am J Physiol*, vol. 271, no. 4 Pt 2, pp. H1666–96, Oct. 1996.

- [42] E. Grandi, F. S. Pasqualini, and D. M. Bers, “A novel computational model of the human ventricular action potential and Ca transient” *J Mol Cell Cardiol*, vol. 48, no. 1, pp. 112–21, Jan. 2010.
- [43] T. R. Shannon, F. Wang, J. Puglisi, C. Weber, and D. M. Bers, “A mathematical treatment of integrated Ca dynamics within the ventricular myocyte” *Biophys J*, vol. 87, no. 5, pp. 3351–71, Nov. 2004.
- [44] A. Van Oosterom and V. Jacquemet, “Ensuring stability in models of atrial kinetics,” in *Computing in Cardiology*, 2009, vol. 36, pp. 69–72.
- [45] V. Jacquemet, “Steady-state solutions in mathematical models of atrial cell electrophysiology and their stability” *Math Biosci*, vol. 208, no. 1, pp. 241–69, Jul. 2007.
- [46] C. H. Luo and Y. Rudy, “A model of the ventricular cardiac action potential. Depolarization, repolarization, and their interaction” *Circ Res*, vol. 68, no. 6, pp. 1501–26, Jun. 1991.
- [47] T. Shibasaki, “Conductance and kinetics of delayed rectifier potassium channels in nodal cells of the rabbit heart” *J Physiol*, vol. 387, pp. 227–50, Jun. 1987.
- [48] B. Sakmann and G. Trube, “Conductance properties of single inwardly rectifying potassium channels in ventricular cells from guinea-pig heart” *J Physiol*, vol. 347, pp. 641–57, Feb. 1984.
- [49] B. Sakmann and G. Trube, “Voltage-dependent inactivation of inward-rectifying single-channel currents in the guinea-pig heart cell membrane” *J Physiol*, vol. 347, pp. 659–83, Feb. 1984.
- [50] N. Voigt, A. W. Trafford, U. Ravens, and D. Dobrev, “Abstract 2630: Cellular and Molecular Determinants of Altered Atrial Ca²⁺ Signaling in Patients With Chronic Atrial Fibrillation,” *Circulation*, vol. 120, no. 18_MeetingAbstracts, p. S667–d–668, Nov. 2009.
- [51] N. Voigt, N. Li, Q. Wang, W. Wang, A. W. Trafford, I. Abu-Taha, Q. Sun, T. Wieland, U. Ravens, S. Nattel, X. H. T. Wehrens, and D. Dobrev, “Enhanced sarcoplasmic reticulum Ca²⁺ leak and increased Na⁺-Ca²⁺ exchanger function underlie delayed afterdepolarizations in patients with chronic atrial fibrillation” *Circulation*, vol. 125, no. 17, pp. 2059–70, May 2012.
- [52] S. Neef, N. Dybkova, S. Sossalla, K. R. Ort, N. Fluschnik, K. Neumann, R. Seipelt, F. A. Schöndube, G. Hasenfuss, and L. S. Maier, “CaMKII-dependent diastolic SR Ca²⁺ leak and elevated diastolic Ca²⁺ levels in right atrial myocardium of patients with atrial fibrillation” *Circ Res*, vol. 106, no. 6, pp. 1134–44, Apr. 2010.
- [53] M. B. Wagner, Y. Wang, R. Kumar, S. M. Tipparaju, and R. W. Joyner, “Calcium transients in infant human atrial myocytes” *Pediatr Res*, vol. 57, no. 1, pp. 28–34, Jan. 2005.
- [54] L. F. Shampine and M. W. Reichelt, “The MATLAB ODE Suite,” *SIAM J Sci Comput*, vol. 18, no. 1, pp. 1–22, Jan. 1997.
- [55] A. J. Workman, K. A. Kane, and A. C. Rankin, “The contribution of ionic currents to changes in refractoriness of human atrial myocytes associated with chronic atrial fibrillation” *Cardiovasc Res*, vol. 52, no. 2, pp. 226–235, Nov. 2001.
- [56] B. U. Agar, B. F. Culleton, R. Fluck, and J. K. Leyboldt, “Potassium kinetics during hemodialysis” *Hemodial Int*, Aug. 2014.

- [57] A. G. Kleber, “Resting membrane potential, extracellular potassium activity, and intracellular sodium activity during acute global ischemia in isolated perfused guinea pig hearts,” *Circ Res*, vol. 52, no. 4, pp. 442–450, Apr. 1983.
- [58] O. E. Osadchii, “Mechanisms of hypokalemia-induced ventricular arrhythmogenicity” *Fundam Clin Pharmacol*, vol. 24, no. 5, pp. 547–59, Oct. 2010.
- [59] J L. Smeets, M. A. Allesie, W. J Lammers, F. I. Bonke, and J Hollen, “The wavelength of the cardiac impulse and reentrant arrhythmias in isolated rabbit atrium. The role of heart rate, autonomic transmitters, temperature, and potassium” *Circ Res*, vol. 58, no. 1, pp. 96–108, Jan. 1986.
- [60] E. Downar, M. J Janse, and D. Durrer, “The effect of ‘ischemic’ blood on transmembrane potentials of normal porcine ventricular myocardium” *Circulation*, vol. 55, no. 3, pp. 455–462, Mar. 1977.
- [61] J W. Buchanan, T. Saito, and L. S. Gettes, “The effects of antiarrhythmic drugs, stimulation frequency, and potassium-induced resting membrane potential changes on conduction velocity and dV/dt_{max} in guinea pig myocardium” *Circ Res*, vol. 56, no. 5, pp. 696–703, May 1985.
- [62] R. Veeraraghavan and S. Poelzing, “Mechanisms underlying increased right ventricular conduction sensitivity to flecainide challenge” *Cardiovasc Res*, vol. 77, no. 4, pp. 749–56, Mar. 2008.
- [63] R. M. Shaw and Y. Rudy, “Electrophysiologic effects of acute myocardial ischemia. A mechanistic investigation of action potential conduction and conduction failure” *Circ Res*, vol. 80, no. 1, pp. 124–38, Jan. 1997.
- [64] S. Severi, C. Corsi, and E. Cerbai, “From in vivo plasma composition to in vitro cardiac electrophysiology and in silico virtual heart: the extracellular calcium enigma” *Philos Trans A Math Phys Eng Sci*, vol. 367, no. 1896, pp. 2203–23, Jun. 2009.
- [65] E. Grandi, F. S. Pasqualini, C. Pes, C. Corsi, A. Zaza, and S. Severi, “Theoretical investigation of action potential duration dependence on extracellular Ca^{2+} in human cardiomyocytes” *J Mol Cell Cardiol*, vol. 46, no. 3, pp. 332–42, Mar. 2009.
- [66] N. Nagy, K. Acsai, A. Kormos, Z. Sebök, A. S. Farkas, N. Jost, P. P. Nánási, J G. Papp, A. Varró, and A. Tóth, “[Ca^{2+}] _i-induced augmentation of the inward rectifier potassium current (IK1) in canine and human ventricular myocardium” *Pflugers Arch*, vol. 465, no. 11, pp. 1621–35, Nov. 2013.
- [67] S. S. Waikar, G. C. Curhan, and S. M. Brunelli, “Mortality associated with low serum sodium concentration in maintenance hemodialysis” *Am J Med*, vol. 124, no. 1, pp. 77–84, Jan. 2011.
- [68] F. R. Mc Causland, S. M. Brunelli, and S. S. Waikar, “Dialysate sodium, serum sodium and mortality in maintenance hemodialysis” *Nephrol Dial Transplant*, vol. 27, no. 4, pp. 1613–8, Apr. 2012.
- [69] S. Koumi, C. E. Arentzen, C. L. Backer, and J A. Wasserstrom, “Alterations in muscarinic K^{+} channel response to acetylcholine and to G protein-mediated activation in atrial myocytes isolated from failing human hearts” *Circulation*, vol. 90, no. 5, pp. 2213–24, Nov. 1994.

- [70] C. Xia, J Xia, Z. Shui, J Liu, W. Sun, Y. Du, and G. Hao, “Effects of acetylcholine on electrical remodeling of human atrial fibers” *J Huazhong Univ Sci Technolog Med Sci*, vol. 31, no. 2, pp. 164–8, Apr. 2011.
- [71] F. Halimi, O. Piot, L. Guize, and J Y. Le Heuzey, “Electrophysiological effects of vasoactive intestinal peptide in rabbit atrium: a modulation of acetylcholine activity” *J Mol Cell Cardiol*, vol. 29, no. 1, pp. 37–44, Jan. 1997.
- [72] M. M. Maleckar, J L. Greenstein, N. A. Trayanova, and W. R. Giles, “Mathematical simulations of ligand-gated and cell-type specific effects on the action potential of human atrium” *Prog Biophys Mol Biol*, vol. 98, no. 2–3, pp. 161–70, 2008.
- [73] E. J Vigmond, V. Tsoi, S. Kuo, H. Arevalo, J Kneller, S. Nattel, and N. Trayanova, “The effect of vagally induced dispersion of action potential duration on atrial arrhythmogenesis” *Heart Rhythm*, vol. 1, no. 3, pp. 334–44, Sep. 2004.
- [74] E. Passini and S. Severi, “Extracellular Calcium and L-Type Calcium Current Inactivation Mechanisms: a Computational Study,” *Computing in Cardiology*, vol. 40, 2013.
- [75] H. J Kramer, D. Gospodinov, and F. Krück, “Functional and metabolic studies on red blood cell sodium transport in chronic uremia” *Nephron*, vol. 16, no. 5, pp. 344–58, Jan. 1976.
- [76] J R. Cotton, T. Woodard, N. W. Carter, and J P. Knochel, “Resting skeletal muscle membrane potential as an index of uremic toxicity. A proposed new method to assess adequacy of hemodialysis” *J Clin Invest*, vol. 63, no. 3, pp. 501–6, Mar. 1979.
- [77] L. Minkoff, G. Gaertner, M. Darab, C. Mercier, and M. L. Levin, “Inhibition of brain sodium-potassium ATPase in uremic rats” *J Lab Clin Med*, vol. 80, no. 1, pp. 71–8, Jul. 1972.
- [78] J T. Cheng, T. Kahn, and D. M. Kaji, “Mechanism of alteration of sodium potassium pump of erythrocytes from patients with chronic renal failure” *J Clin Invest*, vol. 74, no. 5, pp. 1811–20, Nov. 1984.
- [79] J M. Krzesinski, L. Christiaens, M. Palem-Vliers, D. Fenghe, M. L. Pequeux-Bar, M. R. Lomba-Pignon, P. Genard, and G. Rorive, “[Arguments for the existence of an endogenous inhibitor of renal Na-K ATPase with steroid structure and natriuretic action]” *Arch Mal Coeur Vaiss*, vol. 83, no. 8, pp. 1229–31, Jul. 1990.
- [80] G. Deray, M. G. Pernollet, M. A. Devynck, J Zingraff, A. Touam, J Rosenfeld, and P. Meyer, “Plasma digitalislike activity in essential hypertension or end-stage renal disease” *Hypertension*, vol. 8, no. 7, pp. 632–8, Jul. 1986.
- [81] S. Genovesi, D. Pogliani, A. Faini, M. G. Valsecchi, A. Riva, F. Stefani, I. Acquistapace, A. Stella, G. Bonforte, A. DeVecchi, V. DeCristofaro, G. Buccianti, and A. Vincenti, “Prevalence of atrial fibrillation and associated factors in a population of long-term hemodialysis patients” *Am J Kidney Dis*, vol. 46, no. 5, pp. 897–902, Nov. 2005.
- [82] S. Genovesi, A. Vincenti, E. Rossi, D. Pogliani, I. Acquistapace, A. Stella, and M. G. Valsecchi, “Atrial fibrillation and morbidity and mortality in a cohort of long-term hemodialysis patients” *Am J Kidney Dis*, vol. 51, no. 2, pp. 255–62, Feb. 2008.
- [83] P. Stafford, P. Denbigh, and R. Vincent, “Frequency Analysis of the P Wave: Comparative Techniques,” *Pacing Clin Electrophysiol*, vol. 18, no. 2, pp. 261–270, Feb. 1995.

- [84] M. Malik, J T. Bigger, A. J Camm, R. E. Kleiger, A. Malliani, A. J Moss, and P. J Schwartz, “Heart rate variability: Standards of measurement, physiological interpretation, and clinical use,” *Eur Heart J*, vol. 17, no. 3, pp. 354–381, Mar. 1996.
- [85] A. Remppis and E. Ritz, “Cardiac problems in the dialysis patient: beyond coronary disease” *Semin Dial*, vol. 21, no. 4, pp. 319–25, Jan. .
- [86] G. Mall, W. Huther, J Schneider, P. Lundin, and E. Ritz, “Diffuse Intermyocardiocytic Fibrosis in Uraemic Patients,” *Nephrol Dial Transplant*, vol. 5, no. 1, pp. 39–44, Jan. 1990.
- [87] A. M. Siedlecki, X. Jin, and A. J Muslin, “Uremic cardiac hypertrophy is reversed by rapamycin but not by lowering of blood pressure” *Kidney Int*, vol. 75, no. 8, pp. 800–8, Apr. 2009.
- [88] M.-L. Gross and E. Ritz, “Non-coronary heart disease in dialysis patients: hypertrophy and fibrosis in the cardiomyopathy of uremia--beyond coronary heart disease” *Semin Dial*, vol. 21, no. 4, pp. 308–18, 2008.
- [89] R. J Glasscock, R. Pecoits-Filho, and S. H. Barberato, “Left ventricular mass in chronic kidney disease and ESRD” *Clin. J Am Soc Nephrol*, vol. 4 Suppl 1, no. Supplement_1, pp. S79–91, Dec. 2009.
- [90] G. Tripepi, F. A. Benedetto, F. Mallamaci, R. Tripepi, L. Malatino, and C. Zoccali, “Left atrial volume in end-stage renal disease: a prospective cohort study” *J Hypertens*, vol. 24, no. 6, pp. 1173–80, Jun. 2006.
- [91] G. Tripepi, F. A. Benedetto, F. Mallamaci, R. Tripepi, L. Malatino, and C. Zoccali, “Left atrial volume monitoring and cardiovascular risk in patients with end-stage renal disease: a prospective cohort study” *J Am Soc Nephrol*, vol. 18, no. 4, pp. 1316–22, Apr. 2007.
- [92] I. Atar, D. Konaş, S. Açikel, E. Külah, A. Atar, H. Bozbaş, O. Gülmez, S. Sezer, A. Yildirir, N. Ozdemir, H. Müderrisoğlu, and B. Ozin, “Frequency of atrial fibrillation and factors related to its development in dialysis patients” *Int J Cardiol*, vol. 106, no. 1, pp. 47–51, Jan. 2006.
- [93] J Daugirdas, P. Blake, and I. TS, *Handbook of Dialysis*, 4th ed. Boston: Wolters Kluwer/Lippincott Williams & Wilkins, 2006, p. 774.
- [94] W. Zareba, P. Maison-Blanche, E. Locati, S. Dorbala, and J Steinberg, “Signal averaging of the P wave,” in *Noninvasive Electrocardiology in Clinical Practice*, 2001, pp. 31–48.
- [95] Y. Abe, M. Fukunami, T. Yamada, M. Ohmori, T. Shimonagata, K. Kumagai, J Kim, S. Sanada, M. Hori, and N. Hoki, “Prediction of Transition to Chronic Atrial Fibrillation in Patients With Paroxysmal Atrial Fibrillation by Signal- Averaged Electrocardiography: A Prospective Study,” *Circulation*, vol. 96, no. 8, pp. 2612–2616, Oct. 1997.
- [96] J S. Steinberg, S. Zelenkofske, S. C. Wong, M. Gelernt, R. Sciacca, and E. Menchavez, “Value of the P-wave signal-averaged ECG for predicting atrial fibrillation after cardiac surgery,” *Circulation*, vol. 88, no. 6, pp. 2618–2622, Dec. 1993.
- [97] N. Hayashida, T. Shojima, Y. Yokokura, H. Hori, K. Yoshikawa, H. Tomoeda, and S. Aoyagi, “P-wave signal-averaged electrocardiogram for predicting atrial arrhythmia after cardiac surgery” *Ann Thorac Surg*, vol. 79, no. 3, pp. 859–64, Mar. 2005.
- [98] D. Cicek, A. Camsari, H. Pekdemir, A. Kiykim, N. Akkus, K. Sezer, and E. Diker, “Predictive Value of P-Wave Signal-Averaged Electrocardiogram for Atrial Fibrillation in

- Acute Myocardial Infarction,” *Ann Noninvasive Electrocardiol*, vol. 8, no. 3, pp. 233–237, Jul. 2003.
- [99] P. J STAFFORD, K. KAMALVAND, K. TAN, R. VINCENT, and N. SULKE, “Prediction of Maintenance of Sinus Rhythm after Cardioversion of Atrial Fibrillation by Analysis of Serial Signal-Averaged P Waves,” *Pacing Clin Electrophysiol*, vol. 21, no. 7, pp. 1387–1395, Jul. 1998.
- [100] T. Yamada, “Dispersion of signal-averaged P wave duration on precordial body surface in patients with paroxysmal atrial fibrillation,” *Eur Heart J*, vol. 20, no. 3, pp. 211–220, Feb. 1999.
- [101] Z. Szabo, “Effects of haemodialysis on maximum P wave duration and P wave dispersion,” *Nephrol Dial Transplant*, vol. 17, no. 9, pp. 1634–1638, Sep. 2002.
- [102] U. K. Tezcan, B. Amasyali, I. Can, K. Aytemir, S. Kose, I. Yavuz, H. Kursaklioglu, E. Isik, E. Demirtas, and A. Oto, “Increased P Wave Dispersion and Maximum P Wave Duration after Hemodialysis,” *Ann Noninvasive Electrocardiol*, vol. 9, no. 1, pp. 34–38, Jan. 2004.
- [103] T. Ozcan, M. Horoz, G. Genctoy, B. Uyar, A. Camsari, and A. A. Kiykim, “The influence of hemodialysis on P-wave signal-averaged electrocardiogram findings” *Artif Organs*, vol. 31, no. 8, pp. 612–6, Aug. 2007.
- [104] A. J Jaroszyński, A. Głowniak, T. Sodolski, W. Zaluska, T. Widomska-Czekajska, and A. Ksiazek, “Effect of haemodialysis on signal-averaged electrocardiogram P-wave parameters” *Nephrol Dial Transplant*, vol. 21, no. 2, pp. 425–30, Feb. 2006.
- [105] A. Drighil, J E. Madias, A. Yazidi, M. Bennani, A. Bennis, B. Ramdan, and A. Tahiri, “P-wave and QRS complex measurements in patients undergoing hemodialysis” *J Electrocardiol*, vol. 41, no. 1, pp. 60.e1–7, Jan. .
- [106] B. Ozben, A. Toprak, M. Koc, M. Sumerkan, A. M. Tanrikulu, N. Papila-Topal, U. S. Kefeli, A. A. Cincin, O. Baykan, and A. S. Fak, “P wave dispersion increases during hemodialysis sessions” *Nephron Clin Pract*, vol. 112, no. 3, pp. c171–6, Jan. 2009.
- [107] K. Shimada, T. Tomita, Y. Kamijo, M. Higuchi, K. Ito, Y. Koizumi, K. Yamamoto, K. Aizawa, M. Koshikawa, H. Kasai, A. Izawa, Y. Miyashita, S. Kumazaki, J Koyama, and U. Ikeda, “Hemodialysis-Induced P-Wave Signal-Averaged Electrocardiogram Alterations Are Indicative of Vulnerability to Atrial Arrhythmias,” *Circ J*, vol. 76, no. 3, pp. 612–617, Feb. 2012.
- [108] J E. Madias, “P waves in patients with changing edematous states: implications on interpreting repeat P wave measurements in patients developing anasarca or undergoing hemodialysis” *Pacing Clin Electrophysiol*, vol. 27, no. 6 Pt 1, pp. 749–56, Jun. 2004.
- [109] J E. Madias, “Increases in P-wave duration and dispersion after hemodialysis are totally (or partially) due to the procedure-induced alleviation of the body fluid overload: a hypothesis with strong experimental support” *Ann Noninvasive Electrocardiol*, vol. 10, no. 2, pp. 129–33, Apr. 2005.
- [110] P. Fabbrini, E. Sironi, F. Pieruzzi, E. Galbiati, M. Viganò, and A. Stella, “P wave duration, atrial dimension and atrial fibrillation in hemodialysis patients,” *Nephrol Dial Transplant*, vol. 27, no. S2, p. 244, 2012.
- [111] R. Hainsworth, “Reflexes from the heart,” *Physiol Rev*, vol. 71, no. 3 , pp. 617–658, Jul. 1991.

- [112] B. F. Palmer and W. L. Henrich, “Recent advances in the prevention and management of intradialytic hypotension” *J Am Soc Nephrol*, vol. 19, no. 1, pp. 8–11, Jan. 2008.
- [113] M. G. W. BARNAS, W. H. BOER, and H. A. KOOMANS, “Hemodynamic Patterns and Spectral Analysis of Heart Rate Variability during Dialysis Hypotension,” *J Am Soc Nephrol*, vol. 10, no. 12, pp. 2577–2584, Dec. 1999.
- [114] S. Genovesi, R. Rivera, P. Fabbrini, C. Dossi, G. Bonforte, L. Mircoli, A. U. Ferrari, A. Stella, and M. Stramba-Badiale, “Dynamic QT interval analysis in uraemic patients receiving chronic haemodialysis” *J Hypertens*, vol. 21, no. 10, pp. 1921–6, Oct. 2003.
- [115] S. Genovesi, O. Bracchi, P. Fabbrini, E. Luisetto, M. R. Viganò, D. Lucini, M. Malacarne, A. Stella, and M. Pagani, “Differences in heart rate variability during haemodialysis and haemofiltration” *Nephrol Dial Transplant*, vol. 22, no. 8, pp. 2256–62, Aug. 2007.
- [116] S. Cavalcanti, S. Severi, L. Chiari, G. Avanzolini, G. Enzmann, G. Bianco, and G. Panzetta, “Autonomic nervous function during haemodialysis assessed by spectral analysis of heart-rate variability” *Clin Sci (Lond)*, vol. 92, no. 4, pp. 351–9, Apr. 1997.
- [117] D. Rubinger, R. Backenroth, and D. Sapoznikov, “Sympathetic activation and baroreflex function during intradialytic hypertensive episodes” *PLoS One*, vol. 7, no. 5, p. e36943, Jan. 2012.
- [118] D. Rubinger, N. Revis, A. Pollak, M. H. Luria, and D. Sapoznikov, “Predictors of haemodynamic instability and heart rate variability during haemodialysis” *Nephrol Dial Transplant*, vol. 19, no. 8, pp. 2053–60, Aug. 2004.
- [119] B. A. Kingwell, J. M. Thompson, D. M. Kaye, G. A. McPherson, G. L. Jennings, and M. D. Esler, “Heart rate spectral analysis, cardiac norepinephrine spillover, and muscle sympathetic nerve activity during human sympathetic nervous activation and failure,” *Circulation*, vol. 90, no. 1, pp. 234–240, Jul. 1994.
- [120] M. S. Houle and G. E. Billman, “Low-frequency component of the heart rate variability spectrum: a poor marker of sympathetic activity” *Am J Physiol*, vol. 276, no. 1 Pt 2, pp. H215–23, Jan. 1999.
- [121] M. Pagani, F. Lombardi, S. Guzzetti, O. Rimoldi, R. Furlan, P. Pizzinelli, G. Sandrone, G. Malfatto, S. Dell’Orto, and E. Piccaluga, “Power spectral analysis of heart rate and arterial pressure variabilities as a marker of sympatho-vagal interaction in man and conscious dog,” *Circ Res*, vol. 59, no. 2, pp. 178–193, Aug. 1986.
- [122] A. Malliani, M. Pagani, F. Lombardi, and S. Cerutti, “Cardiovascular neural regulation explored in the frequency domain,” *Circulation*, vol. 84, no. 2, pp. 482–492, Aug. 1991.
- [123] A. L. Mark, “The Bezold-Jarisch reflex revisited: Clinical implications of inhibitory reflexes originating in the heart,” *J Am Coll Cardiol*, vol. 1, no. 1, pp. 90–102, Jan. 1983.
- [124] “Gruppo Emodialisi e Patologie Cardiovascolari. Multicentre, cross-sectional study of ventricular arrhythmias in chronically haemodialysed patients,” *Lancet*, vol. 2, no. 8606, pp. 305–9, Aug. 1988.
- [125] S. Abe, M. Yoshizawa, N. Nakanishi, T. Yazawa, K. Yokota, M. Honda, and G. Sloman, “Electrocardiographic abnormalities in patients receiving hemodialysis,” *Am Heart J*, vol. 131, no. 6, pp. 1137–1144, Jun. 1996.
- [126] A. Santoro, E. Mancini, G. London, L. Mercadal, H. Fessy, B. Perrone, L. Cagnoli, E. Grandi, S. Severi, and S. Cavalcanti, “Patients with complex arrhythmias during and after

- haemodialysis suffer from different regimens of potassium removal” *Nephrol Dial Transplant*, vol. 23, no. 4, pp. 1415–21, Apr. 2008.
- [127] T. Lewis, A. Rury, and H. Bulger, “Observation upon atrial flutter and fibrillation.VI. Refractory period and rate of propagation in the auricle: their relation to block in the auricular walls and to flutter,” *Heart*, vol. 8, pp. 84–134, 1921.
- [128] H. E. Hoff and L. A. Geddes, “Cholinergic Factor in Auricular Fibrillation,” *J Appl Physiol*, vol. 8, no. 2, pp. 177–192, Sep. 1955.
- [129] J Armour, J Ardell, and W. Randall, “Changing perspectives concerning neural control of the heart,” in *Neurocardiology*, New York: Oxford University Press, 1994.
- [130] J A. Armour, D. A. Murphy, B. X. Yuan, S. Macdonald, and D. A. Hopkins, “Gross and microscopic anatomy of the human intrinsic cardiac nervous system” *Anat Rec*, vol. 247, no. 2, pp. 289–98, Feb. 1997.
- [131] B. J Scherlag, W. Yamanashi, U. Patel, R. Lazzara, and W. M. Jackman, “Autonomically induced conversion of pulmonary vein focal firing into atrial fibrillation” *J Am Coll Cardiol*, vol. 45, no. 11, pp. 1878–86, Jun. 2005.
- [132] J Zhou, B. J Scherlag, J Edwards, W. M. Jackman, R. Lazzara, and S. S. Po, “Gradients of atrial refractoriness and inducibility of atrial fibrillation due to stimulation of ganglionated plexi” *J Cardiovasc Electrophysiol*, vol. 18, no. 1, pp. 83–90, Jan. 2007.
- [133] O. F. Sharifov, V. V Fedorov, G. G. Beloshapko, A. V Glukhov, A. V Yushmanova, and L. V Rosenshtraukh, “Roles of adrenergic and cholinergic stimulation in spontaneous atrial fibrillation in dogs” *J Am Coll Cardiol*, vol. 43, no. 3, pp. 483–90, Feb. 2004.
- [134] S. S. Po, B. J Scherlag, W. S. Yamanashi, J Edwards, J Zhou, R. Wu, N. Geng, R. Lazzara, and W. M. Jackman, “Experimental model for paroxysmal atrial fibrillation arising at the pulmonary vein-atrial junctions” *Heart Rhythm*, vol. 3, no. 2, pp. 201–8, Feb. 2006.
- [135] B. J Scherlag, Y.-L. Hou, J Lin, Z. Lu, S. Zacharias, T. Dasari, G. Niu, M. Ghias, E. Patterson, W. M. Jackman, R. Lazzara, and S. S. Po, “An acute model for atrial fibrillation arising from a peripheral atrial site: evidence for primary and secondary triggers” *J Cardiovasc Electrophysiol*, vol. 19, no. 5, pp. 519–27, May 2008.
- [136] Y. Hou, B. J Scherlag, J Lin, Y. Zhang, Z. Lu, K. Truong, E. Patterson, R. Lazzara, W. M. Jackman, and S. S. Po, “Ganglionated plexi modulate extrinsic cardiac autonomic nerve input: effects on sinus rate, atrioventricular conduction, refractoriness, and inducibility of atrial fibrillation” *J Am Coll Cardiol*, vol. 50, no. 1, pp. 61–8, Jul. 2007.
- [137] K. Lemola, D. Chartier, Y.-H. Yeh, M. Dubuc, R. Cartier, A. Armour, M. Ting, M. Sakabe, A. Shiroshita-Takeshita, P. Comtois, and S. Nattel, “Pulmonary vein region ablation in experimental vagal atrial fibrillation: role of pulmonary veins versus autonomic ganglia” *Circulation*, vol. 117, no. 4, pp. 470–7, Jan. 2008.
- [138] Z. Lu, B. J Scherlag, J Lin, G. Niu, K.-M. Fung, L. Zhao, M. Ghias, W. M. Jackman, R. Lazzara, H. Jiang, and S. S. Po, “Atrial fibrillation begets atrial fibrillation: autonomic mechanism for atrial electrical remodeling induced by short-term rapid atrial pacing” *Circ Arrhythm Electrophysiol*, vol. 1, no. 3, pp. 184–92, Aug. 2008.
- [139] E. Patterson, S. S. Po, B. J Scherlag, and R. Lazzara, “Triggered firing in pulmonary veins initiated by in vitro autonomic nerve stimulation” *Heart Rhythm*, vol. 2, no. 6, pp. 624–31, Jun. 2005.

- [140] Z. Lu, B. J. Scherlag, J. Lin, L. Yu, J-H. Guo, G. Niu, W. M. Jackman, R. Lazzara, H. Jiang, and S. S. Po, “Autonomic mechanism for initiation of rapid firing from atria and pulmonary veins: evidence by ablation of ganglionated plexi” *Cardiovasc Res*, vol. 84, no. 2, pp. 245–52, Nov. 2009.
- [141] M. C. E. F. Wijffels, R. Dorland, and M. A. Allesie, “Pharmacologic Cardioversion of Chronic Atrial Fibrillation in the Goat by Class IA, IC, and III Drugs” *J Cardiovasc Electrophysiol*, vol. 10, no. 2, pp. 178–193, Feb. 1999.
- [142] A. Vincenti, R. Brambilla, M. G. Fumagalli, R. Merola, and S. Pedretti, “Onset mechanism of paroxysmal atrial fibrillation detected by ambulatory Holter monitoring” *Europace*, vol. 8, no. 3, pp. 204–10, Mar. 2006.

SECTION III

Computational Modelling of Human Hypertrophic Cardiomyopathy

CHAPTER 7

Pro-Arrhythmic Mechanisms and Potential Therapeutic Targets in Human Hypertrophic Cardiomyopathy

The content of this chapter was partly published in:

Passini E, Rodriguez B, Mincholé A, Coppini R, Cerbai E, Severi S, Bueno-Orovio A.

Late Sodium Current Inhibition Counteracts Pro-arrhythmic Mechanisms in Human Hypertrophic Cardiomyopathy.

Computing in Cardiology, vol. 41, pp. 861–864, 2014

Abstract

Hypertrophic cardiomyopathy (HCM) is a genetic disorder characterised by unexplained thickening of the left ventricle, including the septum, and myofibre disarray, and is the main cause of sudden cardiac death in young athletes. Usually asymptomatic, it leads to diastolic dysfunction and increased arrhythmic risk.

However, due to the limited understanding of the cellular mechanisms underlying the disease, the causes are still unclear and a specific pharmacological treatment is lacking. Potential pro-arrhythmic mechanisms may include increased temporal and spatial variability in action potential duration (APD) as well as repolarisation abnormalities, such as early after-depolarisations (EADs).

Recently, new experimental data assessed the electrophysiological profile of human HCM, compared with control (CTRL): diseased cardiomyocytes are characterised by prolonged action potential (AP) and Ca^{2+} -transient (CaT), mostly related to an increase of Late Na^+ current (I_{NaL}) and L-type Ca^{2+} current (I_{CaL}), together with a decrease of K^+ repolarising currents, and also changes in the Ca^{2+} subsystem, i.e. decrease in SERCA pump Ca^{2+} uptake (J_{up}) and ryanodine receptors Ca^{2+} release (J_{rel}), and increase of Na^+/Ca^+ exchanger current (I_{NCX}).

The aim of this study has been to investigate the ionic mechanisms underlying the electrical remodelling occurring in HCM, in order to identify potential therapeutic targets, by using a new computational method: population of models.

Compared to traditional modelling techniques, in which a single AP model is used to reproduce the average cellular behaviour, the population of models approach accounts for inter- and intra- subjects variability. Therefore, it is particularly appropriate to study HCM, since biological variability seems to play an important role in this disease.

Based on this experimental dataset, we constructed two populations of human cardiac AP models, to reproduce CTRL and HCM phenotypes respectively, and to account for biological variability.

We investigated in silico the contribution of each ionic mechanism to the electrophysiological phenotype of the disease, by evaluating AP and CaT biomarkers, when adding/restoring each remodelling elements, one at a time, starting respectively from the CTRL/HCM population.

The simulated HCM phenotype was in agreement with the experimental observations, showing prolonged AP and CaT compared to CTRL, together with an increase in their variability. In addition, simulation results show that HCM promotes EADs (16%), especially in models characterised by very low I_{Kr} , together with high I_{NaL} , I_{CaL} and I_{NCX} .

Both selective I_{NaL} and I_{NCX} block partially reversed the HCM phenotype, and reduced EADs occurrence. Their simultaneous block turned out to be even more effective, suggesting the combination of both treatments as a potential anti-arrhythmic strategy in HCM.

INTRODUCTION

Hypertrophic Cardiomyopathy

Hypertrophic cardiomyopathy (HCM) is the most common monogenic cardiac disorder and the main cause of sudden cardiac death in young athletes [1], with a reported prevalence of 1 in 500 worldwide [2].

Usually asymptomatic, it is characterised by an unexplained thickening (hypertrophy) of the left ventricle, with predominant involvement of the inter-ventricular septum, and sometime also of the right ventricle; other hallmark features of the disease are myocyte disarray and fibrosis (Figure 7.1).

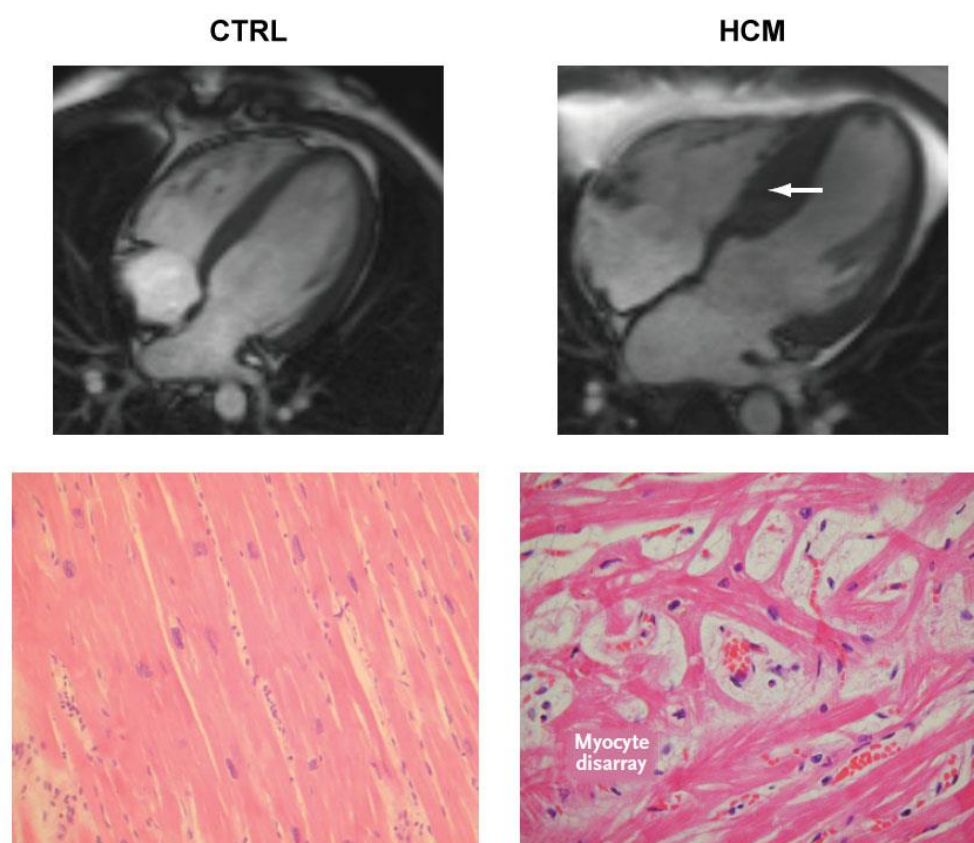


Figure 7.1: Alterations in hypertrophic cardiomyopathy (HCM, right) compared to non-diseased control (CTRL, left): HCM promotes disarray and fibrosis, often resulting in hypertrophy, especially in the left ventricle and in the inter-ventricular septum (white arrow), as shown on the cardiac magnetic resonance images (modified from [3]).

Hypertrophic cardiomyopathy was defined a “disease of the sarcomere” more than 20 years ago [4], when the first three disease genes to be identified were found to encode components of the contractile apparatus of heart muscle. Mutations in

nine genes encoding sarcomeric proteins have now been convincingly shown to cause HCM. These mutations generally increase myofilament activation and result in myocyte hyper-contraction and excessive energy use. Alterations in myocardial energetics and in Ca^{2+} -handling, combined with stimulation of signalling pathways, promote myocyte growth with aberrant tissue architecture (i.e. myofibrillar disarray and myocardial fibrosis) [3]. In addition, the changes in Ca^{2+} -handling confer a predisposition to arrhythmias [5] and may be implicated in diastolic dysfunction, another trait of this disease.

At least two mechanisms explain how sarcomeric mutations alter Ca^{2+} balance [3]. First, mutations affecting the thin-filament regulatory proteins tropomyosin, troponin T, and troponin I all enhance calcium sensitivity by increasing the affinity of troponin C for calcium [6]: since troponin is the principal dynamic Ca^{2+} buffer in the sarcoplasm the increased affinity should elevate Ca^{2+} levels during diastole. Second, sarcomeric mutations increase the energy requirements of myosin ATPase. Since the cross-bridge cycle, which generates the contractile force of the myocyte, accounts for about 70% of the cardiomyocyte ATP consumption, contractile inefficiency could compromise the cell energetics [7]. This would be expected to compromise in turn the energy-requiring transporters, e.g. Na^+/K^+ and SERCA pumps, thus affecting intracellular concentrations (mainly Na^+ and Ca^{2+}).

More recently, new experimental data assessed the electrophysiological profile of human HCM compared with non-diseased controls (CTRL) [8], by highlighting the subtle changes occurring at the molecular and cellular levels which had received limited attention before, and are likely to play a crucial role in arrhythmias onset.

Diseased cardiomyocytes are characterised by prolonged action potential (AP) and Ca^{2+} transient (CaT), mostly depending on the increase of Late Na^+ current (I_{NaL}) and L-type Ca^{2+} current (I_{CaL}), together with a decrease of K^+ repolarising currents. $\text{Na}^+/\text{Ca}^{2+}$ exchanger (NCX) activity is enhanced, while cellular Ca^{2+} -handling is impaired, i.e. SERCA uptake and ryanodine receptors (RyRs) release are reduced. AP prolongation leads to an increased occurrence of early after-depolarisations (EADs), i.e. spontaneous depolarisation during the plateau phase, often associated with re-opening of Na^+ or Ca^{2+} channels, and considered a primary electrophysiological trigger for ventricular arrhythmias [9]. Also, delayed after-depolarisations (DADs), occurring during the diastolic period and related to

spontaneous Ca^{2+} release, are more frequent in HCM than in CTRL, suggesting additional arrhythmogenic mechanisms.

Intracellular Ca^{2+} concentration during diastole is significantly increased in HCM, leading in turn to an enhanced Ca^{2+} /calmodulin kinase II (CaMKII) activity and phosphorylation of its downstream targets. By slowing down I_{CaL} inactivation and increasing I_{NaL} amplitude, CaMKII contributes to APD prolongation and related arrhythmias. The enhanced I_{NaL} is responsible for intracellular Na^+ overload, which favours reverse over forward NCX mode, contributing to cytosolic Ca^{2+} overload and further promoting CaMKII activation, thus setting up a vicious circle [8]. Finally, an increased background Na^+ current (I_{Nab}) may contribute as well to intracellular Na^+ and Ca^{2+} overload, as suggested for heart failure [10].

Despite its epidemiological relevance, HCM is largely an orphan condition because it still lacks a disease-specific pharmacological treatment [11, 12], and this is partly due to the limited understanding of the cellular mechanisms involved. Therapeutic targets in HCM are likely to be most effective when directed to the molecular predeterminants of the HCM phenotype. As an example, the potential implications of I_{NaL} inhibition have been already shown: ranolazine at therapeutic concentrations partially reverses the HCM-related cellular abnormalities via I_{NaL} inhibition, with negligible effects in CTRL [8]. Since many other ionic currents and mechanisms are affected by this disease, a more detailed understanding of the cellular processes underlying the HCM phenotype is definitely needed to highlight other potential therapeutic targets and strategies.

Computational cardiac modelling constitutes a valuable tool in this context: by correlating the ion channel remodelling measured in human HCM cells with the electrophysiological phenotype of the disease, *in silico* simulations may help to understand the ionic mechanisms involved at the cellular level and to identify possible therapeutic targets to reduce the arrhythmic risk in HCM patients. In addition, biological variability is very high in HCM [8], and it is likely to play a major role in characterising the individual response to drug treatment: therefore, the population of models approach (POFs) is particularly appropriate to investigate this disease, since it accounts for variability, usually neglected in the traditional modelling techniques.

Population of Models

The population of models (POMs) approach, recently developed by the University of Oxford (UK) [13–16], is a novel methodology in computational cardiac AP modelling. Instead of a single AP model, representative of the average cell behaviour, simulations are performed in thousands of models at the same time (a population, indeed), all generated by varying some of the model parameters around their nominal values. Each model represents a different cell and the cell-to-cell differences account for both inter- and intra- subject variability.

As an example, Figure 7.2 shows different experimental APs (pink traces) all recorded from rabbit purkinje cells. The biological variability, well represented here, is neglected when using a single Purkinje AP model to reproduce these experimental data, e.g. the Corrias-Giles-Rodriguez [17] (left panel, black trace), while a population of models (right panel, black traces) allows for a better coverage of the experimental dataset.

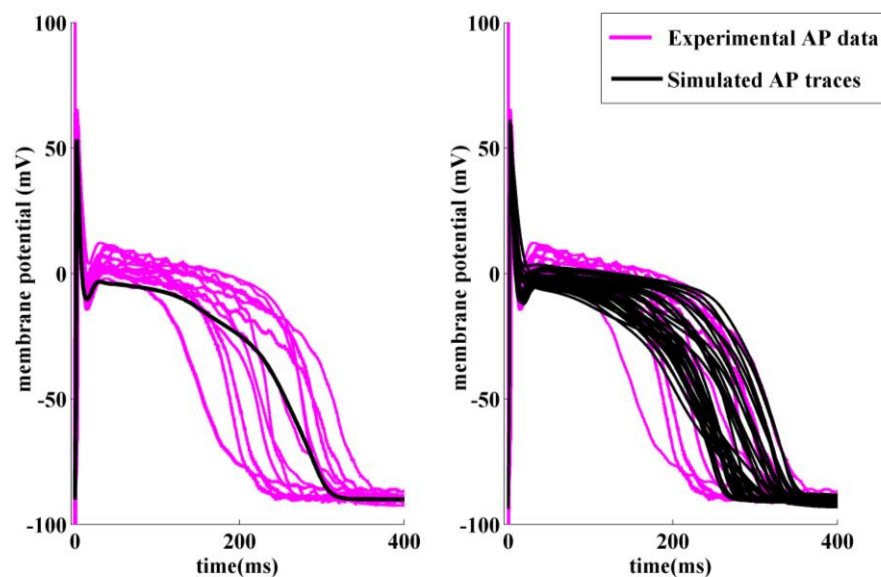


Figure 7.2: Experimental AP recordings (pink traces, both panels) from rabbit purkinje cells (data by Janssen Pharmaceutica). When considering only a single AP model (black trace, left panel), the biological variability is completely neglected, while the population of models (black traces, right panel) is able to better reproduce the experimental dataset (modified from [14]).

All the models in the population share the same differential equations, but each of them has a different parameter set. Depending on the purpose of the study, the number of generated models, the parameters to be varied, the scaling factors to

apply to the nominal parameter values and the sampling of the parameter space, may be different. More details about the POMs approach are given in Appendix B1.

Aims

The aim of this work has been to investigate the electrophysiological phenotype of human HCM using the population of models approach, to account for the biological variability. By integrating experimental data and computer simulations, we aimed to improve the understanding of the ionic mechanisms underlying the electrical remodelling occurring in this disease, and also their individual contribution to the disease-related arrhythmogenicity. The ultimate goal was therefore to identify possible therapeutic targets and to test in simulations the potential anti-arrhythmic effects of their selective/combined block.

METHODS

Experimental Data

All the experimental data used in this work were collected by our collaborators from the University of Florence (Coppini et al. [8]), using human cardiomyocytes from n=26 HCM patients, compared with n=8 non-failing non-hypertrophic controls (CTRL). HCM cardiomyocytes were hypertrophic, as indicated by an increased cell volume and capacitance compared with CTRL.

AP and CaT recordings

Single cell patch-clamp measurements and intracellular Ca^{2+} studies produced an extensive set of AP and CaT biomarkers: AP duration (APD), computed at 20%, 50% and 90% of repolarisation (APD_{20} , APD_{50} and APD_{90} , respectively), AP amplitude (AP_{amp}), mean upstroke velocity ($\text{dV/dt}_{\text{MEAN}}$, computed as the mean dV/dt value during the upstroke phase), resting membrane potential (RMP), CaT duration (CaTD), computed at 50% and 90% of CaT decay (CaTD_{50} and CaTD_{90}), CaT time to peak (CaT_{tpp}), CaT amplitude (CaT_{amp}) and diastolic Ca^{2+} concentration ($[\text{Ca}^{2+}]_i$). A summary of all the AP and CaT biomarkers considered in this study is shown in Figure 7.3 and Figure 7.4. In addition, both early and delayed after-depolarisations frequencies were monitored in HCM and CTRL.

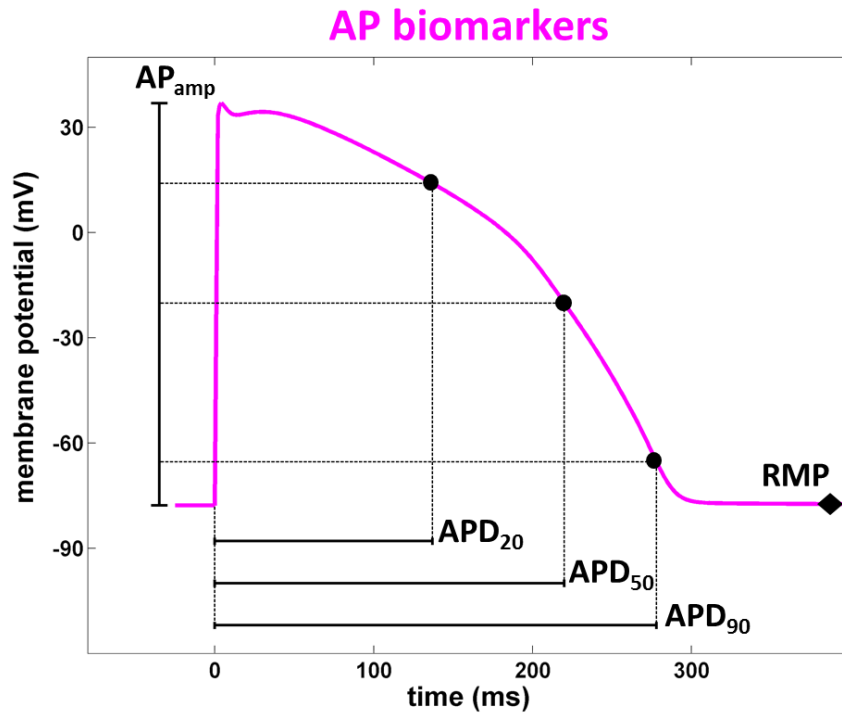


Figure 7.3: Summary and description of the AP biomarkers considered in this study: AP duration (APD), computed at 20%, 50% and 90% of repolarisation (APD_{20} , APD_{50} and APD_{90} , respectively), AP amplitude (AP_{amp}), mean upstroke velocity (dV/dt_{MEAN} , computed as the mean dV/dt value during the upstroke phase), mean resting potential (RMP).

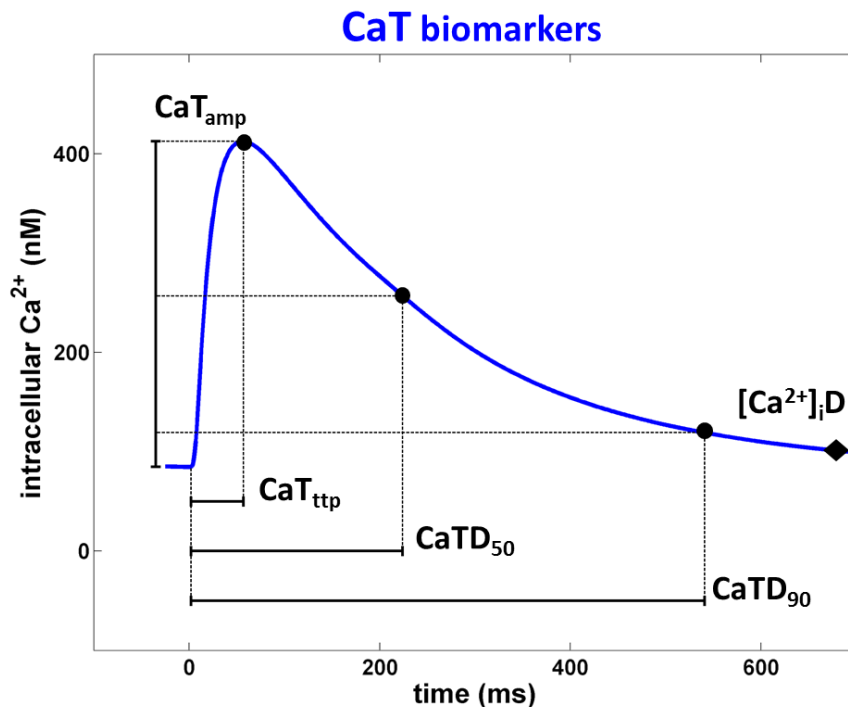


Figure 7.4: Summary and description of the CaT biomarkers considered in this study: CaT duration (CaTD), computed at 50% and 90% of CaT decay ($CaTD_{50}$ and $CaTD_{90}$), CaT time to peak (CaT_{ttp}), CaT amplitude (CaT_{amp}) and diastolic Ca^{2+} concentration ($[Ca^{2+}]_iD$).

Experimental data have been acquired at three different stimulation frequencies (0.2, 0.5 and 1 Hz) and results were consistent. In this study, only experiments recorded at 1 Hz have been preliminary considered, because low frequencies simulations are computationally more expensive.

Voltage-Clamp experiments

Voltage clamp experiments were also performed for different ionic currents: late component of Na^+ current (I_{NaL}), L-type Ca^{2+} current (I_{CaL}), transient outward K^+ current (I_{to}) and in the inward rectifier K^+ current (I_{K1}).

Protein and mRNA expression

Protein and mRNA expressions were analysed, in order to quantify the changes occurring in the main ionic current subunits. In addition to all the currents already considered for Voltage-Clamp (I_{Na} , I_{CaL} , I_{to} and I_{K1}), data have been acquired for the rapid and slow delayed rectifier K^+ currents (I_{Kr} and I_{Ks}), $\text{Na}^+/\text{Ca}^{2+}$ exchanger (NCX), SERCA pump and ryanodine receptors (RyRs).

I_{NaL} inhibition

The effect of 10 μM of Ranolazine, a selective I_{NaL} inhibitor [18], have been evaluated to assess the role of this current, highly increased in HCM compared to CTRL. All the AP and CaT biomarkers have been measured 3 min after drug exposure and repeated 5 min after washout, both for HCM and CTRL cells, and together with I_{NaL} Voltage-Clamp recordings.

Baseline Model

As baseline to build the population, we used the endocardial version of the human ventricular AP model published by O'Hara-Rudy in 2011 (ORd [19]): it is the most recent human ventricular AP model and it has been developed and extensively validated on experimental data acquired in small tissue preparations from more than 100 undiseased human hearts.

A schematic representation of this model, showing all its ionic currents, pumps/exchangers, buffers, fluxes and compartments is shown in Figure 7.5.

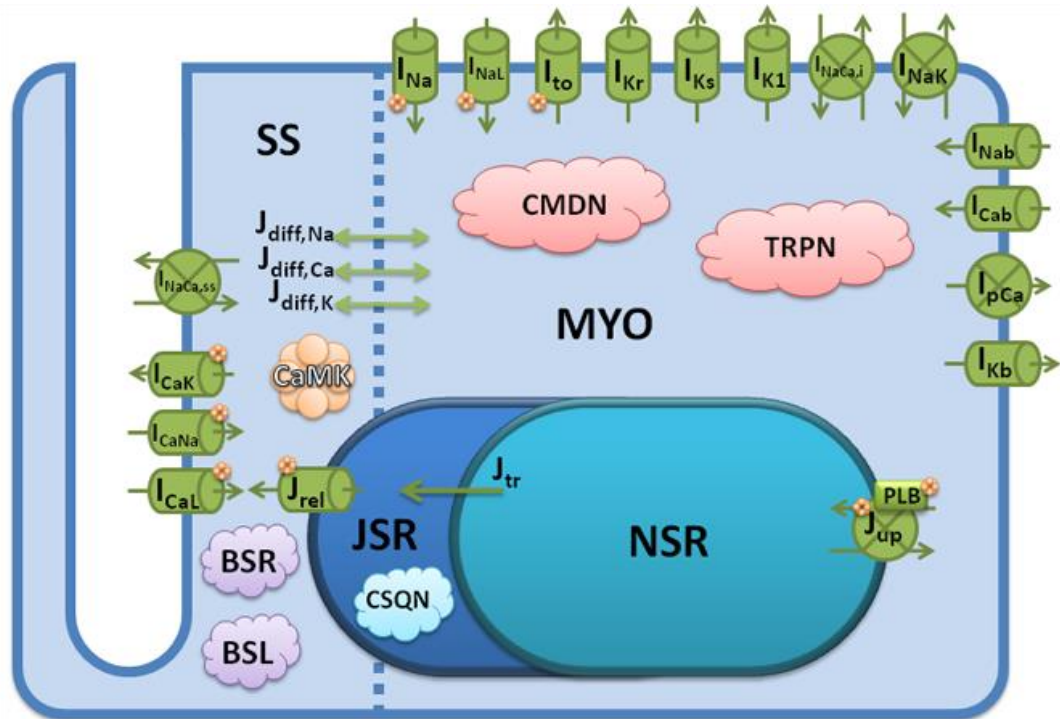


Figure 7.5: Schematic representation of the ORd model, showing all its ionic currents, pumps/exchangers, buffers, fluxes and compartments [19].

However, a few changes have been required to the original model, in order to better reproduce the experimental CTRL data considered in this study: the maximal conductance of the transient outward K^+ current (I_{to}) has been increased 2.5 times, based on the corresponding experimental I_{to} I-V curve; intra- and extra-cellular ionic concentrations have been set as in the AP experimental recordings; since the resting membrane potential in the experiments was about 10 mV higher than the one of the ORd model, and the K^+ equilibrium potential was different from the one resulting from the Nernst equation, using the experimental K^+ concentrations, we fixed the K^+ equilibrium potential to the one measured for the I_{K1} I-V curve.

In addition, the fast Na^+ current (I_{Na}) inactivation gates have been modified, to fix a well-known problem concerning the I_{Na} in the ORd model, which prevent propagation in 2D or 3D tissue when considering hyperkalaemia.

Finally, the current stimulus duration has been extended to 1 ms, and the current stimulus amplitude has been set to twice the AP threshold, to allow a larger integration step to solve the model ODEs. All the changes to the original ORd model mentioned above are discussed in details in Appendix B2.

The CTRL population

An initial population of 30,000 models was developed, starting from the baseline model and varying a total of 11 parameters, including the maximal conductances of the main ionic currents/pumps/exchangers characterising the human ventricular AP.

These parameters were probabilistically sampled in the [0-200%] range, with respect to their baseline parameter values, using the Latin Hypercube Sampling (LHS) [20]. The list of all the parameters which have been varied, together with their original value in the ORd model, is shown in Table 7.1.

Table 7.1: List and description of all the parameters scaled to build the CTRL population:

#	Parameter	Description	Original Value
1	g_{Kr}	max conductance of rapid delayed rectifier K^+ current (I_{Kr})	0.046 mS/ μ F
2	g_{Ks}	max conductance of slow delayed rectifier K^+ current (I_{Ks})	0.0034 mS/ μ F
3	g_{K1}	max conductance of inward rectifier K^+ current (I_{K1})	0.1908 mS/ μ F
4	g_{to}	max conductance of transient outward K^+ current (I_{to})	0.02 mS/ μ F
5	P_{Ca}	permeability of L-type Ca^{2+} channel (I_{CaL} current)	0.0001 1/s
6	g_{NaL}	max conductance of Late Na^+ current (I_{NaL})	0.0075 mS/ μ F
7	g_{Na}	max conductance Fast Na^+ current (I_{Na})	75 mS/ μ F
8	g_{NCX}	max current of Na^+/Ca^{2+} exchanger (I_{NCX})	0.0008 μ A/ μ F
9	P_{NaK}	max conductance of Na^+/K^+ pump (I_{NaK})	30 mS/ μ F
10	$SF_{J_{rel}}$	scaling factor for Ca^{2+} release, via ryanodine receptors (J_{rel})	1 nu *
11	$SF_{J_{up}}$	scaling factor for Ca^{2+} uptake, via SERCA pump (J_{up})	1 nu *

* In the ORd model, J_{rel} and J_{up} do not have any parameter to represent their max conductances. Therefore, $SF_{J_{rel}}$ and $SF_{J_{up}}$ were added to the original formulations, to scale both currents in the selected range, and to allow these currents to vary in the CTRL population models.

Hereafter, all the variables listed above will be referred to using their corresponding scaling factors, i.e. $SF_{I_{Kr}}$, $SF_{I_{Ks}}$, $SF_{I_{K1}}$, $SF_{I_{to}}$, $SF_{I_{CaL}}$, $SF_{I_{NaL}}$, $SF_{I_{Na}}$, $SF_{I_{NCX}}$, $SF_{I_{NaK}}$, $SF_{J_{rel}}$ and $SF_{J_{up}}$. All these variables will be ranging from 0 to 2, according to the [0-200%] range used to build the CTRL population.

Population results will be often presented using boxplots of these scaling factors, in order to highlight the currents whose densities are particularly high/low with respect to the baseline model (in which all the scaling factors are equal to one). On each box, the central mark is the median, the edges of the box are the 25th and 75th percentiles, the whiskers extend to the most extreme data points not considered outliers, and outliers are plotted individually. To compute statistical significance, two-sample t-test (function *ttest2* in Matlab) has been used for samples comparison.

When considering a special subgroup of models (e.g. all the models showing EADs), a scaling factor distributed only in a small portion of the whole [0-200%] range may imply an important role played by its corresponding current in that special subgroup. In the initial population, all the scaling factors have a similar distribution, and they cover the whole range from 0 to 2, where 1 indicates that the corresponding ionic current is unaltered from the baseline model, while big/small scaling factors correspond to its up/down regulation. Therefore, for the initial population, all the scaling factor boxplots will be equally distributed (Figure 7.6).

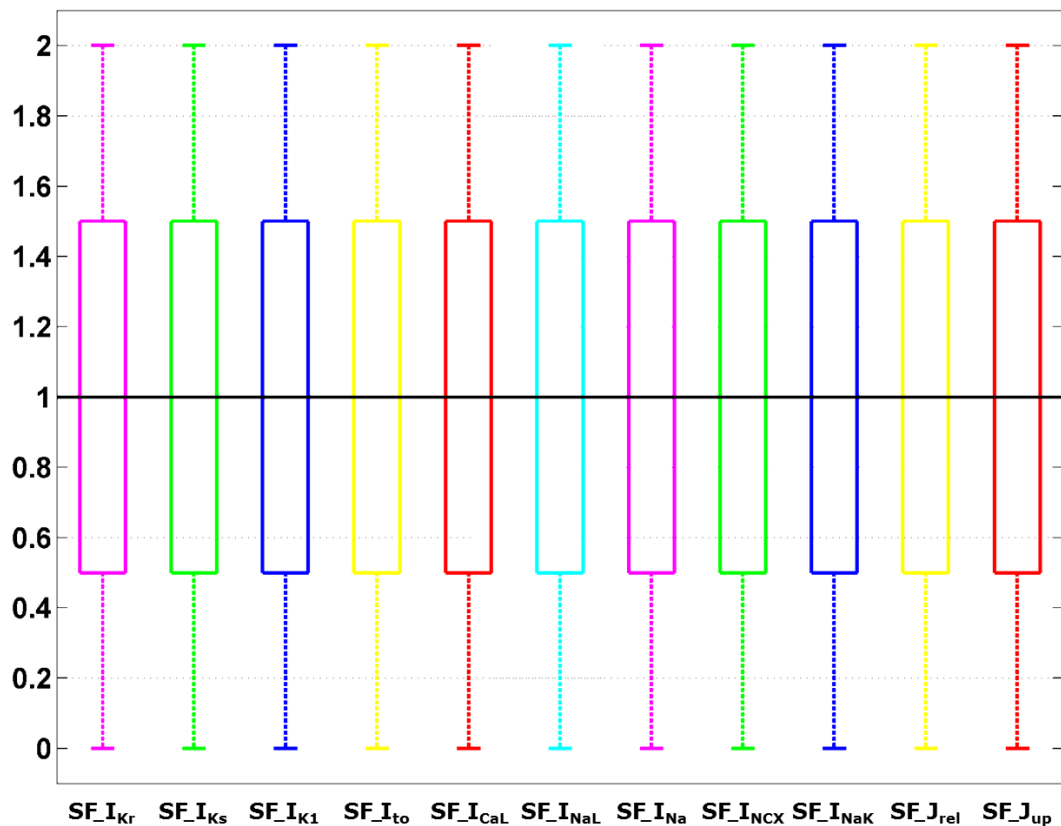


Figure 7.6: Scaling factors distribution in the initial population of 30,000 models. Parameters have been probabilistically sampled with LHS in the [0-200%] range with respect to their original value. They span from 0 to 2, where 1 indicates that the corresponding ionic current is unaltered from the baseline model, while big/small scaling factors correspond to its up/down regulation.

After running simulations for the initial 30,000 models, a calibration process is required, in order to select only the ones fully in agreement with the experimental data described in the corresponding Methods section. Examples of this calibration process are shown in Figure 7.7, considering only 2 AP/CaT biomarkers at a time. Calibration ranges (thick black lines) are defined considering the minimum and maximum values of the experimental data (light blue squares), except outliers (dark grey squares). Models whose biomarkers are within these ranges are accepted (blue dots), while the other ones are discarded (light grey dots). The baseline model is shown as a white diamond. This calibration is repeated for all the AP and CaT biomarkers available, and only the models satisfying all the considered constraints at the same time are included in the final CTRL population.

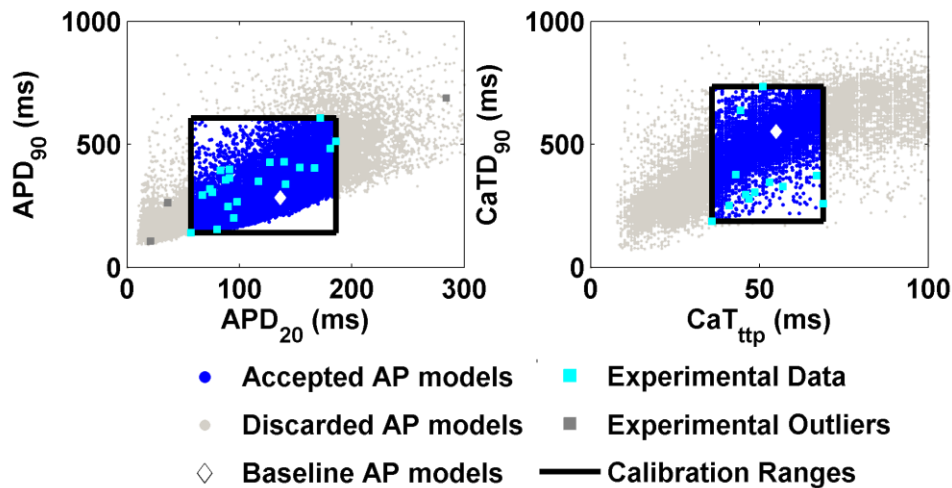


Figure 7.7: Two examples of the CTRL calibration process, considering two AP and two CaT biomarkers: experimental data/outliers (light blue/dark grey dots); calibration ranges (thick black lines); accepted/discarded models (blue/light grey dots); baseline model (white diamond). Models satisfying the single AP or CaT constraints are selected in every step, and only the ones which satisfy all of them at the same time are included in the final CTRL population.

The HCM population

The HCM population was built from the CTRL one, by applying the electrical remodelling experimentally found in HCM ventricular myocytes [8], as described in the Experimental Data Methods section. All the ionic currents have been modified by up- or down- regulating the corresponding conductance. Based on V-clamp experiments, we included an increase of I_{NaL} (+165%) and I_{CaL} (+30%), and a decrease of I_{to} (-70%) and I_{K1} (-30%), together with an increase of I_{CaL} inactivation slow and fast time constants (+20% and 30%, respectively). In addition, experimental data on mRNA expressions were used to modulate the K^+ repolarizing

currents (I_{Kr} , -45% and I_{Ks} , -60%), SERCA pump (J_{up} , -15%), RyRs release (J_{rel} , -15%) and Na^+/Ca^{2+} exchanger (I_{NCX} , +25%). Finally, we increased cell volume (+90%) and, based on literature review, we included an increased affinity of Troponin for Ca^{2+} ($TRPN_{max}$, +50%) [6], a reduction of Na^+/K^+ pump (I_{NaK} , -30%) [21] and an increase of background Na^+ current (I_{Nab} , +165% as for I_{NaL}) [10].

All the changes listed above have been tested in the baseline model first, and then extended to the whole CTRL population, in order to build the HCM one.

Simulation Details

All models were paced at 1 Hz until steady state (500 s). For every model, the last ten AP and CaT traces were saved and used to compute an average set of AP and CaT biomarkers, as done in the experiments. All numerical simulations and biomarkers evaluation were performed with the open source cardiac software Chaste [22], using a CellML [23] implementation of the ORd model, modified as described in the CTRL population methods section. Post-processing of AP and CaT traces, together with data analysis, were performed in Matlab (Mathworks, Inc.).

I_{NaL} and I_{NCX} inhibition

The effects of I_{NaL} and I_{NCX} inhibition have been tested in simulation by reducing the corresponding maximal conductance by 60% and 30%, respectively, in both the CTRL and HCM populations. I_{NaL} block percentage has been set accordingly to experimental data acquired in presence of Ranolazine 10 μ M [8], also used to compare simulation results. Since no experimental data were available for I_{NCX} , we tried different block percentages and we finally chose 30% because many models, both CTRL and HCM, were not repolarising properly for higher block values.

Repolarisation Abnormalities

All the 10 saved APs have been checked for repolarisation abnormalities. The AP traces not able to repolarise properly during the diastole ($V_m > -65$ mV) or showing a positive derivative of voltage over time after the AP peak (150 ms) have been selected as abnormal. Repolarisation abnormalities were divided in: short EADs (when the model repolarised before 1000 ms), long EADs (when the model was able to repolarise, but it required more than 1000 ms) and repolarization failures (RF), when the model was not going back to its resting potential.

RESULTS

The CTRL population

As a result of the calibration process, only 2,254 models out of the initial 30,000 were accepted in the final CTRL population. The calibration was based on the experimental data presented in the corresponding Methods section, and it was divided into two steps.

As first step, all the models in which Chaste failed to compute AP and CaT biomarkers were discarded (1897 models, about 6% of the population). These are models which often fail to repolarise: therefore, the software is not able to find the reference points needed to compute AP and CaT biomarkers. As expected, these models are usually characterised by a very low I_{Kr} when compared to the baseline model, but other mechanisms are involved too, e.g. low I_{Ks} and I_{K1} , high I_{CaL} and I_{NCX} and low I_{NaK} . Figure 7.8 shows the scaling factors distribution for these rejected models, using a boxplot for each parameter varied in the population.

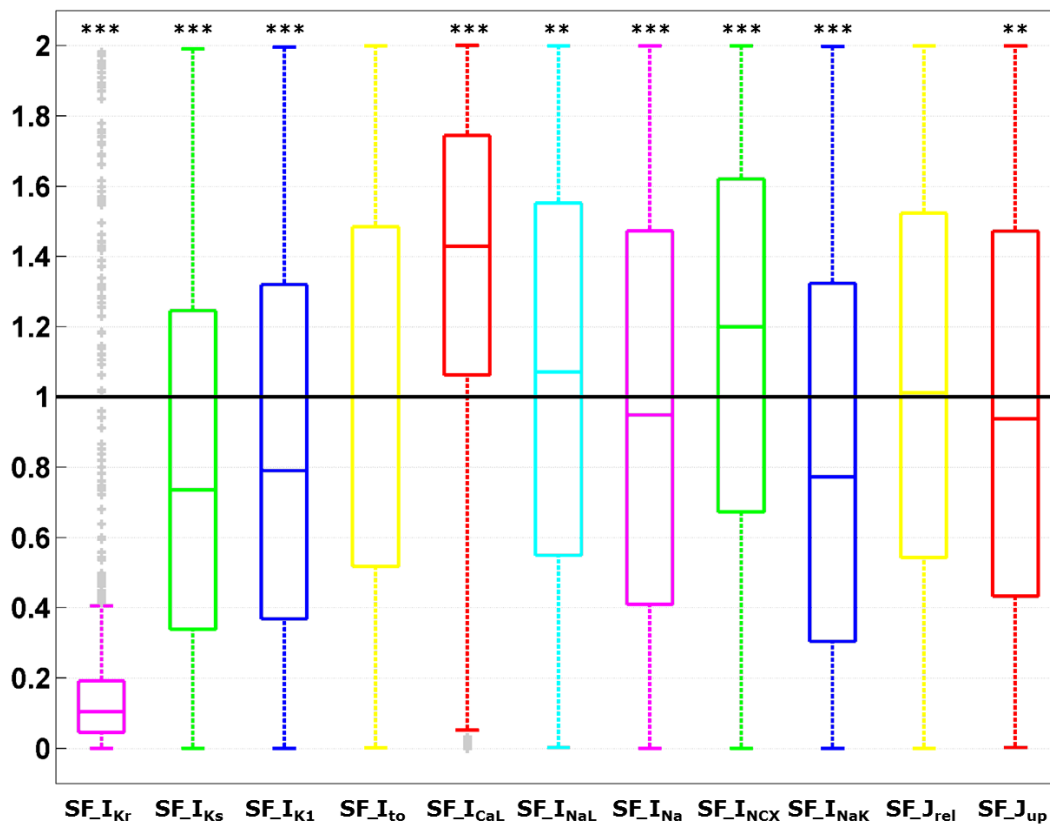


Figure 7.8: Scaling factor boxplots for the models in which Chaste was unable to compute the AP and CaT biomarkers. Among other ionic mechanisms, these models are characterised by a very low I_{Kr} and a high I_{CaL} compared to the baseline model: therefore they often fail to repolarise (* $p < 0.01$, * $p < 0.001$, *** $p < 0.0001$, compared to all the initial population of 30,000).

To highlight potential correlations between the scaling factors of these rejected models, Figure 7.9 shows all the 2-by-2 combinations of each scaling factor against the other ones. Each grey dot corresponds to a different model, and it is quite interesting to see how these models are distributed in the scaling factors space, e.g. almost all the models have a very small SF_{IKr} (from 0 to 0.5) while only a few of them have a low SF_{ICaL} , in agreement with the results shown in Figure 7.8.

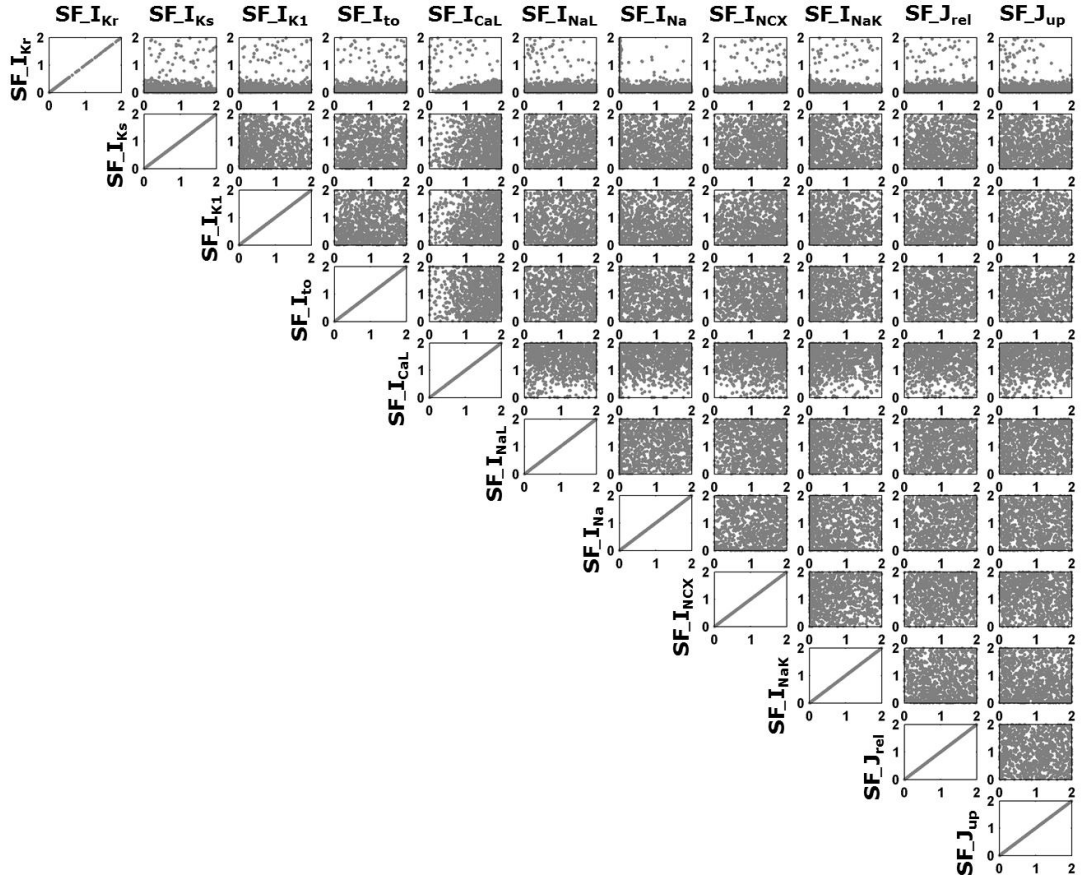


Figure 7.9: 2-by-2 plots of the scaling factors space, for the AP models in which Chaste was unable to compute the AP and CaT biomarkers. This representations highlights scaling factor distributions, e.g. almost all the models have a very small SF_{IKr} while only a few of them have a low SF_{ICaL} .

As second step, calibration ranges based on the minimum and maximal experimental data for the AP and CaT biomarkers were considered: only the models satisfying all the experimental constraints at the same time were included in the final CTRL population, for a total amount of 2,254 models out of the 28,104 remaining after the previous calibration step.

As shown in Table 7.2, the major constraints for the population were the ones defined by the CaT biomarkers, especially CaT_{itp} and CaT_{amp} , while most of the simulated AP biomarkers were within the corresponding experimental ranges.

$[Ca^{2+}]_iD$ was not considered in the calibration process because the model values were completely out of range with respect to the experimental data: since $[Ca^{2+}]_iD$ has been computed by converting a fluorescence signal, with poor quantitative reliability, we used this biomarker only to compare HCM vs CTRL, and we didn't consider its numerical value *per se*.

Table 7.2: Number of models satisfying the single/combined AP and CaT biomarker constraints.

Biomarkers		Models satisfying the single/combined biomarker constraints		
All AP Biomarkers	APD ₂₀	23,306	22,725	17,551
	APD ₅₀	26,231		
	APD ₉₀	26,618		
	RMP	27,994	-	
	dV/dt _{MEAN}	22,207	-	
	AP _{amp}	27,163	-	
All CaT Biomarkers	CaTD ₅₀	16,663	15,048	3,509
	CaTD ₉₀	18,086		
	CaT _{itp}	7,104	-	
	CaT _{amp}	4,558	-	
	$[Ca^{2+}]_iD$	11,626	<i>not included in the final population</i>	
Final Calibration		2,254		

Figure 7.10 shows the accepted/discarded models distribution for the CTRL population, considering 2-by-2 plots of the biomarkers space, together with the experimental data and the corresponding calibration ranges. As for AP biomarkers (top half), APD₉₀ is plotted against all the other ones, while for CaT biomarkers (bottom half) CaTD₉₀ is plotted vs all the other ones. Since $[Ca^{2+}]_iD$ was not considered in the calibration, its experimental ranges are marked with a dotted line.

Representative AP and CaT traces of both accepted and discarded models in the CTRL population are shown in Figure 7.11 and Figure 7.12.

Finally, the scaling factors distribution in the CTRL population is shown as both boxplots and 2-by-2 plots in Figure 7.13 and Figure 7.14, respectively. Compared to the initial population, the accepted models have a slightly higher I_{Kr} , I_{Na} and J_{up} .

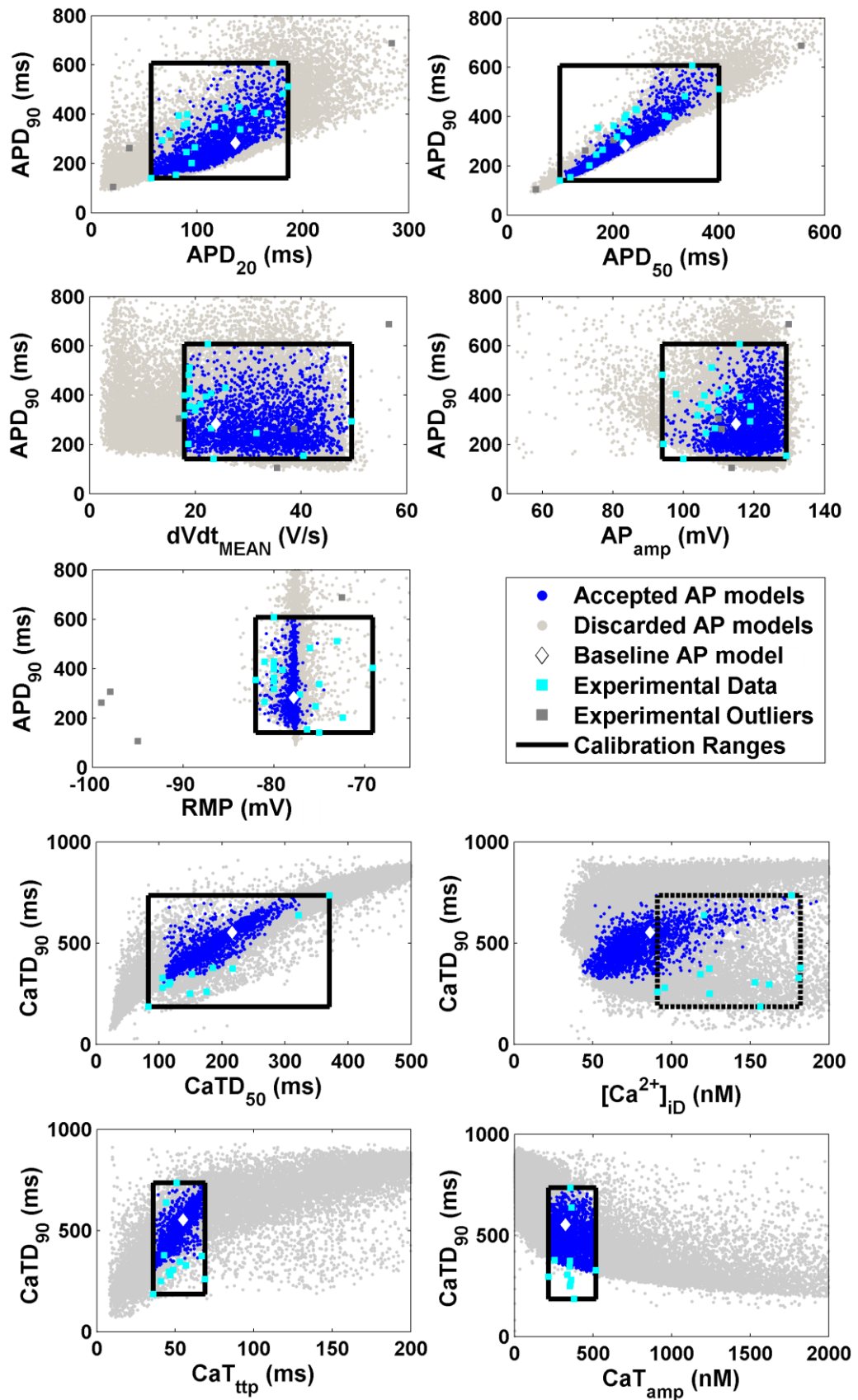


Figure 7.10: Calibration process of the CTRL population, showing how the accepted/discarded model biomarkers. The models included in the population are the ones in agreement with the experiments and their corresponding calibration ranges, defined considering the minimum and maximum experimental value. $[Ca^{2+}]_{iD}$ has not been considered in the calibration process.

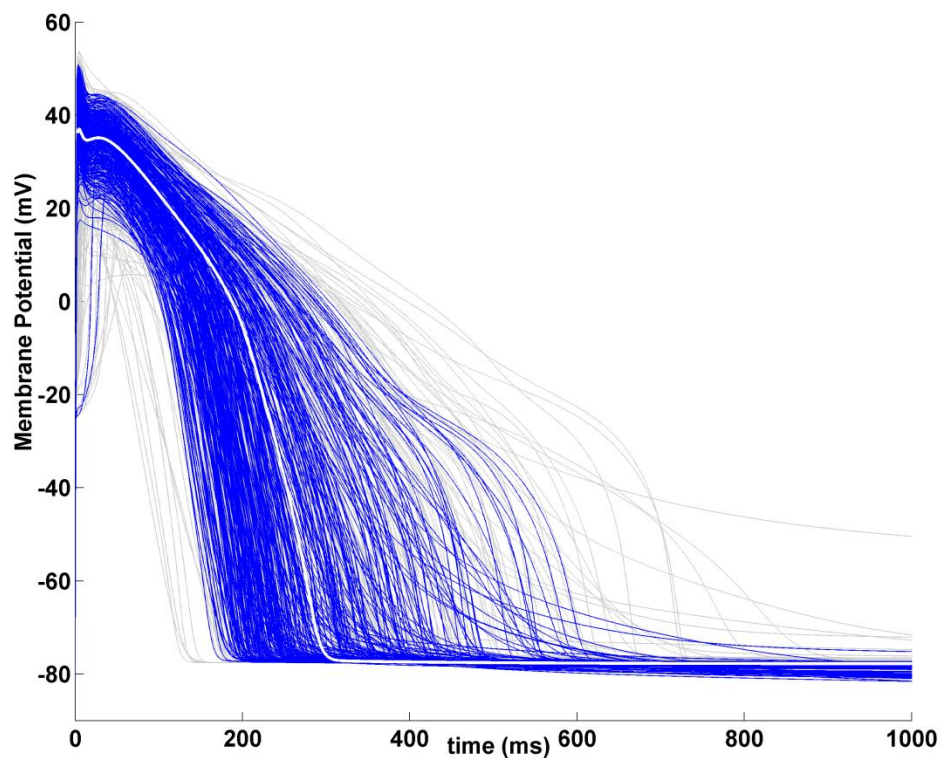


Figure 7.11: Representative AP traces of accepted/discarded (blue/grey lines) models in the CTRL population. The baseline model AP is shown in white.

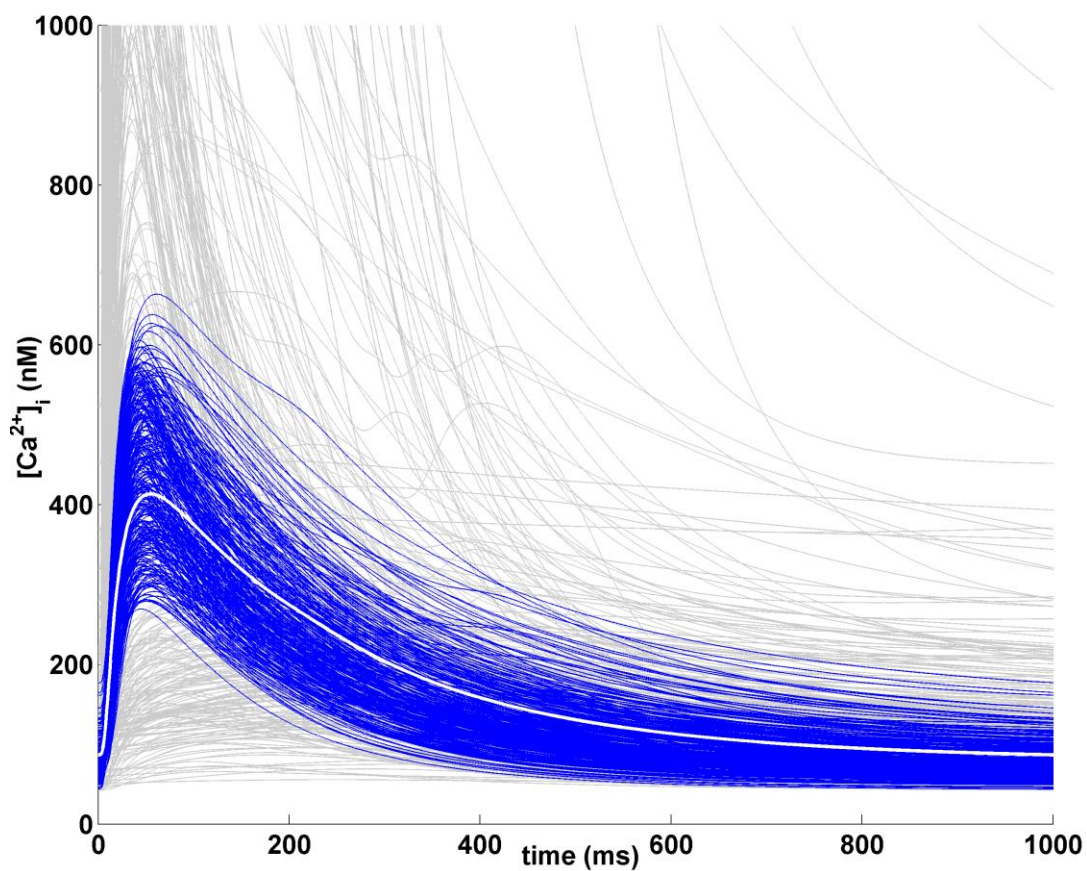


Figure 7.12: Representative CaT traces of accepted/discarded (blue/grey lines) models in the CTRL population. The baseline model CaT is shown in white.

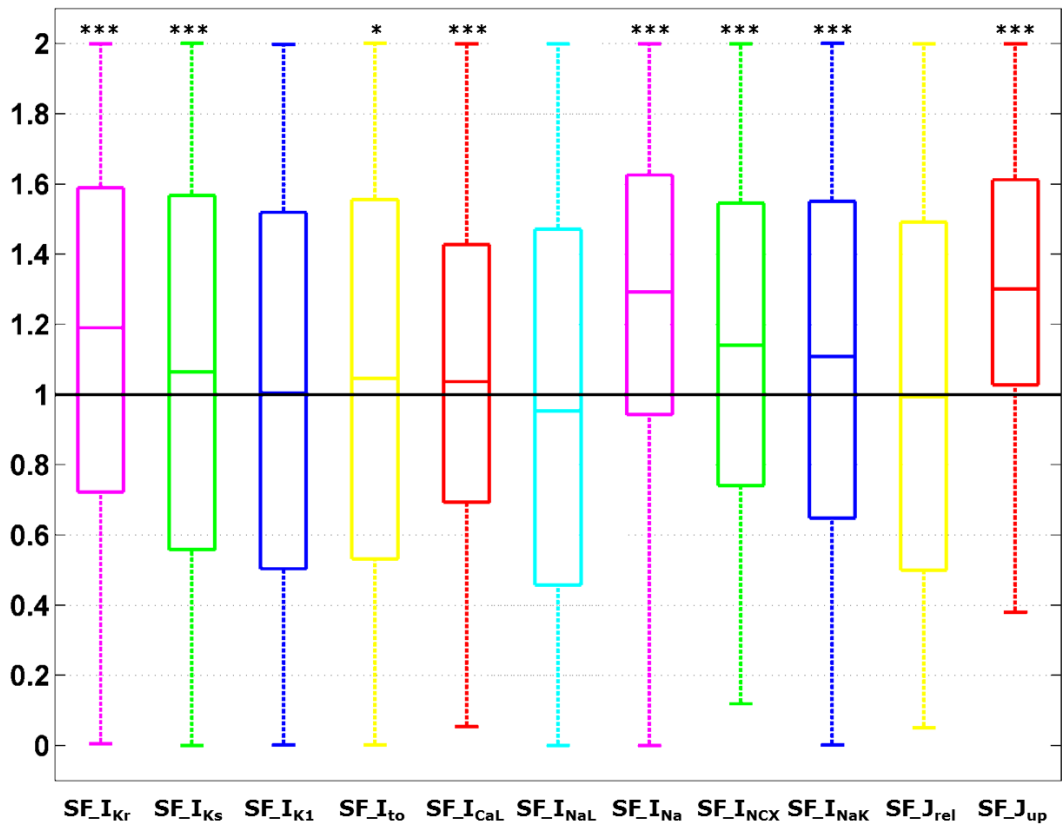


Figure 7.13: Scaling factor boxplots for the CTRL population. Compared to the initial population, the accepted models have a slightly higher I_{Kr} , I_{Na} and J_{up} (* $p < 0.01$, * $p < 0.001$, *** $p < 0.0001$).

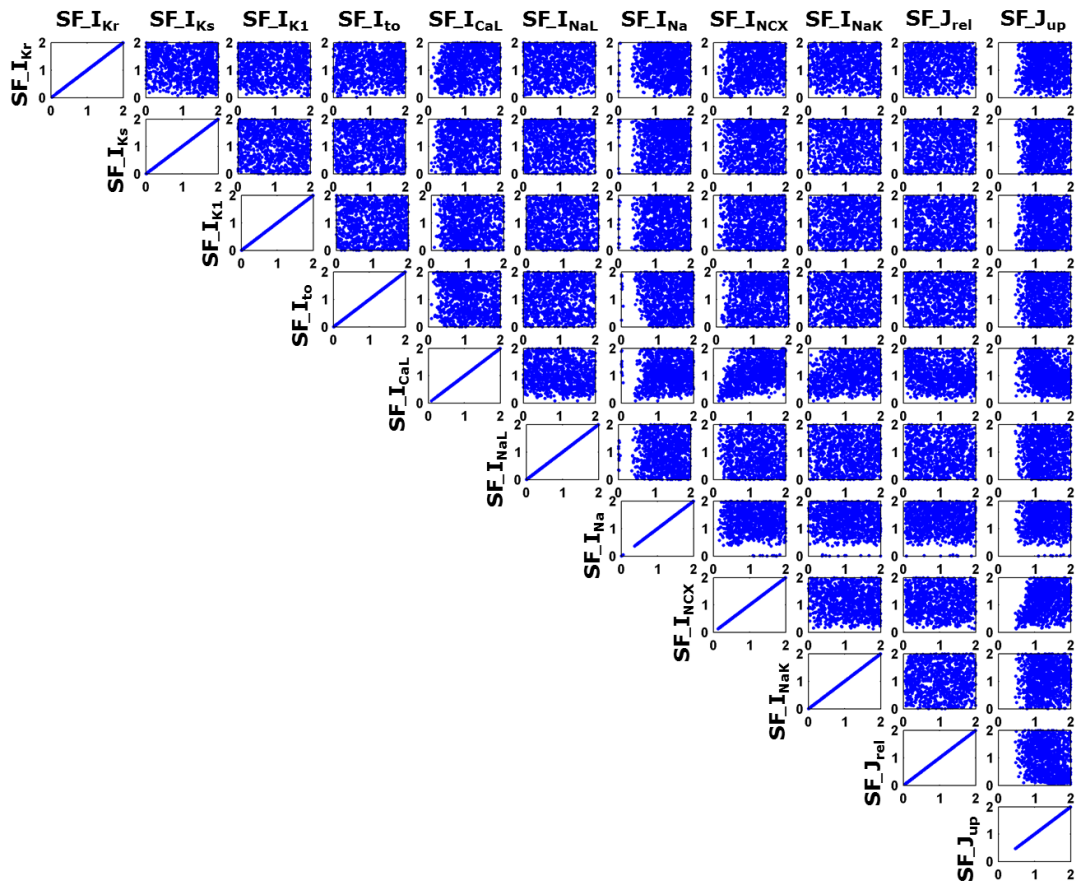


Figure 7.14: 2-by-2 plots of the scaling factors space for the models in the CTRL population.

Table 7.3 reports the average AP and CaT biomarker values in the CTRL population, compared with the corresponding experiments (both data are shown as mean \pm stdTD). As already evident from Figure 7.10, the calibrated CTRL population well represents the experimental data ranges (apart from $[Ca^{2+}]_iD$).

Table 7.3: Comparison of the AP and CaT biomarkers computed from the experimental CTRL data and the ones from the experimentally-calibrated population of models.

<i>AP Biomarkers in CTRL</i>			<i>CaT Biomarkers in CTRL</i>		
	Experiments (n = 24)	Models (n = 2,254)		Experiments (n = 12)	Models (n = 2,254)
APD₂₀	115 \pm 40 ms	117 \pm 29 ms	CaTD₅₀	175 \pm 89 ms	187 \pm 43 ms
APD₅₀	230 \pm 77 ms	212 \pm 58 ms	CaTD₉₀	364 \pm 161 ms	492 \pm 86 ms
APD₉₀	354 \pm 117 ms	285 \pm 91 ms	CaT_{ttp}	50 \pm 10 ms	50 \pm 8 ms
AP_{amp}	110 \pm 9 mV	118 \pm 6 mV	CaT_{amp}	351 \pm 72 mV	359 \pm 84 mV
RMP	-77.6 \pm 3.5 mV	-77.9 \pm 0.5 mV	[Ca²⁺]_iD	140 \pm 32 nM	81 \pm 23 nM
dV/dt_{MEAN}	24 \pm 8 V/s	32 \pm 8 V/s	[Na⁺]_i	N.A.	7.1 \pm 1.7 mM

An additional comparison between the CTRL population and experimental biomarkers is shown in Figure 7.15. Statistical significance is not shown because p-values were all very small due to the high difference in sample sizes (n=12/24 cells vs n=2,254 models), even when the values were very close one another.

Finally, to determine correlations between the properties of individual ionic currents, represented by the corresponding scaling factors, and the AP and CaT biomarkers, we used partial correlation method [24]. We chose to use partial correlation over other correlation measures because partial correlation controls for the effects of one or more additional variables when looking for correlations between two quantities, which is particularly important here, given that our models are generated by varying multiple parameters simultaneously. Partial correlation coefficients span from -1 to +1, where -1 indicates a strong negative correlation between the two considered variables, and +1 a strong positive one. Results are shown in Figure 7.16: as expected, K⁺ repolarising currents are negatively correlated with APDs, while I_{NaL} and I_{CaL} are positively correlated with it. J_{up} and J_{rel} have a strong influence on CaT, and both dV/dt_{MEAN} and AP_{amp} are positively correlated with I_{Na}.

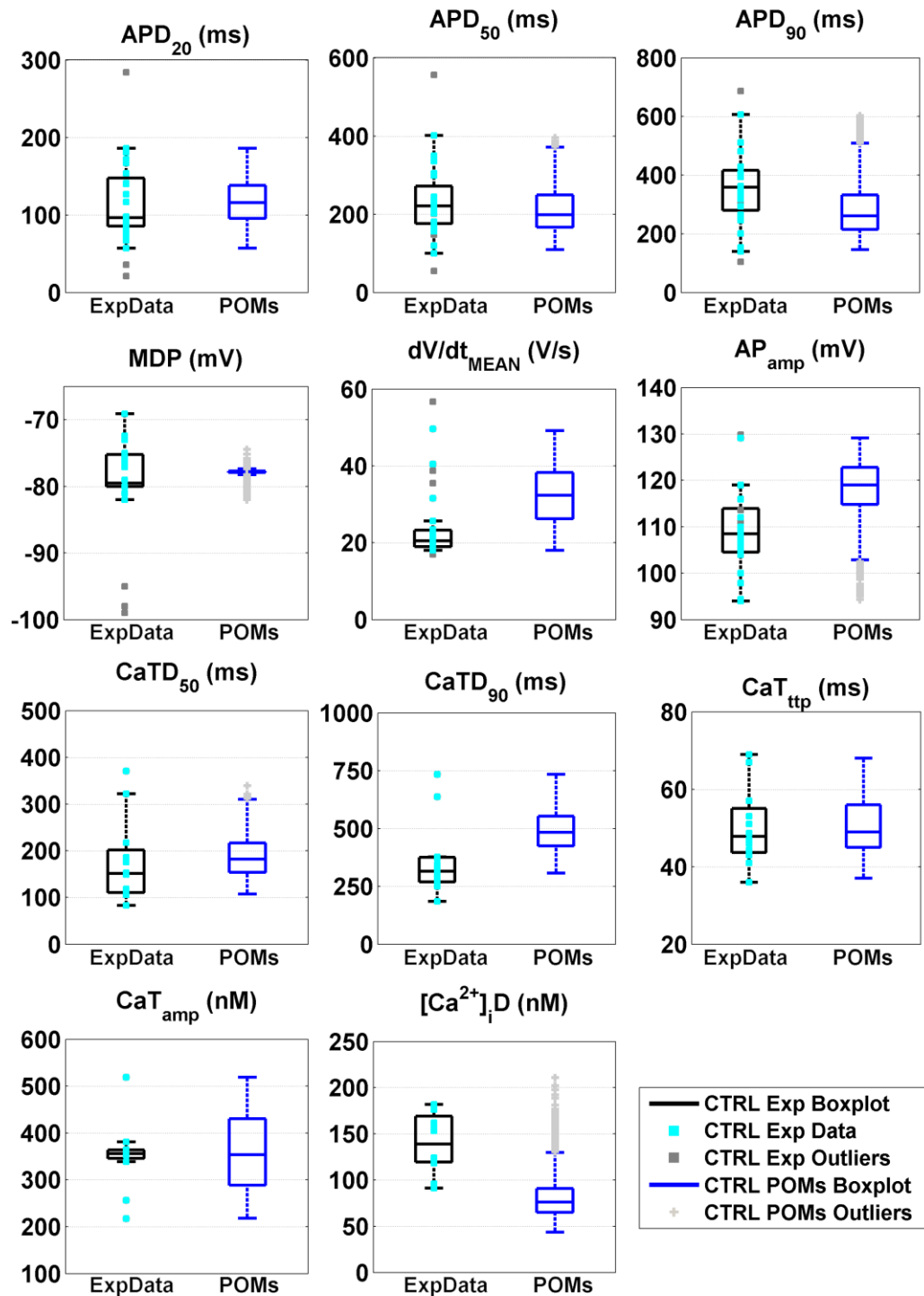


Figure 7.15: Comparison of the AP and CaT biomarkers between the CTRL population (blue boxplot) and the experiments (black boxplots): on each box, the central mark is the median, the edges of the box are the 25th and 75th percentiles, the whiskers extend to the most extreme data points not considered outliers, and outliers are plotted individually (light grey crosses). The experimental data have been superimposed to their boxplot (light blue squares), as well as the experimental outlier (dark grey squares), not considered for the calibration process. The experimental data and their variability are well reproduced by the CTRL population for all the biomarkers, apart from $[Ca^{2+}]_{iD}$ which is lower in most of the models.

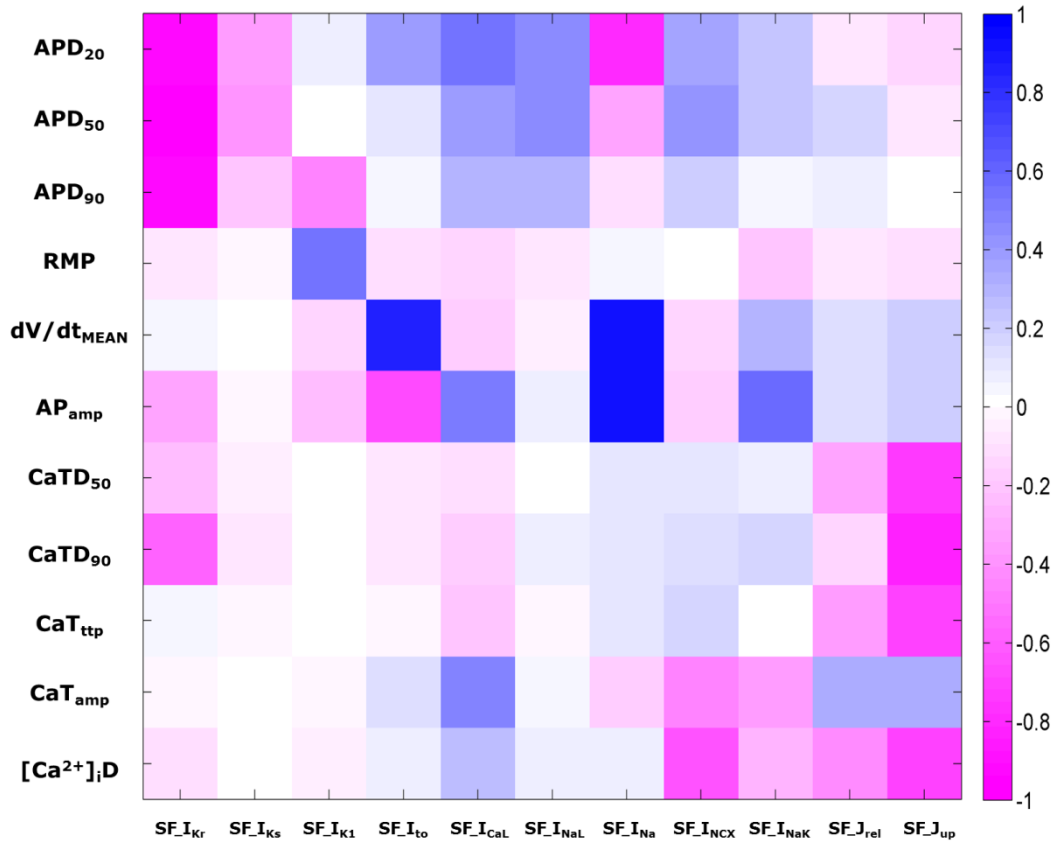


Figure 7.16: Partial correlation coefficients to highlight the potential correlations between each of the parameters varied in the CTRL population and the corresponding model biomarkers. As expected, K^+ repolarising currents are negatively correlated with APDs, while I_{NaL} and I_{CaL} are positively correlated with it. J_{up} and J_{rel} have a strong influence on CaT, and both dV/dt_{MEAN} and AP_{amp} are positively correlated with I_{Na} .

The HCM population

In agreement with experiments, all the APDs were significantly longer in HCM than in CTRL (e.g. APD_{90} 458 ± 109 vs 285 ± 91 ms). Moreover, the HCM population showed an increased CaTD, smaller CaT_{amp} and higher $[Ca^{2+}]_{iD}$, all consistent with experiments. From a qualitative point of view, the simulated HCM phenotype is fully in agreement with the experimental data, even if the quantitative variations are sometimes different.

The full list of AP and CaT biomarkers in the HCM experimental data and in the corresponding POMs is shown in Table 7.4, followed by a quantitative comparison between HCM and CTRL, both for experiments and POMs (Table 7.5). It is worth noticing that only the models with normal APs (i.e. not showing any repolarisation abnormalities) have been considered to compute the reported values.

Table 7.4: Comparison of the AP and CaT biomarkers computed from the experimental HCM data and the ones computed from the HCM population of models (data are presented as mean±std).

<i>AP Biomarkers in HCM</i>			<i>CaT Biomarkers in HCM</i>		
	Experiments (n = 57)	Models (n = 1,894)		Experiments (n = 19)	Models (n = 1,894)
APD₂₀	298±123 ms	165±26 ms	CaTD₅₀	329±121 ms	287±76 ms
APD₅₀	428±170 ms	321±58 ms	CaTD₉₀	602±174 ms	677±86 ms
APD₉₀	578±217 ms	458±109 ms	CaT_{ttp}	116±36 ms	60±12 ms
AP_{amp}	111±11 mV	120±5 mV	CaT_{amp}	292±63 mV	282±104 mV
RMP	-77.2±7.8 mV	-77.3±1.0 mV	[Ca²⁺]_iD	222±81 nM	100±28 nM
dV/dt_{MEAN}	21±3 V/s	24±6 V/s	[Na⁺]_i	N. A.	8.1±1.7 mM

Table 7.5: Comparison of HCM vs CTRL for both experiments and POMs (data are presented as mean±std)

<i>AP Biomarkers in HCM vs CTRL</i>			<i>CaT Biomarkers in HCM vs CTRL</i>		
	Experiments	Models		Experiments	Models
APD₂₀	+159% (***)	+40%	CaTD₅₀	+88% (**)	+53%
APD₅₀	+86% (***)	+52%	CaTD₉₀	+66% (**)	+38%
APD₉₀	+63% (***)	+61%	CaT_{ttp}	+131% (***)	+19%
AP_{amp}	+2.0%	+1.8%	CaT_{amp}	-17%	-22%
RMP	-0.6%	-0.7%	[Ca²⁺]_iD	+58% (*)	+24%
dVdt_{MEAN}	-11%	-25%	[Na⁺]_i	N. A.	+14%

* $p < 0.01$, ** $p < 0.001$, *** $p < 0.0001$ (statistical significance not shown for POMs, since all p values were really small due to the high number of models)

To better show the HCM population and its variability, both in comparison with the CTRL one and the experimental data, alternative representations are shown in Figure 7.17 and Figure 7.18, considering 2-by-2 plots of the AP and CaT biomarkers space and boxplots. In addition, some representative AP, CaT, I_{NaL} and I_{CaL} traces are shown in Figure 7.19, Figure 7.20, Figure 7.21 and Figure 7.22 respectively.

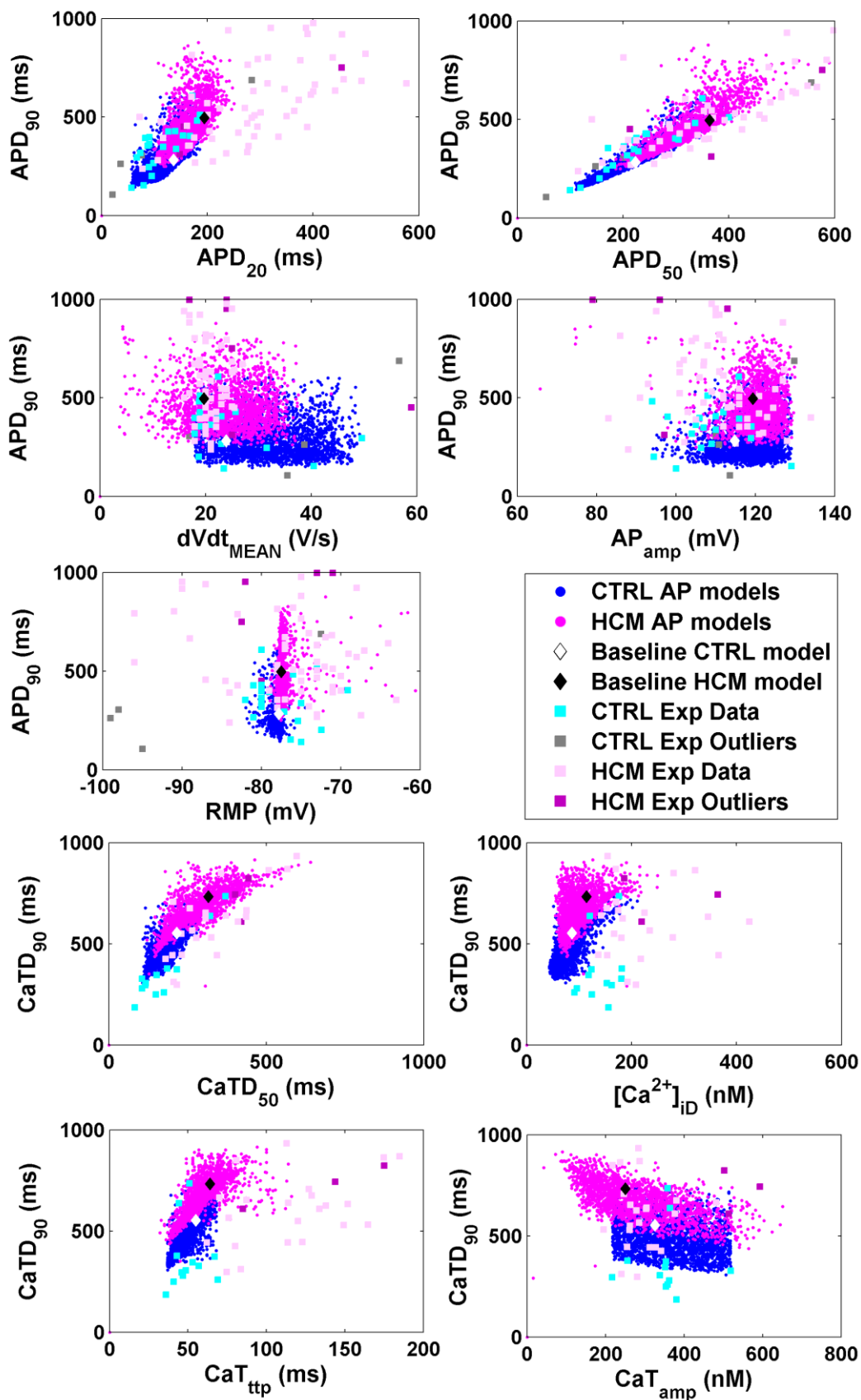


Figure 7.17: Visual representation of the HCM POMs in the biomarkers space, compared to CTRL. The POMs is able to reproduce quite well the HCM phenotype from a qualitative point of view, even if with respect to the corresponding experimental data, HCM models have a shorter APD₂₀ and a shorter CaT_{ttp}.

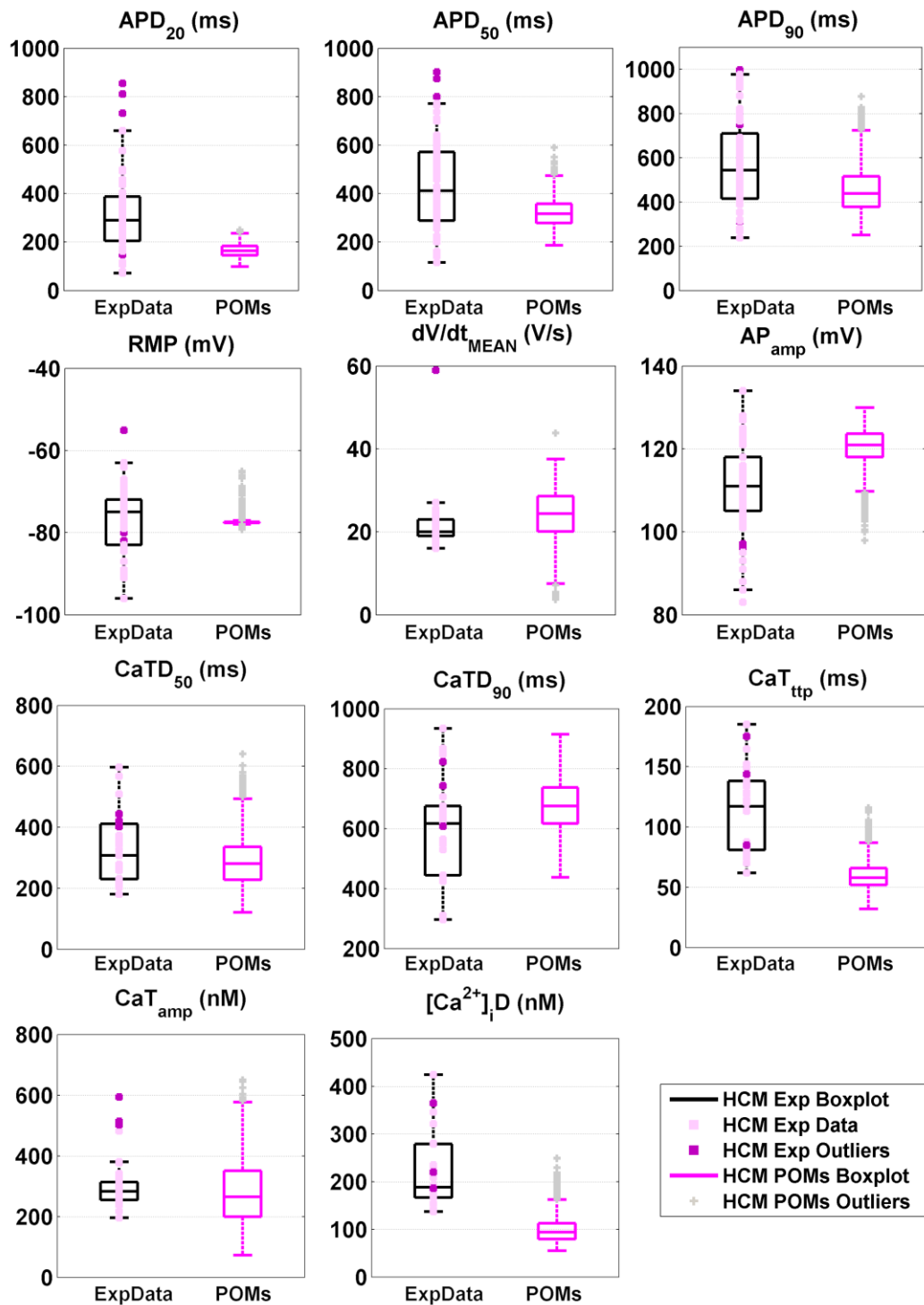


Figure 7.18: Comparison of the AP and CaT biomarkers between the HCM population (pink boxplots) and the experiments (black boxplot): on each box, the central mark is the median, the edges of the box are the 25th and 75th percentiles, the whiskers extend to the most extreme data points not considered outliers, and outliers are plotted individually (light grey crosses). The experimental data have been superimposed to their boxplot (light pink squares), as well as the experimental outlier (purple squares). The experimental data and their variability is well reproduced by the HCM population for most of the biomarkers, apart from APD_{20} and CaT_{ttp} , both shorter in the models, and $[Ca^{2+}]_iD$, already out of range in the CTRL population.

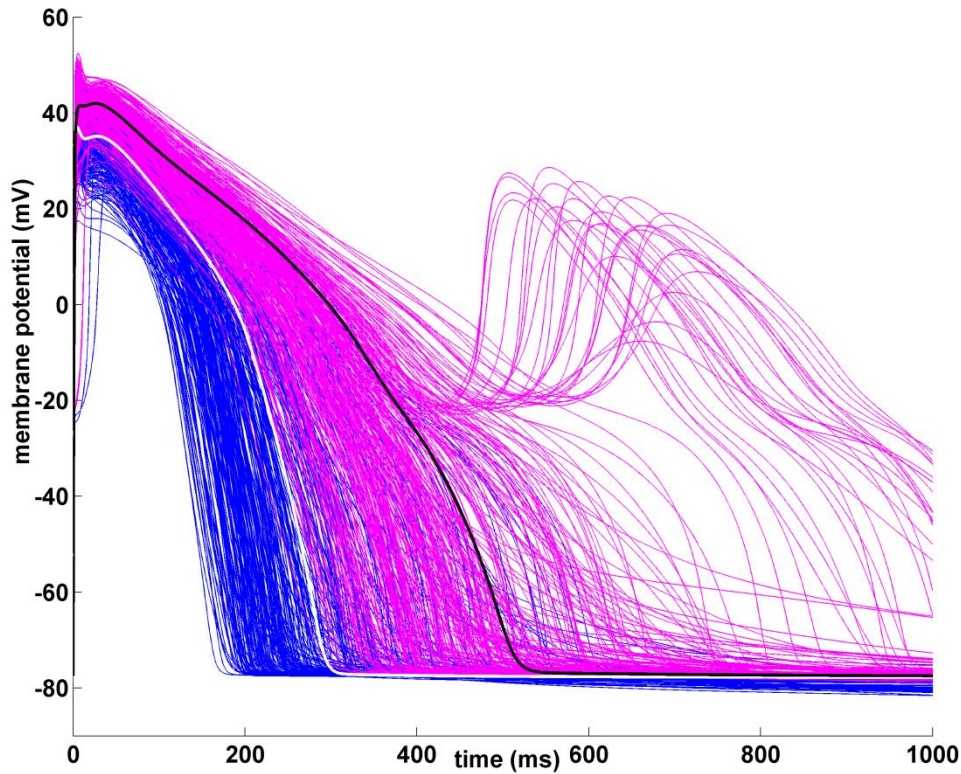


Figure 7.19: Representative AP traces from the HCM POMs (pink lines), compared with the corresponding CTRL ones (blue lines). The baseline CTRL model and its correspondent HCM version are shown in white and black, respectively.

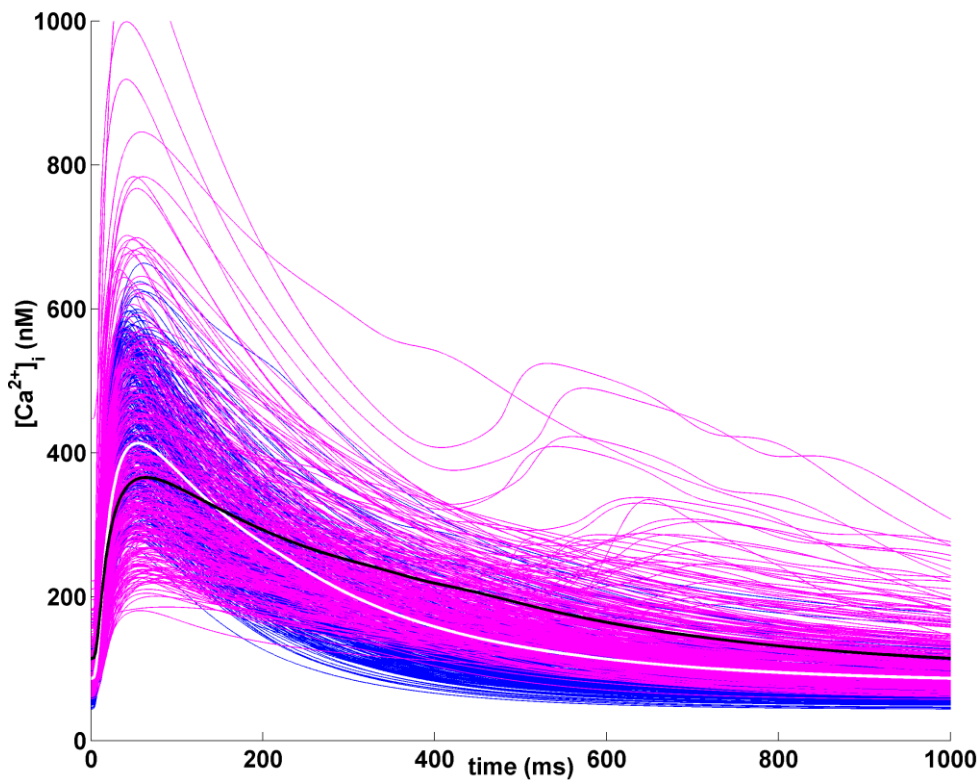


Figure 7.20: Representative CaT traces from the HCM POMs (pink lines), compared with the corresponding CTRL ones (blue lines). The baseline CTRL model and its correspondent HCM version are shown in white and black, respectively.

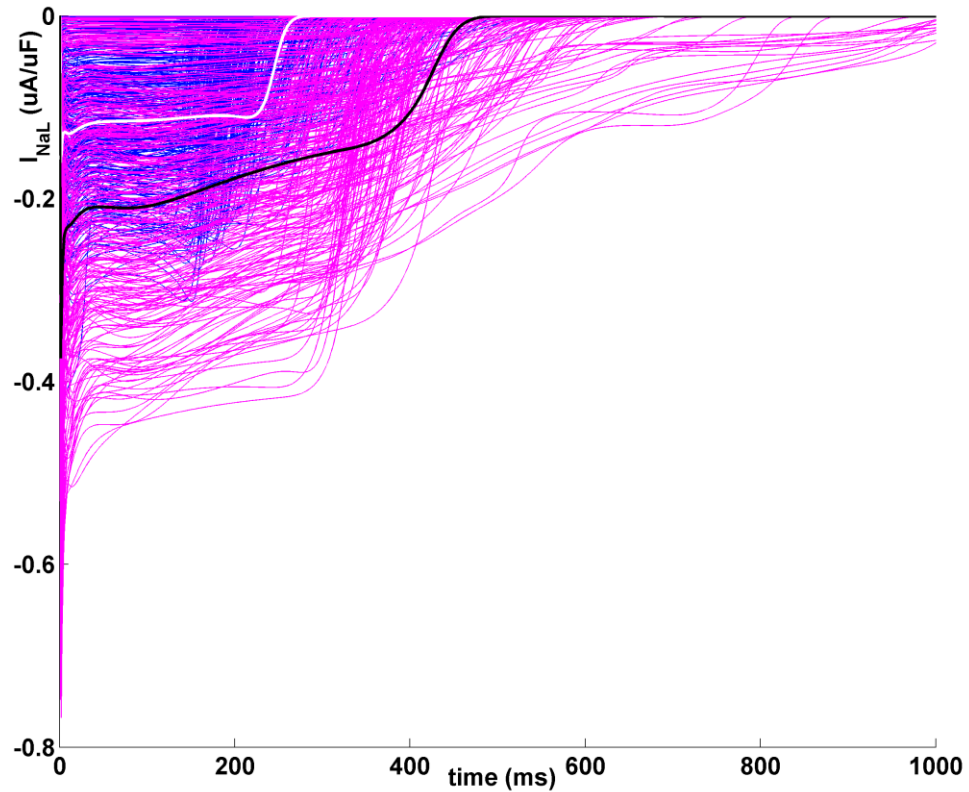


Figure 7.21: Representative I_{NaL} traces from the HCM POMs (pink lines), compared with the corresponding CTRL ones (blue lines). The baseline CTRL model and its correspondent HCM version are shown in white and black, respectively.

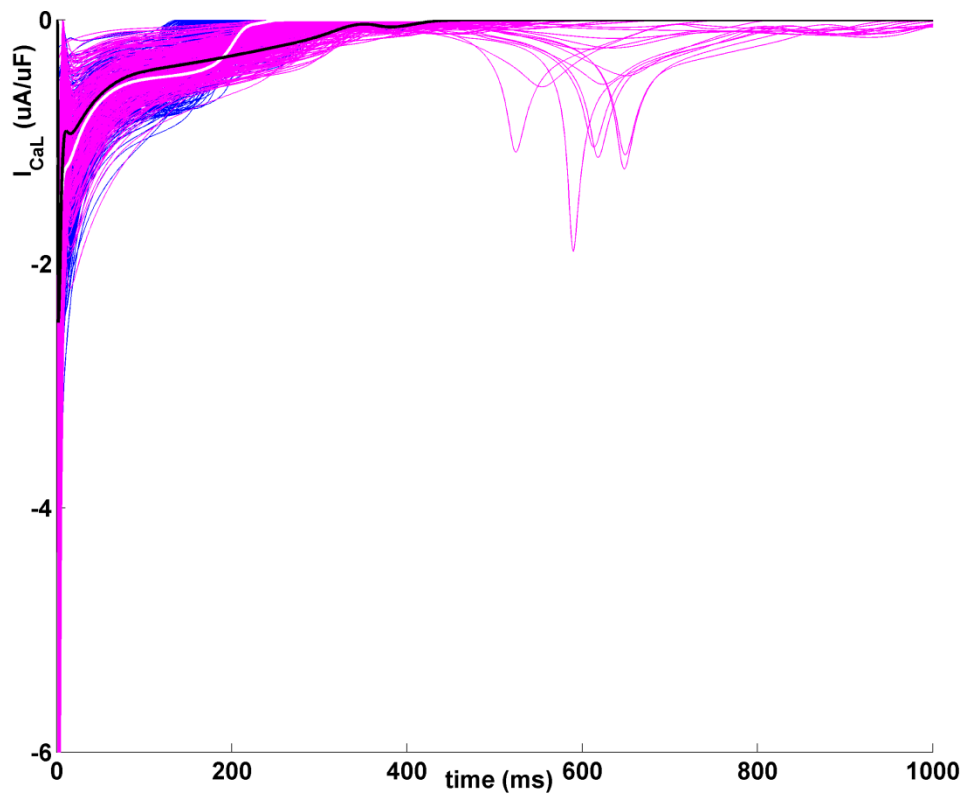


Figure 7.22: Representative I_{CaL} traces from the HCM POMs (pink lines), compared with the corresponding CTRL ones (blue lines). The baseline CTRL model and its correspondent HCM version are shown in white and black, respectively.

As already done for the CTRL population, we computed the partial correlation coefficients to verify the effect of the electrical remodelling occurring in HCM on the correlations between ionic currents and AP and/or CaT biomarkers. Partial correlation results are shown in **Figure 7.23**, with the same colour code used for **Figure 7.16**. Compared to CTRL, in the HCM population I_{NaL} (highly increased in HCM) has a much stronger effect on APDs, while I_{K1} and I_{to} (both reduced in HCM) have a lighter effect on RMP, dV/dt_{MEAN} and AP_{amp} . As for CaT biomarkers, J_{rel} and J_{up} seem to have a stronger effect on CaTD, together with I_{NCX} and I_{NaK} .

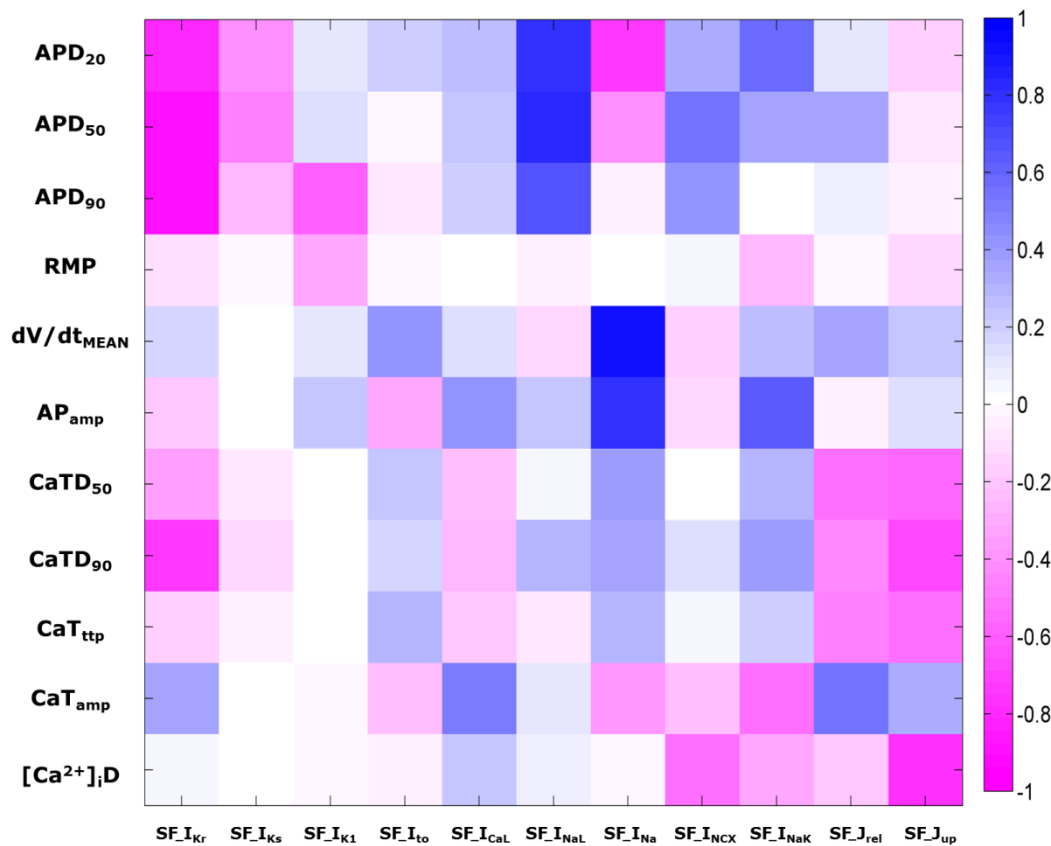


Figure 7.23: Partial correlation coefficients to highlight the potential correlations between each of the parameters varied in the HCM population and the corresponding model biomarkers. Compared to CTRL (Figure 7.16) the currents which are increased in HCM have a bigger effects on biomarkers (e.g. I_{NaL} on APDs), while the ones which are reduced have lower impact.

Finally, a comprehensive comparison of HCM vs CTRL, considering all the AP and CaT biomarkers, and showing both POMs and experimental data, is given in Figure 7.24. The simulated HCM phenotype well reproduces the experimental dataset and its variability, although there are some qualitative differences, which may be related to intrinsic characteristics of the baseline model used to build the CTRL population or to choice of parameters varied to build the population.

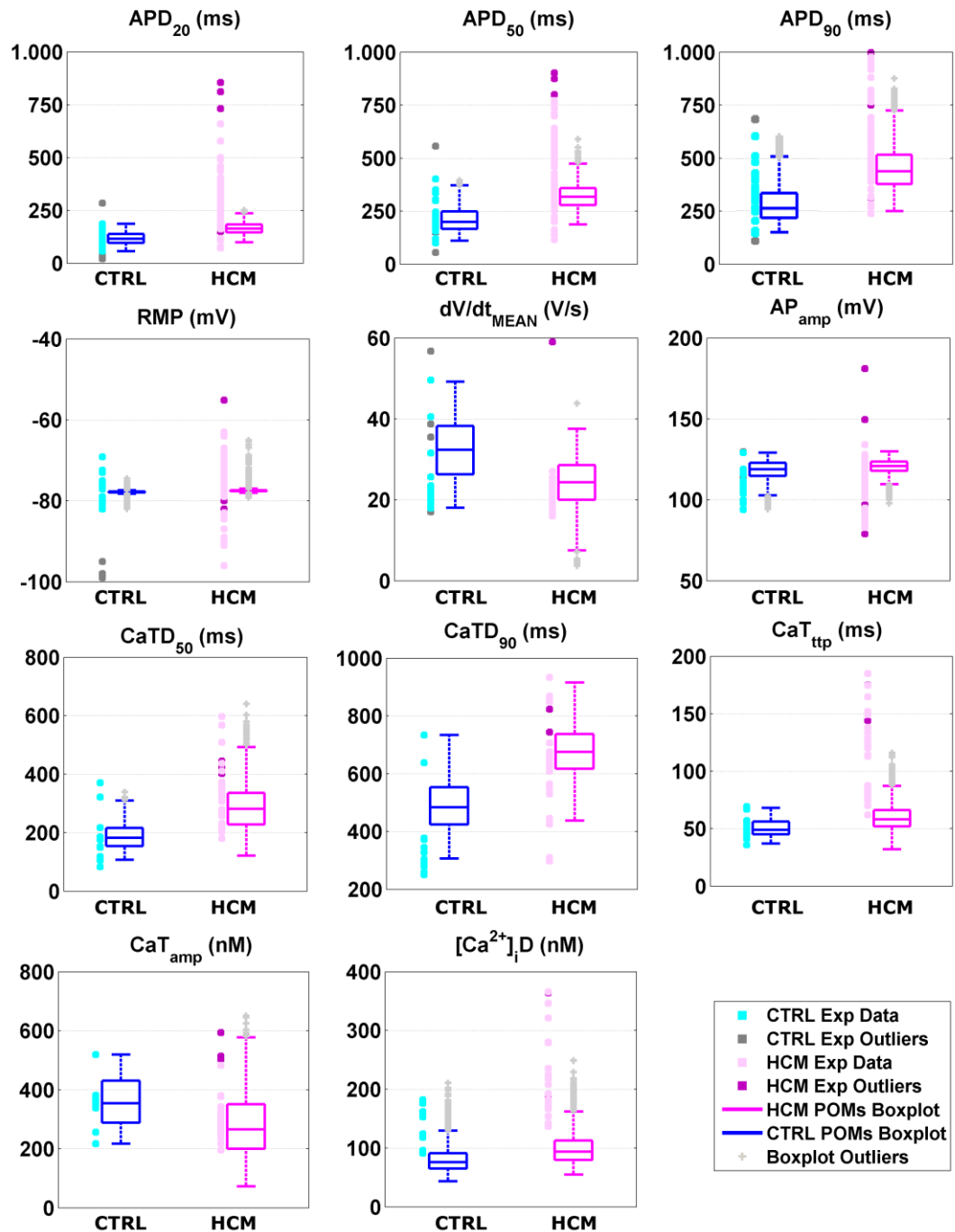


Figure 7.24: Visual comparison of HCM vs CTRL, showing both POMs and experimental data. For each of the 11 AP and CaT biomarkers, the boxplots represent POMs values, while the experiments are shown individually as small squares. The colour legend is the same used for the entire Results chapter: CTRL is blue (light blue for data) and HCM is pink (light pink for data). The simulated HCM phenotype well reproduces the experimental dataset and its variability, although there are some qualitative differences: the APD_{20} increase in HCM vs CTRL is much higher in the experimental data than in the POMs. The same happens for CaT_{ttp} and $[Ca^{2+}]_iD$, already out of range in the CTRL population. Some of these limitations may be overcome by slightly tuning the electrical remodelling considered to build the HCM population, starting from the CTRL one (e.g. $[Ca^{2+}]_iD$), while other are more related to the baseline model and the population design, e.g. the increase in CaT_{ttp} cannot be achieved by acting on current conductances only.

Repolarisation Abnormalities

Repolarisation abnormalities have been found in 360 HCM models out of 2,254 (16%), and they have been classified as described in the Methods section, i.e. short/long EADs and repolarisation failure (RF). Their relative occurrence, together with a representative trace for each type, is shown in Figure 7.25.

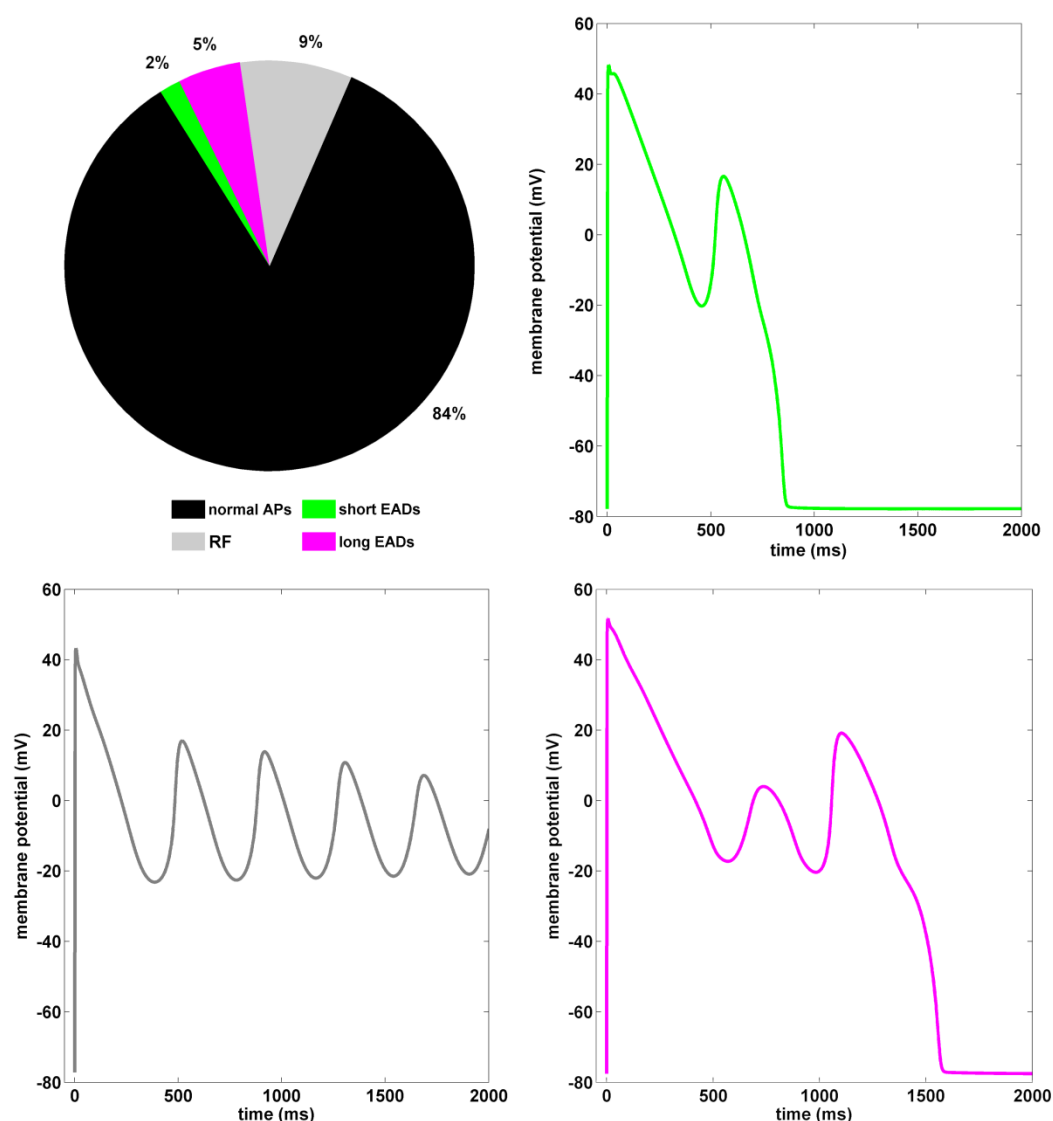


Figure 7.25: Occurrence of repolarisation abnormalities in the HCM population, classified in three different types: short/long EADs and RF. For each type, a representative trace is shown, in agreement with the colour legend (green, pink and grey respectively).

To better understand the ionic mechanisms underlying these repolarisation abnormalities, scaling factor boxplots for each of the subgroups have been compared: normal APs (Figure 7.26), short EADs (Figure 7.27), long EADs (Figure 7.28) and RF (Figure 7.29).

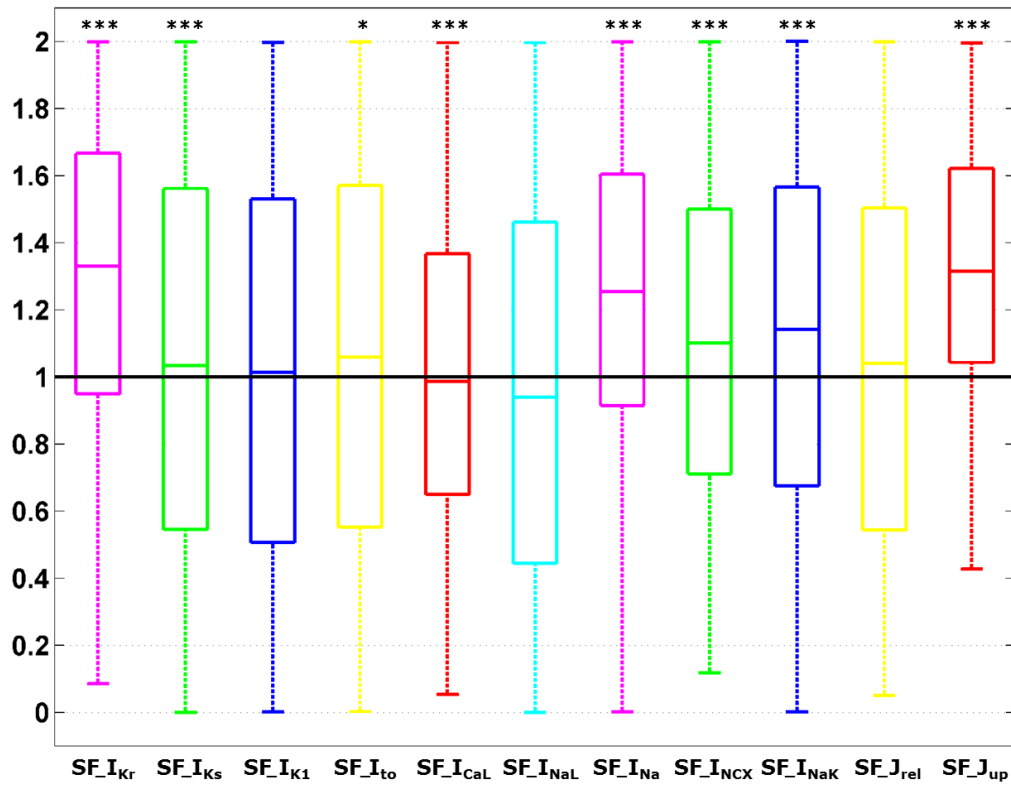


Figure 7.26: Scaling factor boxplots of the HCM models having a normal AP, i.e. not showing any repolarisation abnormality. As for the CTRL population, these models have a slightly higher I_{Kr} , I_{Na} and J_{up} (* $p < 0.01$, * $p < 0.001$, *** $p < 0.0001$ compared to the initial parameter distribution).

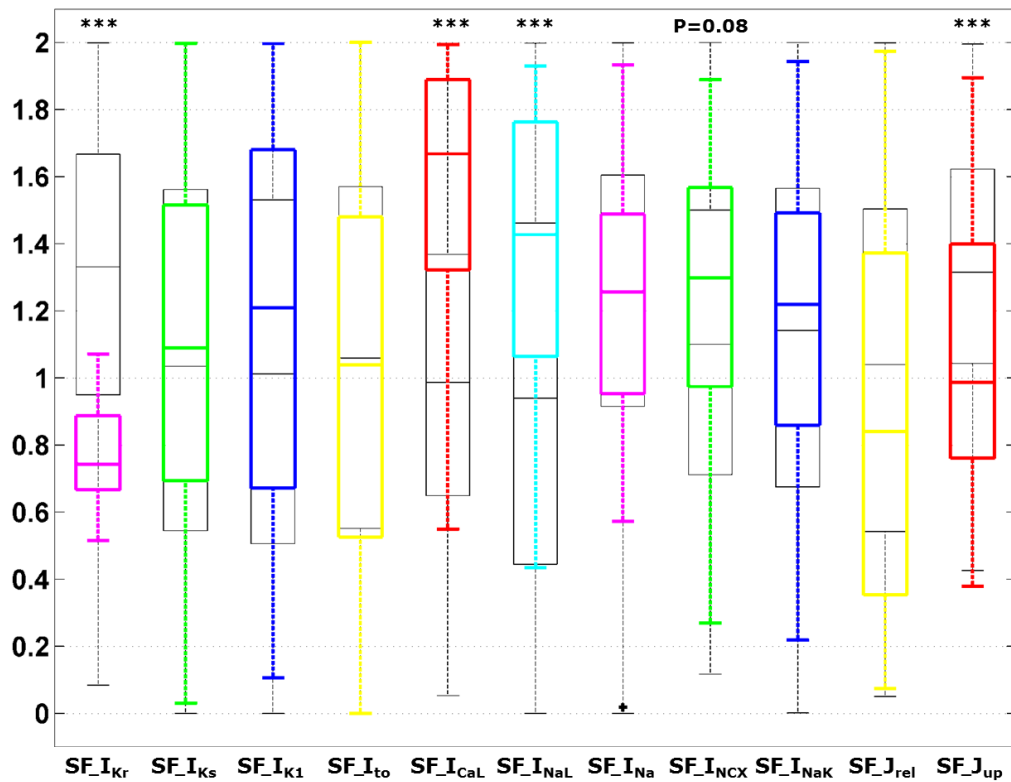


Figure 7.27: Scaling factor boxplots of the HCM models showing short EADs, compared to the ones with a regular AP (* $p < 0.01$, * $p < 0.001$, *** $p < 0.0001$). These models are characterised by low I_{Kr} , high I_{CaL} and I_{NaL} , slightly high I_{NCX} and low J_{up} .

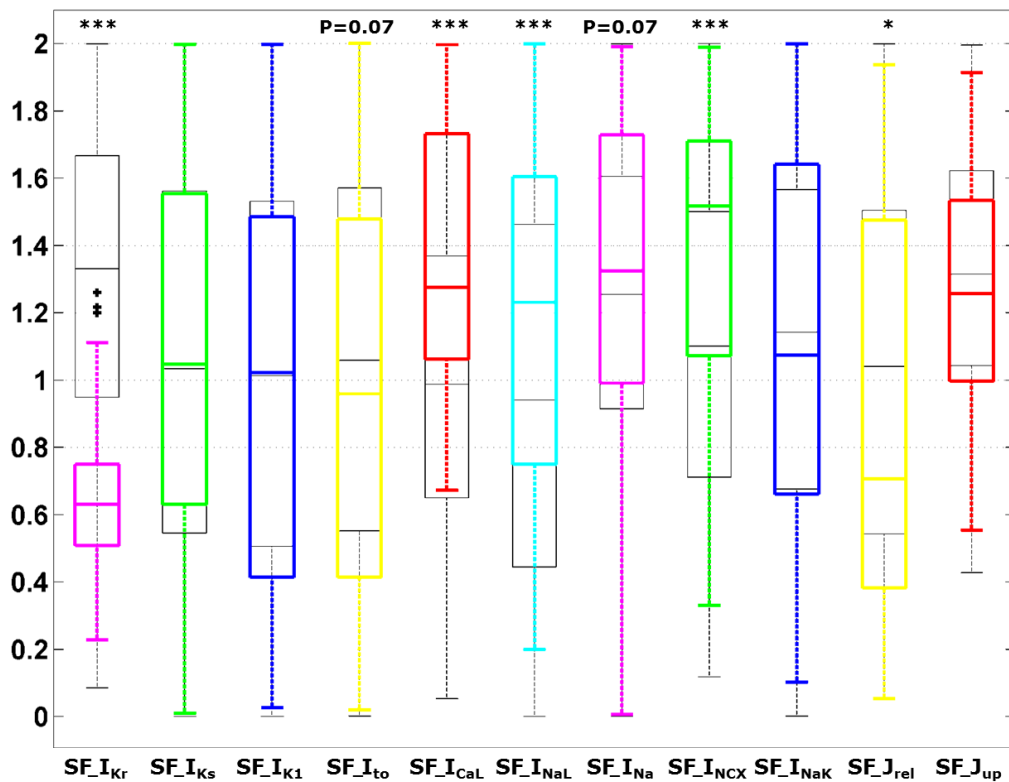


Figure 7.28: Scaling factor boxplots of the HCM models showing long EADs, compared to the ones with a regular AP (* $p < 0.01$, * $p < 0.001$, *** $p < 0.0001$). These models are characterised by low I_{Kr} , high I_{CaL} and I_{NaL} , very high I_{NCX} and lower J_{rel} .

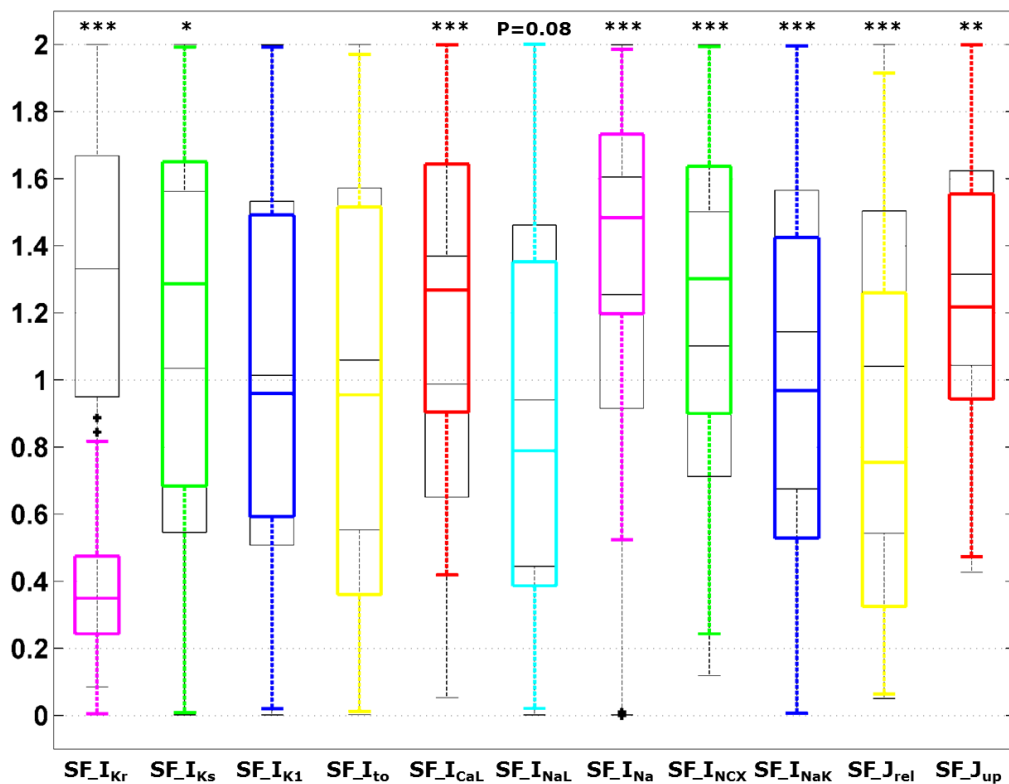


Figure 7.29: Scaling factor boxplots of the HCM models showing RF, compared to the ones with a regular AP (* $p < 0.01$, * $p < 0.001$, *** $p < 0.0001$). These models are characterised by a very low I_{Kr} , high I_{CaL} , I_{Na} and I_{NCX} and low J_{rel} .

Therefore, the ionic mechanism who seems to play the major role in repolarisation abnormalities is I_{Kr} : the smaller its scaling factor, and therefore the current density, the more severe the EADs, up to RF. In addition, short and long EADs are often characterised by a high I_{NaL} and I_{CaL} , both contributing toward an additional increase of APDs, and also an increased activity of NCX.

The link between low scaling factors for I_{Kr} and repolarisation abnormalities is even more evident when considering 2-by-2 plots of the scaling factors space, comparing the EADs/RF subgroups with the normal APs one (Figure 7.30, Figure 7.31 and Figure 7.32 for short EADs, long EADs and RF, respectively).

In the different subgroups, the models are always clustered in the bottom half of the $SF_{I_{Kr}}$ range, with values decreasing from short/long EADs to RF. Additional correlations between other ionic mechanisms (I_{NaL} , I_{CaL} and I_{NCX}) is emerging as well, e.g. many of the models showing short EADs have both I_{NaL} and I_{CaL} up-regulated at the same time.

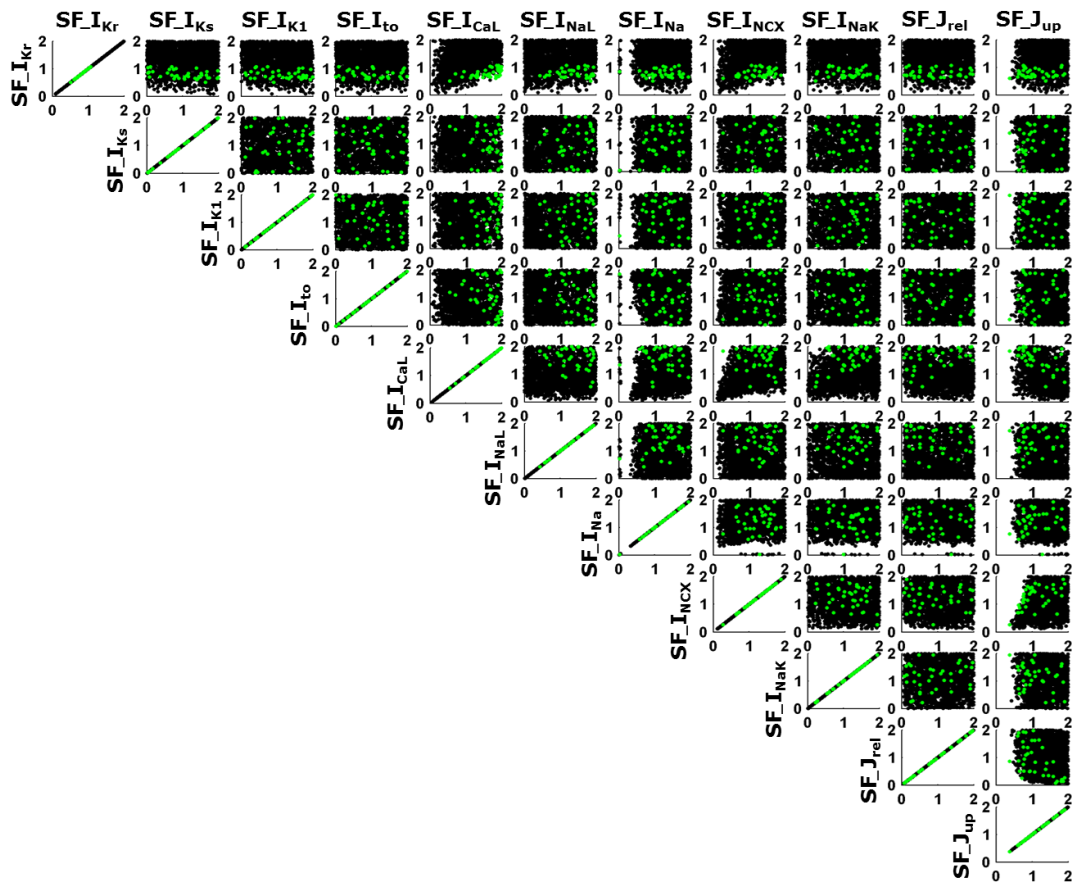


Figure 7.30: 2-by-2 plots of the scaling factors space for the HCM models showing short EADs (green dots), compared the ones with normal APs (black dots).

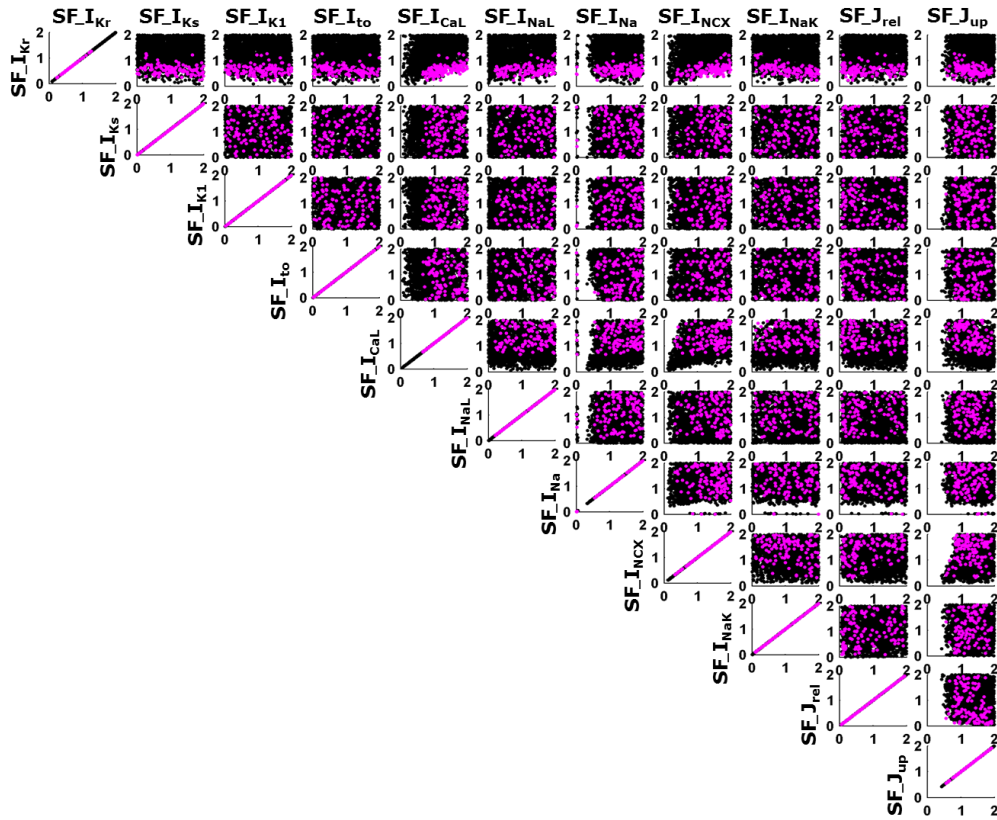


Figure 7.31: 2-by-2 plots of the scaling factors space for the HCM models showing long EADs (pink dots), compared the ones with normal APs (black dots).

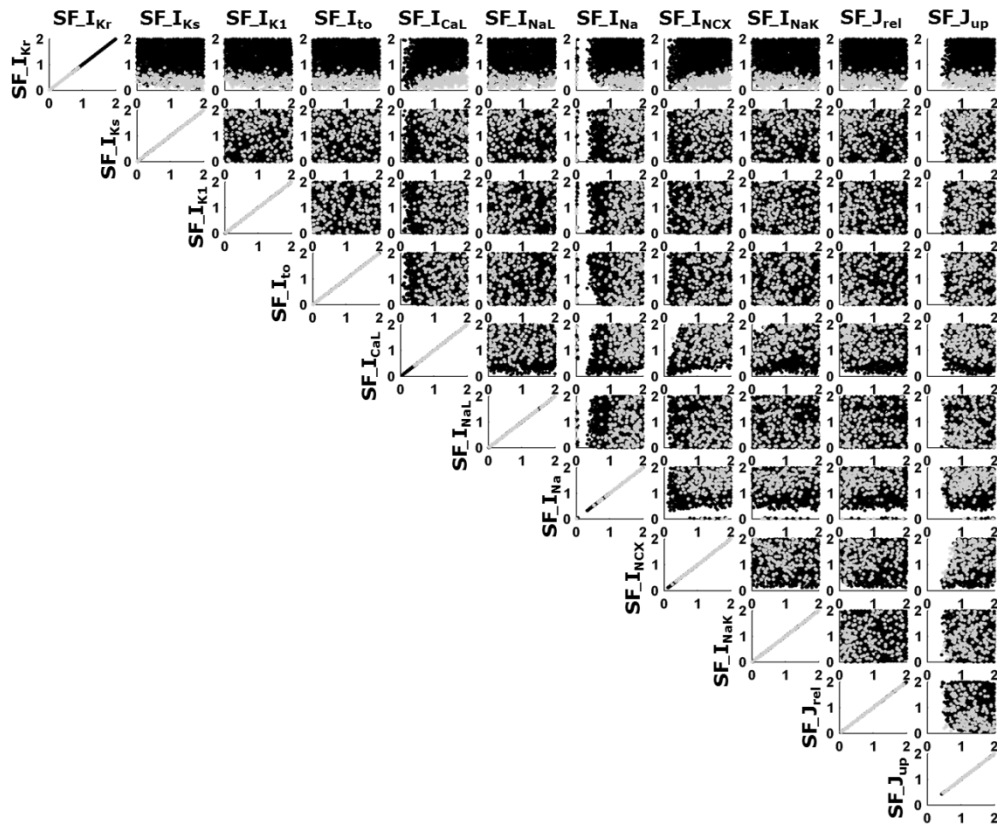


Figure 7.32: 2-by-2 plots of the scaling factors space for the HCM models showing RF (grey dots), compared the ones with normal APs (black dots).

In order to highlight the main ionic currents who seems to play a role in repolarisation abnormalities, the corresponding scaling factor boxplots have been compared in Figure 7.33, considering their distribution in the different subgroups: normal HCM APs, short/long EADs and repolarisation failure.

All these subgroups are characterised by a very low I_{Kr} : indeed, this current is the main contributor to APD prolongation in HCM. Most of the models show a high I_{CaL} , further increasing the APD. I_{NaL} is higher in the subgroups showing short/long EADs. I_{NCX} is increased in all the subgroup, but especially in long EADs and RF.

This analysis provided the basis to identify possible anti-arrhythmic therapies in HCM, which will be discussed in the Ionic Current Block section below.

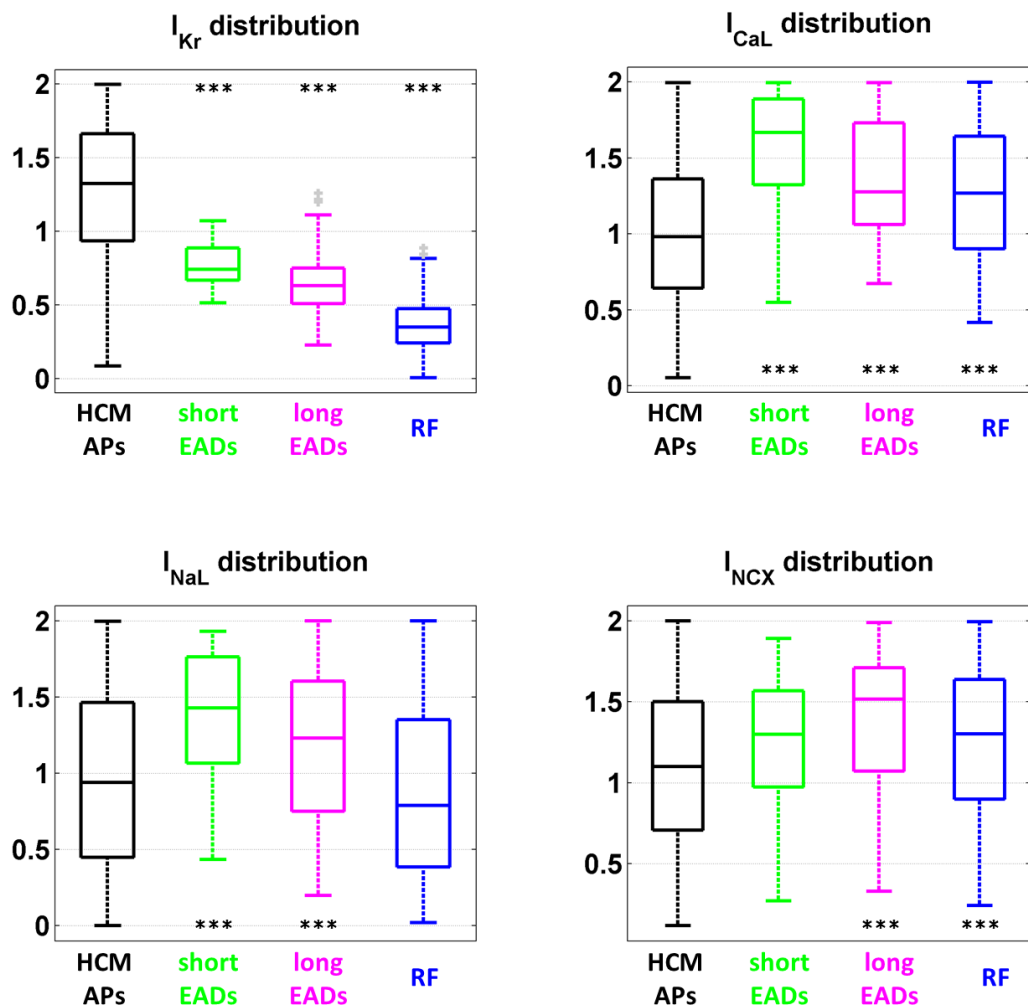


Figure 7.33: Boxplots comparison of the scaling factors for the ionic currents who seems to be involved in repolarisation abnormalities in HCM (***) $p < 0.0001$, with respect to normal HCM APs). The reduced I_{Kr} density seems to play the major role in determining repolarisation abnormalities: the lower its scaling factor range, the more severe they are. Also, a high I_{CaL} , further increasing the APD, is present in all the subgroups. The I_{NaL} density is higher in the subgroups showing EADs, while the I_{NCX} is increased mostly in long EADs and RF subgroups.

Ionic Mechanisms contribution to the HCM Phenotype

In order to analyse the contribution of every single ionic mechanisms to the global HCM phenotype, we ran some additional simulations.

As first, starting from the CTRL POMs, we introduced the HCM remodelling mechanisms, one at a time, and we evaluated their impact on the considered AP and CaT biomarkers (Figure 7.34). As expected, I_{Kr} and I_{NaL} are contributing to APD prolongation, while I_{CaL} , I_{NCX} , J_{up} and $TRPN_{max}$ have a high effect on CaT.

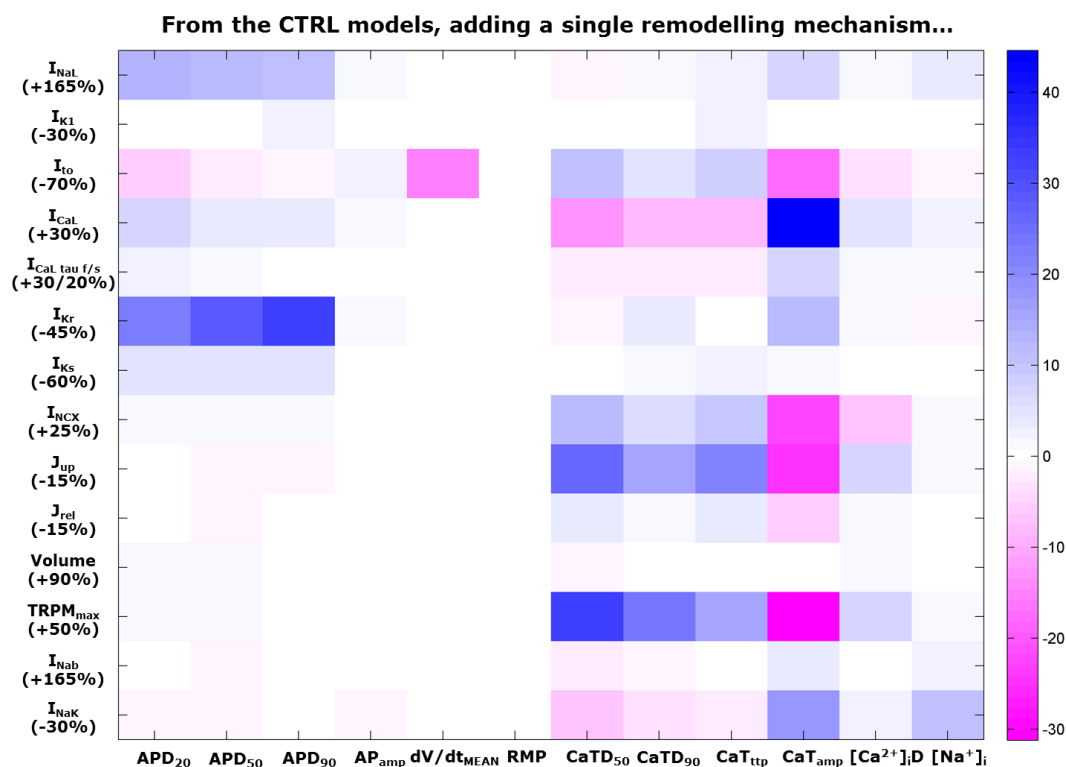


Figure 7.34: Summary of the contribution of each ionic mechanism to the global HCM phenotype. Starting from the CTRL POMs, the single remodelling mechanisms have been included individually, and their effect on AP and CaT biomarkers has been evaluated. Numerical values represent the % changes induced by each mechanism on the corresponding biomarker, with respect to CTRL POMs.

As second, starting from the HCM POMs, we restored the HCM remodelling mechanisms, one at a time, and we evaluated their impact on the considered AP and CaT biomarkers (Figure 7.35). As expected, I_{Kr} and I_{NaL} are contributing to APD prolongation, while I_{CaL} , I_{NCX} , J_{up} and $TRPN_{max}$ have a high effect on CaT.

In both simulation series, we monitored the occurrence of short/long EADs and RFs, and results are shown in Figure 7.36: the numerical values represent the % changes in EADs/RF occurrence compared to CTRL (left panel) or HCM (right panel), depending on whether the mechanisms were individually added or restored.

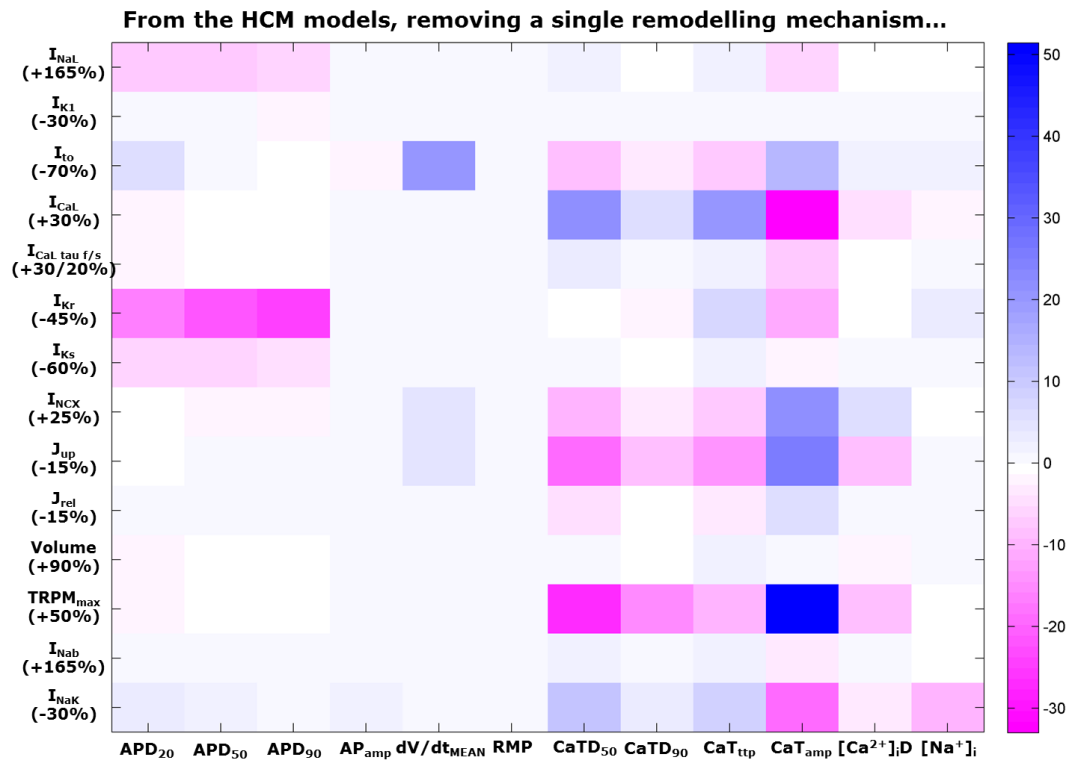


Figure 7.35: Summary of the contribution of each ionic mechanism to the global HCM phenotype. Starting from the HCM POMs, the single remodelling mechanisms have been restored individually, and their effect on AP and CaT biomarkers has been evaluated. Numerical values represent the % change induced by each mechanism on the corresponding biomarker, with respect to HCM POMs.

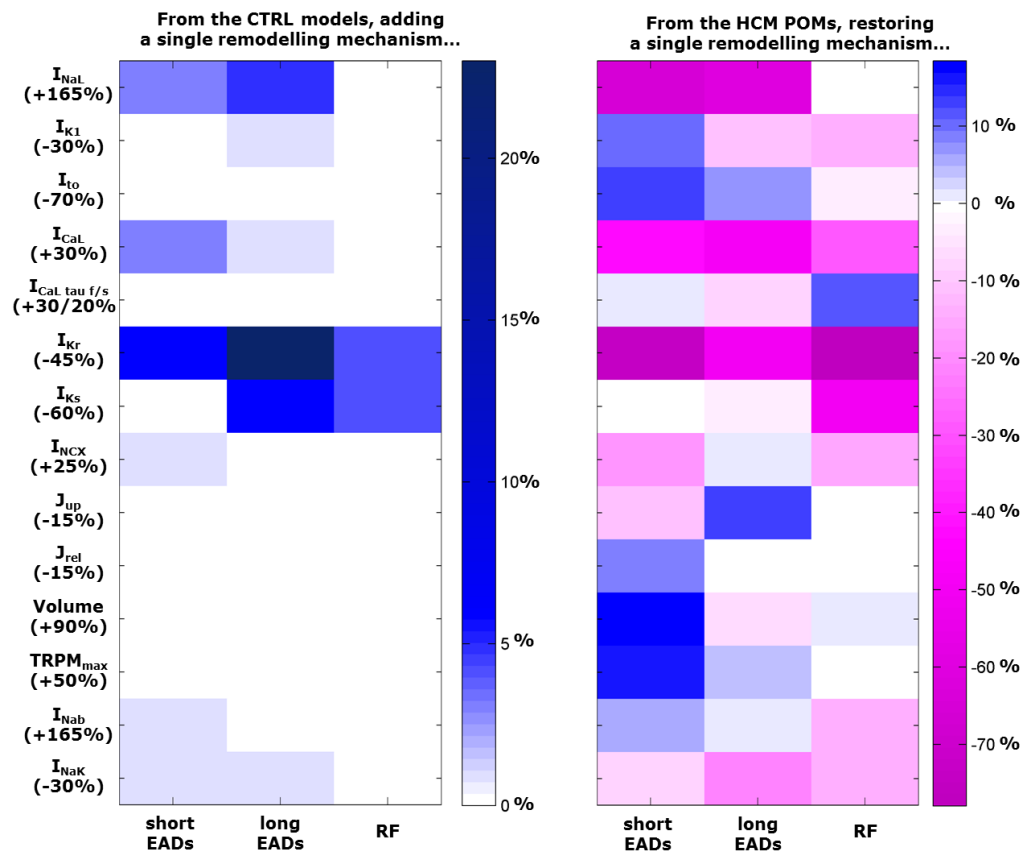


Figure 7.36: EADs/RF occurrence changes when adding a single remodelling mechanisms to the CTRL POMs (left panel) or restoring it in the HCM POMs (right panel).

Ionic Current Blocks

Based on the ionic mechanisms identified as relevant in the HCM models showing repolarisation abnormalities, we investigated *in silico* the effects of I_{NaL} and I_{NCX} blocks (-60% and -30%, respectively), since specific compounds are already available for these currents. The currents have been blocked both individually and simultaneously, and the effects have been evaluated on AP and CaT biomarkers, and repolarisation abnormalities occurrence. As a comparison, current blocks have been applied also to the CTRL models. Simulations results for selective I_{NaL} block have been compared with experimental data acquired with Ranolazine 10 μ M, while no experiments are available for I_{NCX} block.

A summary of current block effects on AP and CaT biomarkers is shown in Table 7.6 and Table 7.7, for CTRL and HCM respectively. Only the HCM models that didn't show repolarisation abnormalities in any of the simulation settings were considered to compute the numerical values, presented as mean \pm std.

Table 7.6: Summary of current block effects for CTRL (experimental data and POMs).

<i>CTRL AP biomarkers</i>	<i>I_{NaL} block</i>				<i>I_{NCX} block</i>		<i>Both blocks</i>	
	Experiments (n = 10)		Models (n = 2,254)		Models (n = 2,254)		Models (n = 2,254)	
APD₂₀ (ms)	87 \pm 46	-6.0%	112 \pm 29	-5%	116 \pm 27	-2%	110 \pm 27	-6%
APD₅₀ (ms)	175 \pm 73	-5.2%	202 \pm 55	-5%	204 \pm 55	-4%	194 \pm 52	-8%
APD₉₀ (ms)	261 \pm 115	-8.3%	273 \pm 86	-4%	276 \pm 87	-3%	263 \pm 82	-7%
AP_{amp} (mV)	109 \pm 11	+0.1%	118 \pm 6	+0.0%	118 \pm 6	+0.5%	119 \pm 6	+0.2%
RMP (mV)	-82 \pm 8	+0.7%	-78 \pm 1	+0.1%	-78 \pm 0.5	+0.1%	-78 \pm 0.5	+0.1%
dV/dt (V/s)	29 \pm 12	+0.6%	33 \pm 8	+1.2%	32 \pm 7	-0.0%	33 \pm 7	+2%
<i>CTRL CaT biomarkers</i>	<i>I_{NaL} block</i>				<i>I_{NCX} block</i>		<i>Both blocks</i>	
	Experiments (n = 12)		Models (n = 2,254)		Models (n = 2,254)		Models (n = 2,254)	
CaTD₅₀ (ms)	N.A.		190 \pm 43	+1%	160 \pm 35	-15%	161 \pm 35	-14%
CaTD₉₀ (ms)	N.A.		492 \pm 84	+0.1%	446 \pm 76	-9%	446 \pm 75	-9%
CaT_{tp} (ms)	N.A.		51 \pm 11	+2%	45 \pm 14	-11%	45 \pm 11	-10%
CaT_{amp} (nM)	N.A.		344 \pm 82	-4%	538 \pm 144	+50%	519 \pm 139	+44%
[Ca²⁺]_iD (nM)	N.A.		80 \pm 23	-1%	91 \pm 25	+12%	90 \pm 26	+12%
[Na⁺]_i (mM)	N.A.		7.0 \pm 1.7	-2%	7.0 \pm 1.7	-1%	6.9 \pm 1.6	-3%

Table 7.7: Summary of current block effects for HCM (experimental data and POMs).

<i>HCM AP biomarkers</i>	<i>I_{NaL} block</i>				<i>I_{NCX} block</i>		<i>Both blocks</i>	
	Experiments (n = 26)		Models (n = 1,891)		Models (n = 1,891)		Models (n = 1,891)	
APD ₂₀ (ms)	251±124	-18%	152±25	-7%	162±26	-1%	150±23	-9%
APD ₅₀ (ms)	350±164	-20%	294±53	-8%	308±60	-3%	282±51	-12%
APD ₉₀ (ms)	536±190	-19%	419±101	-8%	440±110	-4%	402±97	-12%
AP _{amp} (mV)	106±12	-3%	120±5	+0.5%	120±8	+0.3%	121±5	+0.7%
RMP (mV)	-82±8	+3%	-78±2	+0.7%	-77±5	+0.2%	-78±2	+0.9%
dV/dt (V/s)	21±3	-5%	25±6	+3%	25±6	+4%	26±6	+7%
<i>HCM CaT biomarkers</i>	<i>I_{NaL} block</i>				<i>I_{NCX} block</i>		<i>Both blocks</i>	
	Experiments (n = 25)		Models (n = 1,891)		Models (n = 1,891)		Models (n = 1,891)	
CaTD ₅₀	280±95	-18%	293±72	+3%	245±65	-14%	252±60	-12%
CaTD ₉₀	501±129	-19%*	670±80	-1%	635±91	-6%	629±76	-7%
CaT _{ttp}	100±30	-15%	62±12	+3%	53±18	-11%	55±11	-9%
CaT _{amp}	231±52	-28%**	259±90	-8%	387±137	+38%	360±115	+28%
[Ca ²⁺] _i D	163±50	-28%*	99±28	-1%	109±31	+9%	108±30	+9%
[Na ⁺] _i	N.A.		7.9±1.6	-3%	8.0±1.7	-2%	7.7±1.6	-5%

Considering the AP biomarkers, results of I_{NaL} block are qualitatively similar between models and experiments, both in HCM and CTRL. All the APDs are reduced when blocking I_{NaL} , and the effect is stronger in HCM where this current plays a major role. I_{NCX} alone doesn't affect much the AP biomarkers, but the variations are in the same direction, so that the APD shortening increases when blocking both currents at the same time.

As for CaT biomarkers, Ranolazine seems to affect them in the experiments much more than what blocking I_{NaL} does in models: probably a more detailed simulation of Ranolazine should consider its effect on other ionic currents as well (e.g. I_{Kr} and I_{CaL}) [25]. However, we are not interested in simulating Ranolazine but rather a very selective I_{NaL} block, since hopefully more specific compounds will be available soon [26]. As for I_{NCX} block, it reduces CaTD both in CTRL and HCM, while increasing CaT_{amp} and [Ca²⁺]_iD. The same effects are shown when considering I_{NCX} in association with I_{NaL} block. Both CaTD and CaT_{amp} variations are contrasting the changes induced by HCM remodelling, while the increase in [Ca²⁺]_iD, already higher in HCM, may be a drawback of blocking the exchanger.

We also analysed how the repolarisation abnormalities occurrence changed when considering current blocks. Both selective I_{NaL} and I_{NCX} blocks had a strong anti-arrhythmic effect in HCM, reducing especially short/long EADs. The simultaneous block of both currents proved to be even more successful, suppressing all the short EADs and 83% of the long ones. RF occurrence was reduced as well, but in a minor percentage. The distribution of repolarisation abnormalities in HCM with and without current blocks is shown in Figure 7.37.

It is worth noticing that about 20% of short/long EADs (33 models) were not suppressed by I_{NaL} nor I_{NCX} selective block, while they disappeared when considering the simultaneous block of both currents. A representative trace of a HCM model in this subgroup is shown in Figure 7.38.

Actually, the number of models in each subgroup is not enough to have a full comprehension of the current block effect on repolarisation abnormalities, since models can change subgroup: e.g. some of long EADs which appear in the population with I_{NaL} block were RF in the HCM population and not long EADs not suppressed by the considered block. Therefore, a full description of EADs/RF distribution is shown in Table 7.8. In addition, an alternative visual representation is given in Figure 7.39, using Circos, a software package for visualizing data and information in a circular layout [27], which is ideal for exploring relationships between objects or subgroups.

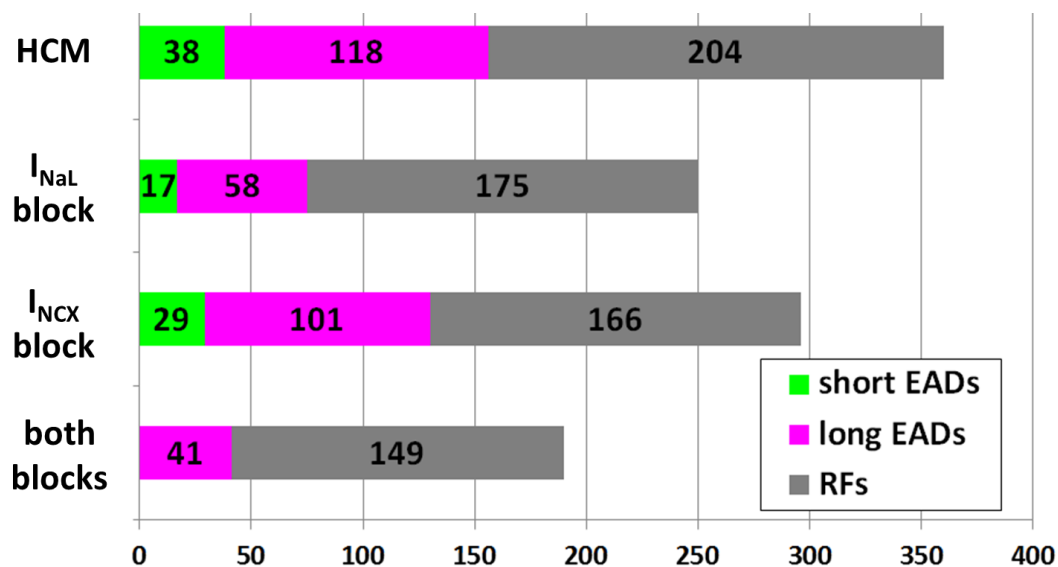


Figure 7.37: Repolarisation abnormalities occurrence in the HCM population, and the relative changes induced by current blocks. The values refer to the number of models in each subgroup.

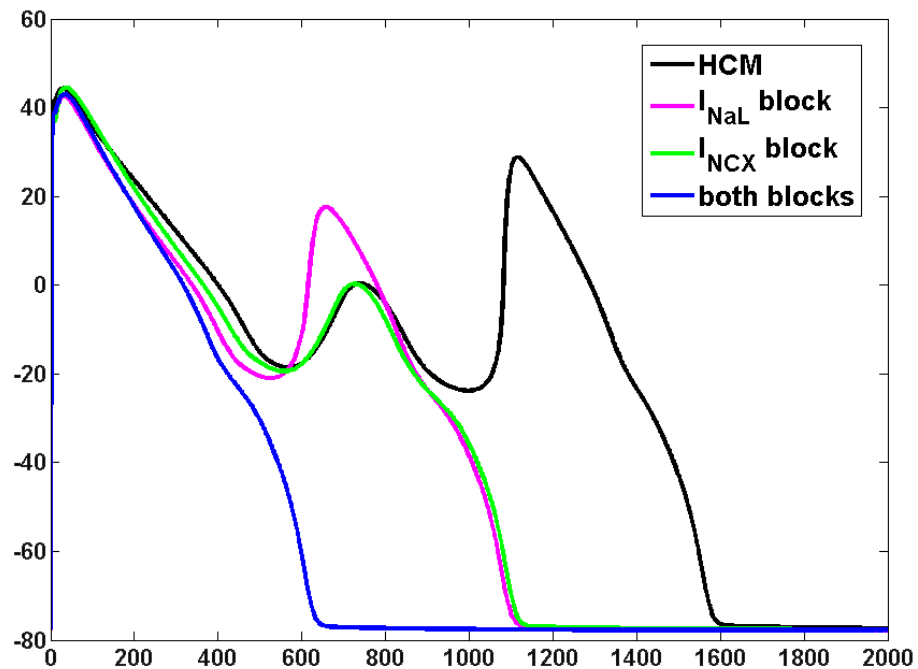


Figure 7.38: Representative AP traces of a HCM model showing long EAD, before and after adding in simulation the different current blocks. Both selective blocks failed to suppress the EAD, while the simultaneous I_{NaL} and I_{NCX} block proved to be successful. This happened in 33 HCM models.

Table 7.8: Detailed description of repolarisation abnormalities changes in HCM when considering the different current blocks. The percentage in bold shows the fraction of models in which the repolarisation abnormalities was successfully suppressed, leading to a normal HCM APs.

HCM population		HCM + I_{NaL} block		HCM + I_{NCX} block		HCM + both blocks	
short EADs	38	normal APs	37 (97%)	normal APs	27 (71%)	normal APs	38 (100%)
		short EADs	1	short EADs	9	short EADs	-
		long EADs	-	long EADs	2	long EADs	-
		RF	-	RF	-	RF	-
long EADs	118	normal APs	60 (51%)	normal APs	30 (25%)	normal APs	98 (83%)
		short EADs	15	short EADs	18	short EADs	2
		long EADs	35	long EADs	68	long EADs	17
		RF	8	RF	2	RF	1
RF	204	normal APs	13 (6%)	normal APs	10 (5%)	normal APs	31 (15%)
		short EADs	1	short EADs	-	short EADs	1
		long EADs	23	long EADs	30	long EADs	24
		RF	167	RF	164	RF	148

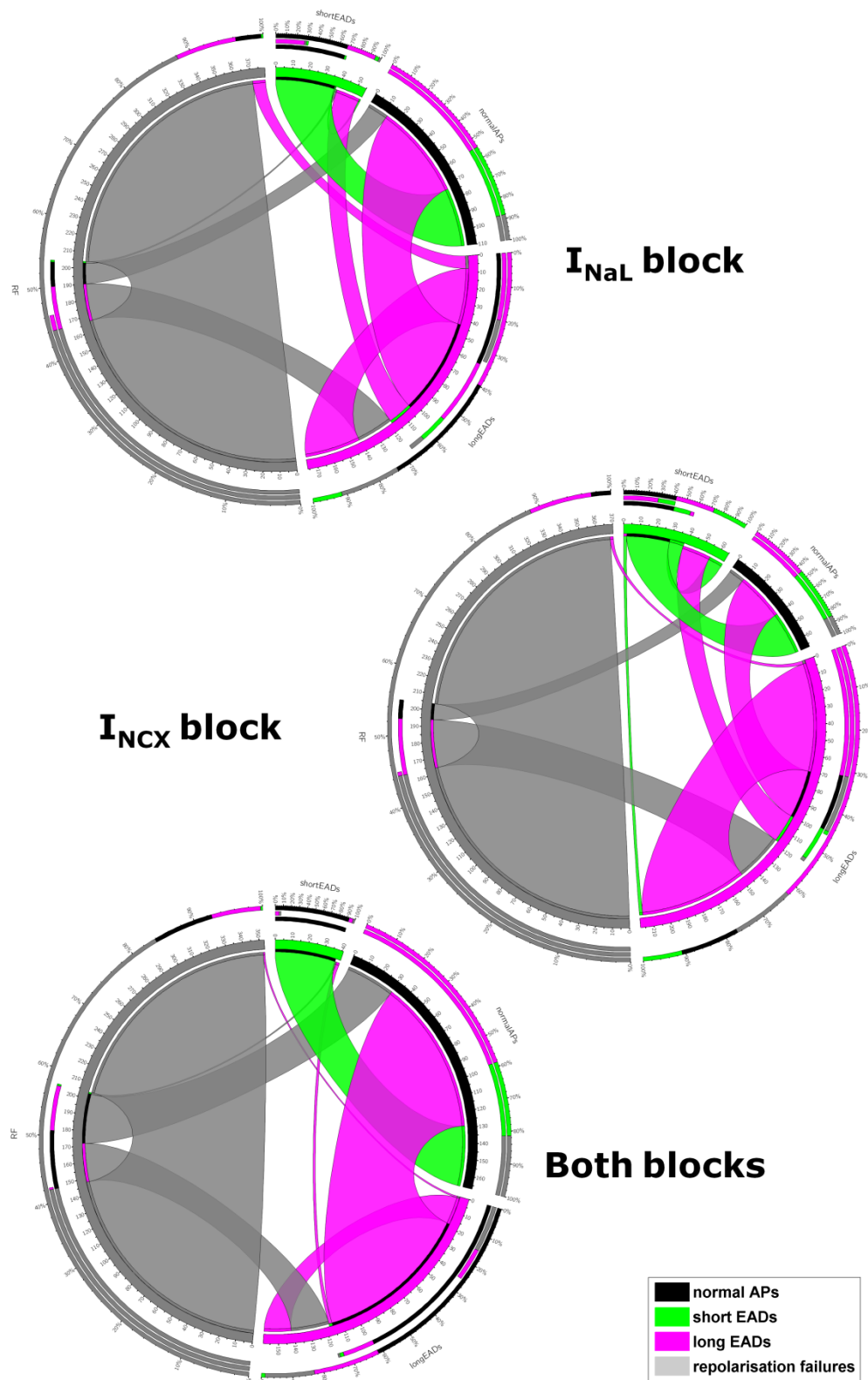


Figure 7.39: Circos plots to represent repolarisation abnormalities distribution in the HCM population. Every plot shows the number of models for each subgroup, before and after adding the current block, together with the incoming and outgoing fluxes from one subgroup to all the other ones. Considering e.g. the pink section in the top plot: when including I_{NaL} block, many long EADs disappear (they go into normal HCM APs subgroup), some of them become short EADs and some other just remain long EADs. A few models change from long EADs to RF, instead. In addition, there is an incoming flux of models from the RF subgroup, which have now become long EADs. The same apply to all the other subgroups and for all the considered ionic current blocks [27].

CONCLUSIONS

The population of model approach has been used to reproduce experimental data acquired from healthy (CTRL) and diseased (HCM) human single cells. Starting from the baseline AP model, an initial population has been generated, by varying 11 parameters probabilistically sampled in the [0%-200%] range, with respect to their original values. This initial population have been calibrated using the experimental data, i.e. by including only the models fully in agreement with a set of AP and CaT biomarkers: the final CTRL population consists of 2,254 models.

Starting from the CTRL population, we built the corresponding HCM one, by applying the electrical remodelling observed in experiments. Most of the main ionic currents have been modified according to voltage-clamp and protein expression data. In addition, we made three novel hypotheses, based on a literature review on HCM: an increased affinity of TRPN for Ca^{2+} , which is likely to elevate Ca^{2+} levels during diastole [3], a reduced maximal current of the Na^+/K^+ pump, due to energy depletion, which would be expected to compromise the regulation of energy-requiring transporters [7, 12], and an increase of the background Na^+ current, likely to be involved in the process of intracellular Ca^{2+} accumulation as well, by means of an increase in intracellular Na^+ and the consequent increase of $\text{Na}^+/\text{Ca}^{2+}$ exchanger current [10].

The simulated HCM phenotype was found qualitatively in agreement with the HCM experimental data, e.g. HCM population showed increased AP and CaT durations, reduced upstroke velocity and high intracellular Ca^{2+} concentration during diastole.

The contribution of each remodelling element has been investigated, by running two additional sets of simulations. As first, starting from the CTRL population, we introduced each remodelling mechanism, one at a time. Then, starting from the HCM population, we restored each one of them, again one at a time. In each of these stages, we evaluated the considered set of AP and CaT biomarkers.

About 16% of the HCM population showed EADs or repolarization failures. By analysing the population parameters, we pointed out the ionic mechanisms more likely underlying these repolarisation abnormalities, i.e. a very low I_{Kr} , high I_{CaL} , I_{NaL} and I_{NCX} .

Since specific compounds are already available for I_{NaL} and I_{NCX} , we investigated in simulation the effects occurring when blocking these currents. Both I_{NaL} and I_{NCX} blocks proved to have an anti-arrhythmic effect in HCM, partially reversing the HCM remodelling. In particular, their simultaneous block is suggested as an effective anti-arrhythmic therapy to suppress repolarisation abnormalities in HCM. I_{CaL} block has not been included up to now, since most of the compounds currently blocking this current are also reducing I_{Kr} , which is already compromised in HCM.

In conclusions, this study confirmed the population of models as a valid approach to include biological variability in computational modelling, especially when considering potential therapeutic targets and drug blocks. The HCM phenotype has been reproduced by using experimental data together with some novel hypotheses based on literature, thus highlighting the ionic mechanisms more likely to be involved in the electrical remodelling observed in this disease. In addition, current block results about the simultaneous block of I_{NaL} and I_{NCX} may constitute the basis for a new set of experiments, in order to check if model predictions are actually verified in single cells.

Future works will address the analysis of other pro-arrhythmic mechanisms, e.g. APD alternans and DADs, and the evaluation of other potential therapeutic targets, e.g. I_{CaL} . In addition, it would be interesting to replicate the same study considering a different AP model as baseline to build the population, to verify how much these results are dependent on the considered model. In particular, since Ca^{2+} handling seems to play a major role in HCM and the O'Hara-Rudy ventricular AP model has been used as baseline to generate the population of models considered in this study, it would be interesting to replicate it with the hybrid model introduced in Chapter 3, where the Ca^{2+} subsystem has been partly revisited.

Finally, some additional work has already been done: since most of the models showing repolarisation abnormalities, and especially RF, were characterised by a very low I_{Kr} , we repeated part of this study considering a new population of models, in which the same parameters have been varied in a reduced range ([50-150%], with respect to their original values). Results for the new population are consistent with the ones presented here, and RF occurrence is much lower in the population (0.5% compared to 9%). Some of the Figures/Tables presented in this chapter have been reproduced for the new population, and they have been included in Appendix B3.

References

- [1] B. J. Maron, “Sudden death in young athletes” *N Engl J Med*, vol. 349, no. 11, pp. 1064–75, Sep. 2003.
- [2] B. J. Maron and M. S. Maron, “Hypertrophic cardiomyopathy” *Lancet*, vol. 381, no. 9862, pp. 242–55, Jan. 2013.
- [3] H. Watkins, H. Ashrafian, and C. Redwood, “Inherited cardiomyopathies” *N Engl J Med*, vol. 364, no. 17, pp. 1643–56, Oct. 2011.
- [4] L. Thierfelder, H. Watkins, C. MacRae, R. Lamas, W. McKenna, H. P. Vosberg, J. G. Seidman, and C. E. Seidman, “Alpha-tropomyosin and cardiac troponin T mutations cause familial hypertrophic cardiomyopathy: a disease of the sarcomere” *Cell*, vol. 77, no. 5, pp. 701–12, Jun. 1994.
- [5] S. Huke and B. C. Knollmann, “Increased myofilament Ca²⁺-sensitivity and arrhythmia susceptibility” *J Mol Cell Cardiol*, vol. 48, no. 5, pp. 824–33, May 2010.
- [6] P. Robinson, P. J. Griffiths, H. Watkins, and C. S. Redwood, “Dilated and hypertrophic cardiomyopathy mutations in troponin and alpha-tropomyosin have opposing effects on the calcium affinity of cardiac thin filaments” *Circ Res*, vol. 101, no. 12, pp. 1266–73, Dec. 2007.
- [7] H. Ashrafian, C. Redwood, E. Blair, and H. Watkins, “Hypertrophic cardiomyopathy: a paradigm for myocardial energy depletion” *Trends Genet*, vol. 19, no. 5, pp. 263–8, May 2003.
- [8] R. Coppini, C. Ferrantini, L. Yao, P. Fan, M. Del Lungo, F. Stillitano, L. Sartiani, B. Tosi, S. Suffredini, C. Tesi, M. Yacoub, I. Olivotto, L. Belardinelli, C. Poggesi, E. Cerbai, A. Mugelli, M. B. Sikkil, K. T. MacLeod, and F. Gordon, “Late sodium current inhibition reverses electromechanical dysfunction in human hypertrophic cardiomyopathy” *Circulation*, vol. 128, no. 10, p. e156, Sep. 2013.
- [9] W. T. Clusin, “Calcium and Cardiac Arrhythmias: DADs, EADs, and Alternans” Sep. 2008.
- [10] S. Morotti, A. G. Edwards, A. D. McCulloch, D. M. Bers, and E. Grandi, “A novel computational model of mouse myocyte electrophysiology to assess the synergy between Na⁺ loading and CaMKII” *J Physiol*, vol. 592, no. Pt 6, pp. 1181–97, Mar. 2014.
- [11] R. Spoladore, M. S. Maron, R. D’Amato, P. G. Camici, and I. Olivotto, “Pharmacological treatment options for hypertrophic cardiomyopathy: high time for evidence” *Eur Heart J*, vol. 33, no. 14, pp. 1724–33, Jul. 2012.
- [12] H. Ashrafian, W. J. McKenna, and H. Watkins, “Disease pathways and novel therapeutic targets in hypertrophic cardiomyopathy” *Circ Res*, vol. 109, no. 1, pp. 86–96, Jun. 2011.
- [13] J. Walmsley, J. F. Rodriguez, G. R. Mirams, K. Burrage, I. R. Efimov, and B. Rodriguez, “mRNA expression levels in failing human hearts predict cellular electrophysiological remodeling: a population-based simulation study” *PLoS One*, vol. 8, no. 2, p. e56359, Jan. 2013.
- [14] O. J. Britton, A. Bueno-Orovio, K. Van Ammel, H. R. Lu, R. Towart, D. J. Gallacher, and B. Rodriguez, “Experimentally calibrated population of models predicts and explains intersubject variability in cardiac cellular electrophysiology” *Proc Natl Acad Sci USA*, vol. 110, no. 23, pp. E2098–105, Jun. 2013.

- [15] P. Gemmell, K. Burrage, B. Rodriguez, and T. A. Quinn, “Population of computational rabbit-specific ventricular action potential models for investigating sources of variability in cellular repolarisation” *PLoS One*, vol. 9, no. 2, p. e90112, Jan. 2014.
- [16] C. Sánchez, A. Bueno-Orovio, E. Wettwer, S. Loose, J. Simon, U. Ravens, E. Pueyo, and B. Rodriguez, “Inter-Subject Variability in Human Atrial Action Potential in Sinus Rhythm versus Chronic Atrial Fibrillation” *PLoS One*, vol. 9, no. 8, p. e105897, Jan. 2014.
- [17] A. Corrias, W. Giles, and B. Rodriguez, “Ionic mechanisms of electrophysiological properties and repolarization abnormalities in rabbit Purkinje fibers” *Am J Physiol Heart Circ. Physiol.*, vol. 300, no. 5, pp. H1806–13, May 2011.
- [18] C. Antzelevitch, L. Belardinelli, A. C. Zygmunt, A. Burashnikov, J. M. Di Diego, J. M. Fish, J. M. Cordeiro, and G. Thomas, “Electrophysiological effects of ranolazine, a novel antianginal agent with antiarrhythmic properties” *Circulation*, vol. 110, no. 8, pp. 904–10, Aug. 2004.
- [19] T. O’Hara, L. Virág, A. Varró, and Y. Rudy, “Simulation of the undiseased human cardiac ventricular action potential: model formulation and experimental validation” *PLoS Comput Biol*, vol. 7, no. 5, p. e1002061, May 2011.
- [20] M. D. McKay, R. J. Beckman, and W. J. Conover, “A Comparison of Three Methods for Selecting Values of Input Variables in the Analysis of Output from a Computer Code” *Technometrics*, vol. 21, no. 2, p. 239, May 1979.
- [21] H. Ashrafian, C. Redwood, E. Blair, and H. Watkins, “Hypertrophic cardiomyopathy: a paradigm for myocardial energy depletion” *Trends Genet*, vol. 19, no. 5, pp. 263–8, May 2003.
- [22] G. R. Mirams, C. J. Arthurs, M. O. Bernabeu, R. Bordas, J. Cooper, A. Corrias, Y. Davit, S.-J. Dunn, A. G. Fletcher, D. G. Harvey, M. E. Marsh, J. M. Osborne, P. Pathmanathan, J. Pitt-Francis, J. Southern, N. Zenzemi, and D. J. Gavaghan, “Chaste: an open source C++ library for computational physiology and biology” *PLoS Comput Biol*, vol. 9, no. 3, p. e1002970, Jan. 2013.
- [23] C. M. Lloyd, J. R. Lawson, P. J. Hunter, and P. F. Nielsen, “The CellML Model Repository” *Bioinformatics*, vol. 24, no. 18, pp. 2122–3, Sep. 2008.
- [24] S. Marino, I. B. Hogue, C. J. Ray, and D. E. Kirschner, “A methodology for performing global uncertainty and sensitivity analysis in systems biology” *J Theor Biol*, vol. 254, no. 1, pp. 178–96, Sep. 2008.
- [25] P.-C. Yang, Y. Song, W. R. Giles, B. Horvath, Y.-C. Izu, L. Belardinelli, S. Rajamani, and C. E. Clancy, “A computational modeling approach combined with cellular electrophysiology data provides insights into the therapeutic benefit of targeting late INa” *J Physiol*, Dec. 2014.
- [26] L. Belardinelli, G. Liu, C. Smith-Maxwell, W.-Q. Wang, N. El-Bizri, R. Hirakawa, S. Karpinski, C. H. Li, L. Hu, X.-J. Li, W. Crumb, L. Wu, D. Koltun, J. Zablocki, L. Yao, A. K. Dhalla, S. Rajamani, and J. C. Shryock, “A novel, potent, and selective inhibitor of cardiac late sodium current suppresses experimental arrhythmias” *J Pharmacol Exp Ther*, vol. 344, no. 1, pp. 23–32, Jan. 2013.
- [27] M. Krzywinski, J. Schein, I. Birol, J. Connors, R. Gascoyne, D. Horsman, S. J. Jones, and M. A. Marra, “Circos: an information aesthetic for comparative genomics” *Genome Res*, vol. 19, no. 9, pp. 1639–45, Sep. 2009.

GENERAL CONCLUSIONS

“For over half a century now, computational models have been used in synergy with experimental techniques to improve our understanding of the heart in health and disease. The contributions of computational modelling in cardiac physiology are numerous and the methodology is now well established within the cardiac basic science community. Currently, one of the challenges that the scientific community is facing is its translation to research closer to the bedside, through investigating the pathological states of the human heart and improving diagnosis and therapy”.

from “Computational cardiac electrophysiology is ready for prime time”

S Severi, B Rodriguez and A Zaza, Europace 2014

The research discussed in this thesis aims to contribute to this translation, focusing in particular on human cardiac action potential (AP) models. Definitely, there are still a lot of challenges to be solved before these models may be fully useful in translational research and clinical practice.

Here, some of these challenges have been faced:

- To extend models applicability, in order to reproduce *in vivo* more than *in vitro* conditions. As a relevant example, we investigated what happens when extracellular Ca^{2+} is set to the values measured in the interstitial fluid instead of the ones used for Tyrods’e solutions and how its variations affect the cardiac AP (**Section I, Chapter 3 and Chapter 4**).
- To find clinical contexts in which it is possible to compare macroscopic measures with simulation results, in order to better understand the correlation between the ionic mechanisms involved at a single cell level and the clinical patient phenotype. As a relevant example, we considered haemodialysis therapy (**Section II, Chapter 5 and Chapter 6**).
- To include biological variability in computational modelling, in order to extend model predictions to a population level, instead of considering results referring only to the average cell behaviour. As a relevant example, we considered hypertrophic cardiomyopathy (HCM), where variability seems to play a major role, especially when considering patient response to drugs (**Section III, Chapter 7**).

All these aspects have been investigated by using human cardiac AP models, and each one is discussed in details in a separate Section of this thesis. Every chapter has its own detailed conclusions at the end: therefore, here is only a brief summary of the main objectives achieved, together with a description of future works.

As discussed in **Chapter 3**, a new Markov model for the L-type Ca^{2+} current has been developed and integrated into the most recently published human ventricular AP model (O'Hara-Rudy, 2011), to improve its response to extracellular Ca^{2+} ($[\text{Ca}^{2+}]_o$) variations. The design of the new current model has been based on the hypothesis that Ca^{2+} -dependent inactivation is actually a fast voltage-dependent gating mechanism, activated when there is a high Ca^{2+} concentration in the cell, and also assuming that this inactivation is underestimated in most of the human cardiac AP models currently available. Based on these assumptions, the new hybrid model is indeed able to reproduce the inverse dependence experimentally observed between AP duration (APD) and $[\text{Ca}^{2+}]_o$, not properly reproduced in the original O'Hara-Rudy one. The hybrid model has already been validated against a wide range of experimental data, to check its consistency with the original one. Once fully validated, it will constitute a great tool to explore those clinical contexts in which electrolyte variations may occur, to evaluate the corresponding changes in cardiac electrophysiology, and to assess the possibly increased arrhythmic risk.

As future works, we are planning a more comprehensive analysis of electrolyte variations (considering also extracellular Na^+ and K^+) and the evaluation of their combined effects on a set of AP and Ca^{2+} transient (CaT) biomarkers, taking into account also potential pro-arrhythmic mechanisms, such as APD alternans and early/delayed after-depolarisations (EADs/DADs).

As an example, in **Chapter 4** the hybrid model has been used to analyse experimental data acquired during a bed-rest campaign organised by the European Space Agency, to assess the possibly increased arrhythmic risk for astronauts during space flights, due to microgravity exposure. Single cell and 1D simulation results were in agreement with ECG data analysis, providing evidence of a biphasic change in repolarisation occurring during bed-rest. Moreover, simulations supported a causal relation between the observed QT prolongation and the changes in electrolytes occurring during bed-rest. Unfortunately, the variability was really high among the volunteers and data acquisitions have been performed only a few times in the whole campaign: therefore, additional data are required to have a more accurate analysis. A new bed-rest experiment has been recently completed by ESA and new experimental data are expected to be available for further investigations in the near future.

In **Chapter 5** and **Chapter 6**, the haemodialysis (HD) therapy effects on cardiac AP have been investigated in end-stage renal disease (ESRD) patients, taking into account changes in extracellular electrolyte concentrations, heart rate and cell volume, together with the effect of different acetylcholine concentrations. Here, human atrial AP models have been considered, since atrial fibrillation (AF) incidence is high in ESRD patients.

The case report of a patient showing recurring paroxysmal AF during HD therapy has been used to speculate on intra-dialytic AF onset mechanisms, by combining experimental data, ECG analysis and computational simulations (**Chapter 6**). The HD therapy induces a slowdown in conduction velocity and a decrease of the refractory period, thus producing a vulnerable acute substrate which, in presence of a trigger (e.g. ectopic beats), may lead to AF.

The model used to analyse the patient data has been chosen after benchmarking all the available atrial AP models, with respect to their suitability to the HD context (**Chapter 5**).

Since none of the considered models was fully able to reproduce all the HD-induced effects on human atrial AP, future works will address specific changes in the most recent atrial models, in order to improve their performance in HD-related conditions. In addition, a similar benchmark of human ventricular models may be useful to explore the pro-arrhythmic mechanisms potentially induced by HD in ventricular cells.

Finally, **Chapter 7** shows an example of the population of models approach, used to investigate the electrical remodelling occurring in human HCM, based on experiments acquired in human single cells. The ionic mechanisms underlying the electrical remodelling and their contribution to the HCM phenotype have been evaluated, based on the experimental data available and new original hypotheses. Late Na^+ current (I_{NaL}) and $\text{Na}^+/\text{Ca}^{2+}$ exchanger (I_{NCX}), both up-regulated in HCM, have been identified as potential therapeutic targets in this disease. Since compounds to block these currents are already available on the market, both I_{NaL} and I_{NCX} inhibitions have been tested in the HCM population of models, evaluating the occurrence of pro-arrhythmic mechanisms, such as EADs and repolarisation failure. Simulation results showed that both current blocks have a positive effect, partially reversing the HCM phenotype and reducing repolarisation abnormalities

occurrence. In particular, the combined block of both I_{NaL} and I_{NCX} is suggested as an effective anti-arrhythmic strategy in human HCM.

Future works will address the analysis of other pro-arrhythmic mechanisms, e.g. APD alternans and DADs, and the evaluation of other potential therapeutic targets, e.g. I_{CaL} . In addition, since the O'Hara-Rudy ventricular AP model has been used as baseline to generate the population of models considered in this study, it would be very interesting to see how model dependent are these results, by reproducing the same study with a different model as baseline. In particular, since Ca^{2+} handling plays a big role in HCM, it would be worth considering the hybrid model introduced in Chapter 3, where the Ca^{2+} subsystem has been partly revisited.

As general conclusions, a few observations can be made:

- The currently published AP models, both atrial and ventricular, still have some open issues, especially when applied to contexts different from those considered for their development and validation. An accurate description of the cellular electrophysiology is particularly crucial to avoid misinterpretations when model are needed for predictions.
- Biological variability plays a major role in cardiac electrophysiology and it cannot be ignored in computational modelling. The population of models approach proved to be a valid tool to account for it, providing the means to investigate pro-arrhythmic mechanisms or drug action in a probabilistic way: e.g. % of EADs occurrence in HCM.
- Nowadays, models allow to investigate and understand very specific clinical situations, such as the patient-specific response to a therapy (e.g. the patient with paroxysmal AF during HD), or the effect of current blockers in a cell population. This is particularly relevant for drug action studies, for which the importance of *in silico* techniques is increasing year by year. The US Food and Drug administration, recently announced a new paradigm for the evaluation of new molecular entities: “the comprehensive *in-vitro* pro-arrhythmia assay” (Sager et al. “Rechanneling the cardiac pro-arrhythmia safety paradigm: a meeting report from the Cardiac Safety Research Consortium”, Am. Heart J. 2014), in which the integration of ion channel/drug interaction data into *in silico* models of human ventricular

electrophysiology is proposed, to predict and evaluate the corresponding changes in the human AP.

From all these observations, the need for a close link between experimental data and computational models clearly emerges. In fact, *in vivo* observations, *in vitro* experiments and *in silico* predictions have to be combined together to gain new insights into cardiac electrophysiology, linking ionic mechanisms to clinical patient phenotypes both in physiological and pathological conditions, thus improving patient diagnosis and treatment.

APPENDIX A

This Appendix includes part of the Matlab code used to generate the results presented in Chapter 3 and Chapter 4:

1. Modified ORd model: Matlab function file modORd.m
2. Script with the model parameters: file modORd_par.m
3. Script to run the model: file modORd_main.m

1. Modified ORd model: Matlab function file modORd.m

```
function output = modORd(t,X,varargin)
%%%%%%%%%%%%%%%%%%%%%%%%%%%%%%%%%%%%%%%%%%%%%%%%%%%%%%%%%%%%%%%%%%%%%%%%
% O'Hara-Rudy Human Ventricular Model (2011)
%
% Original Matlab file from:
% http://rudylab.wustl.edu/research/cell/code/AllCodes.html
%
% Related Journal Paper
% http://www.ncbi.nlm.nih.gov/pubmed/21637795
%
% * Structure & ICaL modified by Ely (Last Update: Jan 2014)
%
%%%%%%%%%%%%%%%%%%%%%%%%%%%%%%%%%%%%%%%%%%%%%%%%%%%%%%%%%%%%%%%%%%%%%%%%
global kCDI cPCa cVss cVsr cJup bJdiff bGncx bGKr klr_down...
jncass_n jncass_s jncass_d jncass_k... % jca
tau_nca Km_nca k2n_nca km2n_nca... % nca
dss_n dss_k dss_s dss_d taud_k taud_k1 taud_k2 taud_s1 taud_s2... % d
jss_n jss_s jss_d jss_k tj_max tj_min tj_media tj_sd... % j
flss_n flss_s flss_d flss_k... % f1
tf1_kk tf1_n tf1_k tf1_k1 tf1_k2 tf1_s1 tf1_s2 tf1_d1 tf1_d2... % tf1
tf2_kk tf2_n tf2_k tf2_k1 tf2_k2 tf2_s1 tf2_s2 tf2_d1 tf2_d2... % tf2
a2_rel n_rel s_rel exp_rel ntau1_rel ntau2_rel n2_rel % RyRs
%%%%%%%%%%%%%%%%%%%%%%%%%%%%%%%%%%%%%%%%%%%%%%%%%%%%%%%%%%%%%%%%%%%%%%%%
%% Optional Inputs:
% (Default values *)
% 1) flag_ode:
% - flag_ode=0 -> "computed variables" output
% - flag_ode=1* -> dX output
% 2) celltype:
% - celltype=0* -> endo
% - celltype=1 -> epi
% - celltype=2 -> M
% 3) pstim: stimulation protocol and parameters
% - pstim=1* -> I-clamp, single beat
% - pstim=[2 CL] -> I-clamp, multiple beats with CL as input
% - pstim=[3 vclamp] -> Ely V-clamp, single V-step
% - pstim=[4 vclamp] -> Grandi-Bers 2010 V-clamp, single V-step
% 4) Extracellular Ionic Concentrations [cCao cNao cKo] mM:
% default values: Cao = 1.8mM*; Nao = 140mM*; cKo = 5.4mM*
% - if length=1 -> [cCao] only
% - if length=2 -> [cCao cNao]
% - if length=3 -> [cCao cNao cKo]
% 5) bn: % of ICaL CDI block (VDI-only ICaL)
% - bn=1* -> no CDI block
% - bn=0 -> CDI total block
% 6) Ib: currents block -> [0-1] for each current/flux (11 total):
% Ib=[bINa bINaL bito bICaL bIKr bIKs bIKl bINaCa bINaK bJup bJrel];
%%%%%%%%%%%%%%%%%%%%%%%%%%%%%%%%%%%%%%%%%%%%%%%%%%%%%%%%%%%%%%%%%%%%%%%%
%% Optional Inputs setting:
% Set default values for optional inputs
cEx0 = [1.8, 140.0, 5.4];
Ib0 = ones(11,1);
ki_cost0 = 0;
optargs = {1,0,1,cEx0,1,Ib0,ki_cost0};
% skip any new inputs, if empty
newVals = cellfun(@(x) ~isempty(x), varargin);
% overwrite inputs specified in varargin
optargs(newVals) = varargin(newVals);
% [optargs(1:length(varargin))] = varargin{:};
[flag_ode, celltype, pstim, cEx, bn, Ib,ki_cost]=optargs{:};
```

```

%%%%%%%%%%%%%%%%%%%%%%%%%%%%%%%%%%%%%%%%%%%%%%%%%%%%%%%%%%%%%%%%%%%%%%%%
%% State Variables
% -> Membrane Potential V
v = X(1);
% -> Ionic Concentrations
nai = X(2);    nass = X(3);
if ki_cost==0;
ki   = X(4);    kss   = X(5);
else
ki   = ki_cost; kss   = ki_cost;
end
cai = X(6);    cass = X(7);    casr = X(9);
% -> INa gv
m = X(10);    hf = X(11);    hs = X(12);
j = X(13);    hsp = X(14);    jp = X(15);
% -> INaL gv
mL = X(16);    hL = X(17);    hLp = X(18);
% -> Ito gv
a = X(19);    iF = X(20);    iS = X(21);
ap = X(22);    iFp = X(23);    iSp = X(24);
% -> ICaL gv
% d      ff      fs
% fcac  fcas  jca
% nca   ffp   fcafp
% -> IKr
xrf = X(34);    xrs = X(35);
% -> IKs
xsl = X(36);    xs2 = X(37);
% -> IKl
xkl = X(38);
% -> Fluxes
Jrelnp = X(39); Jrelp = X(40);
% -> CaMKt
CaMKt = X(41);
% -> ICaL Markov
I1k = X(42);    I2k = X(43);    Ck = X(44);
I1kp = X(45);   I2kp = X(46);   Ckp = X(47);
I1Cak = X(48);  I2Cak = X(49);  CCak = X(50);
I1Cakp = X(51); I2Cakp = X(52); CCakp = X(53);
Ok = X(26);    Okp = X(27);
jnca = X(54);   nca = bn*X(31);
%%%%%%%%%%%%%%%%%%%%%%%%%%%%%%%%%%%%%%%%%%%%%%%%%%%%%%%%%%%%%%%%%%%%%%%%
%% Extracellular Ionic Concentrations [mM]
if length(cEx)==1
    nao = cEx(2);    %[Na]o mM
    cao = cEx;      %[Ca]o mM
    ko = cEx(3);    %[K]o mM
elseif length(cEx)==2
    nao = cEx(2);    %[Na]o mM
    cao = cEx(1);    %[Ca]o mM
    ko = cEx(3);    %[K]o mM
elseif length(cEx)==3
    nao = cEx(2);    %[Na]o mM
    cao = cEx(1);    %[Ca]o mM
    ko = cEx(3);    %[K]o mM
else
    error('Extracellular Concentrations Error!!!');
end
%%%%%%%%%%%%%%%%%%%%%%%%%%%%%%%%%%%%%%%%%%%%%%%%%%%%%%%%%%%%%%%%%%%%%%%%
%% Physical Constants:
R = 8314.0;    % J/kmol/K
T = 310.0;    % K
F = 96485.0;  % C/mol
vffrt = v*F*F/(R*T);
vfirt = v*F/(R*T);
%%%%%%%%%%%%%%%%%%%%%%%%%%%%%%%%%%%%%%%%%%%%%%%%%%%%%%%%%%%%%%%%%%%%%%%%
%% Cell Geometry (approximate by a cylinder of length L and radius r)
L = 0.01;    % cm
rad = 0.0011; % cm
vcell = 1000*pi*rad^2*L; % 38e-6 uL
% Geometric Area
Ageo = 2*pi*rad^2 + 2*pi*rad*L; % cm^2
% Capacitive Area
Acap = 2*Ageo; % cm^2
% Compartment Volumes (4)
vmyo = 0.68*vcell; % uL
vnsr = 0.0552*vcell; % uL

```

```

vjsr = 0.0048*vcell; % uL
vsr = cVsr*(vnsr+vjsr); % uL
vss = cVss*0.02*vcell; % uL
%%%%%%%%%%%%%%%%%%%%%%%%%%%%%%%%%%%%%%%%%%%%%%%%%%%%%%%%%%%%%%%%%%%%%%%%
%% CaMK Constants
KmCaMK = 0.15; aCaMK = 0.05; bCaMK = 0.00068;
CaMKo = 0.05; KmCaM = 0.0015;
%%%%%%%%%%%%%%%%%%%%%%%%%%%%%%%%%%%%%%%%%%%%%%%%%%%%%%%%%%%%%%%%%%%%%%%%
%% update CaMK -> X(41)
CaMKb = CaMKo*(1.0-CaMkt) / (1.0+KmCaM/cass);
CaMKa = CaMKb+CaMkt;
dCaMkt = aCaMK*CaMKb*(CaMKb+CaMkt) - bCaMK*CaMkt;
%%%%%%%%%%%%%%%%%%%%%%%%%%%%%%%%%%%%%%%%%%%%%%%%%%%%%%%%%%%%%%%%%%%%%%%%
%% Reversal Potentials
ENa = (R*T/F)*log(nao/nai);
EK = (R*T/F)*log(ko/ki);
PKNa = 0.01833;
EKS = (R*T/F)*log((ko+PKNa*nao)/(ki+PKNa*nai));
%%%%%%%%%%%%%%%%%%%%%%%%%%%%%%%%%%%%%%%%%%%%%%%%%%%%%%%%%%%%%%%%%%%%%%%%
%% INa current
mss=1.0/(1.0+exp(-(v+39.57)/9.871));
tm=1.0/(6.765*exp((v+11.64)/34.77)+8.552*exp(-(v+77.42)/5.955));
dm=(mss-m)/tm;
hss=1.0/(1+exp((v+82.90)/6.086));
thf=1.0/(1.432e-5*exp(-(v+1.196)/6.285)+6.149*exp((v+0.5096)/20.27));
ths=1.0/(0.009794*exp(-(v+17.95)/28.05)+0.3343*exp((v+5.730)/56.66));
Ahf=0.99;
Ahs=1.0-Ahf;
dhf=(hss-hf)/thf;
dhs=(hss-hs)/ths;
h=Ahf*hf+Ahs*hs;
jss=hss;
tj=2.038+1.0/(0.02136*exp(-(v+100.6)/8.281)+0.3052*exp((v+0.9941)/38.45));
dj=(jss-j)/tj;
hssp=1.0/(1+exp((v+89.1)/6.086));
thsp=3.0*ths;
dhsp=(hssp-hsp)/thsp;
hp=Ahf*hf+Ahs*hs;
tjp=1.46*tj;
djp=(jss-jp)/tjp;
GNa=75;
fINap=(1.0/(1.0+KmCaMK/CaMKa));
INa=Ib(1)*GNa*(v-ENa)*m^3.0*((1.0-fINap)*h*j+fINap*hp*jp);
%%%%%%%%%%%%%%%%%%%%%%%%%%%%%%%%%%%%%%%%%%%%%%%%%%%%%%%%%%%%%%%%%%%%%%%%
%% INaL current
mLss=1.0/(1.0+exp(-(v+42.85)/5.264));
tmL=tm;
dmL=(mLss-mL)/tmL;
hLss=1.0/(1.0+exp((v+87.61)/7.488));
thL=200.0;
dhL=(hLss-hL)/thL;
hLssp=1.0/(1.0+exp((v+93.81)/7.488));
thLp=3.0*thL;
dhLp=(hLssp-hLp)/thLp;
GNaL=0.0075;
if celltype==1
    GNaL=GNaL*0.6;
end
fINaLp=(1.0/(1.0+KmCaMK/CaMKa));
INaL=Ib(2)*GNaL*(v-ENa)*mL*((1.0-fINaLp)*hL+fINaLp*hLp);
%%%%%%%%%%%%%%%%%%%%%%%%%%%%%%%%%%%%%%%%%%%%%%%%%%%%%%%%%%%%%%%%%%%%%%%%
%% Ito current
ass=1.0/(1.0+exp(-(v-14.34)/14.82));
ta=1.0515 / (1.0/(1.2089*(1.0+exp(-(v-18.4099)/29.3814)))+...
            3.5/(1.0+exp((v+100.0)/29.3814)));
da=(ass-a)/ta;
iss=1.0/(1.0+exp((v+43.94)/5.711));
if celltype==1
    delta_epi=1.0-(0.95/(1.0+exp((v+70.0)/5.0)));
else
    delta_epi=1.0;
end
tiF=4.562+1/(0.3933*exp(-(v+100.0)/100.0)+0.08004*exp((v+50.0)/16.59));
tiS=23.62+1/(0.001416*exp(-(v+96.52)/59.05)+...
            1.780e-8*exp((v+114.1)/8.079));
tiF=tiF*delta_epi;
tiS=tiS*delta_epi;

```

```

AiF=1.0/(1.0+exp((v-213.6)/151.2));
AiS=1.0-AiF;
diF=(iss-iF)/tiF;
diS=(iss-iS)/tiS;
i=AiF*iF+AiS*iS;
assp=1.0/(1.0+exp((-v-24.34)/14.82));
dap=(assp-ap)/ta;
dti_develop=1.354+1.0e-4/(exp((v-167.4)/15.89)+exp(-(v-12.23)/0.2154));
dti_recover=1.0-0.5/(1.0+exp((v+70.0)/20.0));
tiFp=dti_develop*dti_recover*tiF;
tiSp=dti_develop*dti_recover*tiS;
diFp=(iss-iFp)/tiFp;
diSp=(iss-iSp)/tiSp;
ip=AiF*iFp+AiS*iSp;
Gto=0.02;
if celltype==1
    Gto=Gto*4.0;
elseif celltype==2
    Gto=Gto*4.0;
end
fItop=(1.0/(1.0+KmCaMK/CaMKa));
Ito=Ib(3)*Gto*(v-EK)*((1.0-fItop)*a*i+fItop*ap*ip);
%%%%%%%%%%%%%%%%%%%%%%%%%%%%%%%%%%%%%%%%%%%%%%%%%%%%%%%%%%%%%%%%%%%%%%%%
%% ICaL, ICaNa, ICaK current section
%%%%%%%%%%%%%%%%%%%%%%%%%%%%%%%%%%%%%%%%%%%%%%%%%%%%%%%%%%%%%%%%%%%%%%%%
% -> p vs np ICaL
fICaLp=(1.0/(1.0+KmCaMK/CaMKa));
% -> up/down rates
r_down = bn*(k1r_down);
r_up = bn*(r_down*nca/(1-nca));
% n gate -> CDI vs VDI
jncass = jncass_n/(1.0+exp((v+jncass_s)/jncass_d))+jncass_k;
tjnca = tau_nca;
djnca = (jncass-jnca)/tjnca;
Kmn = Kmn_nca;
k2n = k2n_nca;
km2n = km2n_nca*jnca;
anca=1/(k2n/km2n+(1.0+Kmn/cass)^4.0);
dnca=bn*(anca*k2n-nca*km2n);
%%%%%%%%%%%%%%%%%%%%%%%%%%%%%%%%%%%%%%%%%%%%%%%%%%%%%%%%%%%%%%%%%%%%%%%%
%% -> Activation (d) rates: alpha/beta
% dss = 1.0/(1.0+exp((-v+3.940)/4.230));
% td = 0.6+1.0/(exp(-0.05*(v+6.0))+exp(0.09*(v+14.0)));
dss = dss_n/(1.0+exp((-v+dss_s)/dss_d))+dss_k;
td = (taud_k+1.0/(exp(taud_k1*(v+taud_s1))+exp(taud_k2*(v+taud_s2)))));
alpha = dss/td;
beta = (1-dss) / td;
%%%%%%%%%%%%%%%%%%%%%%%%%%%%%%%%%%%%%%%%%%%%%%%%%%%%%%%%%%%%%%%%%%%%%%%%
%% -> Recovery (j) rates: psi/omega
jcss_new= jss_n/(1.0+exp((v+jss_s)/jss_d)) + jss_k;
jcss_VD = jcss_new; jcss_CD = jcss_new;
jcss_VDp = jcss_new; jcss_CDP = jcss_new;
tjca_new = tj_min + tj_max*exp(-(v-tj_media)^2/(2*tj_sd^2));
tjca_VD = tjca_new; tjca_VDp = tjca_new;
tjca_CD = tjca_new; tjca_CDP = tjca_new;
psi_VD=jcss_VD/tjca_VD; psi_VDp=jcss_VDp/tjca_VDp;
psi_CD=jcss_CD/tjca_CD; psi_CDP=jcss_CDP/tjca_CDP;
omega_VD=(1-jcss_VD)/tjca_VD; omega_VDp=(1-jcss_VDp)/tjca_VDp;
omega_CD=(1-jcss_CD)/tjca_CD; omega_CDP=(1-jcss_CDP)/tjca_CDP;
%%%%%%%%%%%%%%%%%%%%%%%%%%%%%%%%%%%%%%%%%%%%%%%%%%%%%%%%%%%%%%%%%%%%%%%%
%% -> Fact Inactivation (f1) rates: gamma/delta
% flss = 1.0 / (1.0+exp((v+19.58)/3.696));
% tff = 7.0 + 1.0/(0.0045*exp(-(v+20.0)/10.0)+0.0045*exp((v+20.0)/10.0));
% tfcaf = 7.0 + 1.0/(0.04*exp(-(v-4.0)/7.0)+0.04*exp((v-4.0)/7.0));
flss_0 = flss_n / (1.0+exp((v+flss_s)/flss_d)) + flss_k;
tf1_0 = tf1_kk*(tf1_k + tf1_n./ (tf1_k1*exp((v+tf1_s1)/tf1_d1)+...
    tf1_k2*exp((v+tf1_s2)/tf1_d2)));
ktaup = 2.5;
gamma_VD = (1-flss_0) / tf1_0;
delta_VD = flss_0 / tf1_0;
gamma_VDp = gamma_VD/ktaup;
delta_VDp = delta_VD/ktaup;
gamma_CD=gamma_VD*kCDI; delta_CD=delta_VD*kCDI;
gamma_CDP=gamma_VDp*kCDI; delta_CDP=delta_VDp*kCDI;
tf1_VD = 1/(gamma_VD+delta_VD);
tf1_CD = 1/(gamma_CD+delta_CD);
flss_VD = gamma_VD / (gamma_VD+delta_VD);

```

```

flss_CD = gamma_CD / (gamma_CD+delta_CD);
%%%%%%%%%%%%%%%%%%%%%%%%%%%%%%%%%%%%%%%%%%%%%%%%%%%%%%%%%%%%%%%%%%%%%%%%
%% -> Slow Inactivation (f2) rates: gamma/delta
% fss=1.0/(1.0+exp((v+19.58)/3.696));
% tfs=1000.0+1.0/(0.000035*exp(-(v+5.0)/4.0)+0.000035*exp((v+5.0)/6.0));
% tfcas=100.0+1.0/(0.00012*exp(-v/3.0)+0.00012*exp(v/7.0));
tf2_VD = tf2_kk*(tf2_k + tf2_n./ (tf2_k1*exp((v+tf2_s1)/tf2_d1)+...
                                tf2_k2*exp((v+tf2_s2)/tf2_d2)));

tf2_CD = tf2_VD/kCDI;
tf2_VDp = tf2_VD*ktaup;
tf2_CDP = tf2_VD/kCDI*ktaup;
% Reversibility
theta_VD = alpha*gamma_VD*psi_VD/tf2_VD/...
           (alpha*gamma_VD*psi_VD+beta*delta_VD*omega_VD);
theta_CD = alpha*gamma_CD*psi_CD/tf2_CD/...
           (alpha*gamma_CD*psi_CD+beta*delta_CD*omega_CD);
theta_VDp = alpha*gamma_VDp*psi_VDp/tf2_VDp/...
           (alpha*gamma_VDp*psi_VDp+beta*delta_VDp*omega_VDp);
theta_CDP = alpha*gamma_CDP*psi_CDP/tf2_CDP/...
           (alpha*gamma_CDP*psi_CDP+beta*delta_CDP*omega_CDP);

eta_VD=1/tf2_VD - theta_VD;
eta_VDp=1/tf2_VDp - theta_VDp;
eta_CD=1/tf2_CD - theta_CD;
eta_CDP=1/tf2_CDP - theta_CDP;
tf2_VD = 1/(eta_VD+theta_VD);
tf2_CD = 1/(eta_CD+theta_CD);
f2ss_VD=eta_VD/(eta_VD+theta_VD);
f2ss_CD=eta_CD/(eta_CD+theta_CD);
%%%%%%%%%%%%%%%%%%%%%%%%%%%%%%%%%%%%%%%%%%%%%%%%%%%%%%%%%%%%%%%%%%%%%%%%
%% -> Driving Forces
PhiCaL=4.0*vffrt*(cass*exp(2.0*vfrt)-0.341*cao)/(exp(2.0*vfrt)-1.0);
PhiCaNa=1.0*vffrt*(0.75*nass*exp(1.0*vfrt)-0.75*nao)/(exp(1.0*vfrt)-1.0);
PhiCaK=1.0*vffrt*(0.75*kss*exp(1.0*vfrt)-0.75*ko)/(exp(1.0*vfrt)-1.0);
PCa=0.0001*cPca;
if celltype==1
    PCa=PCa*1.2;
elseif celltype==2
    PCa=PCa*2.5;
end
PCap=1.1*PCa;
PCaNa=0.00125*PCa;
PCaK=3.574e-4*PCa;
PCaNap=0.00125*PCap;
PCaKp=3.574e-4*PCap;
%%%%%%%%%%%%%%%%%%%%%%%%%%%%%%%%%%%%%%%%%%%%%%%%%%%%%%%%%%%%%%%%%%%%%%%%
%% -> Markov Model: VDI states
OCak = 1-CCak-I1Cak-I2Cak-Ck-I1k-I2k-Ok;
OCakp = 1-CCakp-I1Cakp-I2Cakp-Ckp-I1kp-I2kp-Okp;
dOk = alpha*Ck + delta_VD*I1k - (beta+gamma_VD)*Ok - r_up*Ok +
r_down*OCak;
dI2k = eta_VD*I1k + omega_VD*Ck - (theta_VD+psi_VD)*I2k - r_up*I2k +
r_down*I2Cak;
dI1k = theta_VD*I2k + gamma_VD*Ok - (eta_VD+delta_VD)*I1k - r_up*I1k +
r_down*I1Cak;
dCk = beta*Ok + psi_VD*I2k - (omega_VD+alpha)*Ck - r_up*Ck +
r_down*CCak;
dOkp = alpha*Ckp + delta_VDp*I1kp - (beta+gamma_VDp)*Okp - r_up*Okp +
r_down*OCakp;
dI2kp = eta_VDp*I1kp + omega_VDp*Ckp - (theta_VDp+psi_VDp)*I2kp - r_up*I2kp +
r_down*I2Cakp;
dI1kp = theta_VDp*I2kp + gamma_VDp*Okp - (eta_VDp+delta_VDp)*I1kp - r_up*I1kp +
r_down*I1Cakp;
dCkp = beta*Okp + psi_VDp*I2kp - (omega_VDp+alpha)*Ckp - r_up*Ckp +
r_down*CCakp;
%%%%%%%%%%%%%%%%%%%%%%%%%%%%%%%%%%%%%%%%%%%%%%%%%%%%%%%%%%%%%%%%%%%%%%%%
%% -> Markov Model: CDI states
dI2Cak = eta_CD*I1Cak + omega_CD*CCak - (theta_CD+psi_CD)*I2Cak + r_up*I2k -
r_down*I2Cak;
dI1Cak = theta_CD*I2Cak + gamma_CD*OCak - (eta_CD+delta_CD)*I1Cak + r_up*I1k -
r_down*I1Cak;
dCCak = beta*OCak + psi_CD*I2Cak - (omega_CD+alpha)*CCak + r_up*Ck -
r_down*CCak;
dI2Cakp = eta_CDP*I1Cakp + omega_CDP*CCakp - (theta_CDP+psi_CDP)*I2Cakp +
r_up*I2kp - r_down*I2Cakp;
dI1Cakp = theta_CDP*I2Cakp + gamma_CDP*OCakp - (eta_CDP+delta_CDP)*I1Cakp +
r_up*I1kp - r_down*I1Cakp;

```

```

dCCakp = beta*OCakp + psi_CDP*I2Cakp - (omega_CDP+alpha)*CCakp + r_up*Ckp -
r_down*CCakp;
%%%%%%%%%%%%%%%%%%%%%%%%%%%%%%%%%%%%%%%%%%%%%%%%%%%%%%%%%%%%%%%%%%%%%%%%%%%%%%
%% -> ICaL ICaNa ICaK currents
ICaL_VD = Ib(4) * PCa * PhiCaL * Ok;
ICaL_VDp = Ib(4) * PCap * PhiCaL * Okp;
ICaL_CD = Ib(4) * PCa * PhiCaL * OCak;
ICaL_CDP = Ib(4) * PCap * PhiCaL * OCakp;
ICaNa_VD = Ib(4) * PCaNa * PhiCaNa * Ok;
ICaNa_VDp = Ib(4) * PCaNap * PhiCaNa * Okp;
ICaNa_CD = Ib(4) * PCaNa * PhiCaNa * OCak;
ICaNa_CDP = Ib(4) * PCaNap * PhiCaNa * OCakp;
ICaK_VD = Ib(4) * PCaK * PhiCaK * Ok;
ICaK_VDp = Ib(4) * PCaKp * PhiCaK * Okp;
ICaK_CD = Ib(4) * PCaK * PhiCaK * OCak;
ICaK_CDP = Ib(4) * PCaKp * PhiCaK * OCakp;
%%%%%%%%%%%%%%%%%%%%%%%%%%%%%%%%%%%%%%%%%%%%%%%%%%%%%%%%%%%%%%%%%%%%%%%%%%%%%%
%% ICaL VD vs CD & ICaL p vs np
ICaLnp = ICaL_VD + ICaL_CD;
ICaLp = ICaL_VDp + ICaL_CDP;
ICaLVd = ICaL_VD*(1-fICaLp) + ICaL_VDp*fICaLp;
ICaLCD = ICaL_CD*(1-fICaLp) + ICaL_CDP*fICaLp;

ICaNanp = ICaNa_VD + ICaNa_CD;
ICaNap = ICaNa_VDp + ICaNa_CDP;
ICaKnp = ICaK_VD + ICaK_CD;
ICaKp = ICaK_VDp + ICaK_CDP;

ICaL = ICaLp*fICaLp + ICaLnp*(1-fICaLp);
ICaNa = ICaNap*fICaLp + ICaNanp*(1-fICaLp);
ICaK = ICaKp*fICaLp + ICaKnp*(1-fICaLp);

% ICaL "experimental conductance"
gICaL = ICaL/PhiCaL;
%%%%%%%%%%%%%%%%%%%%%%%%%%%%%%%%%%%%%%%%%%%%%%%%%%%%%%%%%%%%%%%%%%%%%%%%%%%%%%
%% IKr current
xrss=1.0/(1.0+exp((-v+8.337)/6.789));
txrf=12.98+1.0/(0.3652*exp((v-31.66)/3.869)+...
4.123e-5*exp((-v-47.78)/20.38));
txrs=1.865+1.0/(0.06629*exp((v-34.70)/7.355)+...
1.128e-5*exp((-v-29.74)/25.94));
Axrf=1.0/(1.0+exp((v+54.81)/38.21));
Axrs=1.0-Axrf;
dxrf=(xrss-xrf)/txrf;
dxrs=(xrss-xrs)/txrs;
xr=Axrf*xrf+Axrs*xrs;
rkr=1.0/(1.0+exp((v+55.0)/75.0))*1.0/(1.0+exp((v-10.0)/30.0));
GKr=0.046*bGKr;
if celltype==1
    GKr=GKr*1.3;
elseif celltype==2
    GKr=GKr*0.8;
end
IKr=Ib(5)*GKr*sqrt(ko/5.4)*xr*rkr*(v-EK);
%%%%%%%%%%%%%%%%%%%%%%%%%%%%%%%%%%%%%%%%%%%%%%%%%%%%%%%%%%%%%%%%%%%%%%%%%%%%%%
%% IKs current
xslss=1.0/(1.0+exp((-v+11.60)/8.932));
txs1=817.3+1.0/(2.326e-4*exp((v+48.28)/17.80)+...
0.001292*exp((-v+210.0)/230.0));
dxs1=(xslss-xsl)/txs1;
xs2ss=xslss;
txs2=1.0/(0.01*exp((v-50.0)/20.0)+0.0193*exp((-v+66.54)/31.0));
dxs2=(xs2ss-xsl)/txs2;
KsCa=1.0+0.6/(1.0+(3.8e-5/cai)^1.4);
GKs=0.0034;
if celltype==1
    GKs=GKs*1.4;
end
IKs=Ib(6)*GKs*KsCa*xs1*xs2*(v-EKs);
%%%%%%%%%%%%%%%%%%%%%%%%%%%%%%%%%%%%%%%%%%%%%%%%%%%%%%%%%%%%%%%%%%%%%%%%%%%%%%
%% IK1 current
xklss=1.0/(1.0+exp(-(v+2.5538*ko+144.59)/(1.5692*ko+3.8115)));
txk1=122.2/(exp((-v+127.2)/20.36)+exp((v+236.8)/69.33));
dxk1=(xklss-xk1)/txk1;
rkl=1.0/(1.0+exp((v+105.8-2.6*ko)/9.493));
GK1=0.1908;

```

```

if celltype==1
    GK1=GK1*1.2;
elseif celltype==2
    GK1=GK1*1.3;
end
IK1=Ib(7)*GK1*sqrt(ko)*rk1*xk1*(v-EK);
%%%%%%%%%%%%%%%%%%%%%%%%%%%%%%%%%%%%%%%%%%%%%%%%%%%%%%%%%%%%%%%%%%%%%%%%
%% INaCa current (i + SS)
kna1=15.0;      kna2=5.0;      kna3=88.12;      kasymm=12.5;
wna=6.0e4;     wca=6.0e4;     wnaca=5.0e3;     KmCaAct=150.0e-6;
kcaon=1.5e6;   kcaoff=5.0e3;   qna=0.5224;     qca=0.1670;
zna=1.0;       Gncx=0.0008*bGncx;   zca=2.0;
if celltype==1
    Gncx=Gncx*1.1;
elseif celltype==2
    Gncx=Gncx*1.4;
end
% INaCa i current
hca=exp((qca*v*F)/(R*T));      hna=exp((qna*v*F)/(R*T));
h1=1+nai/kna3*(1+hna);        h2=(nai*hna)/(kna3*h1);
h3=1.0/h1;                    h4=1.0+nai/kna1*(1+nai/kna2);
h5=nai*nai/(h4*kna1*kna2);    h6=1.0/h4;
h7=1.0+nao/kna3*(1.0+1.0/hna); h8=nao/(kna3*hna*h7);
h9=1.0/h7;                    h10=kasymm+1.0+nao/kna1*(1.0+nao/kna2);
h11=nao*nao/(h10*kna1*kna2); h12=1.0/h10;
k1=h12*cao*kcaon;   k2=kcaoff;      k3p=h9*wca;      k3pp=h8*wnaca;
k3=k3p+k3pp;        k4p=h3*wca/hca;   k4pp=h2*wnaca;  k4=k4p+k4pp;
k5=kcaoff;          k6=h6*cai*kcaon;  k7=h5*h2*wna;   k8=h8*h11*wna;
x1=k2*k4*(k7+k6)+k5*k7*(k2+k3); x2=k1*k7*(k4+k5)+k4*k6*(k1+k8);
x3=k1*k3*(k7+k6)+k8*k6*(k2+k3); x4=k2*k8*(k4+k5)+k3*k5*(k1+k8);
E1=x1/(x1+x2+x3+x4);   E2=x2/(x1+x2+x3+x4);
E3=x3/(x1+x2+x3+x4);   E4=x4/(x1+x2+x3+x4);
allo=1.0/(1.0+(KmCaAct/cai)^2.0);
JncxNa=3.0*(E4*k7-E1*k8)+E3*k4pp-E2*k3pp;
JncxCa=E2*k2-E1*k1;
%
INaCa_i=Ib(8)*0.8*Gncx*allo*(zna*JncxNa+zca*JncxCa);
% INaCa ss current
h1=1+nass/kna3*(1+hna);      h2=(nass*hna)/(kna3*h1);
h3=1.0/h1;                   h4=1.0+nass/kna1*(1+nass/kna2);
h5=nass*nass/(h4*kna1*kna2); h6=1.0/h4;
h7=1.0+nao/kna3*(1.0+1.0/hna); h8=nao/(kna3*hna*h7);
h9=1.0/h7;                   h10=kasymm+1.0+nao/kna1*(1+nao/kna2);
h11=nao*nao/(h10*kna1*kna2); h12=1.0/h10;
k1=h12*cao*kcaon;   k2=kcaoff;      k3p=h9*wca;      k3pp=h8*wnaca;
k3=k3p+k3pp;        k4p=h3*wca/hca;   k4pp=h2*wnaca;  k4=k4p+k4pp;
k5=kcaoff;          k6=h6*cass*kcaon; k7=h5*h2*wna;   k8=h8*h11*wna;
x1=k2*k4*(k7+k6)+k5*k7*(k2+k3); x2=k1*k7*(k4+k5)+k4*k6*(k1+k8);
x3=k1*k3*(k7+k6)+k8*k6*(k2+k3); x4=k2*k8*(k4+k5)+k3*k5*(k1+k8);
E1=x1/(x1+x2+x3+x4);   E2=x2/(x1+x2+x3+x4);
E3=x3/(x1+x2+x3+x4);   E4=x4/(x1+x2+x3+x4);
allo=1.0/(1.0+(KmCaAct/cass)^2.0);
JncxNa=3.0*(E4*k7-E1*k8)+E3*k4pp-E2*k3pp;
JncxCa=E2*k2-E1*k1;
%
INaCa_ss=Ib(8)*0.2*Gncx*allo*(zna*JncxNa+zca*JncxCa);
%%%%%%%%%%%%%%%%%%%%%%%%%%%%%%%%%%%%%%%%%%%%%%%%%%%%%%%%%%%%%%%%%%%%%%%%
%% INaK current
k1p=949.5;      k1m=182.4;      k2p=687.2;      k2m=39.4;
k3p=1899.0;    k3m=79300.0;    k4p=639.0;     k4m=40.0;
Knai0=9.073;   Knao0=27.78;   delta2=-0.1550;
Knai=Knai0*exp((delta2*v*F)/(3.0*R*T));
Knao=Knao0*exp(((1.0-delta2)*v*F)/(3.0*R*T));
Kki=0.5;      Kko=0.3582;      MgADP=0.05;      MgATP=9.8;
Kmgatp=1.698e-7; H=1.0e-7;      eP=4.2;          Khp=1.698e-7;
Knap=224.0;   Kxkur=292.0;
P=eP/(1.0+H/Khp+nai/Knap+ki/Kxkur);
a1=(k1p*(nai/Knai)^3.0)/((1.0+nai/Knai)^3.0+(1.0+ki/Kki)^2.0-1.0);
b1=k1m*MgADP;
a2=k2p;
b2=(k2m*(nao/Knao)^3.0)/((1.0+nao/Knao)^3.0+(1.0+ko/Kko)^2.0-1.0);
a3=(k3p*(ko/Kko)^2.0)/((1.0+nao/Knao)^3.0+(1.0+ko/Kko)^2.0-1.0);
b3=(k3m*P*H)/(1.0+MgATP/Kmgatp);
a4=(k4p*MgATP/Kmgatp)/(1.0+MgATP/Kmgatp);
b4=(k4m*(ki/Kki)^2.0)/((1.0+nai/Knai)^3.0+(1.0+ki/Kki)^2.0-1.0);
x1=a4*a1*a2+b2*b4*b3+a2*b4*b3+b3*a1*a2;
x2=b2*b1*b4+a1*a2*a3+a3*b1*b4+a2*a3*b4;

```

```

x3=a2*a3*a4+b3*b2*b1+b2*b1*a4+a3*a4*b1;
x4=b4*b3*b2+a3*a4*a1+b2*a4*a1+b3*b2*a1;
E1=x1/(x1+x2+x3+x4);    E2=x2/(x1+x2+x3+x4);
E3=x3/(x1+x2+x3+x4);    E4=x4/(x1+x2+x3+x4);
zk=1.0;    JnakNa=3.0*(E1*a3-E2*b3);    JnakK=2.0*(E4*b1-E3*a1);    Pnak=30;
if celltype==1
    Pnak=Pnak*0.9;
elseif celltype==2
    Pnak=Pnak*0.7;
end
INaK=Ib(9)*Pnak*(zna*JnakNa+zk*JnakK);
%%%%%%%%%%%%%%%%%%%%%%%%%%%%%%%%%%%%%%%%%%%%%%%%%%%%%%%%%%%%%%%%%%%%%%%%
%% Background currents: IKb, INab, ICab
% IKb current
xkb = 1.0 / (1.0+exp(-(v-14.48)/18.34));
GKb = 0.003;
if celltype==1
    GKb = GKb*0.6;
end
IKb = GKb*xkb*(v-EK);
% INab current
PNab = 3.75e-10;
INab = PNab*vffrt*(nai*exp(vfirt)-nao)/(exp(vfirt)-1.0);
% ICab current
PCab = 2.5e-8;
ICab = PCab*4.0*vffrt*(cai*exp(2.0*vfirt)-0.341*cao)/(exp(2.0*vfirt)-1.0);
%%%%%%%%%%%%%%%%%%%%%%%%%%%%%%%%%%%%%%%%%%%%%%%%%%%%%%%%%%%%%%%%%%%%%%%%
%% IpCa current
GpCa = 0.0005;
IpCa = GpCa*cai/(0.0005+cai);
%%%%%%%%%%%%%%%%%%%%%%%%%%%%%%%%%%%%%%%%%%%%%%%%%%%%%%%%%%%%%%%%%%%%%%%%
%% Simulation Protocols
switch pstim(1)
case 1
    % 1 - Current_Clamp -> Single Istim current
    amp = -80.0;
    duration = 0.5;
    if t <= duration
        Istim = amp;
    else
        Istim = 0.0;
    end
    % update V -> X(1)
    dv = - (INa+INaL+Ito+ICaL+ICaNa+ICaK+IKr+IKs+IK1+...
            INaCa_i+INaCa_ss+INaK+INab+IKb+IpCa+ICab+Istim);
case 2
    % 2 - Current_Clamp -> Istim current with fixed CL
    CL = pstim(2);
    amp = -80.0;
    duration = 0.5;
    trem = rem(t,CL);
    if trem <= duration
        Istim = amp;
    else
        Istim = 0.0;
    end
    % update V -> X(1)
    dv = - (INa+INaL+Ito+ICaL+ICaNa+ICaK+IKr+IKs+IK1+...
            INaCa_i+INaCa_ss+INaK+INab+IKb+IpCa+ICab+Istim);
case 3
    % 3 - Voltage_Clamp (by Ely), with single Vclamp-step
    Istim = 0;
    % update V -> X(1)
    dv = 0;
case 4
    % 4 - Voltage_Clamp (as in Grandi-Bers 2010), with single Vclamp-step
    Rclamp=0.02;
    Istim = (v-pstim(2))/Rclamp;
    % update V -> X(1)
    dv = - (INa+INaL+Ito+ICaL+ICaNa+ICaK+IKr+IKs+IK1+...
            INaCa_i+INaCa_ss+INaK+INab+IKb+IpCa+ICab+Istim);
end
%%%%%%%%%%%%%%%%%%%%%%%%%%%%%%%%%%%%%%%%%%%%%%%%%%%%%%%%%%%%%%%%%%%%%%%%
%% Diffusion Fluxes
JdiffNa = (nass-nai) /2.0;
JdiffK = (kss-ki) /2.0;
Jdiff = (cass-cai) *bJdiff/0.2;

```

```

%%%%%%%%%%%%%%%%%%%%%%%%%%%%%%%%%%%%%%%%%%%%%%%%%%%%%%%%%%%%%%%%%%%%%%%%
%% RyRs CICR from JSR
bt=4.75;      a_rel=a2_rel*0.5*bt;
Jrel_inf=a_rel*(-ICaL)/(n2_rel+(n_rel/(casr+s_rel))^exp_rel);
if celltype==2
    Jrel_inf=Jrel_inf*1.7;
end
tau_rel=ntau1_rel*bt/(1.0+ntau2_rel/casr);
if tau_rel<0.001
    tau_rel=0.001;
end
dJrelnp=(Jrel_inf-Jrelnp)/tau_rel;

btp=1.25*bt;  a_relp=a2_rel*0.5*btp;
Jrel_infp=a_relp*(-ICaL)/(n2_rel+(n_rel/(casr+s_rel))^exp_rel);
if celltype==2
    Jrel_infp=Jrel_infp*1.7;
end
tau_relp=ntau1_rel*btp/(1.0+ntau2_rel/casr);
if tau_relp<0.001
    tau_relp=0.001;
end
dJrelp=(Jrel_infp-Jrelp)/tau_relp;
fJrelp=(1.0/(1.0+KmCaMK/CaMKa));
Jrel=Ib(11)*((1.0-fJrelp)*Jrelnp+fJrelp*Jrelp);
%%%%%%%%%%%%%%%%%%%%%%%%%%%%%%%%%%%%%%%%%%%%%%%%%%%%%%%%%%%%%%%%%%%%%%%%
%% Ca2+ Uptake Flux
Jupnp=0.004375*cai/(cai+0.00092);
Jupp=2.75*0.004375*cai/(cai+0.00092-0.00017); %provare a cambiare la parentesi
if celltype==1
    Jupnp=Jupnp*1.3;
    Jupp=Jupp*1.3;
end
fJupp=(1.0/(1.0+KmCaMK/CaMKa));
Jleak=0.0039375*casr/15.0;
Jup = cJup*Ib(10)*((1.0-fJupp)*Jupnp+fJupp*Jupp-Jleak);
Vmax_SRCaP = 1.0*5.3114e-3; % [mM/msec] (286 umol/L cytosol/sec)
Kmf = 0.246e-3; % [mM] default
Kmr = 1.7; % [mM]L cytosol
hillSRCaP = 1.787; % [mM]
Jup2=Vmax_SRCaP*((cai/Kmf)^hillSRCaP-(casr/Kmr)^hillSRCaP)...
    /(1+(cai/Kmf)^hillSRCaP+(casr/Kmr)^hillSRCaP);
%%%%%%%%%%%%%%%%%%%%%%%%%%%%%%%%%%%%%%%%%%%%%%%%%%%%%%%%%%%%%%%%%%%%%%%%
%% Calcium Buffer Constants
cmdnmax=0.05;
if celltype==1
    cmdnmax=cmdnmax*1.3;
end
kmcmdn=0.00238;  trpnmax=0.07;  kmtrpn=0.0005;
BSRmax=0.047;   KmBSR=0.00087;
BSLmax=1.124;  KmBSL=0.0087;
csqnmmax=10.0; kmcsqn=0.8;
%%%%%%%%%%%%%%%%%%%%%%%%%%%%%%%%%%%%%%%%%%%%%%%%%%%%%%%%%%%%%%%%%%%%%%%%
%% update [Na+]i, [K+]i and [Ca2+]i
% -> [Na]
dnai=- (Ina+INaL+3.0*INaCa_i+3.0*INaK+INab)*Acap/(F*vmyo)+JdiffNa*vss/vmyo;
dnass=- (ICaNa+3.0*INaCa_ss)*Acap/(F*vss)-JdiffNa;
% -> [K]
if ki_cost==0
    dki=- (Ito+IKr+IKs+IK1+IKb+Istim-2.0*INaK)*Acap/(F*vmyo)+JdiffK*vss/vmyo;
    dkss=- (ICaK)*Acap/(F*vss)-JdiffK;
else
    dki=0;
    dkss=0;
end
% -> [Ca]
Bcai = 1.0 / (1.0+cmdnmax*kmcmdn/(kmcmdn+cai)^2.0 +...
    trpnmax*kmtrpn/(kmtrpn+cai)^2.0);
dcai = Bcai*(-(IpCa+ICab-2.0*INaCa_i)*Acap/(2.0*F*vmyo) -...
    Jup*vsr/vmyo+Jdiff*vss/vmyo);
Bcass = 1.0/(1.0+BSRmax*KmBSR/(KmBSR+cass)^2.0 +...
    BSLmax*KmBSL/(KmBSL+cass)^2.0);
dcass = Bcass*(-(ICaL-2.0*INaCa_ss)*Acap/(2.0*F*vss) +...
    Jrel*vsr/vss-Jdiff);
Bcasr = 1.0/(1.0+csqnmmax*kmcsqn/(kmcsqn+casr)^2.0);
dcasr = Bcasr*(Jup-Jrel);
%%%%%%%%%%%%%%%%%%%%%%%%%%%%%%%%%%%%%%%%%%%%%%%%%%%%%%%%%%%%%%%%%%%%%%%%

```

```

%% Output Computation
% When flag==1 -> dX
if flag_ode==1
    output=[dv      dnai      dnass      dki      dkss...      % 1
            dcai      dcass      0          dcasr      dm...      % 2
            dhf      dhs      dj          dhsp      djp...      % 3
            dmL      dhL      dhLp      da          diF...      % 4
            diS      dap      diFp      diSp      0 ...      % 5
            dOk      dOkp      0          0          0 ...      % 6
            dnca      0          0          dxrf      dxrs...      % 7
            dxs1      dxs2      dxk1      dJrelnp      dJrelp...      % 8
            dCaMKt      dI1k      dI2k      dCk      dI1kp...      % 9
            dI2kp      dCkp      dI1Cak      dI2Cak      dCCak...      % 10
            dI1Cakp      dI2Cakp      dCCakp      djnca      ]';      % 11
% When flag==0 -> Computed Variables: currents, concentrations and fluxes
else
    output=[INa      INaL      Ito      ICaL      IKr...      % 1
            IKs      IK1      INaCa_i      INaCa_ss      INaK...      % 2
            IKb      INab      ICab      IpCa      Jdiff...      % 3
            JdiffNa      JdiffK      Jup      Jleak      0...      % 4
            Jrel      CaMKa      Istim      ICaK      ICaNa...      % 5
            fICaLp      PhiCaL      Kmn      k2n      km2n...      % 6
            Jup      Jup2      anca      r_up      dss...      % 7
            r_up      r_down      eta_VDp      eta_CDP      td...      % 8
            tjca_VD      tf1_VD      tf2_VD      tf1_CD      tf2_CD...      % 9
            alpha      beta      theta_VDp      theta_CDP      omega_VD...      % 10
            omega_VDp      omega_CD      omega_CDP      psi_VD      psi_VDp...      % 11
            psi_CD      psi_CDP      gamma_VD      gamma_VDp      gamma_CD...      % 12
            gamma_CDP      delta_VD      delta_VDp      delta_CD      delta_CDP...      % 13
            eta_VD      eta_CD      theta_VD      theta_CD      flss_VD...      % 14
            flss_CD      f2ss_VD      f2ss_CD      jcass_VD      jcass_CD...      % 15
            tjca_VD      tjca_CD      jcass_VDp      jcass_CDP      gICaL...      % 16
            ICaLVD      ICaLCD      ICaLp      ICaLnp      OCak...      % 17
            ICaL_VDp      ICaL_CDP      ICaL_VD      ICaL_CD      OCakp]';      % 18
end
%%%%%%%%%%%%%%%%%%%%%%%%%%%%%%%%%%%%%%%%%%%%%%%%%%%%%%%%%%%%%%%%%%%%%%%%
%% END FILE
%%%%%%%%%%%%%%%%%%%%%%%%%%%%%%%%%%%%%%%%%%%%%%%%%%%%%%%%%%%%%%%%%%%%%%%%

```

2. Script with the model parameters: file modORd_par.m

```

%%%%%%%%%%%%%%%%%%%%%%%%%%%%%%%%%%%%%%%%%%%%%%%%%%%%%%%%%%%%%%%%%%%%%%%%
% Global parameters for the modified ORd model
%%%%%%%%%%%%%%%%%%%%%%%%%%%%%%%%%%%%%%%%%%%%%%%%%%%%%%%%%%%%%%%%%%%%%%%%
global kCDI cPCa cVss cVsr cJup bJdiff bGncx bGKr k1r_down...
jncass_n jncass_s jncass_d jncass_k... % jca
tau_nca Kmn_nca k2n_nca km2n_nca... % nca
dss_n dss_k dss_s dss_d taud_k taud_k1 taud_k2 taud_s1 taud_s2... % d
jss_n jss_s jss_d jss_k tj_max tj_min tj_media tj_sd... % j
flss_n flss_s flss_d flss_k... % f1
tf1_kk tf1_n tf1_k tf1_k1 tf1_k2 tf1_s1 tf1_s2 tf1_d1 tf1_d2... % tf1
tf2_kk tf2_n tf2_k tf2_k1 tf2_k2 tf2_s1 tf2_s2 tf2_d1 tf2_d2... % tf2
a2_rel n_rel s_rel exp_rel ntau1_rel ntau2_rel n2_rel % RyRs
%%%%%%%%%%%%%%%%%%%%%%%%%%%%%%%%%%%%%%%%%%%%%%%%%%%%%%%%%%%%%%%%%%%%%%%%
%% CDI vs VDI
kCDI = 10;
%% r_up & down
k1r_up = 3;      k2r_up = 6e-3;      k1r_down = 1e-1;
%% nca & jnca
tau_nca = 1;
Kmn_nca = 0.025;
k2n_nca = 1000;
km2n_nca = 1*150;
jncass_n = 1;
jncass_s = 19.58+25;
jncass_d = 3.696;
jncass_k = 0;
%%%%%%%%%%%%%%%%%%%%%%%%%%%%%%%%%%%%%%%%%%%%%%%%%%%%%%%%%%%%%%%%%%%%%%%%
%% Activation d -> steady state
dss_n = 1;
dss_s = 3.940;
dss_d = 4.230;
dss_k = 0;
%%%%%%%%%%%%%%%%%%%%%%%%%%%%%%%%%%%%%%%%%%%%%%%%%%%%%%%%%%%%%%%%%%%%%%%%
%% Activation d -> tau

```

```

taud_k = 0.6;
taud_k1 = -0.05;
taud_s1 = 6;
taud_k2 = 0.09;
taud_s2 = 14;
%%%%%%%%%%%%%%%%%%%%%%%%%%%%%%%%%%%%%%%%%%%%%%%%%%%%%%%%%%%%%%%%%%%%%%%%
%% Recovery j -> steady state
jss_n = 1;
jss_s = 19.58;
jss_d = 3.696;
jss_k = 0;
%%%%%%%%%%%%%%%%%%%%%%%%%%%%%%%%%%%%%%%%%%%%%%%%%%%%%%%%%%%%%%%%%%%%%%%%
%% Recovery j -> tau
tj_min = 35;
tj_max = 350;
tj_media = -20;
tj_sd = 10;
%%%%%%%%%%%%%%%%%%%%%%%%%%%%%%%%%%%%%%%%%%%%%%%%%%%%%%%%%%%%%%%%%%%%%%%%
%% Fast Inactivation f1 -> tau
tf1_kk = 1;           % scaling factor
tf1_k = 70;          % basal value
tf1_n = 1.2;         % num
% - (v-vm)
tf1_k1 = 0.0045;    % scaling factor
tf1_s1 = 20;         % shift
tf1_d1 = -50;        % den
% + (v-vm)
tf1_k2 = 0.0045;    % scaling factor
tf1_s2 = 30;         % shift
tf1_d2 = 10;         % den
%%%%%%%%%%%%%%%%%%%%%%%%%%%%%%%%%%%%%%%%%%%%%%%%%%%%%%%%%%%%%%%%%%%%%%%%
%% Fast Inactivation f1 -> flss
flss_n=0.8;          % num
flss_s=19.58;        % shift
flss_d=3.696;        % den
flss_k=0.2;          % basal value
%%%%%%%%%%%%%%%%%%%%%%%%%%%%%%%%%%%%%%%%%%%%%%%%%%%%%%%%%%%%%%%%%%%%%%%%
%% Slow Inactivation f2 -> tau
tf2_kk = 1;           % scaling factor
tf2_k = 100;          % basal value
tf2_n = 0;            % num
% - (v-vm)
tf2_k1 = 0.0035;    % scaling factor
tf2_s1 = 5;          % shift
tf2_d1 = -84;        % den
% + (v-vm)
tf2_k2 = 0.0035;    % scaling factor
tf2_s2 = 5;          % shift
tf2_d2 = 4;          % den
%%%%%%%%%%%%%%%%%%%%%%%%%%%%%%%%%%%%%%%%%%%%%%%%%%%%%%%%%%%%%%%%%%%%%%%%
%% Slow Inactivation f2 -> f2ss
%
% ***reversibility***
%
%%%%%%%%%%%%%%%%%%%%%%%%%%%%%%%%%%%%%%%%%%%%%%%%%%%%%%%%%%%%%%%%%%%%%%%%
%% RyRs parameters
a2_rel = 1;
n_rel = 1.5;
n2_rel = 1;
s_rel = 0;
exp_rel = 8;
ntau1_rel = 1;
ntau2_rel = 0.0123;
%%%%%%%%%%%%%%%%%%%%%%%%%%%%%%%%%%%%%%%%%%%%%%%%%%%%%%%%%%%%%%%%%%%%%%%%
%% Other Variables
bGKr = 1;           % IKr scaling
bGncx = 1.2;        % INCX scaling
cPCa = 0.9;         % ICaL scaling
bJdiff=2;          % Jdiff Ca2+ scaling
cJup = 10;          % Jup Ca2+ scaling
cVss = 1;           % SS volume scaling
cVsr=0.95;         % SR volume scaling
%%%%%%%%%%%%%%%%%%%%%%%%%%%%%%%%%%%%%%%%%%%%%%%%%%%%%%%%%%%%%%%%%%%%%%%%
%% END FILE
%%%%%%%%%%%%%%%%%%%%%%%%%%%%%%%%%%%%%%%%%%%%%%%%%%%%%%%%%%%%%%%%%%%%%%%%

```

3. Script to run the model: file modORd_main.m

```

clear all; close all; clc;
%%%%%%%%%%%%%%%%%%%%%%%%%%%%%%%%%%%%%%%%%%%%%%%%%%%%%%%%%%%%%%%%%%%%%%%%
%% Main Settings:
nb = 1000; % number of beats to run
BCL = 1000; % basic cycle length (ms)
ODEstep = 1; % max time step (ms)
%%%%%%%%%%%%%%%%%%%%%%%%%%%%%%%%%%%%%%%%%%%%%%%%%%%%%%%%%%%%%%%%%%%%%%%%
%% Parameters cyBCLe
AP_model = @modORd; % AP file function model
file_pars = 'modORd_par'; % ICaL parameters
run(file_pars);
%%%%%%%%%%%%%%%%%%%%%%%%%%%%%%%%%%%%%%%%%%%%%%%%%%%%%%%%%%%%%%%%%%%%%%%%
%% Initial Conditions:
% Original ORd state variables:
v=-87; nai=7; nass=nai; ki=145; kss=ki;
cai=1.0e-4; cass=cai; casr=1.2; m=0; hf=1;
hs=1; j=1; hsp=1; jp=1; mL=0;
hL=1; hLp=1; a=0; iF=1; iS=1;
ap=0; iFp=1; iSp=1; nca=0; xrf=0;
xrs=0; xs1=0; xs2=0; xk1=1;
Jrelnp=0; Jrelp=0; CaMkt=0; jrec=1;
% Modified ORd model NEW state variables:
I1k=0; I2k=0; Ck=1;
I1kp=0; I2kp=0; Ckp=1;
I1Cak=0; I2Cak=0; CCak=0;
I1Cakp=0; I2Cakp=0; CCakp=0;
% Initial Conditions vector:
% N.B. the old gating variables for ICaL have been set to 0
CI = [ v nai nass ki kss...
       cai cass 0 casr m...
       hf hs j hsp jp...
       mL hL hLp a iF...
       iS ap iFp iSp 0 ...
       0 0 0 0 0 ...
       nca 0 0 xrf xrs...
       xs1 xs2 xk1 Jrelnp Jrelp...
       CaMkt I1k I2k Ck I1kp...
       I2kp Ckp I1Cak I2Cak CCak ...
       I1Cakp I2Cakp CCakp jrec ]';
%%%%%%%%%%%%%%%%%%%%%%%%%%%%%%%%%%%%%%%%%%%%%%%%%%%%%%%%%%%%%%%%%%%%%%%%
%% Simulations:
input_args = {}; % see model file for input details
options=odeset('MaxStep',ODEstep);
y0 = CI;
for n=1:nb
    [time,y] = ode15s(AP_model,[0 BCL],y0,options,input_args{:});
    fprintf('Beat %i of %i\n',n,nb);
    y0 = y(end,:);
end
y0_SS = y(end,:);
%%%%%%%%%%%%%%%%%%%%%%%%%%%%%%%%%%%%%%%%%%%%%%%%%%%%%%%%%%%%%%%%%%%%%%%%
%% Computed variables recovery:
input_args{1}=0; % see model file for input details
LCVs=size(feval(AP_model,time(1),y(1,:),input_args{:}),1);
CVs = zeros(length(time),LCVs);
for j=1:length(time)
    CVs(j,:)=feval(AP_model,time(j),y(j,:),input_args{:});
end
%%%%%%%%%%%%%%%%%%%%%%%%%%%%%%%%%%%%%%%%%%%%%%%%%%%%%%%%%%%%%%%%%%%%%%%%
%% AP plot:
figure('Name','Report');
subplot(2,1,1);
plot(time,y(:,1),'m');
title('Action Potential');
xlabel('time (ms)'); ylabel('membrane voltage (mV)');
subplot(2,1,2);
title('L-type Ca^{2+} current');
plot(time,CVs(:,4),'m');
xlabel('time (ms)'); ylabel('I_{CaL} (uA/uF)');
%%%%%%%%%%%%%%%%%%%%%%%%%%%%%%%%%%%%%%%%%%%%%%%%%%%%%%%%%%%%%%%%%%%%%%%%
%% END FILE
%%%%%%%%%%%%%%%%%%%%%%%%%%%%%%%%%%%%%%%%%%%%%%%%%%%%%%%%%%%%%%%%%%%%%%%%

```

Figure A.1 shows representative plot reproduced by using the Matlab code above. The hybrid model has been paced for 1000 s at 1 Hz, and action potential and L-type Ca^{2+} current traces have been displayed.

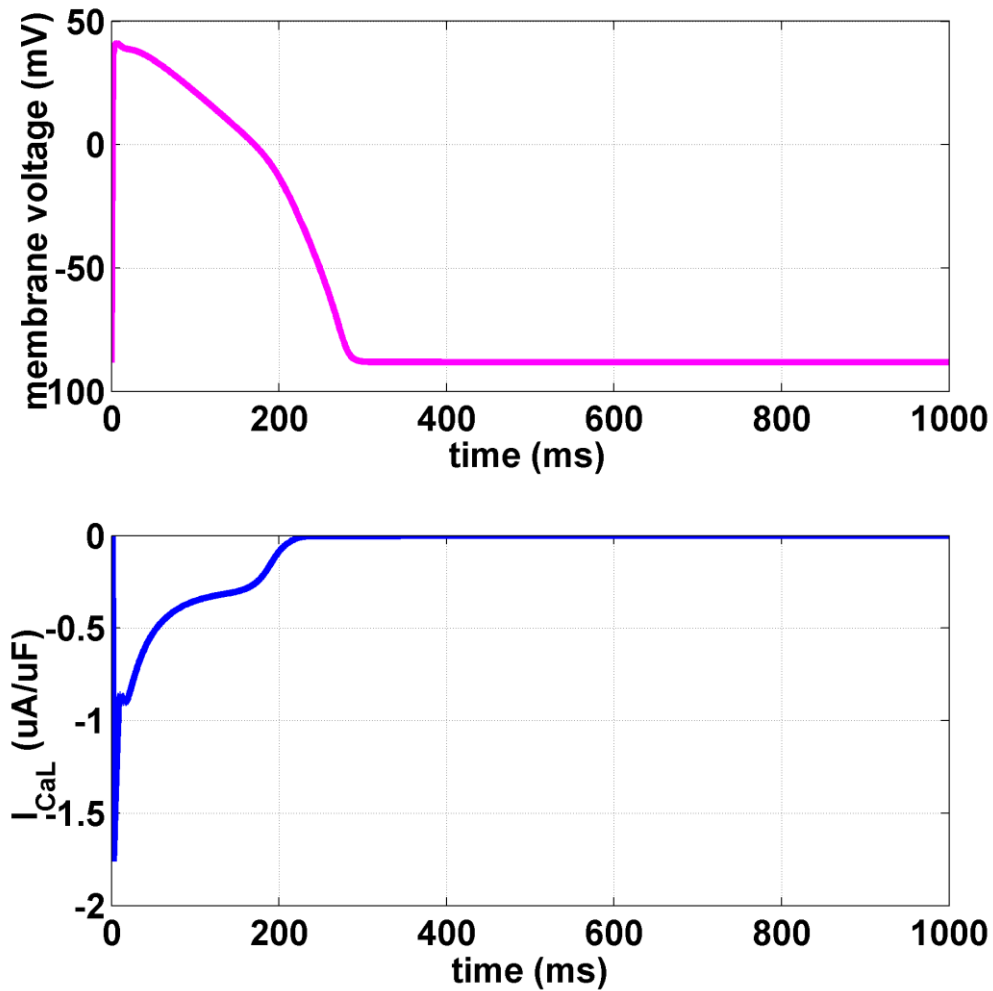


Figure A.1: Action Potential and L-type Ca^{2+} current traces for the hybrid model described in Chapter 3 and Chapter 4. This figure has been obtained by running in Matlab the script given in Appendix A3, who in turn recalls the model and the corresponding parameter files.

APPENDIX B

1. *The Population of Models Approach*

The population of models (POMs) approach, recently developed by the Computational Cardiovascular Science group (Department of Computer Science, University of Oxford, UK) and already applied to different contexts [1–4], is a novel methodology in computational cardiac AP modelling. It provides the means to explore the effects of biological variability, usually neglected when using the traditional modelling techniques. Each individual may have a different response to disease and drug action, and biological variability is the key to understand why.

Instead of considering a single AP model, representative of the average cell behaviour, simulations are performed in thousands of models at the same time (a population, indeed), all generated by varying some of the model parameters around their nominal values. Each model represents a different cell (of the same cell-type) and the cell-to-cell differences account for both inter- and/or intra- subject variability. It is worth noticing that the population is calibrated considering experimental data, either original or from literature (i.e. only the models in agreement with these data are “accepted” in the final population).

As an example, Figure 7.2 **Errore. L'origine riferimento non è stata trovata.** shows different experimental APs (pink traces), all recorded from the same cell type, i.e. rabbit purkinje cells (data by Janssen Pharmaceutica). The biological variability is well represented here: although overall similar, every cell has quite a distinct AP, and the differences are especially evident in the repolarisation phase, leading to a wide range of AP durations (from about 200 to 400 ms). All this information is actually lost when using a single Purkinje AP model to reproduce these experimental data, e.g. the Corrias-Giles-Rodriguez (left panel, black trace) [5]. Even if this single model well represents the average cell behaviour, a population of models (right panel, black traces) allow for a better coverage of the experimental dataset, well reproducing cell-to-cell variability.

All the models in the population share the same differential equations, but each of them has a different parameters set. Indeed, the main hypothesis behind the POMs methodology is that all the cells of the same type (e.g. human ventricular endo- or epi- cardiac cells) share the same structure (ion channels, pumps, exchangers, etc.) and variability may be mostly related to differences in the density

of channels for each cell, leading to different ionic currents and in turn to different APs. Therefore, most of the biological variability observed should be reproduced by varying the maximal conductances of the main ionic currents, related to channel density in the cells. It would be definitely interesting to analyse also variability in current kinetics, e.g. varying the time constants of gating variable, but up to now we have modified ionic current densities only by acting on conductances.

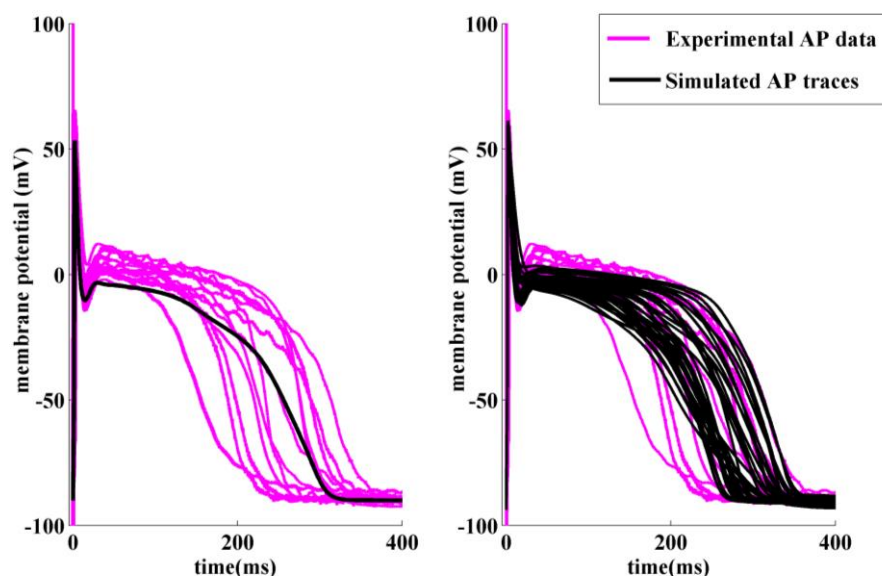


Figure B.1: Experimental AP recordings (pink traces, both panels) from rabbit purkinje cells (data by Janssen Pharmaceutica). When considering only a single AP model (black trace, left panel), the biological variability is completely neglected, while the population of models (black traces, right panel) is able to better reproduce the experimental dataset (modified from [2]).

Depending on the purpose of the study, the number of generated models, the parameters to be varied, the scaling factors to apply to the nominal parameter values and the sampling of the parameter sets, may be different.

In theory, the bigger the population, the more reliable the results: of course, the limitation here is mainly due to the computational costs. It is worth starting with a small population (about 10,000 models) and then increase the size (up to 30,000 or 100,000 or more) if the accepted models resulting from the calibration process are not enough to properly evaluate the results.

As for the parameters to vary, all the ones that may play a role in the study should be considered for the population, e.g. I_{NaL} in HCM. At the same time, varying too many parameters definitely increases complexity, especially when trying to analyse/classify simulation results, e.g. to identify the main ionic mechanisms involved in a specific phenomenon.

Parameter ranges also need to be chosen carefully. The wider the range, the more the models in the population deviate from the original AP model, and sometimes they are not even showing a regular AP. The commonly used range is [0-200%], i.e. $\pm 100\%$ with respect to the original parameter values. This implies that there may be models included in the population having some currents with a very low (close to zero) density, as long as other currents compensate for them, allowing for a physiological AP. These models may represent pathological conditions, and therefore they can provide valuable insights, especially when evaluating *in silico* the effect of specific current blockers. However, to explore variability in healthy controls without including “extreme” pathological conditions, the parameter range can be reduced to [50%-150%], i.e. $\pm 50\%$ with respect to the original parameter values, or even less than that ($\pm 30\%$, $\pm 10\%$). Sometimes, it may be worth to extend the upper limit e.g. up to 300% or more, to represent a pathological condition in which some currents are highly over-expressed. However, as shown in Figure B.2, the AP is much more sensitive to parameter scaling towards the lower values (from 0 to 100% of the original values) than towards the lower ones.

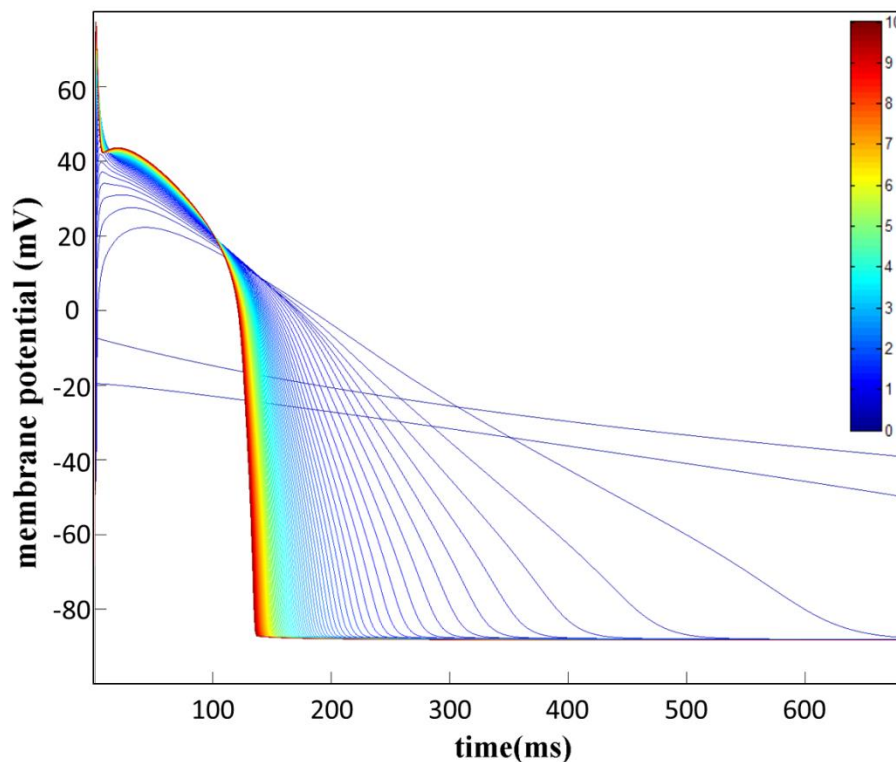


Figure B.2: Effect of parameters scaling on simulated AP: 9 major current conductances of the O’Hara-Rudy model [6] have been simultaneously modified from 0 to 10 times their original value, with a 0.1 step. Step-by-step changes are remarkable when considering low scaling factors (from 0 to 4) while the AP changes very little for high scaling factors (Britton et al. unpublished).

Finally, the different parameter sets have to be probabilistically sampled in the parameter space. The methods which has been used up to now is Latin hypercube sampling, developed by McKay in 1979 [7]. It consists of a generalisation of the Latin square, i.e. a $n \times n$ matrix filled with different symbols, each one occurring exactly once in each row and exactly once in each column: each sample is the only one in each axis-aligned hyper-plane containing it. Recently, two papers have been published, estimating the coverage of parameter space for POMs when using Latin hypercube sampling [8, 9].

It is worth notice than we don't claim to sample the whole parameter space: we rather aim to explore the chosen range for each of the parameters varied in the population. The goodness of the sampling is therefore evaluated when comparing the simulations results and the experimental data, by the ability of the POMs to capture the biological variability observed.

Once the parameters and their relative ranges have been fixed, the initial simulations may be run, using the same baseline AP model with all the sampled parameter sets. Simulated AP traces have to be compared with the experimental data available, usually considering a set of AP or CaT biomarkers: only the models whose biomarkers satisfy all the experimental constraints will be included in the final population, while the other ones will be discarded.

This process (“experimentally-based calibration”) may considerably reduce the size of the initial population. It is important to have enough models left (a few hundreds) to analyse simulation results using statistic tools. When too many models are discarded, it is worth to re-build the population from the beginning, changing the parameters and/or their ranges. Also, it is always very important to check that the baseline model is not too far from the average behaviour of the cells in the considered experimental dataset: if so, some small modifications to the original model may be required before building the population.

A schematic representation of the POMs approach is given in Figure B.3, considering a hypothetic four-dimensional parameter space: simulations are run for the same model with many parameter sets, each of them resulting in a different biomarkers set. Only the models fully in agreement with the experimental data are selected in the final population, while the other ones are discarded.

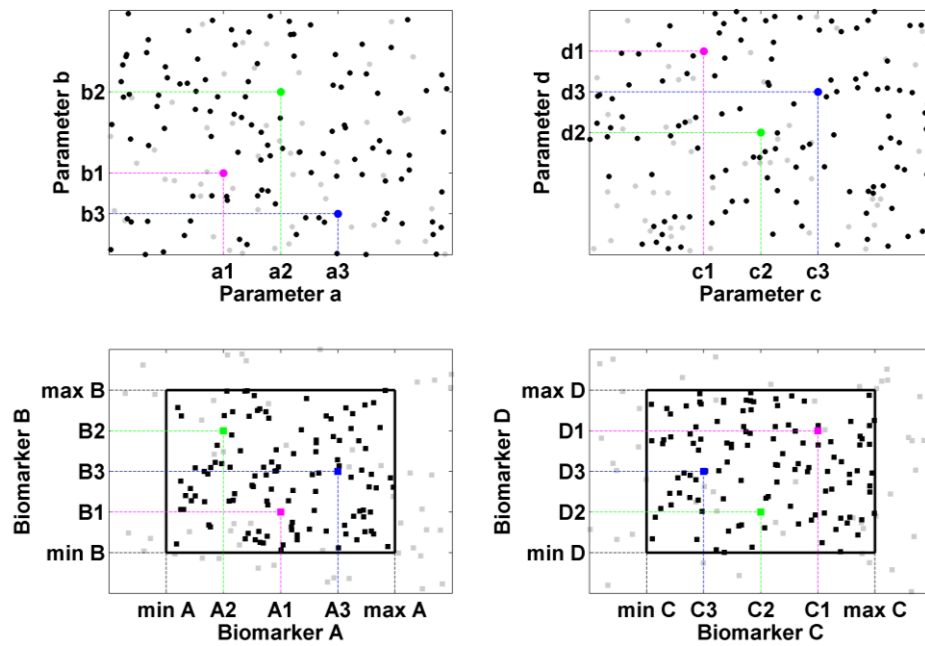


Figure B.3: Simple representation of the population of models technique: simulations are run for the same model with many parameter sets, each of them resulting in a different AP and a corresponding set of biomarkers. Only the models whose biomarkers fall within experimental ranges (black lines) are selected in the final population (black dots/squares) while the other ones are discarded (grey dots/squares). To clarify the links between panels, three models have been highlighted with colours.

2. The Baseline Model

As baseline model to build the CTRL and HCM population, we used the O'Hara-Rudy model (ORd [6]), published in 2011.

However, a few changes have been required to the original model, in order to better reproduce the experimental CTRL data, and to fix a well-known problem concerning the I_{Na} inactivation gates, which prevent propagation in 2D or 3D tissue when considering hyperkalaemia.

Fast Na^+ Current Formulation

Inactivation gates for the fast Na^+ current (I_{Na}), “h” and “j”, are partially closed at normal resting membrane potentials in the ORd model. This was the result of using Sakakibara et al. [10] nonfailing human ventricular I_{Na} data (17° C), corrected for temperature using Nagatomo et al. [11] HEK-expressed hH1 data and also for the time after patch-clamp beginning using Hanck & Sheets data [12]. This is ultimately why the maximum conductance was set to 75 mS/ μ F, substantially larger than in other models, but there are no independent human I_{Na} data available to determine whether the temperature/time corrections applied were in fact accurate.

With hyperkalaemia, “h” and “j” gates are further closed as resting membrane potential depolarises through the steep portion of the steady state inactivation curves. In single cells, this reduces the action potential upstroke velocity within the physiological range. However, in 2D or 3D simulations, where the cells experience a large electrical load, it might cause conduction block at lower levels of hyperkalaemia than observed experimentally.

The solution suggested by the authors was to replace the I_{Na} formulation in the original ORd model with the one from ten Tusscher et al. [13] (TT04). Here, I_{Na} steady state inactivation curves are based on Nagatomo et al. [11] data extrapolated to 37° C, but not corrected for time after patch-clamp beginning. The resulting inactivation curves are about 10 mV depolarised compared to ORd, and therefore less sensitive to resting membrane voltage elevation under hyperkalemic conditions.

Even if we were planning to use the population of models only at single cell level, we decided to modify the I_{Na} as first thing, to save possible problems with future works on 2D or 3D tissues. We didn't follow completely the authors'

suggestion, because the Ten Tusscher formulation is quite complicated and not all immediate to understand, while the ORd one follows the Hodgkin and Huxley formalisms. Moreover, we were interested in the phosphorylation of the I_{Na} current, considered in the ORd formulation only.

Since the propagation problem is ultimately due to the steady state formulation of “h” and “j” gates, which share the same sigmoidal function, we changed their $V_{1/2}$ and slope to get them as close as possible to the ones in Ten Tusscher et al. [13], using the Matlab (Mathworks Inc.) built-in function *fminsearch*, based on the Nelder-Mead Simplex Method [14]. As for the phosphorilated gates, we just applied a -6.2 mV shift in $V_{1/2}$, as already done in the original ORd model, based on the work by Wagner et al. [15].

Here below, the three different h_{ss} formulations are shown and the corresponding plots are compared in Figure B.4.

$$h_{ORd} = j_{ORd} = \frac{1}{1 + e^{\frac{v+82.9}{6.09}}}$$

$$h_{TT04} = j_{TT04} = \frac{1}{(1 + e^{\frac{v+71.6}{7.43}})^2}$$

$$h_{opt} = j_{opt} = \frac{1}{1 + e^{\frac{v+78.5}{6.22}}}$$

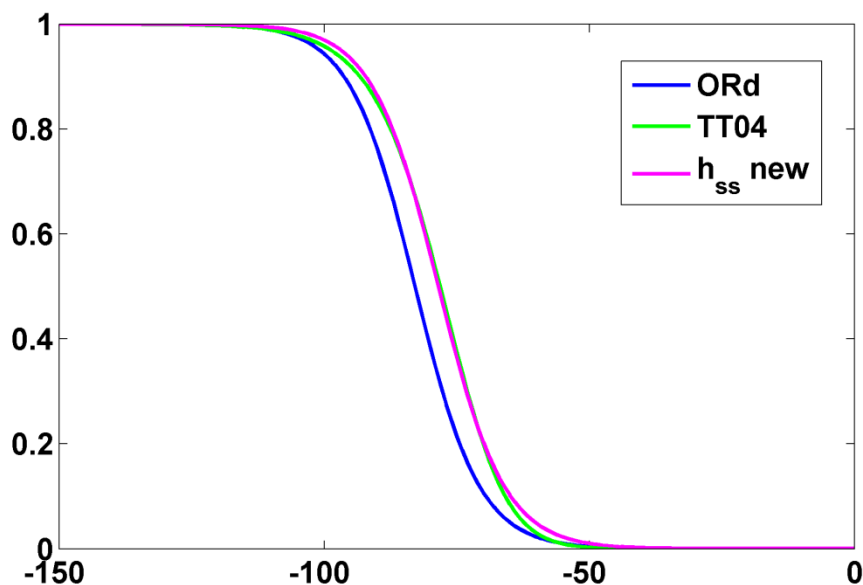


Figure B.4: Comparison of Fast Na^+ current inactivation gates for ORd, TT04 and the baseline model used to build the population of models.

After changing the two inactivation curves, we checked the consistency of the modified ORd model with the original one, pacing the model at 1 Hz until steady state (about 1000 s). The new formulation leads to an increased Na^+ current which, over time, produces some discrepancy with the original ORd model. Therefore, we reduced the maximal I_{Na} conductance in the modified model, to match the original one in steady state conditions (scaling factor 0.66).

Ionic Concentrations

To match the experimental data, we set the intra- and extra- cellular ionic concentration to the ones used in the experiments for the AP and CaT recording:

- Extracellular concentrations:
 - ✓ Na^+ = 132 mM (140 mM in ORd)
 - ✓ K^+ = 5.4 mM
 - ✓ Ca^{2+} = 1.8 mM
- Intracellular concentrations:
 - ✓ Na^+ no changes (7 mM)
 - ✓ K^+ = 140 mM (145 mM in ORd)
 - ✓ Ca^{2+} no changes (1e-4 mM)

The only exception is the extracellular K^+ concentrations ($[\text{K}^+]_o$), which was 4 mM in the experiments. In fact, the ORd model uses $[\text{K}^+]_o$ 5.4 mM even if it has been built using experiments recorded with $[\text{K}^+]_o$ 4 mM, as in our data. Therefore, we decided to keep its original value in our simulations.

New Current Stimulus

In the original ORd model, the stimulus is set to a current pulse of amplitude -80 uA/uF and duration 0.5 ms. When pacing for more than one cycle length, however, the minimum time step has to be equal/smaller than the duration of the current stimulus; otherwise, there are chances of the model missing the upstroke. Since we were planning to use 1 ms as max time step, to reduce simulation time, we increased the stimulus duration to 1 ms. We changed the stimulus amplitude accordingly, considering twice the AP threshold: the new current stimulus amplitude is therefore -53 uA/uF.

I_{to} I-V Curve

We compared the experimental I-V curve for I_{to} and the one obtained for the modified model. When normalised, the two curves are quite similar. However, the experimental CTRL data seem to have a much higher I_{to} than the original ORd model. Therefore, to match the experimental data, we increased the maximal I_{to} conductance of 2.5 fold. As a supporting experimental evidence, the CTRL cells in the experiments show a pronounced notch, which is not present in the original ORd endocardial model, and usually related to I_{to} .

K^+ Equilibrium Potential

When we compared the measured I-V curve of I_{K1} with the one obtained for the model, following the same voltage-clamp protocol, we immediately found out that the reversal potential of K^+ was quite different between model and experiments. In fact the cell RMP, mostly dependent on I_{K1} is more depolarised in the ORd model.

As first, we tried to match the RMP acting on intra- and extra-cellular K^+ concentrations, but this led to values which were too far from the ones actually used into the experimental solutions. Therefore, we decided to use a fixed equilibrium potential for K^+ , instead of using Nernst equation, to match the experimental data.

Once modified the K^+ equilibrium potential, other small changes were needed to preserve consistency with the original ORd model. In particular, the activation curves for I_{Na} , I_{NaL} and I_{K1} have been shifted by the difference between the old and the new K^+ reversal potential (-9.2 mV).

To verify that this change had not any major drawback, we actually generated two populations of models for the CTRL dataset, one with and one without the new RMP. Simulation results were qualitatively similar in terms of number of models and AP and CaT and biomarkers, so we chose to continue using the population with the modified RMP, since a more depolarized membrane potential may have an impact on pro-arrhythmic mechanisms occurrence.

3. Additional Results

The following pages show the simulation results obtained considering an additional population of models, in which the parameters have been varied in a smaller range, i.e. [50-150%], with respect to their original value.

There are no models discarded from the initial population before the experimentally-based calibration, i.e. models in which Chasted failed to compute AP and CaT biomarkers (about 2,000 in the previous one). Since the variability is reduced, more models are in agreement with the experimental data. Accepted CTRL models in this population are 9,124, compared to the 2,254 of the previous one.

Simulation results are consistent with the ones presented in Chapter 7, especially when considering the current block effects on repolarization abnormalities occurrence. In general, RF occurrence is significantly reduced in this new population, while short/long EADs are present in the same fraction (Figure B.5). Indeed, many of the models showing RF in the previous population, as well as short/long EADs, were characterized by very low I_{Kr} scaling factors, which is this population is limited from [50-150%] compared to the original values.

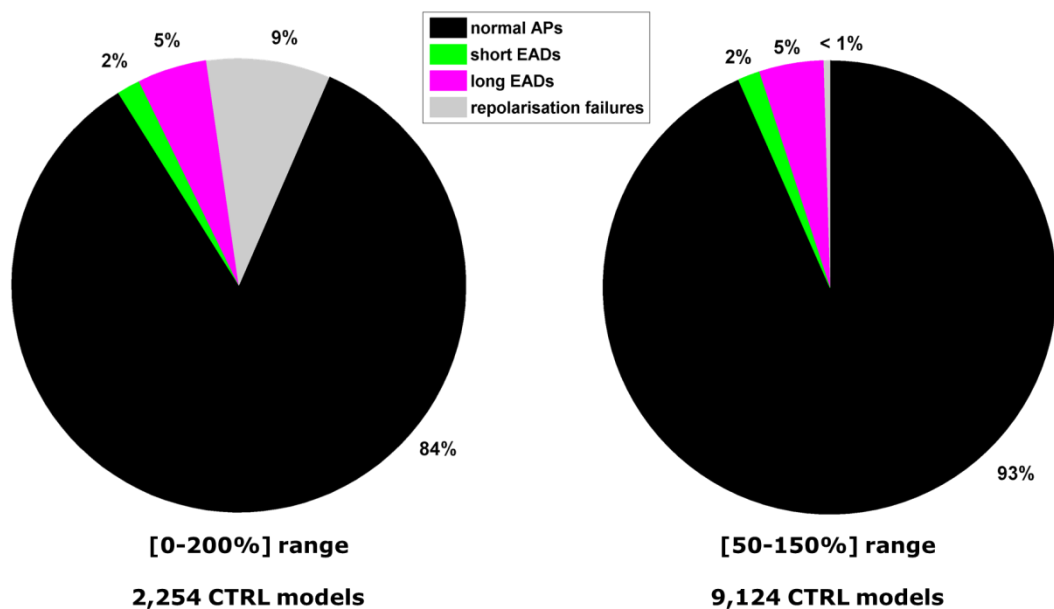


Figure B.5: Comparison of the two different HCM population, generated varying 11 parameters in the [0-200%] (left) or [50-150%] (right) range, with respect to their original values.

Hereafter, a few Tables/Figures from Chapter 7 have been reproduced for the new population. Labels and numbers are unaltered, to facilitate the comparison.

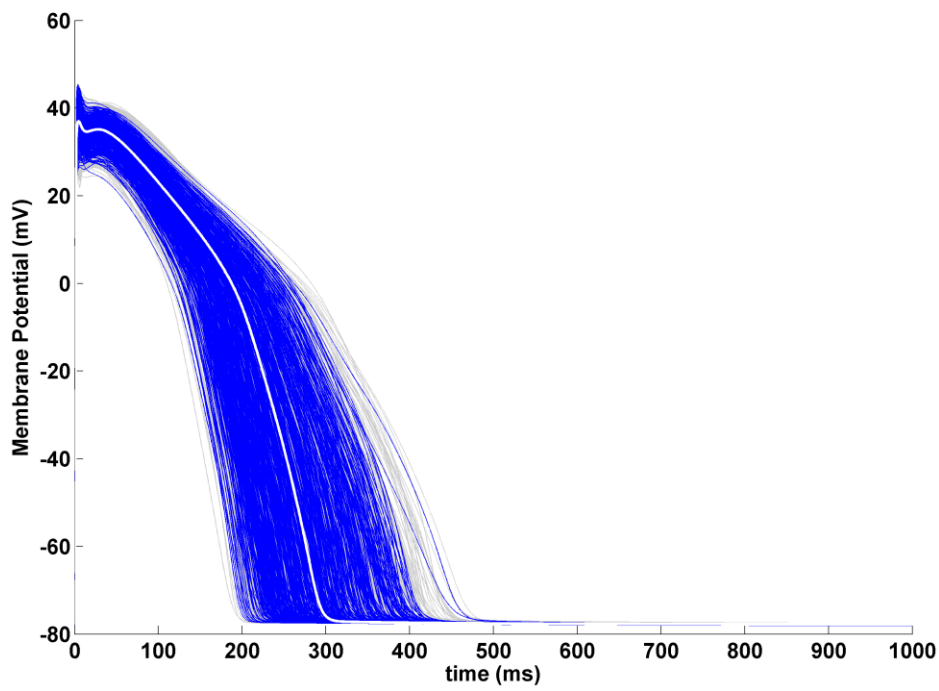


Figure 7.11 (B): Representative AP traces of accepted/discarded (blue/grey lines) models in the CTRL population. The baseline model AP is shown in white.

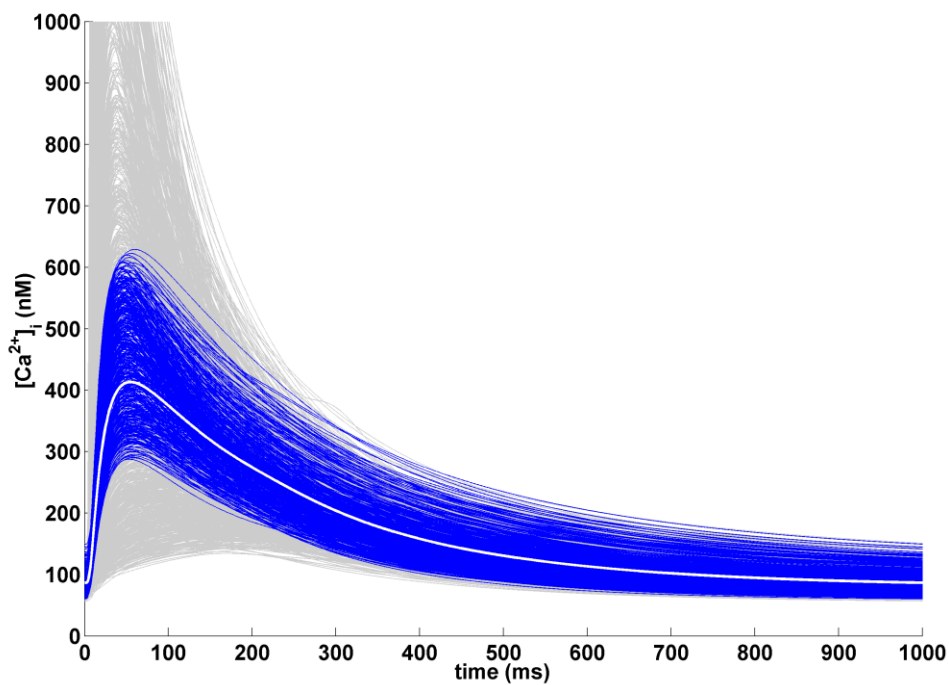


Figure 7.12 (B): Representative CaT traces of accepted/discarded (blue/grey lines) models in the CTRL population. The baseline model CaT is shown in white.

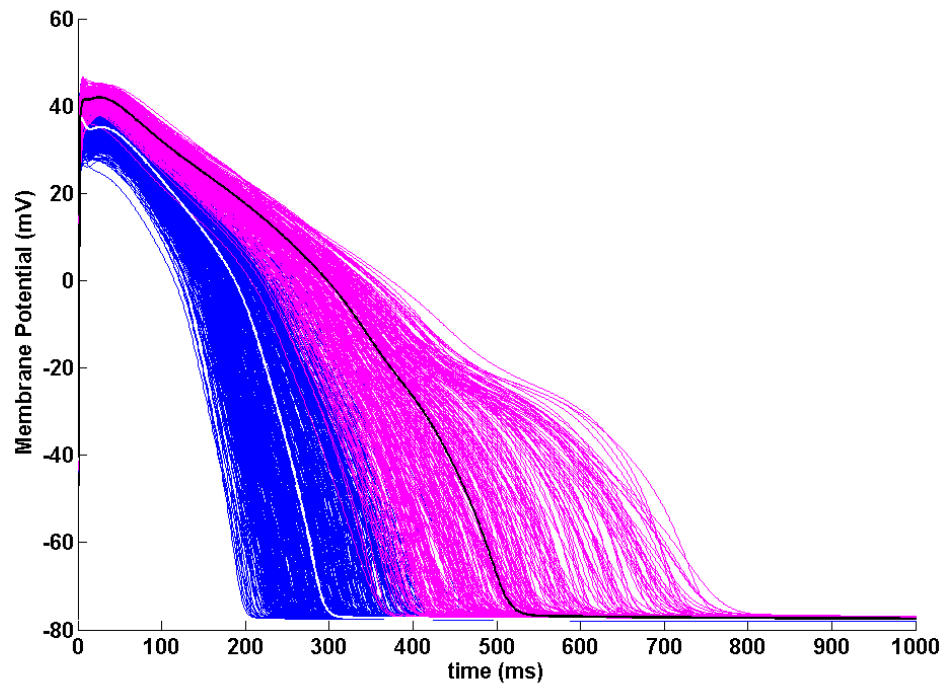


Figure 7.19 (B): Representative AP traces from the HCM POMs (pink lines), compared with the corresponding CTRL ones (blue lines). The baseline CTRL model and its correspondent HCM version are shown in white and black, respectively.

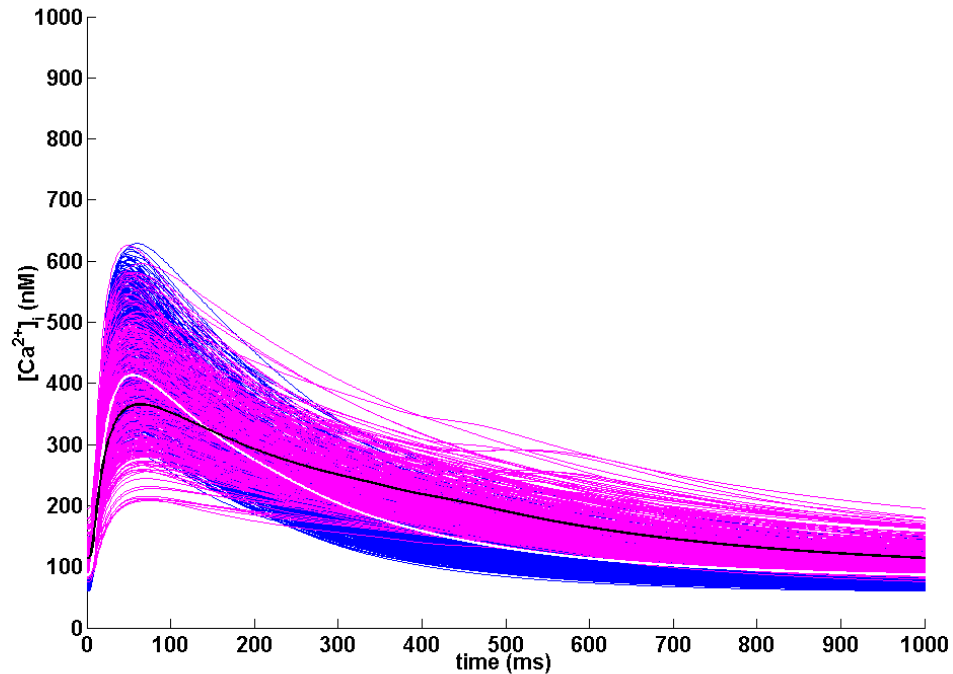


Figure 7.20 (B): Representative CaT traces from the HCM POMs (pink lines), compared with the corresponding CTRL ones (blue lines). The baseline CTRL model and its correspondent HCM version are shown in white and black, respectively.

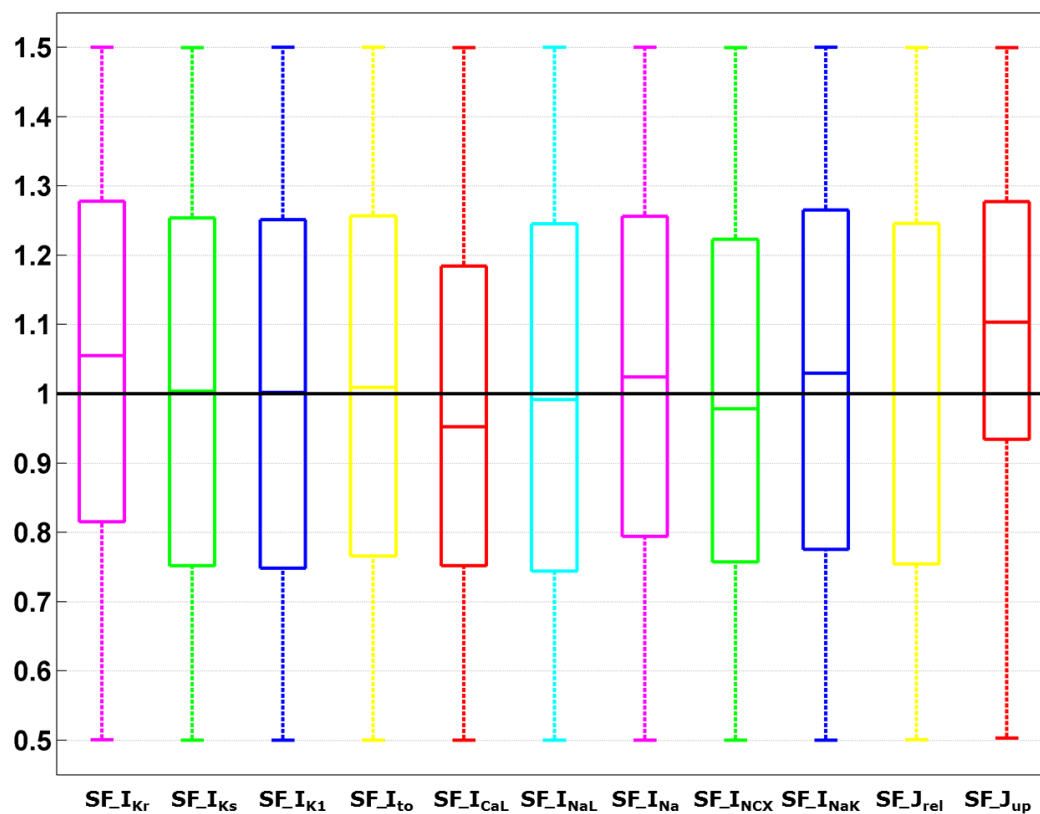


Figure 7.26 (B): Scaling factor boxplots of the HCM models having a normal AP, i.e. not showing any repolarisation abnormality. These models have a slightly higher I_{Kr} and J_{up} .

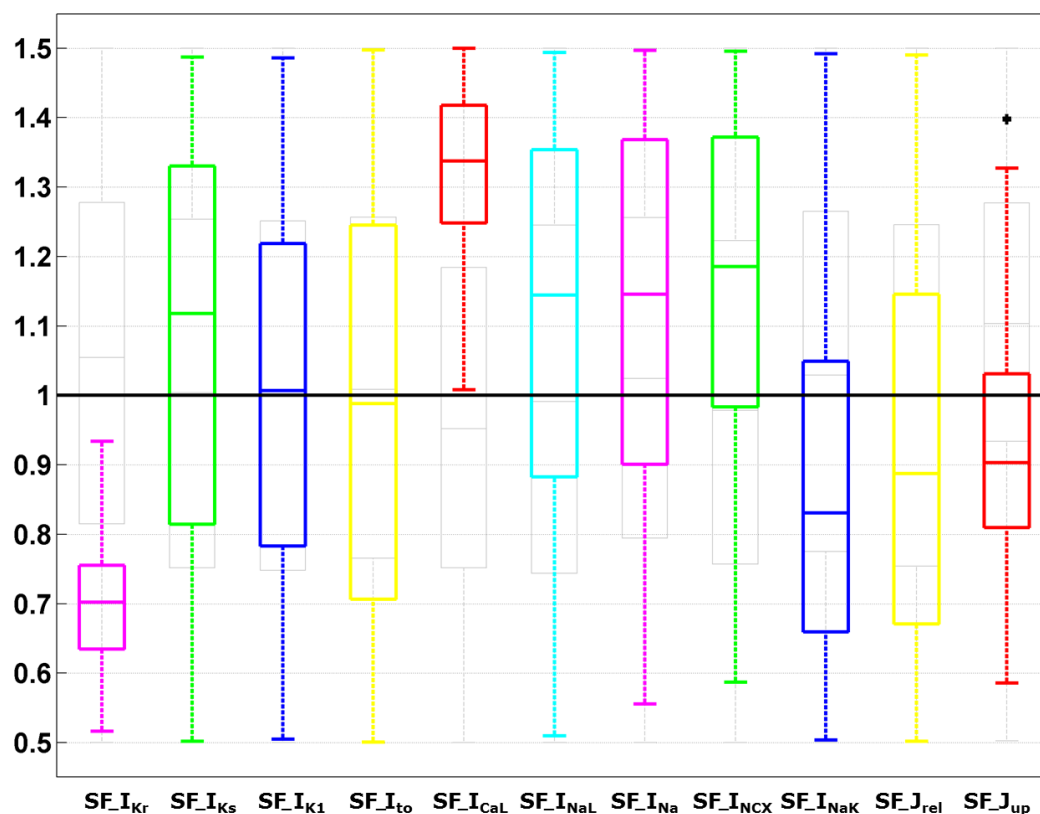


Figure 7.27 (B): Scaling factor boxplots of the HCM models showing short EADs, compared to the ones with a regular AP. These models are characterised by low I_{Kr} , high I_{CaL} , I_{NaL} and I_{NCX} .

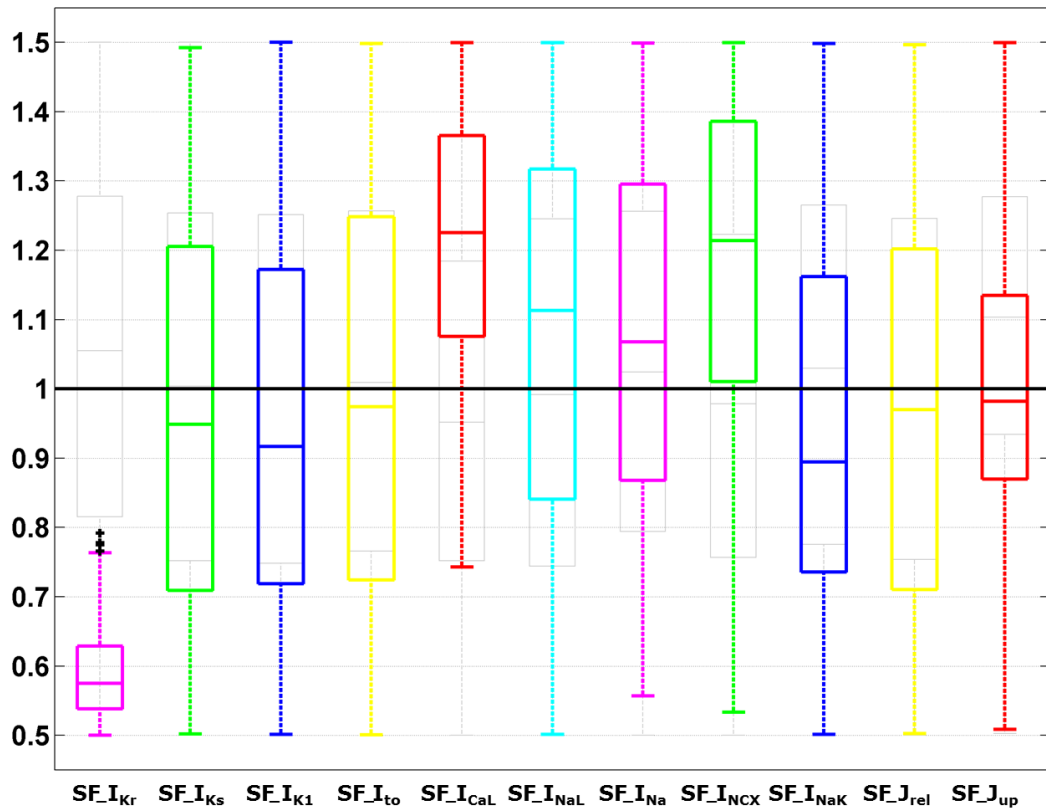


Figure 7.28 (B): Scaling factor boxplots of the HCM models showing long EADs, compared to the ones with a regular AP. These models are characterised by low I_{Kr} , high I_{CaL} and I_{NaL} , very high I_{NCX} .

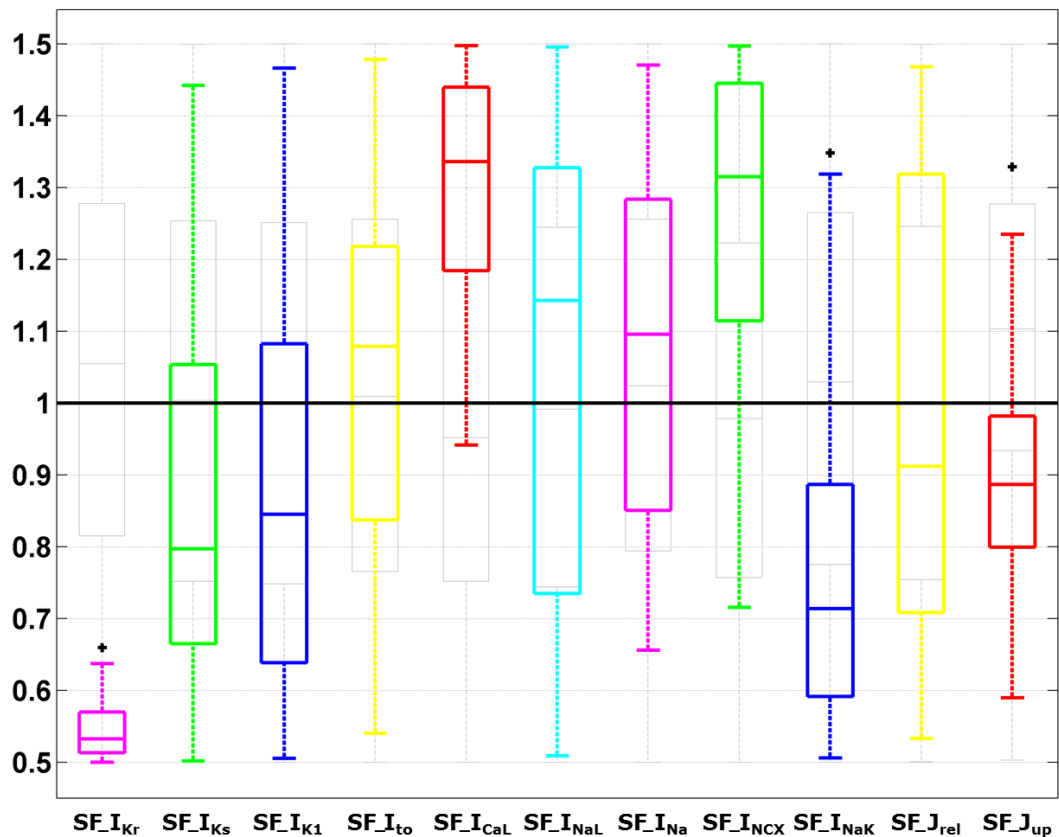


Figure 7.29 (B): Scaling factor boxplots of the HCM models showing RF, compared to the ones with a regular AP. These models are characterised by a very low I_{Kr} , high I_{CaL} , I_{Na} and I_{NCX} and low I_{NaK} .

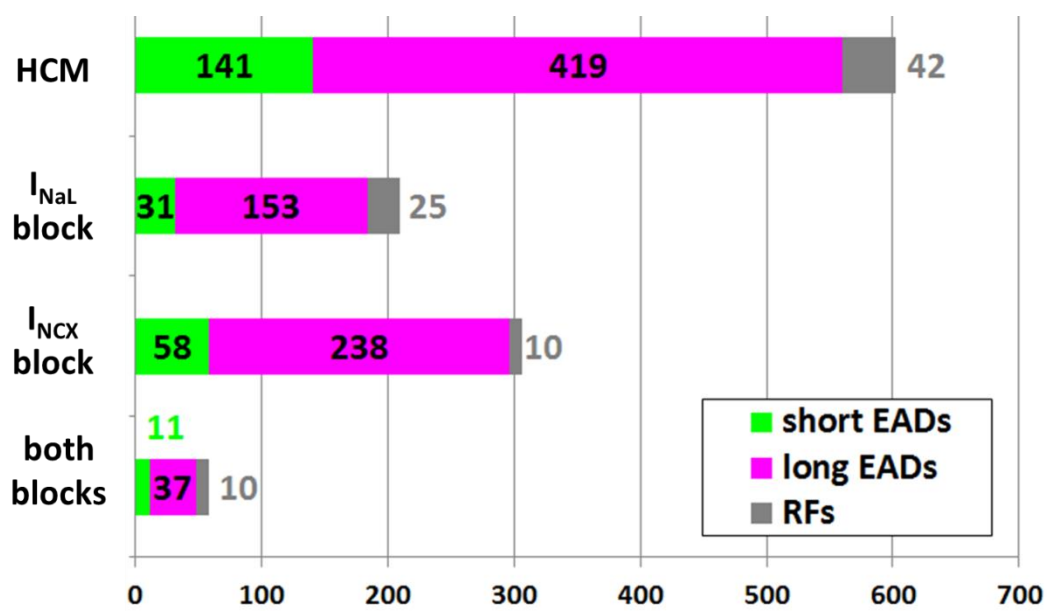


Figure 7.37 (B): Repolarisation abnormalities occurrence in the HCM population, and the relative changes induced by current blocks. The values refer to the number of models in each subgroup.

Table 7.8 (B): Detailed description of repolarisation abnormalities changes in HCM when considering the different current blocks. The percentage in bold shows the fraction of models in which the repolarisation abnormalities was successfully suppressed, leading to a normal HCM APs.

HCM population		HCM + I _{NaL} block		HCM + I _{NCX} block		HCM + both blocks	
short EADs	141	normal APs	136 (96%)	normal APs	119 (84%)	normal APs	140 (99%)
		short EADs	2	short EADs	16	short EADs	-
		long EADs	3	long EADs	6	long EADs	1
		RF	-	RF	-	RF	-
long EADs	419	normal APs	257 (61%)	normal APs	177 (42%)	normal APs	393 (94%)
		short EADs	29	short EADs	42	short EADs	7
		long EADs	127	long EADs	200	long EADs	19
		RF	6	RF	-	RF	-
RF	42	normal APs	- (0%)	normal APs	- (0%)	normal APs	11 (26%)
		short EADs	-	short EADs	-	short EADs	4
		long EADs	23	long EADs	30	long EADs	17
		RF	19	RF	10	RF	10

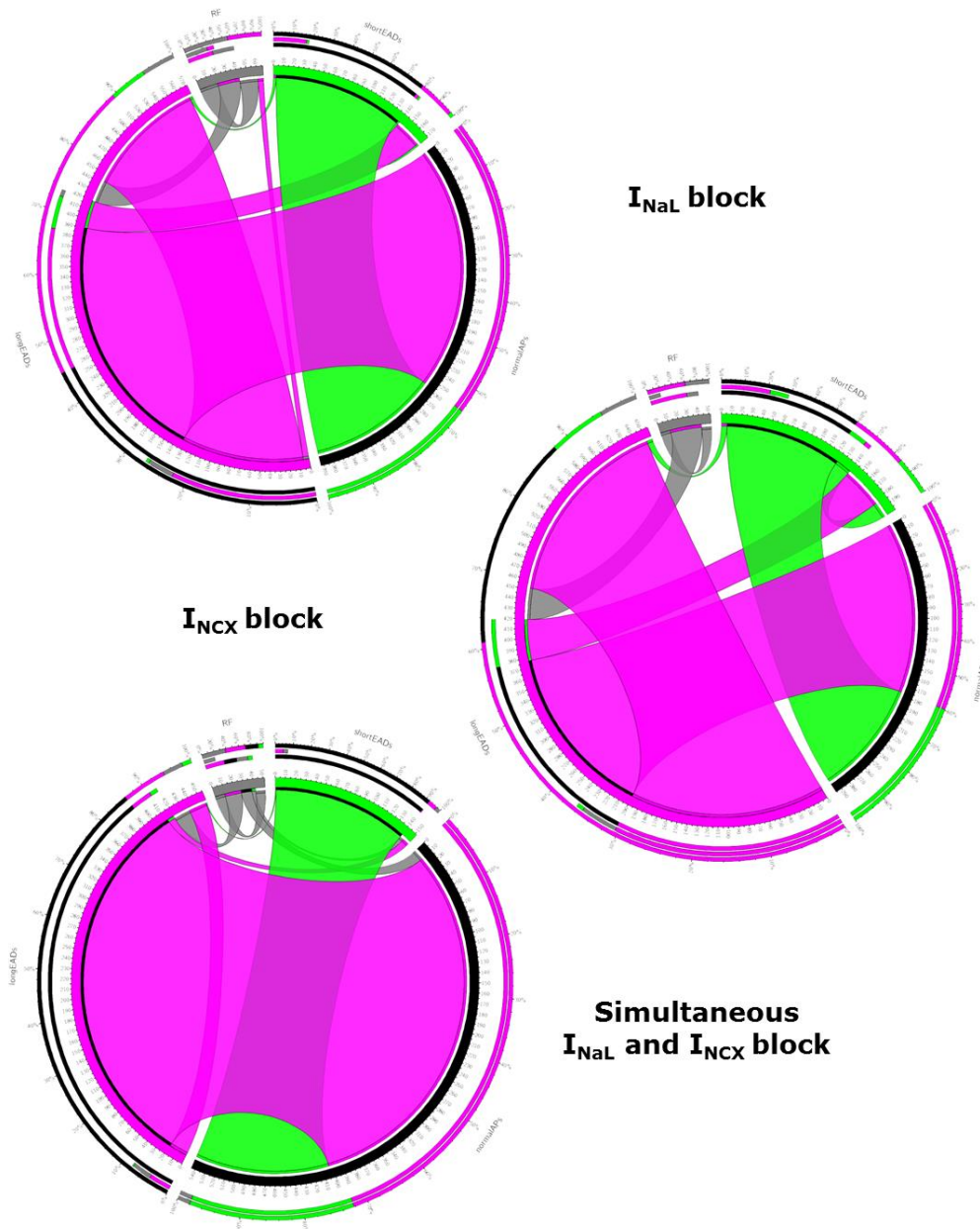


Figure 7.39 (B): Circos plots to represent repolarisation abnormalities distribution in the HCM population. Every plot shows the number of models for each subgroup, before and after adding the current block, together with the incoming and outgoing fluxes from one subgroup to all the other ones. Considering e.g. the pink section in the top plot: when including I_{NaL} block, many long EADs disappear (they go into normal HCM APs subgroup), some of them become short EADs and some other just remain long EADs. A few models change from long EADs to RF, instead. In addition, there is an incoming flux of models from the RF subgroup, which have now become long EADs. The same apply to all the other subgroups and for all the considered ionic current blocks [16].

References

- [1] J. Walmsley, J. F. Rodriguez, G. R. Mirams, K. Burrage, I. R. Efimov, and B. Rodriguez, “mRNA expression levels in failing human hearts predict cellular electrophysiological remodeling: a population-based simulation study” *PLoS One*, vol. 8, no. 2, p. e56359, Jan. 2013.
- [2] O. J. Britton, A. Bueno-Orovio, K. Van Ammel, H. R. Lu, R. Towart, D. J. Gallacher, and B. Rodriguez, “Experimentally calibrated population of models predicts and explains intersubject variability in cardiac cellular electrophysiology” *Proc Natl Acad Sci USA*, vol. 110, no. 23, pp. E2098–105, Jun. 2013.
- [3] P. Gemmell, K. Burrage, B. Rodriguez, and T. A. Quinn, “Population of computational rabbit-specific ventricular action potential models for investigating sources of variability in cellular repolarisation” *PLoS One*, vol. 9, no. 2, p. e90112, Jan. 2014.
- [4] C. Sánchez, A. Bueno-Orovio, E. Wettwer, S. Loose, J. Simon, U. Ravens, E. Pueyo, and B. Rodriguez, “Inter-Subject Variability in Human Atrial Action Potential in Sinus Rhythm versus Chronic Atrial Fibrillation” *PLoS One*, vol. 9, no. 8, p. e105897, Jan. 2014.
- [5] A. Corrias, W. Giles, and B. Rodriguez, “Ionic mechanisms of electrophysiological properties and repolarization abnormalities in rabbit Purkinje fibers” *Am. J. Physiol. Heart Circ Physiol*, vol. 300, no. 5, pp. H1806–13, May 2011.
- [6] T. O’Hara, L. Virág, A. Varró, and Y. Rudy, “Simulation of the undiseased human cardiac ventricular action potential: model formulation and experimental validation” *PLoS Comput Biol*, vol. 7, no. 5, p. e1002061, May 2011.
- [7] M. D. McKay, R. J. Beckman, and W. J. Conover, “A Comparison of Three Methods for Selecting Values of Input Variables in the Analysis of Output from a Computer Code” *Technometrics*, vol. 21, no. 2, p. 239, May 1979.
- [8] K. Burrage, P. M. Burrage, D. M. Donovan, T. A. McCourt, and H. B. Thompson, “Estimates on the Coverage of Parameter Space using Populations of Models” in *Environment and Water Resource Management / 813: Modelling and Simulation / 814: Power and Energy Systems / 815: Health Informatics*, 2014.
- [9] K. Burrage, P. Burrage, D. Donovan, and B. Thompson, “Populations of models, Experimental Designs and coverage of parameter space by Latin Hypercube and Orthogonal Sampling” p. 9, Feb. 2015.
- [10] Y. Sakakibara, T. Furukawa, D. H. Singer, H. Jia, C. L. Backer, C. E. Arentzen, and J. A. Wasserstrom, “Sodium current in isolated human

- ventricular myocytes” *Am J Physiol*, vol. 265, no. 4 Pt 2, pp. H1301–9, Oct. 1993.
- [11] T. Nagatomo, Z. Fan, B. Ye, G. S. Tonkovich, C. T. January, J. W. Kyle, and J. C. Makielski, “Temperature dependence of early and late currents in human cardiac wild-type and long Q-T DeltaKPQ Na⁺ channels” *Am J Physiol*, vol. 275, no. 6 Pt 2, pp. H2016–24, Dec. 1998.
- [12] D. A. Hanck and M. F. Sheets, “Time-dependent changes in kinetics of Na⁺ current in single canine cardiac Purkinje cells” *Am J Physiol*, vol. 262, no. 4 Pt 2, pp. H1197–207, Apr. 1992.
- [13] K. H. W. J. ten Tusscher, D. Noble, P. J. Noble, and A. V Panfilov, “A model for human ventricular tissue” *Am J Physiol Heart Circ Physiol*, vol. 286, no. 4, pp. H1573–89, Apr. 2004.
- [14] J. C. Lagarias, J. A. Reeds, M. H. Wright, and P. E. Wright, “Convergence Properties of the Nelder--Mead Simplex Method in Low Dimensions” *SIAM J Optim*, vol. 9, no. 1, pp. 112–147, Jan. 1998.
- [15] S. Wagner, N. Dybkova, E. C. L. Rasenack, C. Jacobshagen, L. Fabritz, P. Kirchhof, S. K. G. Maier, T. Zhang, G. Hasenfuss, J. H. Brown, D. M. Bers, and L. S. Maier, “Ca²⁺/calmodulin-dependent protein kinase II regulates cardiac Na⁺ channels” *J Clin Invest*, vol. 116, no. 12, pp. 3127–38, Dec. 2006.
- [16] M. Krzywinski, J. Schein, I. Birol, J. Connors, R. Gascoyne, D. Horsman, S. J. Jones, and M. A. Marra, “Circos: an information aesthetic for comparative genomics” *Genome Res*, vol. 19, no. 9, pp. 1639–45, Sep. 2009.

LIST OF PUBLICATIONS

International Journals

- ✓ Vincenti A, **Passini E***, Fabbrini P, Luise MC, Severi S, Genovesi G.
Recurrent intradialytic paroxysmal atrial fibrillation: hypotheses on onset mechanisms based on clinical data and computational analysis.
Europace 2014; 16(3):pp 396–404.

(*Vincenti A. and Passini E. contributed equally to this work).
- ✓ **Passini E**, Genovesi S, Severi S.
Human Atrial Cell Models to Analyse Haemodialysis-related Effects on Cardiac Electrophysiology: Work in Progress.
Computational and Mathematical Methods in Medicine 2014:18 pp.
- ✓ **Passini E**, Ravagli E, Severi S.
Computational models of human ventricular cell electrophysiology: an established tool for arrhythmology.
Review manuscript in preparation, to be submitted to Europace.
- ✓ **Passini E**, Severi S.
Extracellular Calcium effects on human ventricular action potential: a new Markov model to explore L-Type Calcium current inactivation mechanisms.
Manuscript in preparation.
- ✓ **Passini E**, Rodriguez B, Mincholé A, Coppini R, Cerbai E, Severi S, Bueno-Orovio A.
Mechanisms of pro-arrhythmic abnormalities in human ventricular repolarization in hypertrophic cardiomyopathy
Manuscript in preparation, to be submitted to JMCC by May 2015.
- ✓ **Passini E**, Rodriguez B, Mincholé A, Coppini R, Cerbai E, Severi S, Bueno-Orovio A.
Potential Anti-Arrhythmic Therapies in Human Hypertrophic Cardiomyopathy: a computational study.
Manuscript in preparation.

International Conference Proceedings

- ✓ **Passini E**, Severi S.
Computational Analysis of Extracellular Calcium Effects on an Improved Human Ventricular Action Potential Model.
Computing in Cardiology 2012;39: pp873-876.

- ✓ **Passini E, Severi S.**
Human ventricular action potential prolongation in response to extracellular calcium: a computational study
Europace 2013;15, S2:p59.
- ✓ **Passini E, Pellegrini A, Caiani EG, Severi S.**
Computational Analysis of Head-Down Bed-Rest Effects on Cardiac Action Potential Duration.
Computing in Cardiology 2013;40:pp357-360.
- ✓ **Passini E, Severi S.**
Extracellular Calcium and L-Type Calcium Current Inactivation Mechanisms: a Computational Study.
Computing in Cardiology 2013;40: pp839-842.
- ✓ **Passini E, Severi S.**
Computational Analysis of Extracellular Calcium Effect on Action Potential Duration.
Biophysical Journal 2014;106(2), S1: p721a.
- ✓ **Passini E, Rodriguez B, Mincholé A, Coppini R, Cerbai E, Severi S, Bueno-Orovio A.**
Late Sodium Current Inhibition Counteracts Pro-arrhythmic Mechanisms in Human Hypertrophic Cardiomyopathy.
Computing in Cardiology 2014;41: pp861-864.

National Conference Proceedings

- ✓ **Passini E, Severi S.**
Computational Analysis of Rate Adaptation Mechanisms in Human Cardiac Action Potential.
Atti del III Congresso Nazionale in Bioingegneria 2012, (Proceedings of the III National Congress in Bioengineering)
Pàtron Editore, Bologna, pp287-288.
- ✓ **Genovesi S, Vincenti A, Passini E, Fabbrini P, Luise MC, Stella A, Severi S.**
Episodi Ricorrenti di Fibrillazione Atriale Parossistica Intra-Dialitica: Ipotesi sui Meccanismi di Innesco.
Abstract del 54° Congresso Nazionale Società Italiana di Nefrologia 2013, G Ital Nefrol 2013;30 (S61),p30
- ✓ **Passini E, Facciani M, Severi S.**
A new Markov model to explore L-Type Calcium current inactivation mechanisms.
Atti del IV Congresso Nazionale in Bioingegneria 2014, (Proceedings of the IV National Congress in Bioengineering)
Pàtron Editore, Bologna, 3pp.

RINGRAZIAMENTI

Un'amica mi ha fatto notare che i ringraziamenti sono l'unica parte personale di una tesi di Dottorato. Sono d'accordo, ma allo stesso tempo mi piace pensare di aver lasciato qualche traccia personale di capitolo in capitolo, visibile soprattutto nella scelta delle figure e dei colori.

Questa tesi è da consegnare tra circa due ore, l'ennesimo esempio del fallimento delle mie risoluzioni del tipo "non farò mai più nulla all'ultimo momento".

Come prima cosa, grazie al mio Supervisore Dr. Stefano Severi, meglio noto come "Il mio Prof". Mi ha introdotto nel mondo della ricerca ed è stato una guida preziosa negli ultimi tre anni, in questo lungo viaggio chiamato "PhD".

Con la sua passione per la modellistica cardiaca, la sua calma quasi perpetua e la sua disorganizzazione quotidiana, rimarrà per sempre il mio modello *in vivo*.

Grazie alla Prof. Blanca Rodriguez, così come al Dr. Alfonso Bueno-Orovio e alla Dr.ssa Ana Mincholé: mi hanno accolto ad Oxford a braccia aperte, e adesso sono impegnati ad aiutarmi nella transizione da studente a postdoc.

Sembra che sarà un problema non da poco, o meglio una sfida!

Grazie ai miei revisori, per i preziosi commenti e consigli sul mio lavoro: Prof. Mauro Ursino, Prof. Ronald Wilders, and Prof. Esther Pueyo.

Grazie a tutti i membri del collegio di Dottorato, in particolare il Prof. Angelo Cappello e la Prof.ssa Elisa Magosso, per la loro guida e il loro supporto.

Grazie alla Prof.ssa Cristiana Corsi e al Dr. Emanuele Giordano, che mi hanno sempre incoraggiato in questi anni.

Grazie a tutti i nostri collaboratori: Enrico G Caiani (Politecnico di Milano), Simonetta Genovesi e Antonio Vincenti (Università Milano-Bicocca), Raffaele Coppini ed Elisabetta Cerbai (Università di Firenze).

Un ringraziamento speciale alla mia famiglia, in particolare ad Anna (la Mamma), Luca (il mio Fratellone) e Caterina (la mia Sorellina). Sono quasi sicura nessuno di loro sia convinto che io abbia lavorato davvero in questi anni, ma non l'hanno mai confessato in pubblico. Grazie per il vostro affetto, il vostro supporto, le vostre lamentele e la vostra pazienza: in pratica, grazie di tutto. Vi voglio bene, ancora di più adesso che viviamo lontano!

Grazie a tutti i miei amici in Italia, in particolare Davide, Francesca, Teddy e Rossella. Siete troppi per essere nominati, ma so che sapete di chi sto parlando.

Grazie a tutti gli amici italiani a Oxford, in particolare Claudia, Francesca, Lorenzo, Manuele, Marco, Nicola e Stefano. Con voi vicino, vivere lontano da casa è stato molto più facile. Siete la mia famiglia in Inghilterra.

Grazie a tutti i miei colleghi di Cesena e Bologna, in particolare Michelangelo, Chiara, Claudia, Enrico, Aurora, Stefano, Giacomo e Dario.

Grazie a tutti i miei colleghi e amici di Oxford, in particolare Ana, Alfonso, Valentina, Ernesto, Sara, Anna, Simone, James e Alejandro.

Grazie a tutti i colleghi virtuali che ho incontrato in giro per il mondo e con cui ho condiviso splendide serate durante le conferenze.

Grazie ai nuovi e vecchi amici danzanti, sia in Italia sia in Inghilterra, in particolare Antonella, Nadir, Mauro e Graziella. Dopo un'intera giornata in ufficio di fronte al computer, un paio di ore a saltellare sono quello che ci vuole per sentirsi liberi e felici (anche se anche la cioccolata aiuta!).

I minuti a mia disposizione stanno finendo, e ho ancora qualche "piccolo dettaglio" da sistemare prima di consegnare la tesi. Tempo di tirare le somme...

Essere una "scienziata" è sempre stato il mio sogno. C'è ancora un sacco di strada da fare, ma adesso sono un pochino più vicina. Grazie a tutti coloro che hanno condiviso, condividono o condivideranno una parte di quella strada con me.

P.S. Per concludere, un buono proposito:



“La prossima volta, prometto di finire la tesi con un mese di anticipo!”

ACKNOWLEDGEMENTS

A friend once told me that the acknowledgements are the only personal part of a PhD thesis. I completely agree, even if I like to think I left some personal traces along the other chapters as well, especially in the choice of figures and colours.

This thesis is due in less than two hours, just another example of my “never again last minute” resolution failure. So, let’s try to be quick!

First of all, I would like to thank my supervisor Dr. Stefano Severi, better known as “Il mio Prof”. He introduced me to the world of science and research, and he has been a precious guide in the last three years, during this long journey called “PhD”.

With his passion for cardiac modelling, his almost perpetual calm and his chaotic way of organizing the everyday life, he will always be an *in vivo* model for me.

Many thanks to Prof. Blanca Rodriguez, as well as Dr. Alfonso Bueno-Orovio and Dr. Ana Mincholé: they welcomed me in Oxford with open arms, and they are now helping me in the hard transition from PhD student to postdoc.

Apparently, this is going to be a big problem... Well, let’s say a big challenge!

Many thanks to my reviewers, for the precious comments and suggestions about my work: Prof. Mauro Ursino, Prof. Ronald Wilders, and Prof. Esther Pueyo.

Many thanks to all the members of the PhD committee, especially Prof. Angelo Cappello and Prof. Elisa Magosso for their guidance and support.

Many thanks also to Prof. Cristiana Corsi and Dr. Emanuele Giordano, who constantly encouraged me during these three years.

Many thanks to all our collaborators: Enrico G Caiani (Politecnico di Milano), Simonetta Genovesi and Antonio Vincenti (University Milano-Bicocca), Raffaele Coppini and Elisabetta Cerbai (University of Florence).

A special thanks to all my family, especially to Anna (my Mum), Luca (my Brother) and Caterina (my Sister). I am quite sure none of them actually think I

have been really working in the last three years, but they never said that in public. Thank you for your love, your support, your complaints, your patience: basically, thank you for everything. I love you too, especially now that I am living afar!

Thanks to all my friends in Italy, especially Davide, Francesca, Teddy, and Rossella. You are too many to have a place here. I am sure you know who you are.

Thanks to all my Italian friends in Oxford, especially Claudia, Francesca, Lorenzo, Manuele, Marco, Nicola and Stefano. With you around, living far away from home has been much more easier. You are my family in the UK.

Thanks to all my colleagues in Cesena and Bologna, especially Michelangelo, Chiara, Claudia, Enrico, Aurora, Stefano, Giacomo and Dario.

Thanks to all my colleagues and friends in Oxford, especially Ana, Alfonso, Valentina, Ernesto, Sara, Anna, Simone, James and Alejandro.

Thanks to all the virtual colleagues I met around the world, with whom I shared some amazingly funny conference nights.

Thanks to all my old and new dancing friends, both in Italy and in the UK, especially Antonella, Nadir, Mauro and Graziella. After a whole day in the office in front of my laptop, a couple of hours just “jumping around” are exactly what needed to feel super happy (tablet and chocolate may help too!).

The minutes are running out, and I still need to finish some minor details before the final submission. So, it’s time to wrap up...

Being a scientist has always been my dream. There is still a long way to go, but I am now a little bit closer. Thanks to all the people who shared, are sharing and will share part of this journey with me.



P.S. I will conclude these acknowledgements with a new resolution, dedicated to the two people who shared with me the last-minute corrections yesterday night:

“I hereby declare that my next PhD thesis will be ready one month in advance!”